Enhancing Piezocatalysis For Chemical Transformations Using Cocatalysed Ferroelectrics

Guru Prasanna Ganapathi Subramaniam

https://orcid.org/0009-0009-2652-0470

A thesis submitted in partial fulfillment of the
requirements of London South Bank University
for the degree of Doctor of Philosophy

Supervisors:
Professor Steven Dunn *(Director of Studies)*
Dr. Suela Kellici

Chemical Process and Energy Engineering
London South Bank University

May 2024

DECLARATION

I Guru Prasanna Ganapathi Subramaniam, declare that the work presented in this thesis has been composed by myself with the invaluable support of my supervisory team. This thesis is submitted for examination with the intent to fulfill the requirements for the degree of Doctor of Philosophy in Chemical Process and Energy Engineering. I declare that this work represents my personal efforts and is a genuine product that has not been submitted for any other degree or professional qualifications. Moreover, I have taken due diligence to ensure that the work is original and to the best of my knowledge, it does not infringe upon copyright law. Any content derived from external sources has been appropriately cited and acknowledged within the text.

DEDICATION

This thesis is lovingly dedicated to my parents, Mr. Ganapathi Subramaniam and Mrs. Krishnammal, and my brother, Mr. Sriram. I will remain forever grateful for the important role they have played in shaping my life. Their care has been boundless, more than I could have ever imagined, and their constant support has been my foundation throughout this journey. Without their love, prayer, and unwavering encouragement, completing my PhD would have been an impossible task.

ABSTRACT

This thesis presents a comprehensive investigation into the piezocatalytic capabilities of barium titanate (BTO), both as a bare material and in combination with metal and metal oxide cocatalysts, for renewable energy production and environmental remediation. The research emphasises the degradation of organic dye pollutants and the enhancement of water splitting for hydrogen production. The degradation of Rhodamine B (RhB) using BTO nanoparticles is explored with the efficiency of the process depending on variables such as calcination temperature, structural properties, and the influence of atmosphere and agitation. The findings reveal the crucial role of oxygen in the degradation process and identify optimal conditions for catalyst loading and stirring parameters, positioning BTO as a viable candidate for environmental remediation. The application of BTO is extended to hydrogen production by mixing it with metallic Pt nanoparticles through a simple solid-state synthesis method. The interaction between BTO and Pt highlights a significant enhancement in hydrogen evolution rate, marking a substantial increase compared to pristine BTO. The research highlights the importance of BTO's ferroelectric properties and their contribution to improved catalytic activity. The formation of hydrogen peroxide as a byproduct presents both a challenge and an opportunity for future research aimed at optimising the selectivity and efficiency of piezocatalytic reactions.

Furthermore, the investigation delves into BTO-metal oxide composites and their piezocatalytic application for dye degradation. The structural properties of various BTO-metal oxide heterostructures are analysed, with BTO-CuO and BTO-NiO heterojunctions leading to an enhanced piezocatalytic activity compared to the other composites examined. The potential for generating reactive oxygen species (ROS) is discussed in relation to energy band theory, which is useful for understanding the mechanisms occurring at heterojunction interfaces. Collectively, the thesis demonstrates the comprehensive understanding of BTO as a piezocatalyst, and it confirms the role of cocatalysts in increasing BTO's piezocatalytic activity for dye degradation and hydrogen production, whether for environmental or in renewable energy applications.

Overall, the insights and methodologies offered in this work have significant implications for designing and optimising materials for environmental and energy applications in pollution reduction, and the harnessing of renewable energy. This detailed abstract encapsulates the core advancements of the thesis, bridging multiple investigations that showcases both the challenges and breakthroughs encountered throughout the research journey. It offers a comprehensive view of the scholarly contributions made in the domain of piezocatalysis, paving the way for future innovations in the emerging field.

ACKNOWLEDGEMENTS

I would like to express my profound gratitude to all who made it possible for me to complete my PhD journey.

First and foremost, I am sincerely grateful to my supervisor, Prof. Steve Dunn, whose expertise, understanding, and patience added significantly to my graduate experience. I appreciate the continuous support and encouragement to think independently and pursue new ideas. I must extend special thanks to Prof. Steve for providing funding for my exchange research trip to Vietnam, which was instrumental in broadening my cultural diversity and adaptability in research environment.

A special word of thanks also goes to Dr. Matthew Billing, for his insightful feedback and unwavering support throughout my PhD journey. Additionally, I wish to extend my gratitude to my second supervisor Dr. Suela Kellici and the members of RES committee whose assessments and feedback have been helpful in shaping my research direction.

I must acknowledge the LCEE for their PhD scholarship support without which this research would not have been possible. I am also thankful to the School of Engineering for providing me with the necessary resources and an environment conducive to research.

I am grateful to Dr. Phuong for the invitation to spend a month at the Institute of Chemical Technology in Vietnam, an opportunity that developed constructive research collaboration. Special thanks to Mr. Duy and Ms. Mandy for ensuring my stay was both productive and truly enjoyable.

My research colleagues Abinaya, Aritra, Bahattin, Beth, Conor, Dilshan, Esme, Ellie, Falak, Gokul, Himal, Hossam, Maruf, Mishal, Mudasar, Nasif, Neal, Pavan, Shane, and Srikanth at LSBU deserve a special thanks for their constant support and appreciation, which have been a great motivational force. I would also like to thank Dr. Sanjayan, Dr. Hassan, Dr. Kiem, Dr. Yusuf, and Dr. Rabia for their technical assistance in laboratory work and other scientific discussions.

I would like to acknowledge Dr. Zhen, Dr. Sivakumar Bose, Dr. Vishwanathan, Dr. Robert, Bhuvanasundari, Shanmuga Priya, and many others who have contributed in many unseen ways to the successful completion of this thesis.

Last but not least, I express my heartfelt thanks to my family, whose love, sacrifice, and persistent belief in my abilities have supported me during my tough times. Their unwavering support and patience with the sacrifices made for the completion of this research have been the foundation of my strength and perseverance.

Special love and affection go to my nephew, ‘Sahasrajit’.

TABLE OF CONTENTS

LIST OF FIGURES

LIST OF TABLES

CHAPTER 1. INTRODUCTION

1.1 BACKGROUND OVERVIEW

As concerns over climate change and the consumption of fossil fuels continue, the field of catalysis remains of keen interest for alternative solutions. The search for such solutions is more pressing than ever. Catalysis, and in particular piezocatalysis, has emerged as a promising field as a result of its ability to generate reactive species such as hydroxyl radicals, hydroxide ions, and superoxide anion radicals from water and atmospheric oxygen. These reactive agents possess the oxidative process to decompose various pollutants, making piezocatalysis a promising avenue for addressing the environmental challenges posed by hazardous waste, contaminated groundwater, and industrial air pollutants.[1] Beyond environmental cleanup, piezocatalysis shows great promise in sustainable energy generation, notably in the production of hydrogen, a clean and high-energy fuel. The efficiency of conversion of mechanical energy into chemical energy in piezocatalytic processes is critical for challenging chemical transformations. However, despite its potential, the industrial adoption of piezocatalytic reactions has been limited. The effectiveness of these reactions is primarily based on the rate of formation of charge carriers (electrons and holes) stimulated by mechanical energy, the rate of recombination, and the efficiency of the carriers' transfer to adsorbed species on the catalyst's surface.[2] Enhancing the generation of charge carriers and fine-tuning the interface reactions in piezocatalytic materials can lead to more efficient hydrogen generation and pollutant degradation. These factors collectively determine the piezocatalytic reaction efficiency, and improvements in these areas could enhance the practical application of piezocatalysis in a variety of energy, environmental, biological, and diverse applications.

In this context, the role of ferroelectric materials becomes significant. Ferroelectric materials are recognised for their wide-bandgap semiconductor properties. These materials exhibit a unique characteristic, known as intrinsic polarisation, where the centres of positive and negative charges within a unit cell are misaligned. This misalignment leads to the formation of macroscopic charges on the surface of the ferroelectric material. Consequently, an internal field, known as the depolarisation field, is created, prompting charge carriers to move in opposite directions. This movement facilitates the spatial separation of oxidation and reduction reactions, a process crucial for various challenging chemical processes, including piezocatalysis.[3,4] The surface charges generated by inherent polarisation can be neutralised through two mechanisms: internal screening, where free charge carriers and defects within the ferroelectric material themselves compensate for the charges, and external screening, which involves the neutralisation of charges by molecules adsorbed from the surrounding environment. Furthermore, the spontaneous polarisation can interact with the dipoles of adsorbed molecules, effectively reducing the energy barrier for breaking chemical bonds. This interaction enhances the ability of the ferroelectric material to facilitate chemical reactions, particularly in piezocatalysis, making ferroelectric materials promising candidates for innovative piezocatalytic applications.[5,6]

1.2 RESEARCH MOTIVATION

Using ferroelectric materials known for their piezoelectric properties, piezocatalysis presents a promising pathway toward enhanced energy efficiency and sustainability. When mechanical stress is applied to these materials, the resulting induced electric field can influence surface reactions. This has the potential to overcome challenges such as high overpotentials and to reduce energy barriers without reliance on traditional catalysts. The convergence of piezocatalysis with the development of ferroelectric materials marks a significant advance in the field of catalysis. It opens the door to cleaner energy generation, improved environmental remediation techniques, and issues related to the economics and availability of conventional catalysts. As the scientific community explores the multifaceted role of catalysis in renewable energy production and pollutant degradation, the integration of piezocatalysis with the distinctive properties of ferroelectric materials stands out as a particularly promising approach. These materials are compelling because they can induce surface charge polarisation under mechanical stress, potentially modulating the adsorption and desorption processes that are critical to catalysis. Such capabilities open up exciting opportunities for advancing green catalysis in alignment with sustainable development goals.

The enhancement of semiconductors and catalysis, the development of innovative piezoelectric semiconductors, and the design of experimental setups to maximise piezoelectric effects are currently active areas of research. These efforts are poised to overcome existing limitations in catalysis and contribute to a cleaner, more energy-efficient future. This PhD thesis represents an approach to the design and synthesis of piezoelectric materials that contributes significantly to the evolution of chemical transformations. Building on the unique properties of ferroelectric materials discussed earlier, this work introduces innovative engineering strategies for piezoelectric materials to enhance charge carrier transfer. In particular, the integration of cocatalysts, such as metals and metal oxides, is explored, aiming to optimise the piezocatalytic process. The thesis provides a foundation for the scaling of these materials through facile synthesis methods and improving the conversion efficiency of challenging chemical reactions into valuable products, aligning with the global pursuit of sustainable development.

1.3 RESEARCH AIM AND OBJECTIVES

The PhD thesis work delves into the intricate relationship between piezoelectric properties and charge carrier dynamics, further elucidating the critical role previously discussed regarding piezoelectric materials in the acceleration of chemical reactions. Extending the discussion about the integration of piezocatalysis with ferroelectric materials opens up a novel methodology for the design and synthesis of materials. By leveraging the inherent properties of piezoelectric materials to effectively transfer charge carriers, the thesis offers a pathway to expedite chemical transformations, thereby aligning with the objectives of enhancing catalytic efficiency and contributing to greener, more sustainable chemical processes.

Furthermore, the PhD thesis work goes beyond the experimental design and addresses the critical need for scalability in the production of these advanced piezoelectric materials. It proposes innovative techniques that enable cost-effective, large-scale synthesis. These advances are crucial, as they pave the way for the widespread adoption of piezocatalytic materials in industrial applications, providing a substantial impetus for the transition toward sustainable and efficient chemical processes, as previously discussed. This focus on scalability complements the earlier emphasis on novel synthesis methods, thus underscoring the practical significance and potential impact of this research.

Building on the previous discussions which highlighted the critical role of ferroelectric materials in catalytic applications, the objectives of the PhD thesis can be outlined as follows:

Objective 1 investigates the influence of various cocatalysts, particularly metals and metal oxides, on the piezoelectric properties and overall efficiency of these materials. There is a concerted effort to bridge the gap from laboratory research to practical application by developing synthesis methods that are both efficient and scalable, in accord with the thesis's commitment to the development of sustainable chemical processes.

Objective 2 is focused on pioneering techniques for the incorporation of cocatalysts into the production of piezoelectric materials. This is to optimise their effectiveness for critical applications such as hydrogen generation and dye degradation, which are essential for progressing towards a more sustainable future. These efforts aim to conceptualise new design strategies that may provide innovative enhancements to sustainable energy systems.

Building upon the foundational research of designing and synthesising piezoelectric materials with cocatalysts, the thesis advances to:

Objective 3 is dedicated to deepening the understanding of the scientific principles that influence the efficiency of piezoelectric materials. It involves rigorous studies focused on uncovering how piezoelectric properties contribute to intrinsic polarisation with low-energy input. This understanding is crucial to improving chemical reactivity and provides essential insights for the innovation of future material designs.

Objective 4 focused on a practical performance evaluation of piezoelectric materials and their potential role in chemical production. This includes assessing catalyst effectiveness, measuring the energy efficiency of reactions experimentally, and conducting an extensive review of how piezoelectric materials can be integrated into and benefit chemical processes.

1.4 CONTRIBUTIONS TO THE KNOWLEDGE GAP

This PhD research contributes significantly to bridging the current knowledge gap in the field of piezocatalysis. Using a simple and scalable synthesis procedure, this work succeeds in the development of piezocatalysts. Leveraging metal and metal oxide cocatalysts coupled with ferroelectric materials, this research goes beyond the synthesis process, providing a thorough analysis of the catalyst crystal structure, surface morphology, and operating experimental conditions. These efforts not only enhance the piezocatalytic activity but also provide an understanding of the interactions at play within these catalysts and the underlying mechanisms of their catalytic activity. The findings presented in this work, fortified by meticulous studies and robust experimental techniques, represent a significant leap in the understanding of piezocatalytic processes. By fine-tuning the synthesis and operating conditions of piezocatalysts, this work presents optimised solutions to achieve maximum efficiency in piezocatalysis. This research effectively fills critical knowledge gaps within this growing and promising field for the catalytical use of further exploration and innovation in sustainable chemical processes.

1.5 ORGANISATION OF THE THESIS CHAPTERS

This thesis is organised into 7 chapters, each designed to explore different features and progressively build upon the information gathered. The layout of this thesis is as follows:

Chapter 1: Introduction - This initial chapter sets the stage for the thesis, providing background information, stating the research problem, and outlining the main objectives and hypotheses of the study.

Chapter 2: Literature Review - The second chapter reviews existing literature related to the research topic, identifying gaps in knowledge that the thesis aims to address. The discussion includes the background of ferroelectric materials, their surface properties, the mechanisms underlying semiconductor piezocatalysis and its state-of-the-art, as well as current applications of ferroelectric materials in piezocatalysis.

Chapter 3: Experimental Methodology - Here, the research methods used to gather and analyse data are detailed, along with discussions of the study's scope, constraints, and the chosen methodological framework.

Chapter 4: This chapter explores the impact of stirring regimes on the piezocatalytic degradation of RhB dye using BTO nanoparticles. A systematic approach is employed, from synthesising BTO via the solid-state reaction method to characterising its structural and morphological properties through XRD and SEM analyses. The results confirm that optimal stirring significantly enhances piezocatalytic activity, achieving a maximum dye degradation rate. The study concludes with the promise of using mechanical stirring and BTO nanoparticles as an efficient, low-energy method for environmental remediation.

Chapter 5: This chapter investigates the use of piezocatalysis for water splitting by enhancing carrier mobility through a Pt-metal cocatalyst on a ferroelectric substrate BTO. The positive influence of the substrate on the reactions is supported by evidence, highlighting the importance of understanding the sonochemical and piezocatalytic contributions to catalysis. Research demonstrates a fourfold increase in H_2 production with BTO/Pt compared to BTO alone, highlighting the potential of hybrid materials to improve piezocatalytic processes.

Chapter 6: This chapter investigates the piezocatalytic activity of BTO with various metal oxides (NiO, CuO, Fe_2O_3 and Co_3O_4) as a hybrid piezocatalysts, focussing on their synthesis and efficacy in the degradation of RhB. Expanding on the research introduced in Chapter 4, the discussion highlights the use of metal oxides on ferroelectric substrates, employing mechanical stirring as a low-energy input. The improved piezocatalytic performance is analysed in terms of structural influence, with the role of the energy band diagram in enhancing this activity.

Chapter 7: Conclusion and Future Work - The final chapter summarises the key findings of the thesis, draws conclusions based on the research objectives, discusses the limitations of the study, and offers recommendations for future research.

CHAPTER 2. LITERATURE REVIEW

Catalysis plays a central role in the development of sustainable solutions for energy production and environmental management. As global energy demands continue to rise and environmental concerns such as pollution and climate change are increasing, the development of efficient and clean energy sources has become imperative. Catalysis offers a pathway to address these issues by enhancing the rates of chemical reactions, thereby enabling the development of more efficient industrial processes. In the pursuit of energy sustainability, catalytic processes play a crucial role in enabling the challenging chemical transformations necessary for the production of useful chemicals. In the context of energy sustainability, catalysis highlights the production of alternative fuels, including hydrogen, through a variety of challenging chemical transformations. Catalytic reactions are essential for environmental protection and energy production, enabling the complex chemical transformations that modern society demands. Recognised as a clean energy carrier for the future, hydrogen can be produced through various catalytic methods (**Figure 2.1**).[7]

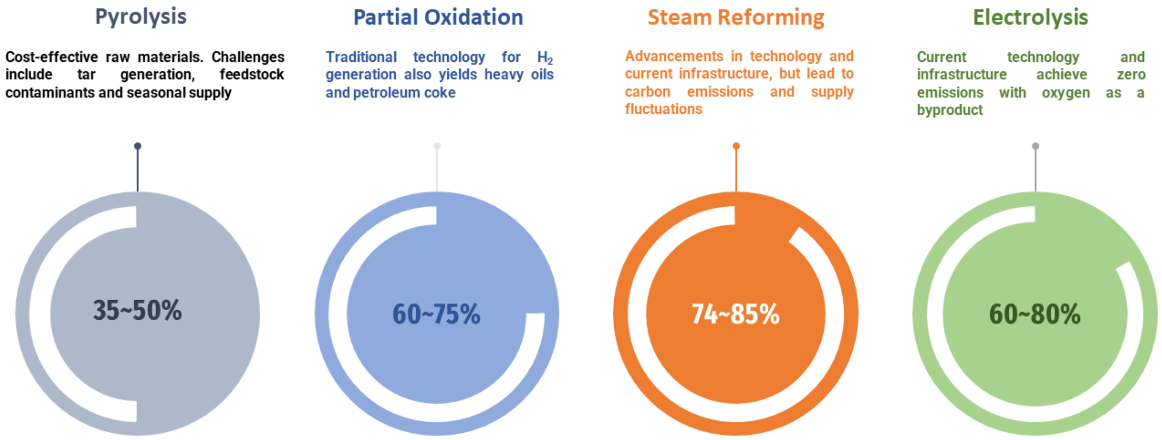

Pyrolysis

Cost-effective raw materials. Challenges include tar generation, feedstock contaminants and seasonal supply

Partial Oxidation

Traditional technology for H_2 generation also yields heavy oils and petroleum coke

Steam Reforming

Advancements in technology and current infrastructure, but lead to carbon emissions and supply fluctuations

Electrolysis

Current technology and infrastructure achieve zero emissions with oxygen as a byproduct

Figure 2.1 Comparative overview of traditional hydrogen production techniques

In each of these processes, catalysts are indispensable for reducing the energy barriers associated with hydrogen evolution reactions. The efficiency of these processes lies in the effectiveness of the catalysts used to accelerate the reactions while minimising energy consumption. This scenario underscores the urgent need to develop renewable and clean energy sources that can reduce carbon footprint and promote energy security. By focussing on the advancement of such technologies, one can pave the way for a more sustainable and environmentally conscious future in which clean and unlimited energy sources form the basis of global energy consumption.[8]

The significance of catalysis extends beyond energy production and plays a key role in environmental protection. It is crucial for the degradation of organic dyes and other pollutants commonly found in industrial wastewater. For example, advanced oxidation processes leverage catalysis to generate reactive species capable of breaking down complex organic molecules into less harmful substances. This action contributes significantly to the preservation of water quality and the health of aquatic ecosystems. The effectiveness of these techniques is largely based on the condition and high efficiency of the catalysts, which transform contaminants into harmless substances while minimising the generation of secondary waste. Various methods are used for wastewater treatment, including physical, chemical, and biological approaches, each designed to remove pollutants such as dyes, ensuring cleaner discharge into the environment (**Figure 2.2**).[9]

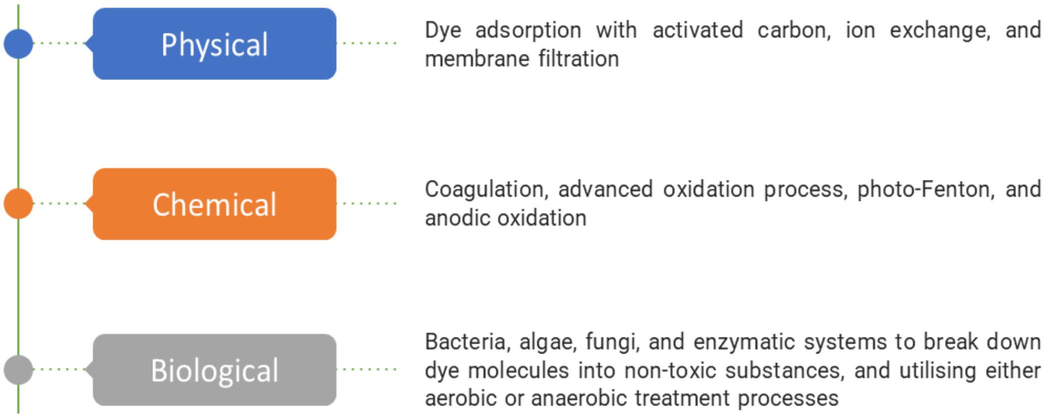

Figure 2.2 Overview of dye removal techniques

Diverse catalytic processes have been explored to address environmental and energy-related challenges, each with distinct mechanisms and applications. In the field of catalysis, researchers currently face several limitations that drive the exploration of advanced materials and the development of innovative techniques. These limitations include scarcity of resources, environmental concerns, scalability, efficiency, etc. These challenges have led researchers to investigate advanced functional materials that offer improved stability, selectivity, and efficiency. Innovative techniques such as nanostructuring, surface modification, and catalyst design are being studied to enhance catalytic performance.

Moreover, a demanding effort to develop catalysts from abundant and nontoxic elements, a move that supports sustainable practices. This research aims to break through current limitations and broaden the scope of catalysis to better address the pressing demands of energy and environmental management. In the past decade, increasing emphasis has been placed on the improvement of catalytic systems and introducing innovative catalytic materials, particularly in the fields of photocatalysis, pyrocatalysis, and electrocatalysis. The focus is on piezocatalysis—a promising area that uses the piezoelectric effect to initiate challenging chemical reactions and shows significant potential as a novel frontier in the field. However, it should be noted that other catalytic processes are governed by specific mechanisms determined by the type of energy input, as shown in **Figure 2.3**.

Photocatalysis depends on light energy to drive chemical reactions, offering a sustainable approach to degrade organic pollutants and generate clean energy. Pyrocatalysis uses thermal energy to facilitate chemical transformations, and electrocatalysis uses electrical currents to accelerate reactions, playing a pivotal role in energy conversion and storage devices such as fuel cells and electrolysers. These catalysis methods are effective in their domains and often encounter constraints.

The Researchers discussed the need for specific reaction conditions, limited catalyst stability, and selectivity.[10–13] Photocatalysis is significantly on the intensity of light, and its efficiency can decrease substantially under conditions with insufficient light. The process of recovering and recycling photocatalysts after their use is often complex, which can make the system less sustainable and economically viable. Additionally, many of the materials currently used as photocatalysts absorb light primarily in the ultraviolet range. Since ultraviolet light comprises only a small fraction of the solar spectrum, this narrow absorption range severely limits the effectiveness of these materials when exposed to natural sunlight, which is mostly composed of visible light. Another critical issue affecting photocatalysis is the recombination of photogenerated charge carriers (electrons and holes), which can occur before they participate in the desired reactions, thereby limiting the overall reaction efficiency. Strategies to extend the absorption spectrum and hamper charge carrier recombination, such as doping with other materials or constructing heterojunction structures, are important areas of research that aim to improve the performance of photocatalytic systems.[10]

Electrocatalysis is a process that depends on the application of electrical potential to drive chemical reactions. Efficient electrocatalysis requires not only suitable electrode materials but also control over the electrical and ionic interfaces. One of the primary factors affecting electrocatalysis is the Faradaic efficiency, which is related to the percentage of electrons used for the desired reaction versus the side reactions. Materials used for electrocatalysts often need to possess high electrical conductivity, catalytic activity, and stability under the operational conditions. Additionally, the design and surface properties of the catalysts are critical in determining their activity and selectivity for specific reactions, such as oxygen reduction or hydrogen evolution in fuel cells. Overcoming the challenges of electrocatalyst degradation over time and optimising the overpotential, the extra energy required to drive a reaction at a given rate, is essential for developing more sustainable and energy-efficient processes. Thus, electrocatalysis represents a crucial field of study, aimed at improving energy conversion systems and contributing to the advancement of renewable energy technologies.[12]

Pyrocatalysis involves the continuous cycling of heating and cooling, that is, thermal fluctuations, to harness the energy required for chemical processes. Temperature

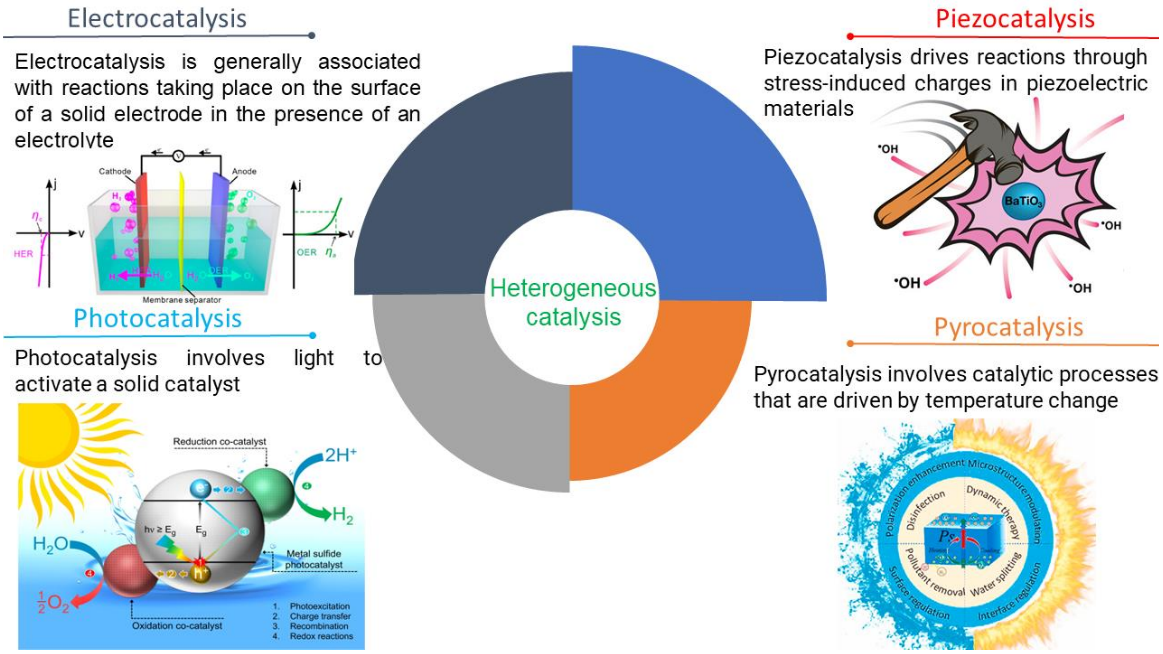

Electrocatalysis

Electrocatalysis is generally associated with reactions taking place on the surface of a solid electrode in the presence of an electrolyte

Photocatalysis

Photocatalysis involves light to activate a solid catalyst

Piezocatalysis

Piezocatalysis drives reactions through stress-induced charges in piezoelectric materials

Pyrocatalysis

Pyrocatalysis involves catalytic processes that are driven by temperature change

Figure 2.3 Classification of heterogeneous catalytic processes. Figures are adapted from Ref[10–13]

oscillations to reach a certain threshold, at which the energy input becomes sufficient to overcome the activation energy for reactions such as CO_2 reduction and water splitting. This method can be particularly advantageous for reactions that benefit from periodic heating and cooling because it can potentially alter reaction pathways, improve selectivity, and enhance yields. However, practical implementation of pyrocatalysis presents challenges, including maintaining the integrity of the catalyst under repeated thermal stress, achieving precise control over temperature fluctuations, and optimising the process's energy efficiency. The impact of these thermal cycles on catalytic activity is a promising area for further research.[13]

This review highlights the paradigm shift toward piezocatalysis and the critical role of ferroelectric materials, with a focus on barium titanate. Piezoelectric materials have gained significant attention in recent scientific research due to their unique electrical properties that address their potential to catalyse chemical reactions through mechanical stress. The method evaluates the synthesis methods, properties, and enhancements brought about by cocatalysts while recognising the proliferation of materials from diverse classes in promoting piezocatalytic reactions. This review not only catalogues an array of materials used in these processes, but also promotes understanding of the latest developments and their potential impact on future research. The following sections will delve into case studies and empirical results that explain the mechanisms and practical applications of these materials.

2.1 OVERVIEW OF FUNCTIONAL MATERIALS

The arrangement of ions within materials not only influences their electronic functionalities, such as dielectric properties, but also dictates their catalytic behaviours. Research efforts are now directed towards a more profound understanding of these materials, aiming to optimise them for various applications, ranging from electronics to catalysis, and to identify new materials that may offer enhanced catalytic properties. The dielectric materials play an indispensable role in the field of electronics and energy storage, known primarily for their ability to resist electric current while exhibiting high dielectric permittivity. These attributes make them crucial for applications such as capacitors, where they act as insulators and store electrical charge. However, within this broad category of materials are a group characterised by an intriguing phenomenon: ferroelectric materials.

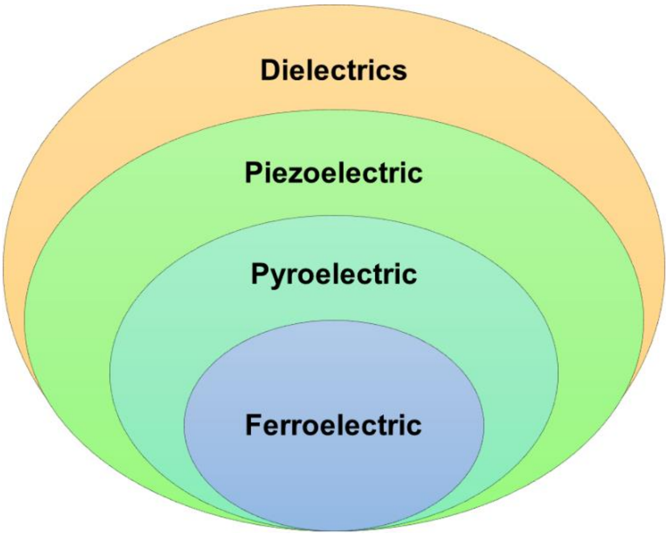

Figure 2.4 Hierarchical relationship among piezoelectric, pyroelectric, and ferroelectric materials

Unlike normal dielectrics, the polarisation in ferroelectric materials is switchable under the application of an external electric field, giving them piezoelectric and pyroelectric qualities, and this property ignites interest in their use for a range of advanced applications beyond that of standard dielectrics, such as non-volatile memory in computers, piezoelectric sensors, and actuators, and as key components in the emerging domain of piezocatalysis. Ferroelectric materials inherently possess both pyroelectric and piezoelectric properties. Although all pyroelectric materials are inherently piezoelectric, the converse is not true: not all piezoelectric materials are pyroelectric. Additionally, not every pyroelectric material is ferroelectric, indicating that these terms describe overlapping but distinct subsets of materials with specific properties (Error! Reference source not found.).[14]

In general, solid materials can be classified as crystalline or amorphous. Crystalline materials have a regular arrangement of atoms that extends over both short-range and long-range order, whereas amorphous materials have an irregular arrangement of atoms with only short-range order. That is, crystalline materials exhibit a symmetrical structure, and amorphous materials exhibit a nonsymmetric structure.

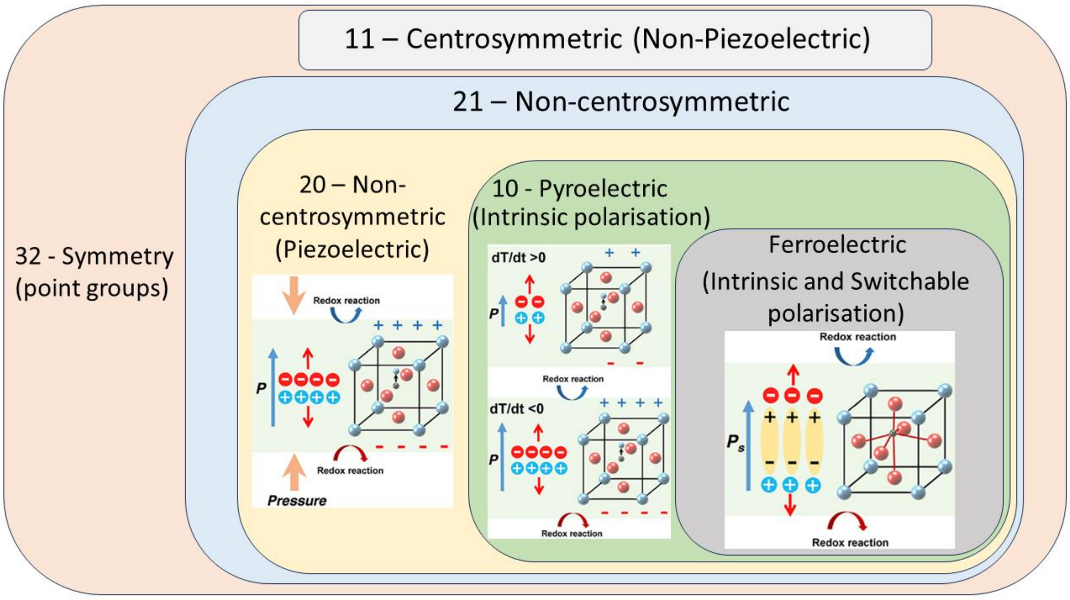

Figure 2.5 Correlation between symmetry point groups and catalytic properties. Adapted from Ref[16]

In crystallography, there are 32-point groups, of which 21 crystal classes are noncentrosymmetric. Among these, the 20-point groups exhibit piezoelectric properties because they do not have a centre of symmetry. However, the cubic 432-point group, while noncentrosymmetric, does not exhibit piezoelectricity. Of the piezoelectric crystal classes, the 10-point groups are polar and exhibit pyroelectric characteristics. These point groups are 1, 2, m, mm2, 4, 4mm, 3, 3m, 6, and 6mm.[15]

Table 2.1 Key distinctions among piezoelectric, pyroelectric, and ferroelectric materials based on polarisation variations

Classification of Dielectric materials	Mechanical stress	Temperature change	Intrinsic polarisation	Switchable Polarisation
Piezoelectric	✖			
Pyroelectric	✖	✖	✖	
Ferroelectric	✖	✖	✖	✖

Figure 2.5 illustrates the subsets of piezoelectric, pyroelectric, and ferroelectric materials based on their catalytic activity.[16] As a subset of dielectric materials, ferroelectric materials not only maintain basic dielectric properties, but also possess inherent electric

polarisation. To understand the unique properties of ferroelectric materials, it is necessary to address their common origin: polarisation,[17] as highlighted in **Table 2.1**.

2.2 FERROELECTRIC PEROVSKITES: IMPLICATIONS FOR PIEZOCATALYSIS

Perovskite materials are integral to numerous advanced technological applications due to their unique ferroelectric, piezoelectric, and photocatalytic properties. As the synthesis of these materials is pivotal in determining their final characteristics and performance, a thorough understanding of the available synthesis methods is essential. The Djellabi *et al.*, review article presents a comprehensive yet brief overview of the synthesis methods for $XTiO_3$ perovskite materials.[18] It elucidates the fundamental processes and their impact on the properties of $XTiO_3$ as piezocatalysts, particularly for environmental remediation and energy harvesting.

The discussion covers central techniques such as hydrothermal, sol-gel, and solid-state reactions, emphasising how each method uniquely optimises ceramic properties for various applications. Hydrothermal synthesis, which involves reactions in a high-temperature, high-pressure aqueous environment, offers control over particle size and morphology through careful adjustment of conditions such as temperature, reaction duration, pH, and precursor characteristics. This method yields high surface area powders with superior crystallinity, which further increases catalytic efficiency compared to traditional preparation techniques. The sol-gel method is a versatile chemical synthesis process widely used to produce ceramic-based materials and composites. Renowned for its simplicity and cost-effectiveness, the sol-gel technique is capable of yielding high-quality products with expansive surface areas. The process is precisely controllable and unfolds in five distinct stages: hydrolysis, condensation, ageing, drying, and crystallisation. This allows for exceptional tailoring of the surface characteristics and functionalities of the resulting materials.

The solid-state reaction route is a well-established and straightforward technique for synthesising perovskite-type oxides that has several benefits, especially in industrial production. It is valued for its ease of implementation, largely due to the simplicity of the ball mill mixing step. The approach involves mechanically mixing solid raw materials such as carbonates and oxides, followed by a high-temperature treatment (typically above 1000°C) to attain the desired crystalline phases. This method is capable of producing high-purity and well-crystallised materials, which is essential for applications requiring precise material properties. However, there are limitations to this methodology. It requires significant energy input, particularly for the high-temperature calcination process. Finally, achieving nanoscale, pure, and single-phase perovskite particles can be challenging, as the success of the method heavily depends on the reactant's particle size and the energy input during the ball milling process. This research highlights a significant advance in the synthesis of nano-crystalline and nanocrystalline titanate perovskites through the solid-state reaction method.[19–21]

By optimising the parameters, specifically the ball impact energy and frequency during the ball-milling process, they achieved a more efficient and effective reaction yielding the desired product. This refined process not only reduced the required reaction time, but also brought down the calcination temperature and duration. Such advancements underscore the method's potential for producing high-quality nanomaterials in a more sustainably and economically. In ferroelectric materials, intrinsic polarisation refers to the level of polarisation within a given domain region. The range of polarisation in these materials is quite broad. For example, Rochelle salt has a reported value of approximately 0.017 μC cm^{-2},[22] while barium titanate has a much higher value of 26 μC cm^{-2}.[23] At or above a certain temperature known as the Curie temperature, this inherent polarisation vanishes, and the ferroelectric crystals transition into a paraelectric phase. The polarisation observed in the ferroelectric crystals is induced by phase transitions at the Curie temperature. These transitions can be classified as either order-disorder or displacive. In the paraelectric phase above the Curie point, atoms exhibit oscillatory motion around a centrosymmetric position; however, below the Curie point, the oscillations occur around a noncentrosymmetric, polar position. Perovskite structures with the ABO_3 formula, such as barium titanate, are classic examples of materials that exhibit displacive ferroelectric transitions. The Curie temperature for bulk $BaTiO_3$ is approximately 120°C to 130°C. Above this transition temperature, the perovskite unit cell assumes a cubic symmetry and exhibits paraelectric properties (i.e. it lacks a net polarisation). Below Curie temperature, $BaTiO_3$ typically exhibits a tetragonal unit cell structure, which is ferroelectric, although it can transform into orthorhombic or rhombohedral structures at even lower temperatures (**Figure 2.6**).[24,25]

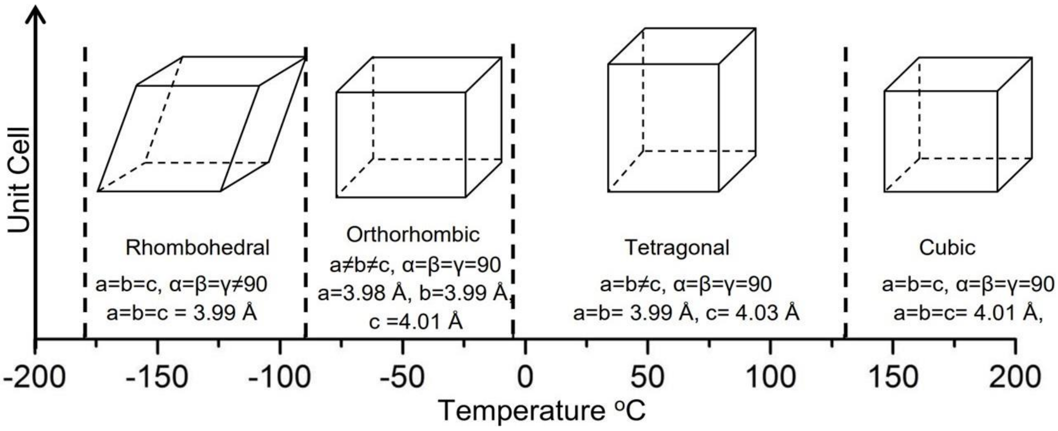

Figure 2.6 Phase transitions of barium titanate as it cools down through its Curie temperature, typically around 120°C to 130°C. The illustration shows the changes in the unit cell structure from cubic (paraelectric) to tetragonal (ferroelectric). Adapted from Ref[24,25]

It is known that cubic unit cells are generally paraelectric, whereas tetragonal unit cells are ferroelectric. Above the Curie point, the structure assumes a body-centred cubic form where the unit cell is centrosymmetric; this means that the charges are evenly distributed, with barium at the cube's corners and a titanium cation centrally located within an octahedron of oxygen. At below the Curie temperature, $BaTiO_3$ undergoes a displacive phase transition that transforms the crystal structure from the cubic paraelectric phase to ferroelectric tetragonal phase (**Figure 2.7**). During this transition, both barium and oxygen shift in the same direction relative to the central titanium. The oxygen octahedra retain their geometric shape despite this shift. Consequently, titanium moves off-center, leading to the formation of a dipole moment within the unit cell and giving $BaTiO_3$ its ferroelectric properties. As a result of the off-center displacement in $BaTiO_3$, the dipole moments within the material can be reoriented under the influence of an external electric field, a behaviour which is captured in the characteristic hysteresis loop.

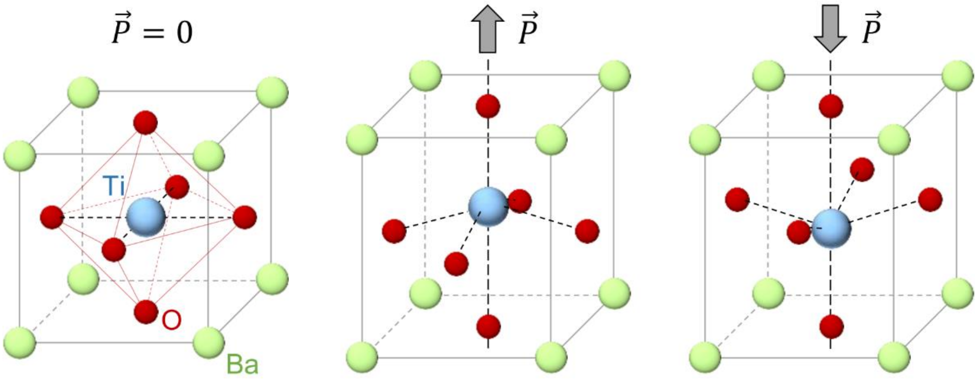

Figure 2.7 Paraelectric phase (Left corner) and ferroelectric phase of $BaTiO_3$ as well as their corresponding polarisation (Middle and Right corner). Adapted from Ref[23]

When an electric field is applied, domains in the ferroelectric material align with the direction of the field, causing an increase in polarisation. As the strength of the field increases, domains that were initially unfavourably orientated begin to switch their direction to align with the field, leading to a further increase in polarisation. This alignment of domains with the external field continues until saturation polarisation is reached. In a ferroelectric material, if an applied external electric field is strong enough to fully align the domains, the material will reach a state known as saturation polarisation, which is the maximum polarisation the material can achieve under an external electric field. If the field is then removed, the material will exhibit remnant polarisation, which is a measure of the polarisation that remains without an external field. However, the remnant polarisation is usually less than the saturation polarisation because not all domains will remain aligned once the external field is removed. If the external field is reversed, the domains switch their orientation, accordingly, eventually leading to a negative saturation polarisation if the field is strong enough and the polarisation will decrease and eventually reach zero. This occurs in a specific field called the coercive field. The coercive field is a measure of the field strength required to change the polarisation of the material to the opposite direction. By increasing the strength of the reversed external field beyond the coercive field, the polarisation will start to increase in the opposite direction until it reaches saturation again, completing the hysteresis loop. The hysteresis loop is a graphical representation of this dependence of polarisation on the applied electric field, indicating the presence of ferroelectricity depicted in **Figure 2.8**.

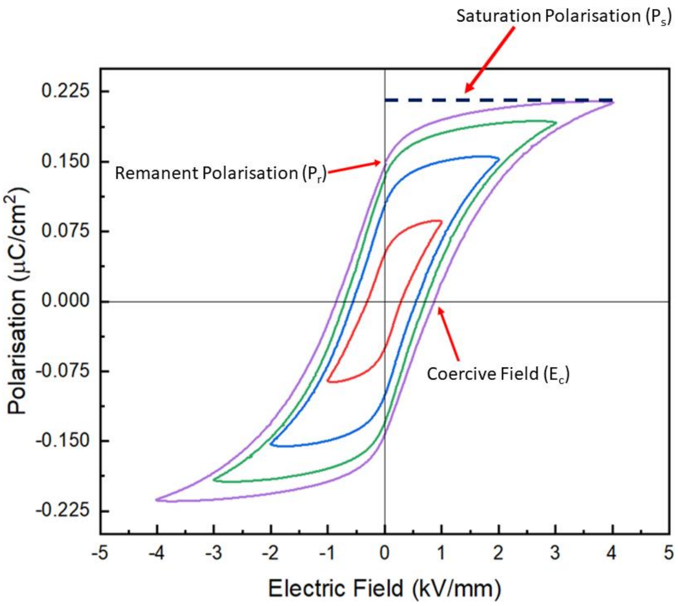

Figure 2.8 Hysteresis loop of a ferroelectric material depicting the dependence of polarisation on an applied electric field

Furthermore, this distinctive behaviour of ferroelectric materials is influenced by not only the external electric fields but also their physical dimensions. Theoretical and experimental research has found that the properties of ferroelectric particles can differ from those of the same materials in a larger, bulk form, a phenomenon known as size effects. The phase transition size of $BaTiO_3$ nanoparticles from tetragonal to cubic has been debated.[26,27] Overall, there is agreement that the tetragonal phase becomes less stable below 100 nm. Initial studies suggested transition sizes ranging from 120 to 350 nm. Later, more accurate characterisation indicated that the transition occurs below 100 nm, with reported threshold sizes of approximately 25 nm, 50 nm, and 70 nm.[28] This discrepancy led to the general acceptance of a core-shell model. This involves a tetragonal core and cubic shell, as well as producing a ferroelectric core and paraelectric shell illustrated in **Figure 2.9**.[29]

The shell has no net dipole, unlike the polarised core. As particle size decreases, the bulk dipole interactions naturally decrease, leading to a reduced correlation length. Consequently, the disordered paraelectric surface layer becomes dominant over the ordered ferroelectric bulk. This model accounts for the size of the phase transition as the nanoparticle shrinks. Key properties such as relative permittivity, inherent polarisation, and Curie temperature tend to decrease with the size of ferroelectric materials, particularly when scaled down to micrometres or less. Furthermore, ferroelectric particles exhibit a size threshold, below which they transition to paraelectric behaviour, lacking inherent polarisation, referred to as the critical size for ferroelectricity.[29] As the particles become smaller, the electrostatic field energy caused by the surface charge density increases, leading to the formation of domain walls. Such walls weaken the polarisation's structural basis—for example, the tetragonality of barium titanate—below 100 nm and cause a complete loss of such geometric structure at a threshold of around 10 nm in cubic nanoparticles.

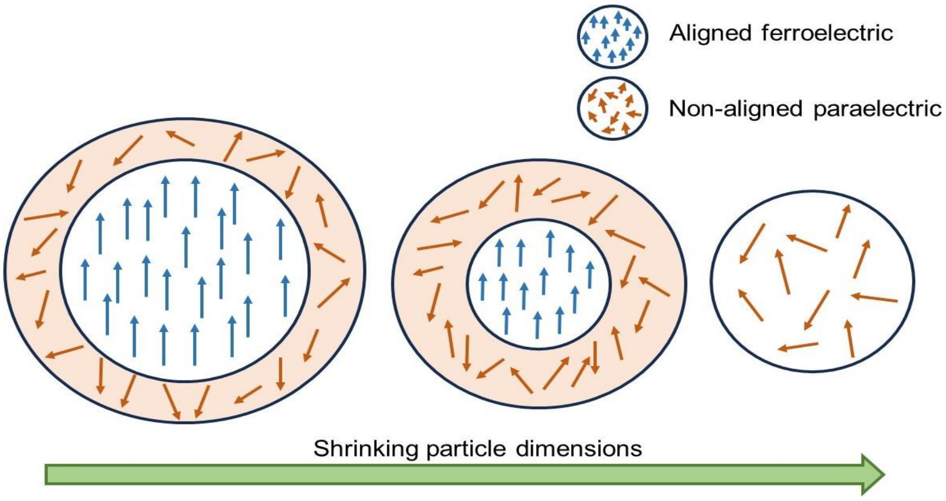

Figure 2.9 Transition of a particle from ordered to partially disordered, and finally to completely disordered state with reducing particle size. Reproduced from Ref[29]

Owing to this size-induced transition, the dielectric permittivity may rise along certain crystallographic directions, as per the Lyddane–Sachs–Teller relation, possibly boosting the permittivity and the pyroelectric coefficient. Meanwhile, other characteristics, including the dipole moment, may become reduced.[30] The fields of ferroelectric materials, such as $BaTiO_3$, in piezocatalysis are rapidly advancing and show promise for sustainable wastewater management. These materials are instrumental in the breakdown of organic pollutants. This review of the literature highlights various energy-harvesting approaches and environmental protection strategies, underscoring the significance of these areas. In the future, the potential for further innovation in piezocatalysis is vast, offering exciting prospects for breakthroughs in renewable energy harvesting and green chemical synthesis. In evaluating the current field of piezocatalysis research, a noticeable trend in the scholarly output has been observed. A bibliometric analysis reveals a significant increase in the number of publications over recent years, reflecting a growing scientific interest in this field as shown in **Figure 2.10**. This surge in literature suggests that piezocatalysis is becoming a focal point for innovative energy solutions and environmental remediation strategies. The trajectory of research outputs in recent years not only shows an escalating volume of work but also highlights a diversification in the scope of investigations, materials studied, and the targeted applications.

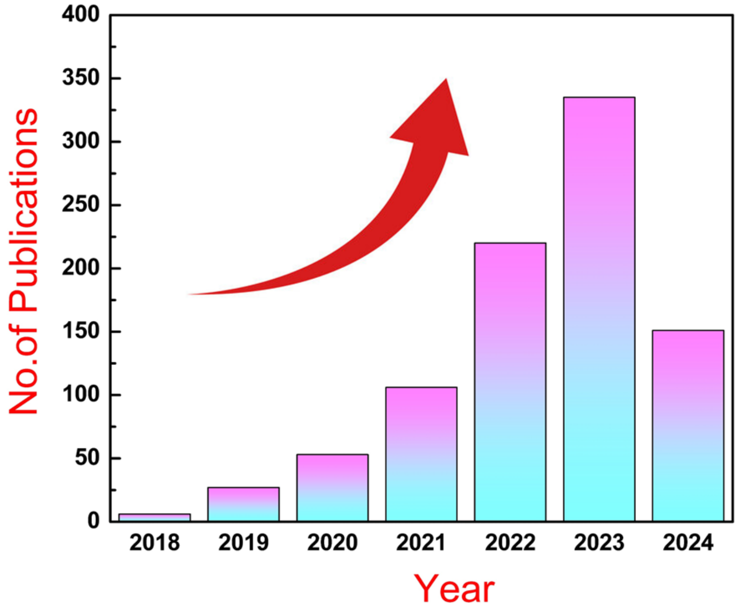

Figure 2.10 An emerging trend in piezocatalysis has been observed in recent years. The data was obtained from the Scopus database using the keyword ‘piezocatalytic’

2.3 UNDERSTANDING PIEZOCATALYSIS: HISTORICAL PERSPECTIVE AND CORE PRINCIPLES

In the seminal work of Ikeda *et al.*, an in-depth analysis was undertaken to detail the characteristic properties of mechano-catalytic water splitting by using metal oxides.[31] This insightful study primarily aimed to address two key questions that have emerged in this developing and intriguing field: (1) elucidating the fundamental reaction mechanisms and (2) determining the efficiency achievable through mechanocatalytic methods. However, there have been few reports related to the study published,[32–34] followed by a significant gap in the field.

Over a decade, in 2010, Hong *et al.*, explored water splitting with piezoelectric microfibers, this work remains a milestone in energy conversion and storage.[35] By harnessing the piezoelectrochemical (PZEC) effect, this study demonstrates a unique mechanism for converting mechanical energy into chemical energy, leading to the generation of hydrogen and oxygen gases from water. This innovative approach not only offers a pathway to improve energy efficiency but also holds promise for using environmental energy wastes, such as noise and vibrations, to produce clean hydrogen fuel. While promising, future research must address scalability, material optimisation, reaction dynamics, and conversion efficiency to fully realise the potential and bring this clean energy approach to the mainstream.

Research on the coupling of piezoelectric materials with electrochemical reactions has gained traction, offering innovative solutions for converting mechanical energy into chemical energy. Investigations led by Starr *et al.*, in 2012 outlined the phenomenon of piezocatalysis, where the application of mechanical strain on piezoelectrics in a liquid phase leads to the energetic manipulation of chemical species and results in hydrogen production.[36]

Furthermore, research from Starr *et al.*, and Zhang and Yates delves into the impact of the piezoelectric effect on band structure engineering at heterojunction interfaces.[37,38] Their studies provide insights into how the coupling of piezoelectric polarisation with intrinsic electric fields can tune charge transport behaviours in semiconductor materials and devices. Manipulation of band alignment at interfaces via piezoelectric effect mechanisms has shown promise in enhancing the performance of various electronic devices, leading to improvements in the quantum efficiency of LEDs, the operation of electromechanical memory diodes, and the efficiency of polymeric solar cells and photoelectrochemical cells. The use of piezoelectric potential to modulate reaction kinetics at semiconductor/solution interfaces offers an innovative method for engineering interfacial band structures without altering the chemical composition, which has potential to advance technologies in electronics, optoelectronics, and photovoltaics. However, it is essential to recognise that the integration of high-performance ferroelectric materials into heterojunction devices presents challenges due to their low conductivity. Careful consideration is crucial in the design of these devices to overcome any potential limitations that may arise.

This foundational work was expanded in 2015 with a comprehensive review of the underlying principles of piezocatalysis,[39] confirming the pivotal role in enhancing electrochemical reactions. Starr's model explains the distinct electrical properties observed in piezoelectric materials, particularly when comparing bare piezoelectric materials to those coated with metal.[40] The important point of the model is the role of the Fermi energy level in metals, which is dense with electronic states that can readily accept or donate electrons, thereby facilitating electrochemical reactions. This contrasts with bare semiconductor piezoelectrics like PZT, which are characterised by an energy gap, i.e., a band gap between the valence band from which electrons are donated and the conduction band into which electrons are accepted. In these materials, the piezoelectric induced potential generated by mechanical stress must overcome this bandgap to drive electrochemical reactions.

However, when piezoelectric materials are coated with metal, the abundance of electronic states at the metal's Fermi level minimises the need for such high piezoelectric potentials. This makes metal-coated piezoelectrics more efficient for initiating electrochemical reactions, as the metallic coating provides a more favourable environment for electron exchange due to its energetic properties, as shown in **Figure 2.11**.[40] Piezocatalysis, which integrates the piezoelectric effect with catalysis, takes advantage of the adjustable electronic states of piezoelectric materials to initiate or accelerate chemical reactions based on the surrounding chemical environment and applied mechanical strain.

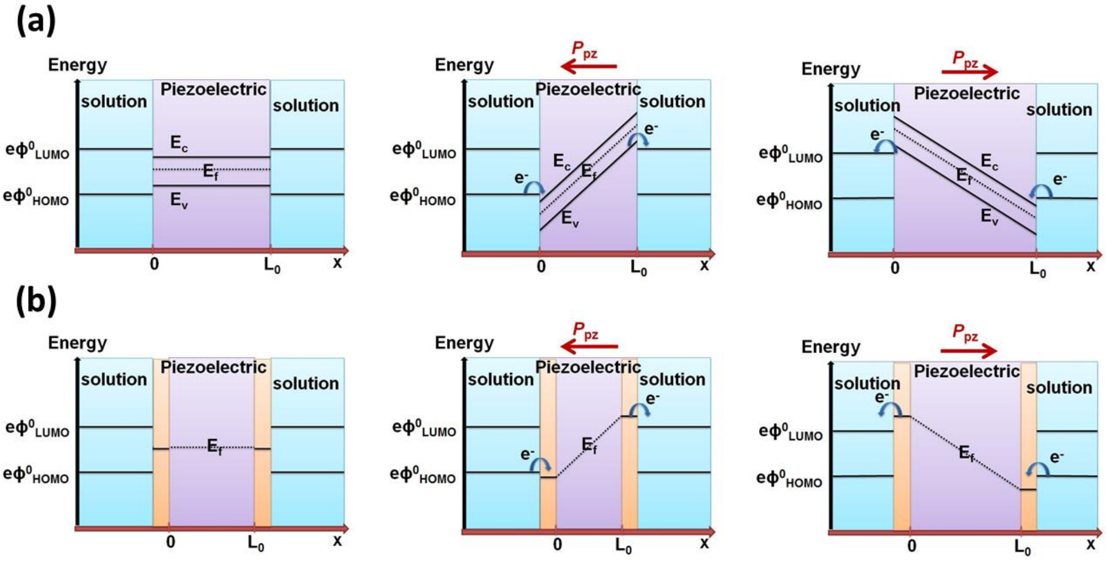

Figure 2.11 Piezoelectric materials as dynamic electron exchangers
(a) In a bare piezoelectric material, the energy bands act as electron reservoirs, interacting with surrounding molecules. Piezoelectric effect shifts energy levels.
(b) With metal electrodes on the piezoelectric material, their Fermi levels align. Piezoelectric effect still modulates energy bias. Adapted from Ref[40]

Two theories have been developed to explain piezocatalysis: the energy band theory and the screening charge effect.[41] Each provides its own valid explanations based on fundamental concepts and experimental evidence. However, they are distinct from each other and are useful in different situations. In the energy band theory, the piezo-induced potential regulates the band structure and controls the migration of internal carriers to the catalyst surface. The energy band alignments (the positions of the valence and conduction bands) that determine the activity of the piezocatalysts in catalysing specific chemical reactions. Specifically, a piezoelectric material is polarised under mechanical stimulation, leading to material deformation as a result of the displacement of the charge centre. The polarised positive and negative charges are then distributed on both sides of the piezoelectric material, and the generated charges will be involved in chemical reactions.

As shown in **Figure 2.12**,[42] the piezo-induced potential generated by the piezoelectric effect determines the energy levels of the valence band (VB) and conduction band (CB) of the piezoelectric material, facilitating charge exchange at the interface of the piezoelectric material and enabling efficient catalysis of redox reactions. For example, when the CB of the piezoelectric material is altered by the piezoelectric effect, the electrons (e^-) in the CB will reduce oxygen molecules to produce superoxide anions ($^{\cdot}O_2^-$). Concurrently, the holes (h^+) in the tilted VB will oxidise water molecules to produce hydroxyl radicals ($^{\cdot}OH$). Screening charges such as electrons and protons are essential in redox reactions for piezocatalysis. In piezoelectric materials, mechanical stress induces a potential that attracts these charges to the surface of the material.

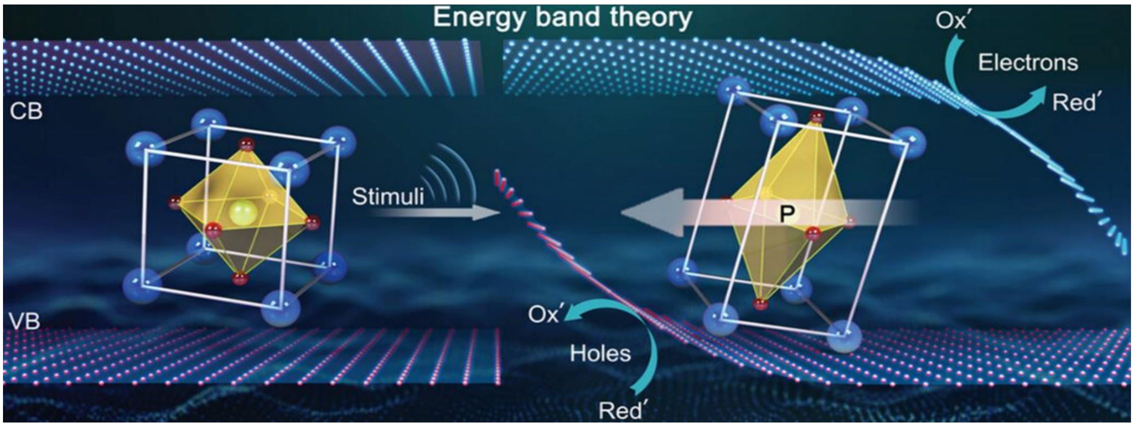

Figure 2.12 illustrating the energy band theory. (P: Represents the direction of piezoelectric polarisation). Adapted from Ref[42]

This charge attraction can lead to the dissociation of water molecules and the donation of electrons by hydroxide ions, while protons may serve as acceptors in oxidation reactions. The piezoelectrically induced potential plays a pivotal role in facilitating charge separation, enhancing transport, and reducing activation energy, thereby preventing electron-hole recombination, and enabling efficient catalysis. The dynamic screening effect, which refers to the temporal fluctuations in charge balance, is a consequence of variations in induced polarisation. For materials like $BaTiO_3$ without spontaneous polarisation, neutrality is maintained under no strain, with a balance between positive and negative centres. With the application of strain, this balance is altered, leading to the adsorption of screening charges. When the strain is released, the decrease in polarisation results in charge dispersion. Such a cyclic process, where mechanical stress leads to polarisation changes and subsequent charge mobilisation, is critical to piezocatalysis. The dynamic effect facilitates the adsorption and desorption of screening charges that are involved in the catalytic reactions, as shown in **Figure 2.13**.[41,43]

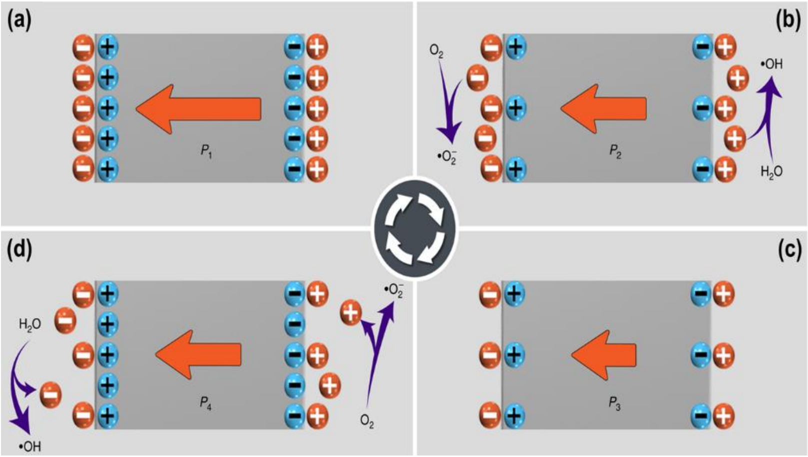

Figure 2.13 Schematic representation of the piezocatalytic mechanism illustrating the screening charge effect, where the orange circles represent surface charges, blue circles symbolise bound charges, and 'P' denotes polarisation. (a) Initial electrostatic equilibrium of a polarised piezoelectric material (b) Reactive oxygen species generation via release of screening charges under compressive strain (c) New electrostatic equilibrium after bound charge minimisation (d) Charge adsorption from electrolyte upon strain relaxation. Adapted from Ref[41]

Mechanical stress applied to piezocatalysts is critical for starting the piezocatalytic reaction because it supplies the initial energy for the transformation process. The polarisation field is essential in piezocatalysis because it cannot be completely neutralised without hampering the generation and separation of reactive charges. Thus, the strain must be applied periodically to maintain ongoing piezocatalytic reactions. Common methods to achieve this cyclical outcome strains include ultrasound-induced cavitation, water flow-induced shear force, ball milling-induced pressure,[44–50] thermal stress, and other forms of mechanical vibration. Additionally, a sufficient thickness of material along the orientation of the electric dipoles is necessary to trigger the piezoelectric chemical process.

The success of the piezocatalytic reaction is greatly dependent on the electric potential difference at the opposite poles, which is in line with thermodynamic principles. A proportional relationship exists between the piezopotential (V_p) and the thickness of the piezoelectric materials, as expressed by the formula in **Eq. 2.1**

$$V_p = \frac{\sigma_n d_{xn} W_x}{\varepsilon_{rx} \varepsilon_o} \quad \textbf{(Eq. 2.1)}$$

where d_{xn} is the piezoelectric coefficient, σ_n denotes the applied stress in dimension n, W_x is the width of the material in the x dimension, ε_{rx} is the relative permittivity in the x dimension, and 'ε_o' represents the permittivity of the free space or electric constant.[51] For example, piezocatalytic water splitting can occur when the 'V_p' exceeds 1.23 V. In terms of energy band theory, an adequate material thickness can induce a desirable piezo-induced potential that alters the energy band structure to facilitate the migration of high-energy charge carriers, ultimately aiding the catalytic reaction. A limited understanding of piezocatalysis mechanisms presents a challenge in the development of piezocatalysts for enhanced catalytic processes. However, insights from the advanced fields of photocatalysis,[52] and electrocatalysis may guide the design principles.[53]

Piezocatalysis, despite its distinct requirements for piezoelectric materials, shares a core objective with these fields: to generate and preserve electron-hole pairs efficiently. The key is to prolong their existence to avoid recombination, sustain their redox potential, and facilitate effective electron transfer for chemical reactions. The design focus on three critical factors according to the chosen mechanism: (1) electronic band structure, (2) surface active sites, and (3) the role of piezoelectric induced potential. The electronic band structure and surface-active sites are crucial in shaping the behaviour of charge carriers, as indicated by the screening charge effect and the energy band theory, ultimately dictating the efficiency of piezocatalytic reactions. The relationship of these determinants is thoroughly outlined by Sudrajat *et al*., and summarised in **Table 2.2**.[17]

Table 2.2 Essential characteristics of piezocatalysts that govern charge carrier behaviours, influencing redox reaction dynamics

	Properties of Charge Carriers		Mechanism of Piezocatalysis	
Piezocatalyst characteristics*	Quantitative (Number of charge carriers and charge density)	Qualitative (Electron-hole pair lifetime and redox potential)	Energy band theory	Screening charge effect
Relative permittivity	✖			✖
Electromechanical coupling coefficient	✖	✖		✖
Induced potential	✖	✖	✖	✖
Electrical conductivity		✖	✖	✖
Lattice defect	✖	✖	✖	✖
Band bending		✖	✖	
Band gap energy	✖		✖	
Band edge potentials		✖	✖	

*Catalyst properties can be adjusted by altering the piezocatalysts composition

Furthermore, the work of Sudrajat *et al*., provides critical perspectives on the design of piezocatalysts relevant to challenging chemical transformations.[17] In redox reactions, it is imperative that electrons possess a strong reduction potential, exceeding that of the reactants, to effectively drive the targeted reduction of desired products. However, materials with wide bandgaps face difficulties in generating an adequate number of charge carriers. Outlined criteria for an efficient piezocatalyst can be referenced for systematic enhancements. These criteria will vary on the expected mechanism within a particular piezocatalyst. Gaining insight from piezocatalysts that are active in similar reactions can inform potential mechanisms of piezocatalysis. However, due to the limited research on piezocatalytic reactions and ongoing investigations into the mechanisms of piezocatalysis, it is currently not feasible to establish generalised guidelines.

Table 2.3 Key factors in the design of an effective piezocatalyst

	Piezocatalysis mechanism	
Standard criteria for evaluating piezocatalysts	Energy band theory	Screening charge effect
A high piezoelectric charge coefficient is crucial for efficient charge carrier separation and transfer and for providing carriers with an adequate redox potential.		✖
A low resonant frequency is key for efficiently converting mechanical energy into electrical charges with high energy		✖
A low tendency for particle agglomeration is essential to maintain ultrasound absorption and ensure optimal acoustic intensity for the reaction	✖	✖
High relative permittivity is crucial for reducing binding energy and increasing charge carrier generation		✖
High electrical conductivity is the key for fast charge carrier migration to the surface	✖	✖
A high electromechanical coupling coefficient is essential for effectively bridging the electrochemical potential difference between internal and external charge carriers		✖
A moderate band gap is necessary to excite a significant number of charge carriers while preserving their redox potential	✖	
A suitable conduction band position, more negative than the standard reduction potential, is critical to efficiently converting chemicals into desired products	✖	
Optimised morphology enhances efficiency: (i) 0D: nanoparticles for greater potential. (ii) 1D: nanorods for improved charge separation; (iii) 2D: nanosheets for enhanced piezoelectricity; (iv) 3D: More branches for effective force capture	✖	✖
Numerous active sites, along with a large surface area, enhance active site accessibility, increase interfacial screening charges, and reduce electron-hole recombination.	✖	✖
Low scattering-to-absorption coefficient ratio for improved utilisation of sonoluminescence	✖	
A high Curie temperature ensures piezoelectricity over a wide temperature range, while a low specific heat capacity allows for efficient temperature modulation in pyroelectrics	✖	✖

Piezocatalytic activity is influenced by many factors that have complex and challenging interconnections, which change according to the specific traits of the piezocatalyst and the design of the catalytic reactor. What is effective in one reaction system may not be applicable in another. Assessing the inherent catalytic capacity of a pristine piezoelectric material, according to the design criteria and considerations presented in **Table 2.3**, is a critical initial step. If it does not meet expectations, it is important to make improvements in four main areas: how well it works, its ability to choose specific reactions, how long it lasts, and how safe it is. In general, a careful step-by-step method for assessing and improve the design of piezoelectric catalysts is really important for moving the field forward.

Challenges persist in the in-situ characterisation of nano-piezo materials due to low surface charge densities and signal detection limitations. Moreover, the presence of ions at higher electrolyte concentrations induces capacitive currents, reducing energy conversion efficiency. Addressing these issues, future research aims to extend the understanding of the influence of polarisation fields on electronic states and species interactions at piezoelectric surfaces and to promote diverse applications in energy storage, environmental remediation, and the development of advanced characterisation techniques. The classification of internal electric fields in energy and environmental catalysis outlined in these review articles,[54–60] is of significant importance as it provides a structured framework to understand the various mechanisms through which internal electric fields can enhance catalytic performance. By categorising internal electric fields into distinct types such as those in polar surface termination, piezoelectrics, and heterostructure materials, the research offers valuable insights into how these fields can be generated and used in catalytic systems as illustrated in **Figure 2.14**.[54]

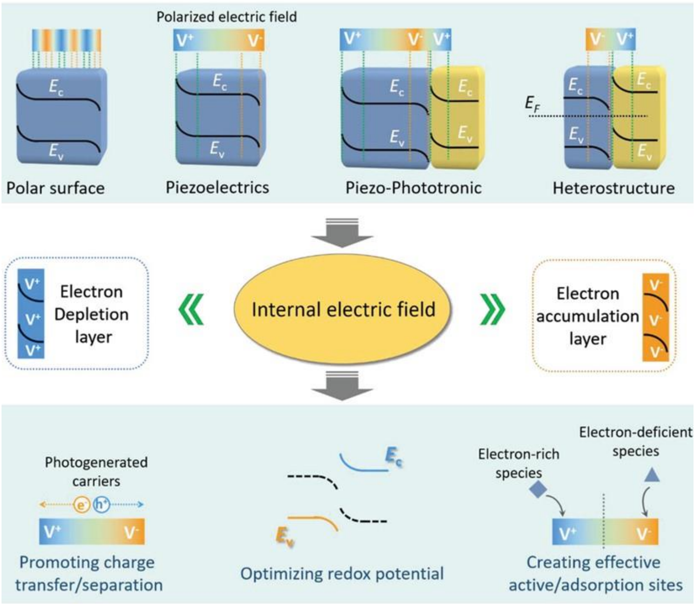

Figure 2.14 There are four types of internal electric fields, categorised based on their locations, each offering distinct advantages in catalysis. Adapted from Ref[54]

However, the study highlights a limitation in the need for precise control over doping and defects when modifying internal electric fields, indicating a current gap in both understanding and optimising these strategies. Overcoming this challenge and advancing the exploration of internal electric fields in harsh electrocatalytic environments could pave the way for more efficient and sustainable energy conversion and storage systems. Although ferroelectrics do not provide free charges for direct involvement in catalysis, this prompts investigation into their roles in this process. Their significant contribution is manifested in dynamic surface charge fluctuations that control the attachment and release of reactant species at the solid-electrolyte interfaces, i.e. the influence of transient surface charge densities on the kinetics of adsorption and desorption at the surface, factors that are critical because they constitute the rate-limiting phase of the catalytic reaction. These interactions change once the interface is disturbed, with the electron transfer kinetics shaping the formation of a layer of immobilised charges, known as the Helmholtz layer, which is characterised by the Debye screening length (d). Beyond the Helmholtz layer lies the diffuse region, where the influence of the solvated ions diminishes. Electron transfer persists until the electrochemical potentials of the ionic solution and the solid catalyst balance, leading to a potential difference, as illustrated in **Figure 2.15**.[61] The magnitude and nature of this potential difference are influenced by the charges in the solid material and the ionic concentration in the solution, modulated by external factors.

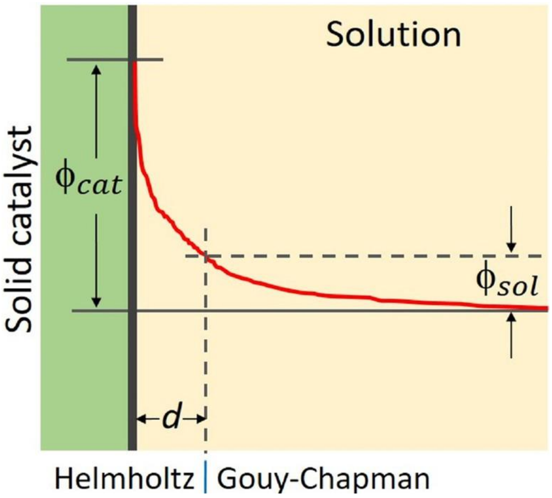

Figure 2.15 Schematic representation showing the charge dynamics at the ferroelectric catalyst interface, depicting the transition from the Helmholtz layer to the diffuse layer, and the modulation of potential by stress-induced piezoelectric effects. Adapted from Ref[61]

The classic theory of Helmholtz has been extended by Gouy, Chapman, and Stern to explain this phenomenon.[62–64] Unlike metallic electrodes, which require external energy sources to generate surface potentials, ferroelectrics inherently possess bound charges that create adjustable internal fields. The application of mechanical stress allows for the modulation of these fields. Such manipulation is crucial as it can align energy bands with redox potentials, facilitating effective charge separation and transfer—key processes for catalysis—without external energy inputs. The piezoelectric properties of ferroelectrics are therefore central to reshaping interfacial charge dynamics, enabling them to act as influential catalysts.[65] The interfacial dynamics governed by the Stern-Helmholtz layer is integral to the Langmuir-Hinshelwood mechanism, which underlines the kinetics of surface-mediated catalytic degradation. The surface charge distribution within the Stern-Helmholtz layer influences the attraction and availability of reactant molecules at the catalyst's active sites. In turn, these interactions directly impact the adsorption process, which is a critical first step in the Langmuir-Hinshelwood model. As such, a more charged surface could facilitate the adsorption of oppositely charged reactants, affecting both the rate and efficiency of the catalytic reaction. Understanding the properties of the Stern-Helmholtz layer can therefore provide insight into optimising the Langmuir-Hinshelwood kinetics, aiding the design of catalysts that are more effective for specific reactions, including the degradation of pollutants in environmental applications.[66] The Langmuir-Hinshelwood model examines the dynamics of surface-mediated reactions, fundamental to the heterogeneous catalysis. It accounts for the adsorption of reactants, their subsequent interactions once adhered, and the formation of products. This mechanism is crucial for decoding and refining a range of catalytic activities, such as the breakdown of organic substances and the oxidation of gases.[67] By delving into the behaviours of ferroelectric materials under stress and linking these to the Langmuir-Hinshelwood model of surface reactions,

$$r_0 = \frac{kKC_0}{1+KC_0} \qquad \textbf{(Eq. 2.2)}$$

The rate at which reactions occur on these catalytic surfaces is summarised by the initial reaction rate ‘r_0’, which is influenced by the starting concentration of RhB ‘C_0‘(mM), the rate constant ‘k’, and the equilibrium constant ‘K’, which reflects the balance between the RhB adsorption and desorption on the catalyst's surface. To determine ‘K’ and ‘k’, **Eq. 2.2** is expressed as a linear equation, where the slope and y-intercept are directly related to ‘K’ and ‘k’, respectively.

$$C_0 = k\frac{C_0}{r_0} - \frac{1}{K} \qquad \textbf{(Eq. 2.3)}$$

For low concentrations, **Eq. 2.2** simplifies to a pseudo-first-order kinetic equation representing the rate of decrease in the concentration of RhB over time.

$$r_i = -\frac{dC_i}{dt} = kKC_i \qquad \textbf{(Eq. 2.4)}$$

(Or)

$$ln\left(\frac{C_o}{C}\right) = K_{obs}\,t \qquad \textbf{(Eq. 2.5)}$$

From **Eq. 2.5**, $ln\left(\frac{C_o}{C}\right)$ versus time (t) plot then gives us the ‘K_{obs}’, which equals the product of ‘k’ (mM.h^{-1}) and ‘K’ (mM^{-1}) indicating rate of the dye concentration rate during a specific period of agitation and is calculated from the slope of this linear relationship.

When the modulation of potentials at the catalyst interface is enabled without the need for an external power source, ferroelectrics offer an innovative method for controlling reaction kinetics. This capability is especially beneficial in the field of piezocatalysis, an emerging area that integrates the principles of traditional heterogeneous catalysis with the distinctive properties of ferroelectrics, targeting environmental cleanup and energy conversion applications. The study by Amaechi *et al.*, conducts a critical evaluation of the efficiencies of various catalytic processes, placing a particular emphasis on the advancing area of piezocatalysis.[61] They calculate the efficiency of a typical photocatalytic process under solar irradiation to be about 0.0267%, considering the energy required for molecular bond breakage. Compared to photovoltaic systems usually exhibit around 15% efficiency. They also point out that solar-to-hydrogen conversion processes can achieve efficiencies of 16% to 20.6%, and the conversion of electrical power to hydrogen can achieve even higher efficiencies, up to 78%. This comparative analysis underscores the differences in performance among renewable energy conversion technologies, emphasising the importance of selecting the most efficient methods based on efficiency. However, Amaechi *et al.*, argue that efficiency should be considered in conjunction with cost-effectiveness to fully assess the viability of these catalytic processes. They proposed this strategy to potentially reshape the commercialisation of piezocatalytic materials for sustainable and energy-efficient water treatment solutions. Amaechi *et al.*, provides significant insight into the field of catalysis, positioning piezocatalysis as a viable, eco-friendly option that goes beyond simply efficiency metrics. Their discussion suggests that piezocatalysis is not only a technological innovation but also a scalable and economically sustainable option for catalytic processes. These perspectives are integral to my thesis, as they offer a comprehensive understanding of piezocatalysis that considers practical applications, economic affordability, and environmental impact.

Asgari *et al.*, and Francke *et al.*, provide a broad explanation of electron/hole catalysis, dividing it into main types based on the external energy that creates the electrons and holes.[68,69] These energies are mechanical energy (piezocatalysis), light (photocatalysis), chemicals (chemocatalysis), and electricity (electrocatalysis). Moving electrons to the right place is the key to making these chemical reactions happen. Piezocatalysis is an emerging field that involves the separation of charges within certain materials when they are subjected to mechanical stress (**Figure 2.16(a)**).[70] This stress can generate a polarisation field that influences the distribution of electrons and holes: electrons drive reduction reactions, while holes facilitate oxidation processes. The idea of using mechanical forces to drive electron/hole catalysis is quite new. These energised particles move to the surface of the material and take part in reactions that decide the speed of various chemical processes, such as the production of organic compounds, the formation of polymers, the generation of hydrogen, and the cleaning of wastewater.

Kubota *et al.*, were the first to use ball-milled piezoelectric nanoparticles to create aryl radicals from salt (**Figure 2.16(b) and (c)**).[44] This led to other reactions, such as adding boron or forming new aryl compounds, with moderate success. When compared to photocatalysis, the mechanochemical method has some advantages, such as being faster, possibly not needing a solvent which helps with solid materials, being simple without the need to carefully control the environment, being cost-effective and able to scale up, and using catalysts that can be reused. This makes it an attractive option for industrial use.

Current efforts in the field are directed towards using mechanochemistry for additional chemical processes, including the synthesis of cyclic compounds through radical reactions and the incorporation of fluorinated functionalities. Mechanical forces also show promise for the making of polymers through electron/hole catalysis, but more research is needed to fully understand how efficiently electrons are used.

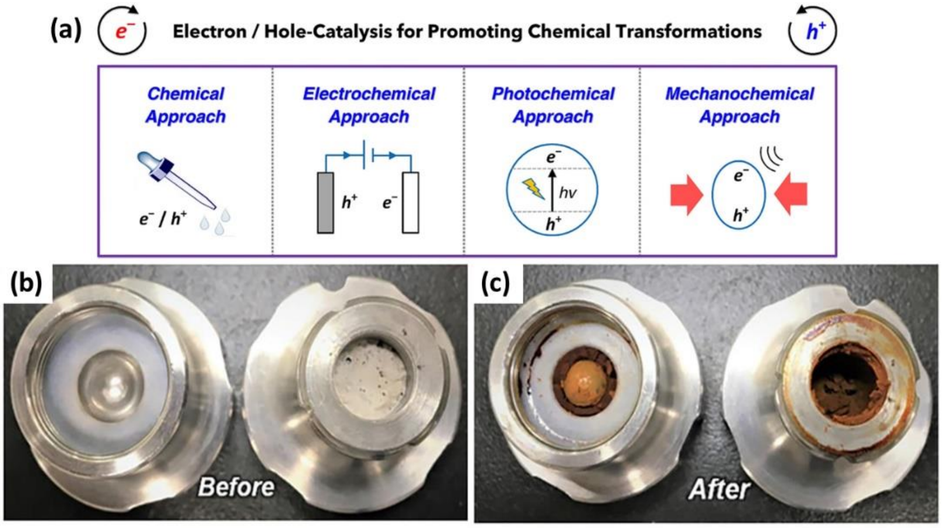

Figure 2.16 (a) Schematic illustration of the four main approaches to Electron/Hole catalysis: chemical, electrochemical, photochemical, and mechano-chemical Methods. Adapted from Ref[70] (b) Before ball-milling, and (c) Post ball-milling reaction mixture for the mechanoredox arylation using a 1.5 ml stainless steel jar and a 5 mm diameter stainless steel ball. Adapted from Ref[44]

Jiao and Stoddart acknowledge mechanochemistry for enabling a wide range of chemical reactions, including breaking bonds, rearranging molecules, coupling metals and triggering complex reaction chains.[70] Furthermore, the literature review details that piezocatalysis benefits from the piezoelectric properties of certain materials, utilising the piezoelectric effect, whereby mechanical stress, or strain results in the generation of an electrical potential. This occurs through the induction of structural anisotropy and polarisation at the atomic level. This response creates a built-in potential within the material, known as the piezo-induced potential, which remains stable as long as the mechanical force is applied, due to the intrinsic properties of the charge carriers. In general, while piezoelectric materials were extensively used in electronic devices for various sensing and actuating applications, their potential in the field of catalysis did not receive as much attention.

However, recent work by Wang *et al.*,[41] and others have begun to explore and showcase the use of mechanically induced polarisation field in piezoelectric materials to control charge carrier transportation behaviours. Through this mechanism, the piezoelectric potential can enhance the separation and transport of charge carriers within the material, potentially improving its catalytic activities. In addition, intrinsic piezoelectric polarisation can modify the semiconductor properties and catalytic activities by causing internal charge accumulation or depletion as well as the adsorption of polar molecules or ions. These changes lead to energy-band adjustments and increased catalytic performance. With the fundamental understanding of catalysis now established, this review of the literature narrows its focus to piezocatalysis and its applications. This promising, yet relatively unexplored frontier carries significant implications for sustainable chemistry and environmental remediation. The subsequent sections will examine the current state of research, interpret recent advances, identify gaps in knowledge, and discuss potential applications.

2.4 TRADITIONAL MATERIALS OF PIEZOCATALYSIS SYSTEMS

The defining characteristic of piezocatalytic materials is their noncentrosymmetric structure. Current research on piezocatalysis primarily explores different types of piezoelectric materials.

First, the hexagonal wurtzite ZnO, which is a widely studied piezoelectric material, has spontaneous polarisation along its c-axis. Stress applied laterally to ZnO nanowires induces positive and negative piezo-induced potentials on their stretched and compressed sides, respectively, according to the results of the first principle calculation and the simulation of finite elements with the maximum potential value (about ~0.3 V) decreasing as the degree of deformation decreases.[71,72] As an n-type semiconductor, ZnO's positive potential is usually screened by free-electron flow on stretched side, resulting in a low detectable positive potential. Reduction of O_2 and OH^- oxidation reactions occur on the compressed and stretched sides, respectively, producing $^{\cdot}O_2$ and ($^{\cdot}OH$) radicals that degrade acid dyes.[73] Hong *et al.*,[35] synthesised single-crystal ZnO nanofibers, which generated H_2 and O_2 in a 2:1 ratio upon ultrasonic vibration, with a mechanical to chemical energy efficiency of 18%. To improve piezocatalytic performance, carbon nanotubes with a high aspect ratio and tensile strength were used to form a flexible network embedding ZnO, offering excellent catalyst dispersion, enhanced electrical conductivity, and accelerated charge transfer, thus increasing piezocatalytic activity (**Figure 2.17(a)**).

Second, perovskite-structured materials with the general formula ABO_3 constitute a crucial category of piezoelectrics. In particular, recent findings have revealed a significant piezoelectric coefficient in organolead halide perovskites labelled as ABX_3.[74–76] Typically, these materials consist of (B) arrays of face-sharing metal-halogen (X) octahedra separated by organic molecular cations (A). In contrast to traditional perovskites, the rotation of molecular cations in ABX_3 can amplify polarisation, providing the materials with exceptionally high ferroelectric and piezoelectric properties. The macroscopic polarity of ABX_3 can be effectively controlled by adjusting the content of molecular cations, as evidenced by the relative second harmonic generation (SHG) intensity curve.[76] It is important to note that both A and B sites in perovskite crystals can influence polarisation, thereby diversifying modification strategies.[75] Nanoscale perovskite titanates can be prepared easily via solid-state, molten-salt, sol-gel, and hydrothermal methods. For example, $BaTiO_3$ nanoparticles,[66] nanofluid $BaTiO_3$,[51] $BaTiO_3$ microdendrites,[77] $(Ba,Sr)TiO_3$ nanowires,[78] $BaTiO_3$ nanofibers,[79] and $Pb(Zr_{0.52}Ti_{0.48})O_3$ fibers[80] synthesised by these methods have shown piezocatalytic activity toward water splitting (**Figure 2.17(b)**)[51] and dye degradation.

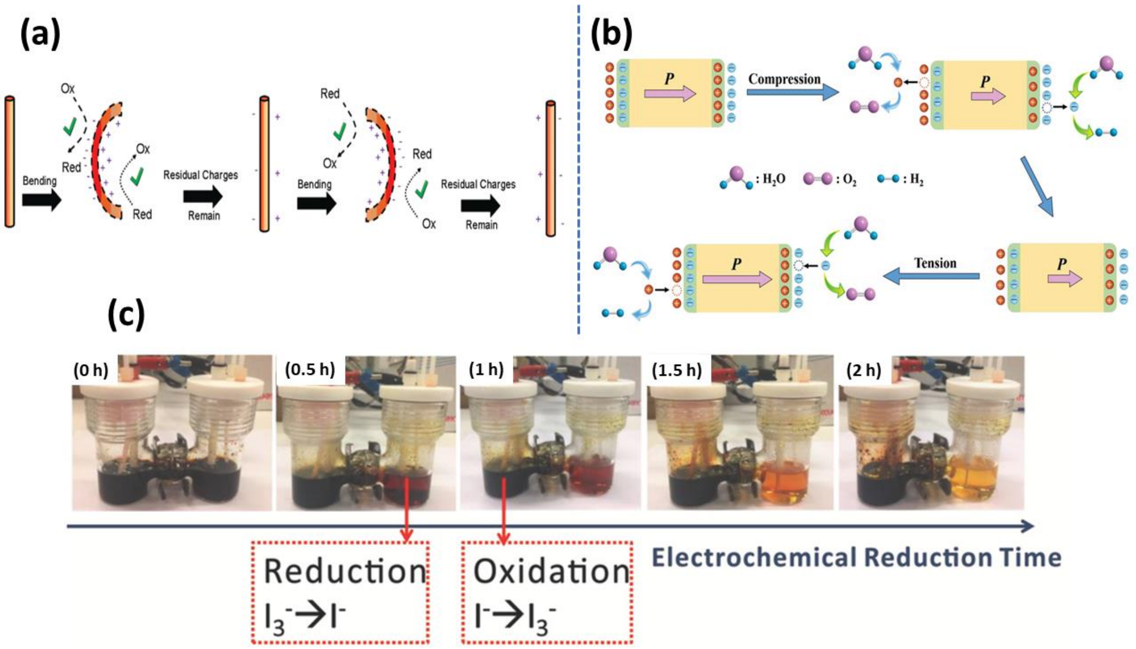

Figure 2.17 (a) Illustration of piezoelectrochemical reactions initiated by fiber flexure, where reactions commence only when the induced potential surpasses water's standard reduction potential. Adapted from Ref[35] (b) Illustrating charge generation on a ferroelectric particle's surface during water splitting. Adapted from Ref[51] (c) Sequential digital images showcase the colour shift in an HI solution undergoing electrochemical treatment over time. A Nafion N117 proton exchange membrane separates the cell's compartments, where I_3^- ions are progressively reduced to I^-, visibly transitioning the solution from dark purple to light yellow. Adapted from Ref[81]

Similarly, $CH_3NH_3PbI_3$ nanoparticles prepared by the co-precipitation method exhibit stronger polarisation due to the larger displacement of the Pb atom, which translates to exceptional piezocatalytic performance in H_2 generation. The improvement in the hydrogen production efficiency of the organolead halide perovskite $CH_3NH_3PbI_3$ involved the addressing of two main challenges.[81] First, the dark colour of I_3^- (triiodide) particles hindered light absorption, requiring an electrochemical reduction process to remove them before experiments, changing the solution from black to light yellow. Monitoring the decrease in I_3^- concentration using UV-vis absorption spectroscopy allowed tracking of hydrogen production progress (**Figure 2.17(c)**). Second, to alleviate photoinduced charge recombination, the noncentrosymmetric piezoelectric crystal structure of $MAPbI_3$ enabled a piezo-photocatalytic approach. Simultaneous ultrasonication and visible-light illumination created a built-in electric field that effectively separated photogenerated charge carriers. This synergistic piezo-photocatalysis strategy markedly improved the hydrogen evolution rate to 23.30 μmol h^{-1}, compared to standalone piezocatalysis at 2.21 μmol h^{-1} or photocatalysis at 3.42 μmol h^{-1} alone, providing an avenue for controlling charge recombination for highly efficient photocatalysis.

Third, In contrast to ZnO and perovskite materials, certain 2D layered substances, which consist of layers held together by van der Waals forces and possess diverse crystalline formations and domain varieties, such as 2D transition metal sulphides/selenides (TMSs), exhibit considerable ease into nanosheets with noncentrosymmetric structures, thus displaying distinct piezoelectric characteristics. For instance, MoS_2's[82] piezoelectric nature is granted by the polarised Mo-S units within a single layer. This quality was confirmed in piezo-electrochemical assessments on flexible MoS_2 devices, where the movement of electrical carriers was detected within the layer. Cyclic stretching and compression of single-layer MoS_2 create a piezoelectric-induced potential, prompting carrier flow and potentially activating piezocatalysis.

However, the inherent noncentrosymmetric – and hence the piezoelectric and piezocatalytic efficacy of MoS_2 can be altered when it intertwines with layers of opposing polarisation, resulting in a pattern where these properties manifest predominantly in odd-numbered layers and reduce with increased layering, highlighting a strong reliance on structural composition.[83,84] Using tunnelling atomic force microscopy, it was found that the piezo-induced charges converge at the layer's perimeter, which corresponds to the area of heightened reactive sites for piezocatalysis. This was further confirmed by the selective deposition of gold or silver on the edges of MoS_2[85] or g-C_3N_4[86] after exposure to ultrasonics, cementing the existence of polarisation in the direction. Black phosphorus,[87,88] known for its exceptional performance in photocatalysis and electrocatalysis, also exhibits an asymmetrical electronic structure, with a noteworthy piezoelectric constant (d_{11}) of 9.48 pm V^{-1}, and maintains its piezoelectric characteristics in both single and multiple layers.

In 2016, Wu *et al.*,[89] made a pioneering discovery when they demonstrated for the first time that MoS_2 nanoflowers exhibit exceptional piezocatalytic activity, achieving up to 93% removal rate of RhB in just 60 seconds under ultrasound, even in the absence of light. The XRD peak shifts to a lower 2θ angle by 0.45°, indicating that the d-spacing is approximately 0.64 nm (**Figure 2.18(a)**). TEM imaging reveals MoS_2 nanoflowers with nanopetals rich in single- to few-layered MoS_2, as seen in **Figure 2.18(b)** (black circles) and its inset. In particular, the nanopetals, shown in **Figure 2.18(c)**, present active edges with up to three layers. Furthermore, **Figure 2.18(d)** confirms a lattice spacing of 0.64 nm, corresponding to the XRD pattern, while **Figure 2.18(e)** details the measurements of lattice constants for single layer MoS_2. This was followed by the development of a MoS_2/PDMS nanocomposite,[90] which was shown to be highly effective in the purification of wastewater by piezocatalysis, taking advantage of the piezoelectric properties of single and multi-layered MoS_2 with an odd number of layers.

Furthering their work, the research group revealed that $MoSe_2$[91] showed an outstanding 90% degradation efficiency of RhB in 30 seconds, marking the fastest rate of decomposition achieved under only mechanical vibration among all catalysts reported at the time. In 2018, the group also reported the first instance of initiating direct water splitting through piezocatalysis driven by mechanical vibration,[92] independently of any light source. This work paved the way for a new understanding and a series of advances in the field of piezocatalysis.[93,94] Since then, piezoelectric materials have been recognised for their extensive utility, far beyond their initial applications in actuators, nanogenerators, biomedicine, transducers, and sensors. The field has progressed to encompass a variety of applications, particularly in areas requiring catalytic processes to operate effectively under mechanical vibration. These materials are now prominently featured in different sectors, ranging from energy,[51,86,95] and environmental solutions,[66,96,97] to medical science,[42,98,99] chemical synthesis,[11,100] and beyond, marking a significant expansion of piezocatalytic applications.

In the research conducted by Li *et al.*,[101] a comprehensive comparative analysis was carried out to evaluate the piezocatalytic efficiency of various transition-metal sulfides and selenides, including MoS_2, WS_2 and WSe_2. The study revealed that the piezocatalytic performance of these materials is closely related to their piezoelectric coefficients (e_{11}), which were determined through theoretical calculations and subsequently verified by direct measurements using piezoresponse force microscopy (PFM). These results highlight the crucial dependence of piezoelectric and piezocatalytic properties on the intrinsic crystal characteristics and external layer configurations, underscoring the significance of material-specific attributes in their functional performance.

Fourth, bismuth-based layered compounds feature a distinctive crystal structure composed of $[Bi_2O_2]^{2+}$ layers interspersed with ions or molecular groups. Due to the lone pair electrons of Bi^{3+}, many of these compounds exhibit an asymmetric crystal structure.[102] Examples include $BiOIO_3$,[103] $Bi_4Ti_3O_{12}$,[104–106] Bi_2WO_6,[107–109] $BiVO_4$,[110–112] $BiFeO_3$,[113–115] BiOCl,[116–118] and $Bi_{0.5}Na_{0.5}TiO_3$,[119–121] all of which have recently been reported to show significant piezocatalytic activity. Hydrothermally synthesised $Bi_4Ti_3O_{12}$ microspheres have been discovered to demonstrate piezocatalytic activity for degrading various pollutants and antibiotics, such as bisphenol A, rhodamine B, and tetracycline hydrochloride. The piezocatalytic degradation efficiency was found to be positively correlated with ultrasonic power, with $^{\cdot}O_2^-$ and $^{\cdot}OH$ identified as the primary active species during degradation. Further research into the piezo-induced potential distribution in $Bi_4Ti_3O_{12}$ of different morphologies revealed that the microsphere assembly might decrease the potential in $Bi_4Ti_3O_{12}$, leading to reduced piezocatalytic activity. For widely recognised photocatalysts BiOCl and $BiFeO_3$, piezocatalytic H_2 generation has been observed for both materials. Separated positive and negative charges on monodisperse nanoplates of BiOCl and $BiFeO_3$ nanoplates served as effective electrodes, promoting the collection of dissociated H^+ ions from water to produce H_2 through the consumption of electron donors.

Interestingly, Jang *et al.*, investigated that Piezoelectric BiOCl nanosheets facilitate the breakdown of Alzheimer's β-amyloid aggregates through ultrasound-driven redox reactions, offering a novel intervention in the treatment of Alzheimer's disease. These sonoactivated sheets produce oxidative stress, which undermines the Aβ fibrils' β-sheet structures, effectively reducing their neurotoxicity and plaque accumulation in brain tissue.[122] This groundbreaking approach demonstrates significant promise for advancing Alzheimer's therapy by targeting one of its major pathological characteristics (**Figure 2.18(f)**).[122]

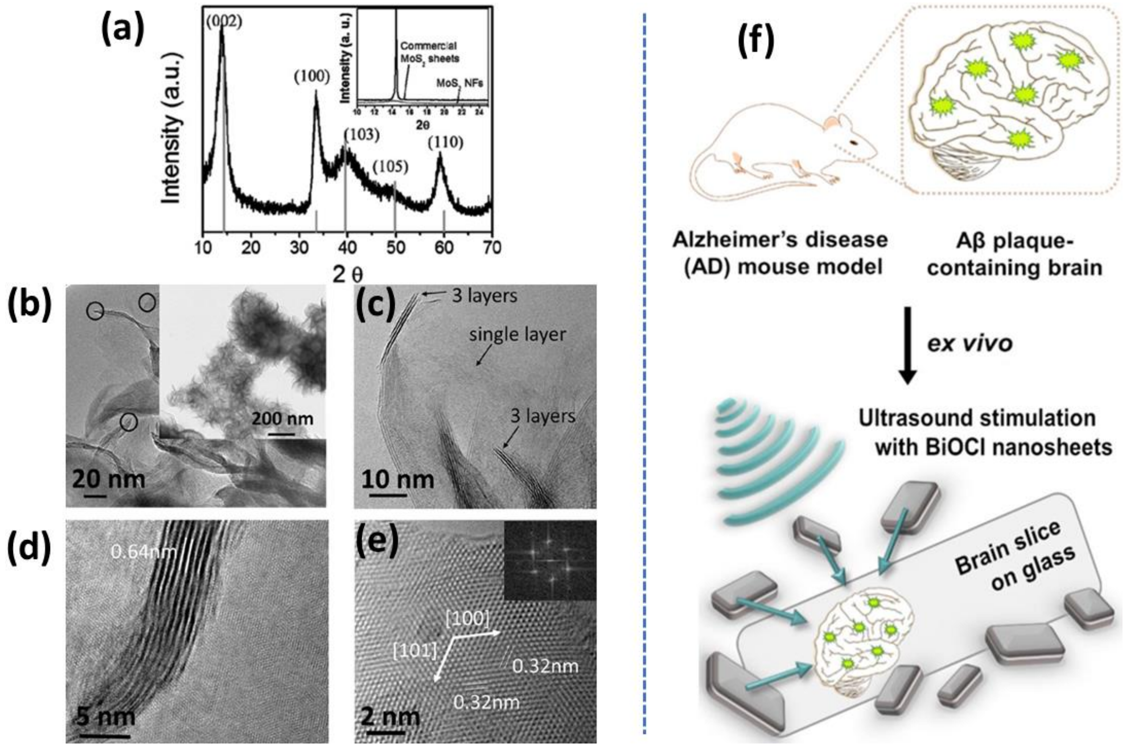

Figure 2.18 (a) The XRD peak shifts to a lower angle by 0.45°, indicating a d-spacing increase to 0.64 nm. (b) TEM images of MoS_2 nanoflowers display nanopetals with single- to few-layered structures (identified by black circles). (c) Close-up of nanopetals showing active edges with up to three layers. (d) Confirmed lattice spacing of 0.64 nm, correlating with XRD results. (e) Lattice constants measured for a single layer of MoS_2. Adapted from Ref[89] (f) Schematic illustration of an ex vivo study using brain slices containing Aβ plaques from a 5xFAD mouse model of Alzheimer's disease. Adapted from Ref[122]

To date, most of the documented studies on layered bismuth-based (LBB) piezocatalysts pertain to powders, which limits their use in practical applications. There is a growing demand for sizable, practical materials that have spurred the development of different strategies to overcome this limitation. For example, these catalysts can be embedded within flexible polymers,[123] or combined into ceramic matrices.[124] Although such methods may cause a reduction in catalytic efficiency, they make LBB materials more amenable to practical applications.

Furthermore, studies have shown that the embedding of bismuth-based piezocatalysts within different matrices can preserve their catalytic properties to a certain extent, while enhancing their mechanical properties and ease of handling. This integration into polymers and ceramics may slightly reduce their piezocatalytic efficiency but significantly improves their usability in real-world applications. The focus on developing larger, more usable forms of these materials is essential to move LBB piezocatalysts from laboratory research to practical environmental and industrial applications.

2.5 IMPACT OF VARIOUS MECHANICAL STIMULATION TECHNIQUES

Determining the impact of various mechanical energy sources on the conversion to chemical energy is crucial. Multiple sources of mechanical energy, such as ultrasonication,[35,51] flow-induced deformation (including stirring,[66,125] and shaking,[126,127]), and vibration induced by mechanical force (ball milling),[44,48] can be harnessed to facilitate piezocatalytic reactivity. It is clear that achieving a sufficient electric potential for reactions to occur requires a minimum level of strain. Prior studies have predominantly explored the effects of ultrasound and flow-induced deformation of piezoelectric particles in a wide range of applications.[81,85,86,122,128–133] In general, ultrasonic waves, produced by a horn or bath, create periodic acoustic pressure and extreme localised pressures due to bubble explosion in water (>100 MPa). These pressures induce inherent piezoelectric potentials in the particles. Furthermore, the intrinsic piezo-induced potential, which is periodic in nature, can serve as an alternating internal electric field that hinders the complete screening of piezoelectric polarisation by free carriers, thereby leading to improved catalytic performance.[134]

Su *et al.*, found that varying the ultrasonic frequency from 10 to 60 kHz increases the generation of hydrogen and oxygen gases through the water splitting process using $BaTiO_3$ nanoparticles (**Figure 2.19(a)**).[135] These findings imply that high-frequency vibrations enhance the absorption and discharge of free charges in water, thereby amplifying the piezoelectric effect and increasing the production of gas.

When using $BiFeO_3$ nanosheets, You *et al.*,[113] observed that the most significant hydrogen production was achieved at a frequency of 45 kHz, which corresponds to the resonance frequency of the nanoparticles calculated (**Figure 2.19(b)**).[113] The effectiveness of piezocatalysis is largely influenced by the frequency, power, properties of the medium, and operational conditions of ultrasound, with frequency playing a pivotal role in ultrasound-driven piezocatalysis. The maximum amplitude at its resonance frequency (f_r) contributes to the optimal energy conversion efficiency as represented by Eq. 2.6,

$$f_r = \frac{\pi}{2}\left(\frac{1}{L^2} + \frac{1}{W^2}\right)\sqrt{\frac{D}{\rho}} \quad \textbf{(Eq. 2.6)}$$

where, ‘L’, ‘W’ and ‘ρ’ represent the length, width, and areal density, respectively. The bending stiffness, denoted by ‘D’, is expressed by the following Eq. 2.7,

$$D = \frac{E * h^3}{12(1-\vartheta^2)} \quad \textbf{(Eq. 2.7)}$$

in which ‘E’, “ and ‘h’ correspond to the catalyst’s elastic modulus of the catalyst, the Poisson ratio and thickness, respectively.

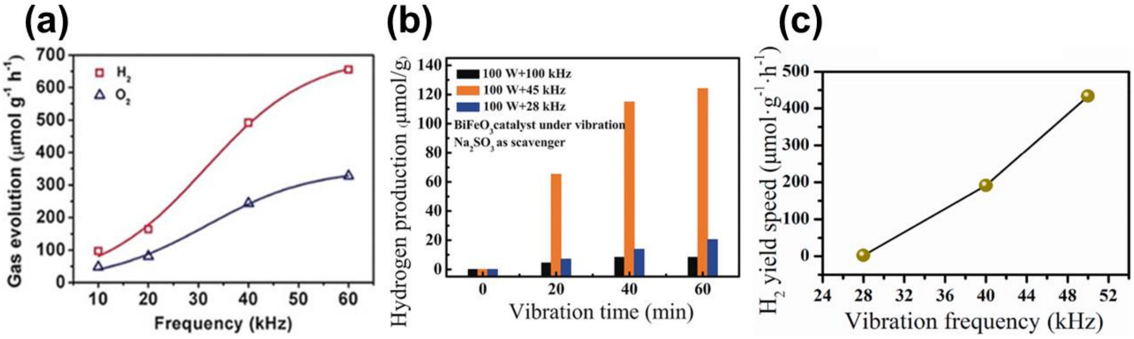

Figure 2.19 Hydrogen output influenced by the ultrasonic vibration frequencies. (a) $BaTiO_3$ nanoparticles. Adapted from Ref[135] (b) $BiFeO_3$ nanosheets. Adapted from Ref[113] (c) Bi_2WO_6 nanoplates. Adapted from Ref[136]

Xu *et al.*,[136] used both equations to determine a normal vibration frequency of 91.69 kHz for piezoelectric Bi_2WO_6 nanoplates. When the applied frequency matches the natural frequency, materials are able to achieve the highest velocity and the greatest amplitude of motion, resulting in the maximum conversion of vibrational energy to electrical energy. As the frequency of the applied ultrasonic vibrations approaches the natural frequency, ranging from 28 to 50 kHz, an improvement in catalytic efficiency is observed, which in turn improves the piezocatalytic hydrogen production from Bi_2WO_6 nanoplates (**Figure 2.19(c)**).[136] These studies provide a comprehensive understanding of how vibrational frequency influences piezocatalytic system performance and present a valuable approach for designing advanced catalytic systems by tuning the applied frequency to approach the natural frequency of piezocatalysts.[137]

Although ultrasonication is a dominant method, its application faces several challenges: (i) it is difficult to differentiate between piezoelectric effects and sonolysis in chemical reactions; (ii) the electric field generated is inconsistent and lacks direction; and (iii) commercial ultrasonic generators typically have fixed frequencies and power settings. One specific application of ultrasonication is sonolysis, which uses ultrasound waves, typically between 20 and 1000 kHz, to degrade molecules in various solutions, often to improve oxidative processes. The sonication creates, grows, and implodes cavitation bubbles in a matter of microseconds. The implosion of these bubbles generates intense energy, facilitating reactions in three distinct zones: the hot-spot zone, with its high temperature and pressure, the bubble-liquid interface where enhanced mass transfer accelerates reaction rates, and the bulk liquid where sonochemical reactions are more limited. Sonolysis, an ultrasonication process, effectively degrades contaminants through pyrolysis and the formation of reactive oxygen species, particularly in the high-energy hotspot zones (**Figure 2.20(a)**).[138]

However, its efficacy is reduced when dealing with hydrophilic toxins, and the process may result in the formation of harmful by-products, as well as potential energy losses due to the conversion of sonication energy into heat.[138] Furthermore, regarding the efficiency of ultrasonication, it is estimated that 80 to 90% of the total ultrasound power actually reaches the liquid.[139] This accounts for various losses that occur from the power source all the way to the liquid, a phenomenon detailed in **Figure 2.20(b)**.[139] However, the efficiency of acoustic wave propagation and energy transfer decreases beyond a certain frequency threshold. Since ultrasound is not commonly found in nature, it is important to explore alternative, more gentle energy sources for piezocatalysis.

In piezocatalytic studies, mechanical stirring is used to simulate water flow (**Figure 2.20(e)**).[142–144] Developing piezocatalytic materials that respond to low-frequency vibrations, such as those from fluid movements in a vortex, is beneficial rather than relying solely on ultrasound. According to the viscosity principles of viscosity,[140] the shearing force generated by the fluids correlates with the viscosity and the stress applied in a specific direction. When this relationship is applied, it is possible to link the flow of the fluid with the generated piezoelectric-induced potential. Experiments have shown that increasing the speed of stirring can improve the breakdown of a dye known as RhB using spherical lead zirconate titanate (**Figure 2.20(c)**).[125] It has also been observed that the shearing force during stirring is effectively captured by the catalysts to produce reactive oxygen species.

Materials with a structured, layered design are more effective in harnessing fluid mechanical energy. For example, nickel foam provides a network that supports the growth of zinc oxide nanorods, offering a larger surface for piezocatalysis. This type of system with its hierarchical structure has demonstrated superior piezoelectric responsiveness to the energy produced by vortexes, leading to greater efficiency in breaking down substances compared to other systems using zinc oxide such as ZnO/ITO or ZnO/glass (**Figure 2.20(d)**).[141] The vibrational energy from water flow also serves as a potential energy source for piezocatalysis.

Zhu *et al.*,[145] synthesised $0.5Ba(Zr_{0.2}Ti_{0.8})O_3$-$0.5(Ba_{0.7}Ca_{0.3})TiO_3$ nanofibers that, at low stirring rates, bent to produce radicals, leading to the effective decomposition of RhB dye. Higher stirring rates resulted in accelerated dye decomposition. This method, which avoids loud ultrasonic vibrations and is less energy-intensive, usually necessitates longer catalytic times compared to ultrasound-induced piezocatalysis.

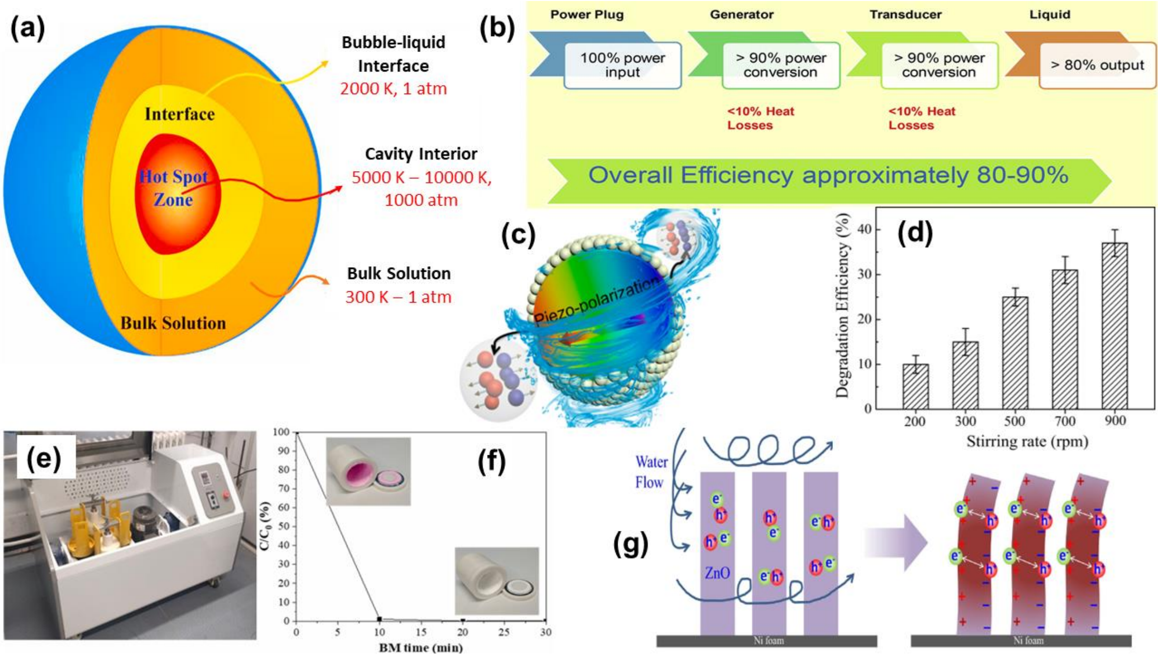

Figure 2.20 (a) Illustrating the process of sonolysis. Adapted from Ref[138] (b) power transmission efficiency of the ultrasonication. Adapted from Ref[139] (c) Proposed mechanism of charge separation in nanoparticles subjected to shearing forces. Adapted from Ref[145] (d) Efficiency of lead zirconate titanate degradation at varying stirring speeds. Adapted from Ref[125] (e) Image of the planetary ball milling equipment. (f) Efficacy metrics for RhB degradation using the planetary ball mill technique. Adapted from Ref[146] (g) Enhanced fluid mechanical energy capture demonstrated by layered design. Adapted from Ref[141]

Prasanna *et al.*,[66] have elucidated key findings on the efficiency of $BaTiO_3$ particles for piezocatalytic dye degradation. Research indicates that $BaTiO_3$ particles are highly effective catalysts, achieving a substantial dye degradation rate of 12.05 mg g^{-1} h^{-1} under optimal conditions. The critical factors that influence piezocatalytic performance include stirring speed, volume of dye solution, and the structural characteristics of $BaTiO_3$, particularly the degree of tetragonality. The studies reveal that a smaller volume of dye solution, below 25 ml, enhances catalytic activity as a result of an increase in turbulence and stirring force. Furthermore, the degradation efficiency is higher in the presence of air rather than in an inert atmosphere such as argon gas. This improvement is attributed to the greater turbulence at the liquid-air interface and the absence of a stern layer in lower volumes of solution. These critical findings of the original research by Prasanna *et al.,* on piezocatalytic dye degradation using $BaTiO_3$ particles have been extensively explained in a separate chapter of this thesis, specifically Chapter 4. The experimental data and analyses therein not only augment the current scientific literature but also advance the understanding of low-energy piezocatalytic mechanisms for dye removal. The rapidly increasing field of piezocatalysis, particularly with ball milling,[45,46,48,49] as the energy source, represents a significant advancement in the realm of catalytic processes. This novel approach boasts several advantages, including the elimination of organic solvents, reduced reaction times, and operational simplicity. Key studies in this area have demonstrated the efficacy and innovative application of this technique in generating reactive species and decomposing pollutants.

Kubota *et al.*,[44] have made a notable contribution by successfully generating aryl radicals from aryl diazonium salts using ball milling in conjunction with the piezoelectric catalyst $BaTiO_3$. This process influences the mechanical energy of ball milling to induce piezoelectric charges on the surface of $BaTiO_3$, which, in turn drive the piezocatalytic reaction. The generation of positive and negative charges on the catalyst's surface is crucial for initiating and sustaining the catalytic activity.

Expanding on this idea, Zhou *et al.*, in 2022, have further explored the capabilities of $BaTiO_3$ nanoparticles as a piezocatalyst in the decomposition of RhB dyes in a solid state by ball milling (**Figure 2.20(f)**).[146] Interestingly, they achieved a 99% decomposition rate of solid RhB dye within just 10 minutes, as shown in **Figure 2.20(g)**, utilising ppm levels of $CuBr_2$ and H_2O_2. This process underscores the efficiency of $BaTiO_3$ nanoparticles in becoming highly polarised under mechanical stress, generating charges that exhibit strong reductive properties. These properties are instrumental in reducing Cu(II) to more reactive Cu(I), and in catalysing the decomposition of H_2O_2 into highly reactive superoxide radicals. Consequently, this leads to the effective decomposition of the solid dye.

2.6 STRATEGIES TO IMPROVE PIEZOCATALYTIC ACTIVITY

Various innovative piezoelectric materials have been explored,[93,104,147–152] each approach aiming to improve the piezocatalytic process and improve its efficiency. In overcoming the limitations of piezocatalysts and boosting their catalytic performance, several strategies have been employed. These strategies encompass morphology control, cocatalyst deposition, and the construction of heterostructures.

2.6.1 STRATEGIES FOR HETEROSTRUCTURE CONSTRUCTION AND COMPOSITES CREATION

A heterojunction is a boundary formed by bringing together two different semiconductor materials. These materials are chosen so that they match well in terms of their crystal structures, how closely spaced their atoms are, and how they expand when heated i.e. thermal expansion coefficient, but they have different energy band gaps. There are different types of heterojunctions depending on the type of semiconductors with which they are in contact, P-P: Both semiconductors are p-type, meaning they have been treated with an excess of positive charge carriers (holes). N-N: Both semiconductors are n-type, which means they have extra negative charge carriers (electrons). P-N: One semiconductor is p-type, and the other is n-type, having both positive and negative charge carriers.

Heterojunctions can also be categorised by how the energy bands of the two semiconductors align with each other as depicted in **Figure 2.21**,[1]

Type I: The conduction band of Semiconductor 1 (SC-1) sits at a higher energy than the conduction band of SC-2, and its valence band sits at a lower energy than SC-2's valence band. This means that when charge carriers are excited, they tend to move into SC-2, which is not good for separating the charges because they both end up in the same material.

Type II: This heterojunction is better for charge separation. The conduction band of SC-1 is at a higher energy compared to SC-2's, but the valence band of SC-2 is at a higher energy compared to SC-1's. When charge carriers are excited, the electrons jump up from SC-1's conduction band to SC-2's, and holes jump down from SC-2's valence band to SC-1's. Electrons and holes are now separated, which is important in devices such as solar cells.

Type III: In this case, the conduction band of SC-1 and the valence band of SC-2 do not overlap at all. There is no good way for electrons or holes to move between the semiconductors, so this type is not great for separating charge carriers either.

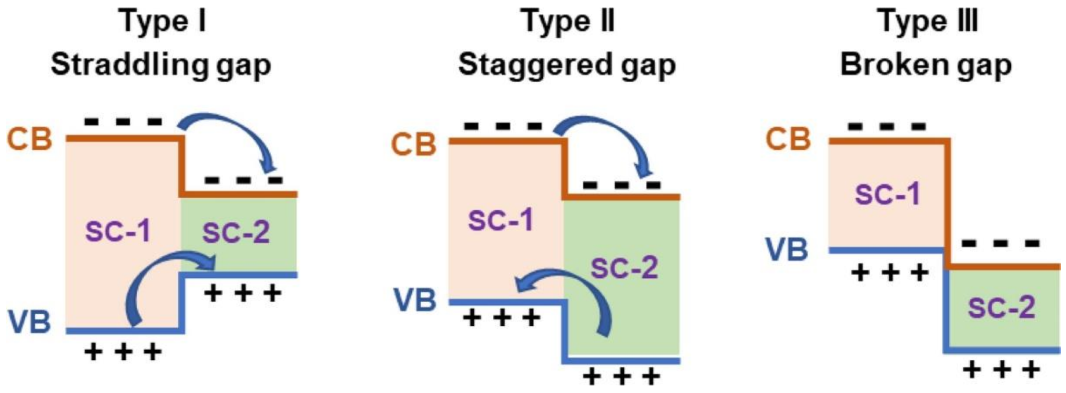

Figure 2.21 Illustrative representation showing the energy band alignment in various heterojunction configurations. Adapted from Ref[1]

A heterojunction that includes piezoelectric semiconductor materials can display improved catalytic performance. This enhancement is due to the surface charges produced by the piezoelectrics or due to changes in the energy band alignment. These changes can trigger or speed up the redox reactions where the semiconductors meet the reactants, helping along the transfer of charges. **Figure 2.22** shows three different heterojunction configurations involving an n-type piezoelectric semiconductor with a p-type nonpiezoelectric semiconductor a p-type piezoelectric semiconductor, and a metal, respectively.[153]

A built-in electric field naturally forms at the boundary of the heterojunction under normal conditions, which originates from an energy-band shift that balances the uneven distribution of charge carriers (illustrated in the left panel of **Figure 2.22**). When external mechanical stress is applied to the piezoelectric semiconductors, a new energy band alignment occurs, which favours charge regulation due to the resulting piezoelectric polarisation (as shown in the middle and right panels of **Figure 2.22**).

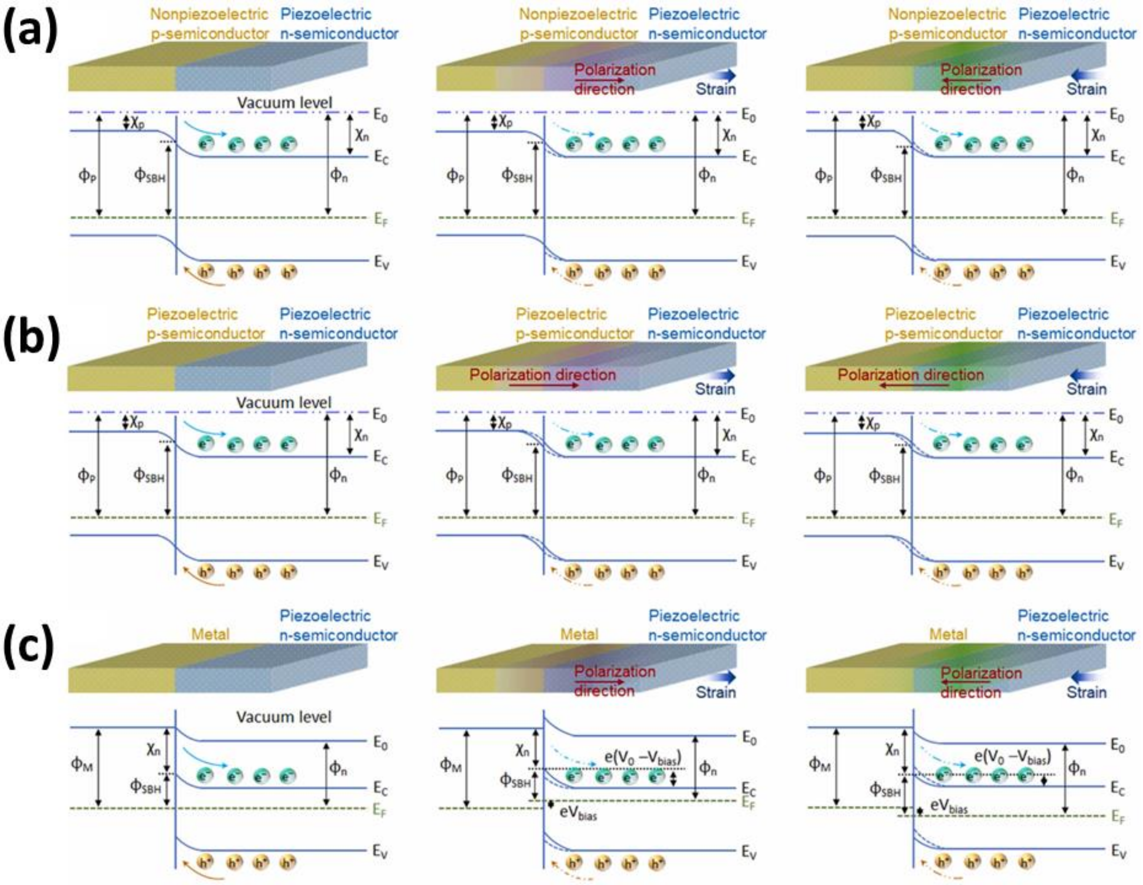

Figure 2.22 Explains the energy band alignment at the interface between an n-type piezoelectric semiconductor and (a) a p-type non-piezoelectric semiconductor, (b) a p-type piezoelectric semiconductor, and (c) a metal. It shows the energy levels under three conditions: equilibrium (left), negative piezoelectric polarisation (middle), and positive piezoelectric polarisation (right). The different symbols represent the work functions (ϕ), electron affinities (X), Schottky barrier height (ϕ_{SBH}), built-in potential (V_0), piezopotential (V_{bias}), electronic charge, vacuum energy level (E_0), Fermi energy (E_F), conduction band (E_c), and valence band (E_v). Adapted from Ref[153]

Cheng *et al.*,[154] reported the fabrication of a Bi_2S_3-Bi_2WO_6 heterojunction through the in situ formation of Bi_2S_3 nanorods on the surface of Bi_2WO_6 nanosheets. They elucidated the piezocatalytic mechanisms by combining structural characterisation with simulations of functional density theory. At the interface of the BS-BWO heterojunction, Bi-S chemical bonds were observed. They conducted DFT simulations using optimised structures, which indicated significant electron accumulation and subsequent utilisation at the heterojunction's interface. It was revealed that electrons from the conduction band of

Bi_2WO_6 migrated to the valence band of Bi_2S_3, supporting interfacial charge transfer dynamics that facilitate piezocatalysis. (**Figure 2.23(a)**).[154]

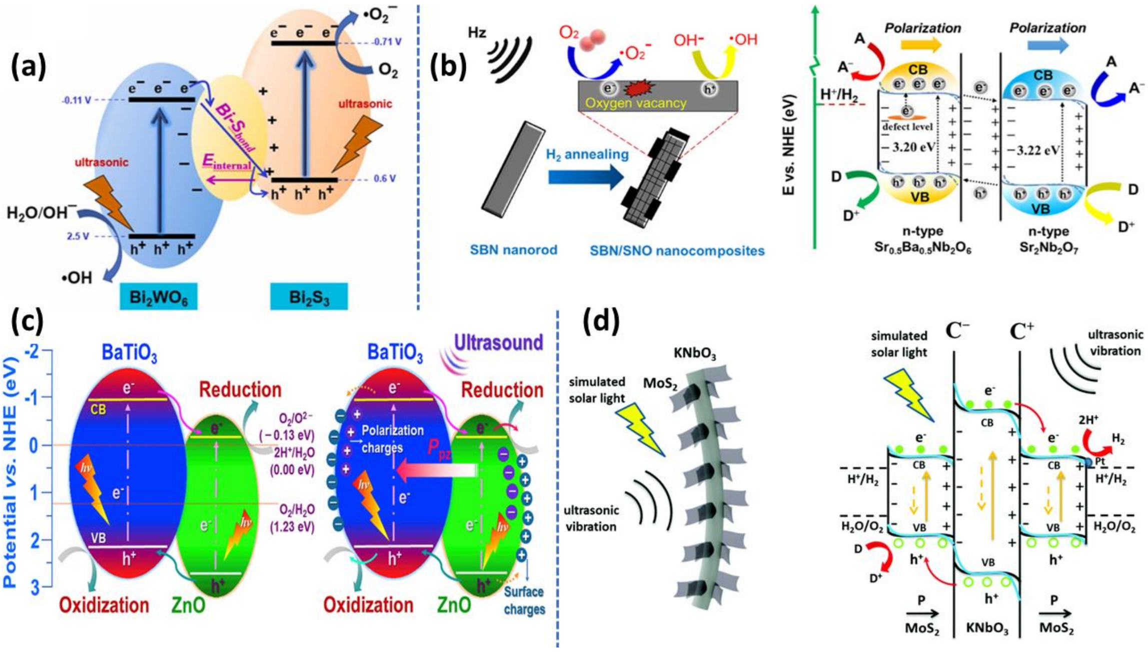

Figure 2.23 Schematic illustration for the heterostructure (a) Bi_2S_3-Bi_2WO_6. Adapted from Ref[154] (b) $Sr_{0.5}Ba_{0.5}Nb_2O_6$/$Sr_2Nb_2O_7$. Adapted from Ref[155] (c) $BaTiO_3$-ZnO. Adapted from Ref[156] and (d) MoS_2 nanosheets were layered onto $KNbO_3$ nanowires. Adapted from Ref[157]

Dai *et al.*,[155] used surface oxygen vacancies to enhance the piezocatalytic efficiency of a heterostructure $Sr_{0.5}Ba_{0.5}Nb_2O_6$ / $Sr_2Nb_2O_7$ (**Figure 2.23(b)**).[155] The presence of oxygen vacancies on the surface of $Sr_{0.5}Ba_{0.5}Nb_2O_6$ provided additional electron-rich sites that facilitated the adsorption and activation of oxygen molecules, leading to the generation of reactive oxygen species such as superoxide and hydroxyl radicals. Moreover, the interfacing area between $Sr_{0.5}Ba_{0.5}Nb_2O_6$ and $Sr_2Nb_2O_7$ contributed to the formation of an intrinsic electric field that further augmented the piezocatalytic capabilities of the heterostructure. Comparative analysis revealed that the hydrogen evolution rate of the engineered $Sr_{0.5}Ba_{0.5}Nb_2O_6$/$Sr_2Nb_2O_7$ heterostructure exhibited a marked increase, with a recorded efficiency of 109.4 $\mu mol\ g^{-1}\ h^{-1}$, which substantially surpassed the performance of the unmodified $Sr_{0.5}Ba_{0.5}Nb_2O_6$ material, with a hydrogen production rate of 12 $\mu mol\ g^{-1}\ h^{-1}$.

Zhou *et al.*,[156] successfully combined two types of piezoelectric semiconductors, ZnO and $BaTiO_3$, to create novel heterostructures (**Figure 2.23(c)**).[156] When subjected to ultrasound at varying intensities, these heterostructures demonstrated a more efficient ability for degrading RhB through piezocatalysis compared to individual ZnO or $BaTiO_3$. This improvement is likely due to the well-aligned energy bands of the heterostructures and the increased piezoelectric potential difference, which is a result of enhanced macroscopic polarisation. Beyond piezocatalysis, these composites also enhance photo-piezocatalytic performance by simultaneously optimising light absorption and charge transportation.

In another study by Jia *et al.*,[157] MoS_2 nanosheets were layered onto $KNbO_3$ nanowires, improving light absorption and charge movement owing to the narrow bandgap of MoS_2 and the synergy within the heterostructure (**Figure 2.23(d)**).[157] When activated by both simulated sunlight and ultrasonic waves, the hybrid catalysts surpassed the hydrogen production rates and degradation reaction rate constants of bare $KNbO_3$ nanowires or MoS_2 nanosheets.

2.6.2 THE ROLE OF MORPHOLOGY IN PIEZOCATALYTIC ENHANCEMENT

Catalytic effectiveness is deeply connected to the shape and structure of catalysts since the activity at their surfaces is critical for the interactions between generated charges and the molecules being targeted. This connection is especially evident in piezocatalysis, where the catalyst's prompt and significant reaction to mechanical pressures generates a sizeable electrical potential, which is essential for high catalytic performance. Therefore, modifying the physical form of catalysts to maximise surface area and improve their mechanical stress response is a pivotal approach for advancing the efficiency of piezocatalytic reactions.

Shi *et al.*,[158] illustrated the impact of particle size on piezocatalytic activity by synthesising $Na_{0.5}Bi_{0.5}TiO_3$ nanoparticles in different sizes (340 nm, 280 nm, and 140 nm), which corresponded to surface areas of 3.45 $m^2\ g^{-1}$, 9.21 $m^2\ g^{-1}$, and 13.57 $m^2\ g^{-1}$, respectively. Their findings revealed that the smallest nanoparticles, with the highest specific surface area, were the most effective in degrading dyes piezocatalytically.

Similarly, Zhu *et al.*,[145] fabricated electrospun $0.5Ba(Zr_{0.2}Ti_{0.8})O_3$-$0.5(Ba_{0.7}Ca_{0.3})TiO_3$ microfibers and adjusted the fiber diameter by varying the electrospinning voltage. They observed that fibers with smaller diameters had higher piezocatalytic efficiency for dye degradation, attributed to their higher piezoelectric coefficient (d_{33}), larger specific surface area with more exposed active sites, and a greater ease of deformation under mechanical stress.

Yu *et al.*,[159] investigated how the shape of nanostructures influences their catalytic behaviour by creating barium titanate in three distinct forms: nanosheet, nanowire, and nanoparticle. Their research revealed that the nanosheets of $BaTiO_3$ were more catalytically active in producing hydrogen (92 $\mu mol\ g^{-1}\ h^{-1}$) than the $BaTiO_3$ nanowires (18 $\mu mol\ g^{-1}\ h^{-1}$) and nanoparticles (2 $\mu mol\ g^{-1}\ h^{-1}$). The superior performance of the nanosheets is primarily attributed to the greater piezoelectric potential they generate, which is a result of their two-dimensional structure's facility for mechanical deformation. These findings agree with those from studies on $Bi_4Ti_3O_{12}$ microplates,[160] which showed a more pronounced piezocatalytic degradation of methylene blue when compared to both hierarchical microrods that are composed of nanosheets and hierarchical microspheres that are composed of nanoflakes. This higher efficiency is due to the dependence of electric potential generation on the morphology and the increased availability of active sites, underlining the importance of morphological design in refining piezocatalytic efficiency.

2.6.3 ENHANCING PIEZOCATALYTIC ACTIVITY THROUGH COCATALYST DEPOSITION AND COUPLED WITH OTHER CATALYTIC METHODS

The integration of metals and metal oxides into piezocatalysts to form composite materials is a proven method for boosting their catalytic efficiency. Under the influence of energy inputs, these composites benefit from the speedy transport of electrons and holes through channels provided by the metallic and metal oxide constituents, which promotes the rapid transfer of charge carriers. Notably, noble metals such as Ag, Au, Pt, and Pd are commonly employed to refine piezocatalytic substances, while metal oxides including CoO_x, NiO, and Fe_2O_3 are utilised to enhance piezocatalytic reactions.

In 2018 study by Lin *et al.*,[161] highlighted the surface modification of barium titanate by using silver nanoparticles through a photochemical approach, effectively enhancing its piezocatalytic capacity. This enhancement was assessed by measuring the degradation efficiency against methyl orange dye, a key indicator of piezocatalytic performance. Following one hour of exposure to light, BTO modified with 2.09 wt% Ag NPs exhibited the highest degradation efficiency, emphasising the precise optimisation of Ag content for maximum catalytic effectiveness. The improved piezocatalytic activity is attributed to the Ag NPs' ability to trap free electrons on BTO surfaces, reducing electron-hole recombination and thereby increasing the generation of reactive species essential for the degradation process. This research significantly contributes to understanding how nanoparticles enhance piezocatalytic performance.

By elucidating the mechanism of Ag NPs in enhancing electron trapping, the findings offer crucial insights for the future development of more efficient piezocatalytic materials. Specifically, BTO modified with 2.09 wt% Ag NPs exhibited a doubled rate constant (‘k_{obs}’) of 16.2×10^{-3} min^{-1} compared to 7.79×10^{-3} min^{-1} for unmodified BTO, indicating a clear improvement in catalytic activity with the addition of silver. However, it is important to note that exceeding the optimal deposition time for Ag can inversely impact catalytic action, emphasising the significance of balancing cocatalyst load for achieving the best piezocatalytic response. This study establishes a precedent for optimising nanoparticle enhancements in piezocatalytic systems, contributing to ongoing efforts to develop high-performance materials for environmental pollutant cleanup and various technological applications.

Dolai *et al.*,[162] discussed about the piezocatalytic property of anisotropic calcium phosphate nanomaterials, when conjugated with Au nanoparticles, showcase a significant elevation in piezocatalytic properties, with performance rivalling that of the widely recognised $BaTiO_3$ in its bulk or nanoparticle form. The development of these nanostructures, including nanowires, nanorods, and nanospheres ranging between 2 nm to 5 nm in diameter and 30 to 1000 nm in length, is accompanied by the integration of 5 nm to 8 nm Au nanoparticles. Piezoresponse force microscopy has revealed that the unique anisotropic structure of calcium phosphate nanowires can double the piezoelectric effect, while conjugation with Au nanoparticles can amplify it by up to tenfold, achieving a piezoelectric constant of 72 pm V^{-1}, comparable to $BaTiO_3$. This pronounced enhancement in piezoelectric property correlates to a tenfold increase in piezocatalytic reaction efficiency. The innovation introduces colloidal nano-bioconjugates for targeted cancer cell labelling and enables wireless cell therapy via medical-grade ultrasound, which generates intracellular reactive oxygen species. This novel approach shows promise for broader applications in wireless therapeutic treatments and intracellular manipulation.

The advancements in piezocatalysis are hampered by several factors, including a weak driving force, rapid recombination of charge carriers, and predominately, the charge screening effect. Wei *et al.*,[163] developed a piezoelectric composite material by incorporating gold nanoparticles into $BiVO_4$ ($Au/BiVO_4$). The capability of $Au/BiVO_4$ as a piezocatalyst was demonstrated through its ability to simultaneously degrade 4-chlorophenol (4-CP) and reduce hexavalent chromium (Cr), achieving removal efficiencies of 91% and 83% respectively in 120 minutes, when subjected to ultrasonic vibration. Lei *et al.*,[164] have developed a dual electric field-driven piezoelectric catalytic system that incorporates Au nanoparticles on the various crystal planes of $Bi_4Ti_3O_{12}$. This synergistic effect between the $Bi_4Ti_3O_{12}$ and Au nanoparticles in achieving an improved H_2 production rate of 194.67 μmol h^{-1} g^{-1}, along with the generation of a valuable by-product, H_2O_2, at the rate of 4.03 μmol h^{-1} g^{-1}. Despite these advances, the uneven molar ratio of H_2 to H_2O_2 indicates an inefficiency in the conversion of $^{\cdot}OH$ radicals to H_2O_2, shedding light on potential areas for further optimisation. The discrepancy in the observed and expected molar ratios of H_2 to H_2O_2 can be attributed to either the incomplete conversion of $^{\cdot}OH$ radicals or the more complex, multiple-stage water oxidation process[147]. This lack of balance signals a need for a deeper understanding of the mechanistic pathways and for addressing kinetic barriers in piezocatalysis.

Research on piezocatalysts and photo-piezocatalysts has uncovered the significant potential of composite construction for enhancing catalytic performance, a finding demonstrated by Zhou *et al.*,[165] investigated the synergistic effects of combining $LiNbO_3$-type $ZnTiO_3{\cdot}TiO_2$ and tetragonal $BaTiO_3$ (ZBTO) with Pt and FeO_x nanoparticle modifications to enhance charge carrier separation, light absorption, and catalytic activity in nanoscale piezoelectric heterostructures. These catalysts are designed for the enhanced generation of reactive oxygen species such as hydroxyl ($^{\cdot}OH$) and superoxide ($^{\cdot}O_2^-$) radicals. Their performance in generating these radicals is superior during integrated piezo-photocatalytic processes as compared to piezocatalysis or photocatalysis alone. The integration of Pt and FeO_x nanoparticles into the catalyst structure leads to a decrease in charge transfer resistance, resulting in approximately 48% and 21% increases in the formation of $^{\cdot}OH$ radicals for ZBTO-Pt and ZBTO-FeO_x, respectively, over bare ZBTO during piezo-photocatalysis. Additionally, the production of $^{\cdot}O_2^-$ radicals is enhanced by about 11% for ZBTO-Pt and 6% for ZBTO-FeOx. Furthermore, the concentration of hydrogen peroxide (H_2O_2) formed on both ZBTO-Pt and ZBTO-FeO_x under piezo-photocatalytic conditions was approximately 315 µM and 206 µM, respectively, after 100 minutes of reaction, which were significantly higher than those generated through either piezocatalytic or photocatalytic processes alone (**Figure 2.24(a) and (b)**).[165]

Feng *et al.*,[166] investigated the specific arrangement of Pt and RuO_2 electrocatalysts on the t-$BaTiO_3$ surface. The RuO_2/t-$BaTiO_3$/Pt nanoparticle, demonstrating a catalytic reaction rate constant of 0.032 min^{-1} for breaking down tricyclazole. The observed kinetic constant was 3.11 times that for pure t-$BaTiO_3$, 2.56 times for t-$BaTiO_3$ with Pt, 2.58 times for t-$BaTiO_3$ with RuO_2, and 2.22 times for a combination of Pt/RuO_2/t-$BaTiO_3$, as well as exceeding the aggregate rate constants of Pt/t-$BaTiO_3$ and RuO_2/t-$BaTiO_3$ when individually loaded. This highlights that the piezoelectric effects in t-$BaTiO_3$, when coupled with either Pt or RuO_2, enhance its piezocatalytic performance; and when employed together, Pt and RuO_2 exhibit a stronger catalytic action than when used separately. The improvement in performance is dependent on the particular spatial configuration of the electrocatalysts on the surface of the t-$BaTiO_3$. Platinum, assuming roles akin to both cathodic and anodic electrocatalysts, primarily facilitated the formation of hydroxyl radicals ($^{\cdot}OH$), superoxide anions ($^{\cdot}O_2^-$), and hydrogen peroxide (H_2O_2). Conversely, RuO_2 predominantly served as an anodic piezocatalyst, enhancing the creation of $^{\cdot}OH$, singlet oxygen ($^1O_2$), and H_2O_2. These findings suggest, Pt and RuO_2 were more efficient in producing all four reactive oxygen species. The size, amount, and distribution of cocatalysts play a pivotal role in influencing the efficiency of piezocatalytic processes.

Yang *et al.*,[167] observed a substantial enhancement in piezocatalytic hydrogen generation rates by a factor of 19 times achieving 11.4 µmol h^{-1} per 10 mg of catalyst when palladium cocatalysts decorated bare $BiFeO_3$. This improvement is attributed to the formation of a Schottky junction, enhanced piezoelectricity, and reduced overpotential for proton reduction reactions. However, the effectiveness of the cocatalyst is dependent on its size and loading amount. While larger Pd nanoparticles can alter the Schottky barrier and influence charge migration at the $BiFeO_3$-Pd interface, excessive loading of Pd can hinder the deformation of $BiFeO_3$ and limit the availability of oxidation sites.

Conversely, insufficient Pd loading may not provide adequate charge separation efficiency or active surface sites. Consequently, the piezocatalytic hydrogen yield exhibits a "volcano" trend as the size or quantity of the Pd cocatalyst increases. Furthermore, the position or distribution of the cocatalyst on the semiconductor surface is equally crucial for optimal piezocatalytic activity. They have observed that the introduction of piezoelectric-induced potential can reduce or even remove the Schottky barrier, facilitating smoother electron migration from $BiFeO_3$ to Pd. Additionally, factors such as the exposed surface area, domain size, and concentration of the Pd cocatalyst on the $BiFeO_3$ surface play a significant role in achieving efficient piezocatalytic performance.

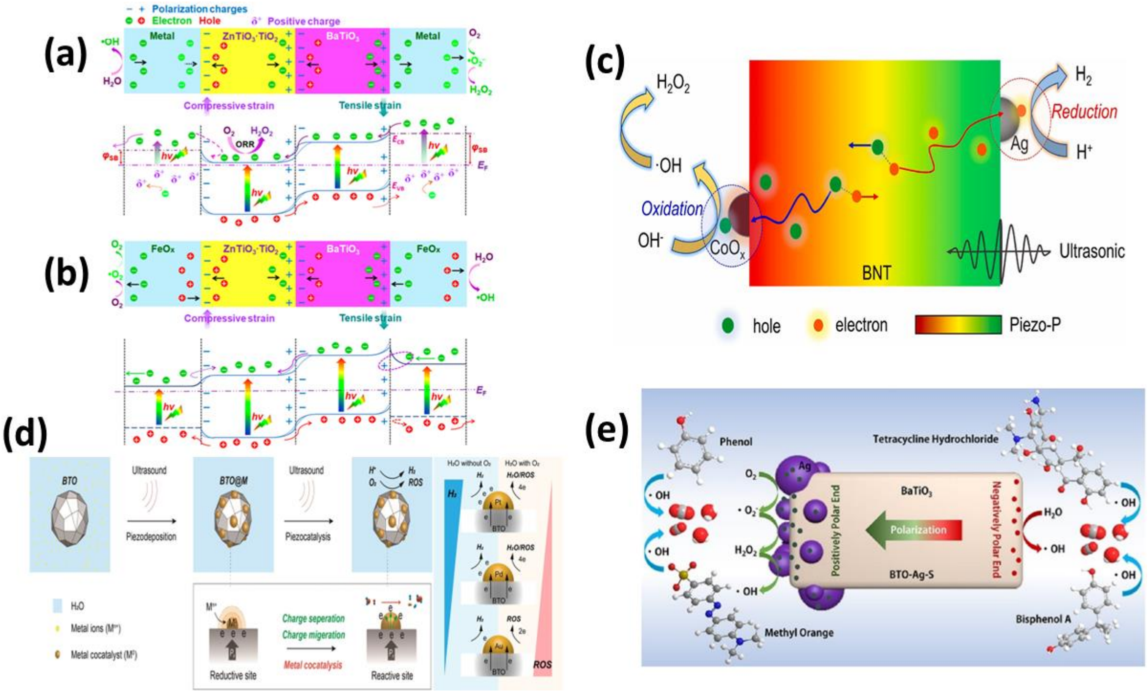

Figure 2.24 Illustrates the movement of charge carriers in (a) $ZnTiO_3{\cdot}TiO_2/BaTiO_3$ with a platinum catalyst, and (b) $ZnTiO_3{\cdot}TiO_2/BaTiO_3$ with an iron oxide catalyst, facilitated by the piezoelectric phenomenon. Adapted from Ref[165] (c) Mechanism of piezocatalytic water splitting of BNT with Ag or CoO_x. Adapted from Ref[168] (d) Schematic of piezodeposition and metal cocatalysts - enhanced piezocatalysis. Adapted from Ref[169] (e) Selectively deposited Ag on BTO surfaces (BTO-Ag-S). Adapted from Ref[170]

Liu *et al.*,[168] hydrothermally synthesised $(Bi_{0.5}Na_{0.5})TiO_3$ (BNT) cubes demonstrate exceptional piezocatalytic hydrogen evolution reaction (HER) performance. These BNT cubes, taking advantage of their strong piezoelectric properties, effectively split water under ultrasonic vibrations, resulting in yields of 0.38 mmol g^{-1} h^{-1} for H_2 and 0.25 mmol g^{-1} h^{-1} for H_2O_2. Enhancements in piezoelectric HER efficiency are achieved by adding silver and cobalt oxide nanoparticles as cocatalysts via a photochemical procedure, subsequently improving HER activity as shown in **Figure 2.24(c)**.[168]

The enhancement in H_2 production is credited to the piezocatalytic effects activated by ultrasonic stimulation of the BNT cubes. A direct relationship is observed between the H_2 yield and the concentration of BNT cubes, but the efficiency decreases from 0.38 to 0.14 mmol g^{-1} h^{-1} when the catalyst loading increases from 0.5 g L^{-1} to 1.5 g L^{-1}. This indicates that too high a concentration can adversely affect piezocatalytic HER efficiency by neutralising the polar surfaces and weakening the intrinsic polarisation field. Significantly, BNT cubes coated with CoO_x show improved piezocatalytic HER performance, with an efficiency of 0.49 mmol g^{-1} h^{-1} higher than that of uncoated BNT. In the case of BNT with varying levels of Ag loadings, the H_2 yield is positively impacted by the presence of Ag, with the peak HER efficiency of 0.51 mmol g^{-1} h^{-1} observed for BNT@Ag-15. The addition of Ag helps to decrease the resistance to charge migration, due to its high conductivity, thus enhancing the HER. Conversely, an excessive amount of Ag can obscure the active sites, which leads to a reduction in HER performance.

A limited number of studies have focused on the piezodeposition of noble metals, such as Au, Pd, and Pt, onto $BaTiO_3$. Utilising these in piezocatalysis has led to significant advances in H_2 production.

In the absence of dissolved oxygen, the piezodeposited noble metal nanoparticles in compositions such as BTO@Pt are observed to promote electron transfer, attribute to their substantial work function, which results in improved efficiency for hydrogen generation when subjected to ultrasonic vibration. Conversely, when dissolved oxygen is present, the behaviour of electron transfer kinetics varies with different metal nanoparticles. Both BTO@Pt and BTO@Pd are involved in a near-four-electron pathway for oxygen reduction, while BTO@Au engages in a two-electron pathway, which is notably more effective for reactive oxygen species production. Among these, BTO@Pd is distinguished by its marginally superior reactive oxygen species yield compared to BTO@Pt, a phenomena linked to the reduced size of its noble metal particles which increases surface area and, consequently, piezocatalytic activity, counterbalancing the adverse effects associated with charge separation and migration (**Figure 2.24(d)**).[169]

One notable breakthrough in this field is the use of selective noble metal deposition, a strategy which has been instrumental in enhancing the activity of piezocatalysts. This approach, however, presents challenges due to the often-negligible energy differences between different facets of nanocatalysts.

Lin *et al.*,[170] has developed a piezoelectrochemical method capable of selectively positioning silver nanoparticles onto the positively charged poles of $BaTiO_3$ nanocubes and cuboids with {001} facets. By doing so, these specially tailored $BaTiO_3$ structures, with precisely deposited Ag nanoparticles, nearly doubled their piezocatalytic activity compared to those with randomly distributed Ag nanoparticles, showcasing a marked superiority over unmodified $BaTiO_3$. This enhanced piezocatalytic effect is driven by the way in which Ag nanoparticles on positive ends act as conductive channels for electrons, promoting reactions at the catalyst/solution interface, while preventing electron accumulation at negative ends which otherwise hinders pollutants' degradation as depicted in **Figure 2.24(e)**.[170]

Complementing this, Liu *et al.*,[171] also utilises low-frequency hydromechanical vibrations for effective water disinfection, eliminating the need for high-frequency ultrasound that piezocatalysts usually depend on. Using $BaTiO_3$@Au piezocatalysts, where the Au cocatalysts are optimally placed using in situ piezodeposition, they achieved superior charge separation and increased production of reactive oxygen species (**Figure 2.25(a)**). The size and quantity of the deposited Au cocatalyst on the $BaTiO_3$ (BTO) nanoparticles increased with prolonged deposition time, although only slight growth was observed beyond 60 minutes, likely due to constraints imposed by the finite ferroelectric domain size and limited electron transfer distance. TEM images revealed the successful deposition of Au nanoparticles with an average size of 10 nm on the surface of BTO after 1 hour of piezodeposition using chloroauric acid ($AuCl_4$) as the precursor and methanol (CH_3OH) as the hole scavenger (**Figure 2.25(b)**). The lattice fringes corresponding to the (111) facet of Au and the (110) facet of BTO were clearly visible, although the preferred deposition facet of Au on BTO could not be determined (**Figure 2.25(c)**). EDS elemental mapping further confirmed the presence of Au nanoparticles on the BTO surface (**Figure 2.25(d)**). XRD patterns indicated the crystallisation of Au and the preservation of the tetragonal phase of BTO as shown in (**Figure 2.25(e)**), suggesting that the BTO@Au composite retained its intrinsic ferroelectric and piezoelectric properties. The piezoelectricity of the obtained BTO@Au was further verified by the characteristic butterfly amplitude curve and a 180° phase switching observed in the localized piezoelectric hysteresis loop (**Figure 2.25(f)**).[171]

This technique accomplishes the degradation of organic matter and deactivation of pathogenic bacteria and viruses effortlessly, through simple vibration in aqueous solutions. By employing this innovative, low-energy, and eco-friendly approach, substantial reductions in intestinal pathogenic bacteria and organic carbon were observed in hospital wastewater, leading the way toward green and sustainable water disinfection solutions.

Wang *et al.*,[172] present an innovative strategy for the improved piezocatalytic degradation of organic pollutants, centering on the breakdown of RhB. This approach utilises cobalt oxide nanoparticles anchored to bismuth ferrite nanodisks, synthesised via a hydrothermal method followed by photodeposition. The relationship between CoO_x nanoparticles and $BiFeO_3$ nanodisks not only significantly enhances piezocatalytic efficiency but also ensures catalyst durability. The degradation rate of RhB by the $CoO_x/BiFeO_3$ composite was found to be 2.38 times greater than that of pure $BiFeO_3$ nanodisks when tested under ultrasonic vibration. In subsequent developments, the same research team engineered a heterojunction composite of $CoO_x/Bi_4Ti_3O_{12}$ using a combined molten salt and photodeposition approach.[173] The composite demonstrated outstanding piezocatalytic capacity in breaking down methyl orange dye, with a degradation rate of 1.09 h^{-1}, which is 2.4 times greater than that of the unmodified $Bi_4Ti_3O_{12}$.

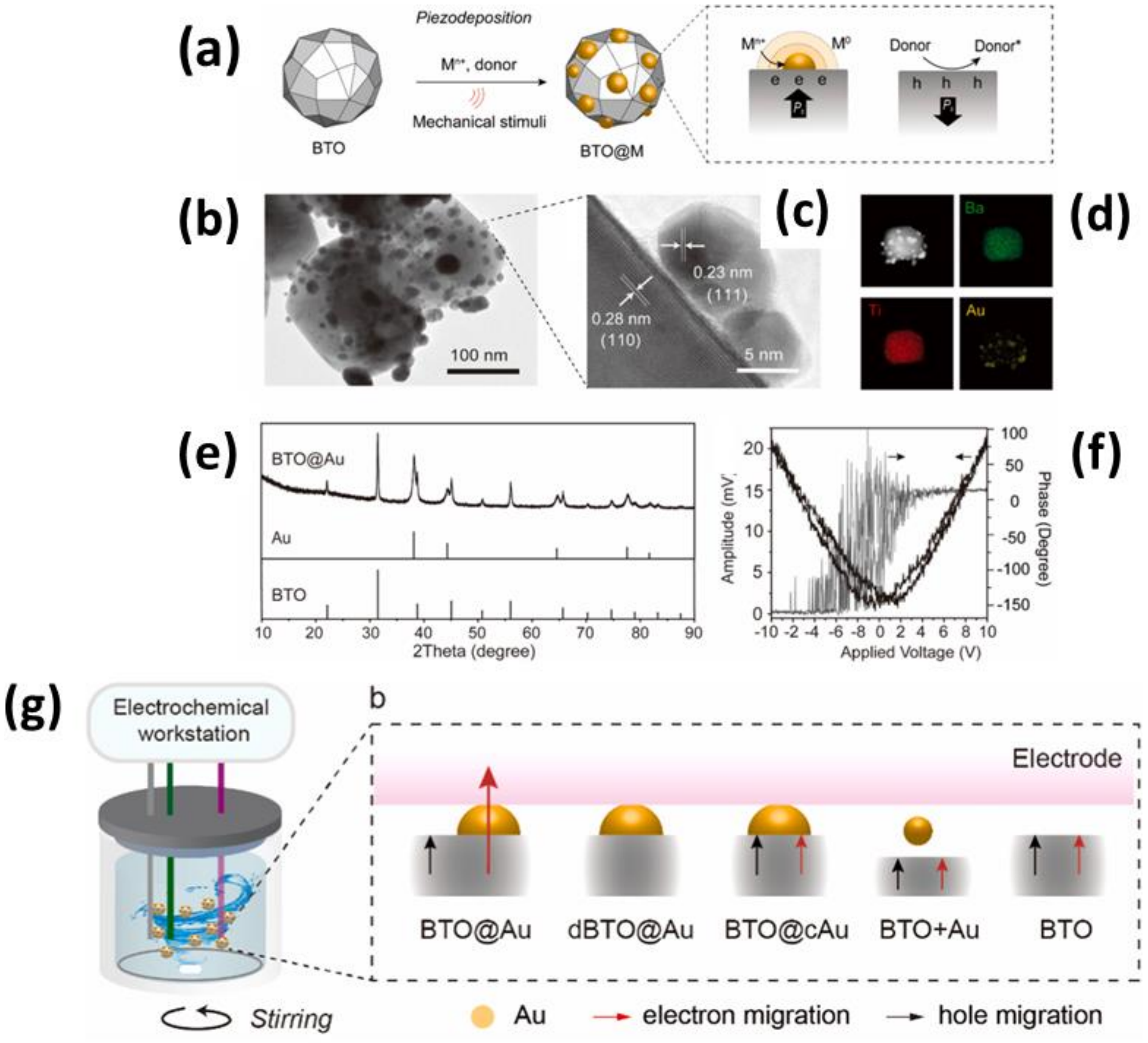

Figure 2.25 (a) Illustrative representation of the piezodeposition technique (b) TEM image (c) Lattice fringes (d) EDS distribution maps, (e) XRD, (f) piezoelectric response profiles including phase and amplitude measurements for BTO@Au composite material, and (g) Diagram depicting the configuration of the experiment, incorporating an electrochemical cell that is linked to the workstation. Adapted from Ref[171]

Further investigations uncovered a type-I P-N heterojunction within the composite, with CoO_x acting as an effective hole trapper that improves the separation and migration of the piezo-induced charge carriers. The composite's efficiency rose to 2.96 h^{-1} for MO degradation under the dual influence of ultrasonic vibration and simulated sunlight. This enhanced activity results from several contributing mechanisms: photoinduced generation of charges in the $CoO_x/Bi_4Ti_3O_{12}$ composite, coupled with polarisation from $Bi_4Ti_3O_{12}$ which increases the dissociation of electron-hole pairs in the bulk, and the heterojunction structure greatly advances the surface charge separation, facilitating greater availability of electrons and holes for the reaction. These enhancements contribute to the observed improvement in the piezocatalytic activity of the composite material, aligning with the established role of CoO_x as a promoter in enhancing the performance of photocatalysts and suggesting its relevance in the context of piezocatalysis as well.

Yu *et al.*,[174] was synthesised $BaTiO_3/CuO$ heterostructures have exceptional catalysts for the disintegration of methyl orange dye, exceeding the performance of bare $BaTiO_3$ nanowires or CuO nanoparticles. The highest degradation efficacy is noted at a 0.8 wt% concentration of CuO. Although pristine $BaTiO_3$ nanowires demonstrate considerable dye degradation capabilities via piezocatalysis, due to their inherent piezoelectric properties, incorporating CuO surprisingly diminishes this effect. Nonetheless, under simultaneous exposure to ultraviolet light and ultrasonic vibration—a process referred to as piezo-photocatalysis—the $BaTiO_3/CuO$ composites exhibit significantly enhanced catalytic performance. This is attributed to a synergistic effect that accelerates the separation of charge carriers. Intriguingly, the catalytic potential of the $BaTiO_3/CuO$ composites can be further improved through electric poling, which supports the piezoelectric attributes of $BaTiO_3$, and thereby potentiates piezo-photocatalytic activity. The pivotal contributors to the degradation mechanism are the dynamic interactions of hydroxyl radicals, superoxide radicals, and holes. Notably, the $BaTiO_3$-0.6CuO composite demonstrates effective and stable catalytic action, showing impressive adaptability and resilience in degrading a variety of organic dyes, indicating an innovative leap in multi-modal catalysis approaches.

Wang *et al.*,[175] was synthesised a $NiO/BaTiO_3$ heterojunction composite via photo-deposition. The piezocatalytic assessments revealed that this $NiO/BaTiO_3$ composite showcased marked efficacy and robustness in the degradation of RhB. Notably, the $NiO/BaTiO_3$ catalyst, prepared with two hours of light irradiation, exhibited a RhB degradation rate of 2.41 h^{-1}, surpassing the pure $BaTiO_3$'s rate by a factor of 6.3. By fine-tuning the reaction parameters, the $NiO/BaTiO_3$ degradation rate constant was further elevated to 4.14 h^{-1}. They have performed systematic characterisations to elucidate the mechanisms highlighting the superior piezocatalytic functionality of the $NiO/BaTiO_3$ composite. It was observed that the band potentials of NiO and $BaTiO_3$ are aligned, potentially forming a type-II P-N heterojunction at their interface. The resulting potential difference and the intrinsic electric field promote the migration of piezoelectrically induced charge carriers between NiO and $BaTiO_3$, leading to enhanced charge separation efficiency and an increase in piezocatalytic performance.

In a type II heterojunction, an incorporated energy level arrangement occurs between two piezoelectric semiconductors, and this arrangement creates a separated pathway for photogenerated carriers. The enhancement of the built-in electric field in this setup significantly boosts the efficiency of separating photogenerated electron-hole pairs[176]. On certain occasions, piezoelectric substances may not exhibit hydrogen generation through piezocatalysis alone, instead, they require photocatalysis. The piezoelectric potential drives charge carriers to move in opposite directions, leading to enhanced catalytic activity when both light and ultrasound are applied, as compared to the effect of light alone. This enhancement is not merely due to the addition of light to improve piezocatalytic effects.

Research indicates that constructing morphology control and applying strain are the most effective techniques to increase the activity of pure water splitting. Moreover, when sacrificial agents are used in piezocatalytic decomposition of water, metal loading demonstrates the most advantageous outcomes in promoting hydrogen production.[137]

2.7 ADVANCEMENTS IN PIEZOCATALYTIC PROCESSES FOR SUSTAINABLE APPLICATIONS

Ammonia is gaining recognition as an alternative energy carrier due to its numerous advantageous properties such as a high energy density of 18.8 MJ kg^{-1}, an efficient liquefaction process with low associated heat loss, affordable storage costs, and the benefit of not emitting carbon during combustion.[177] However, the conversion of nitrogen (N_2) to ammonia is somewhat hampered by the requirement of a high energy input to break the strong $N \equiv N$ bond, which demands 941 kJ mol^{-1}. The bulk production of ammonia has historically depended on the energy-intensive Haber-Bosch process, which also generates greenhouse gases, thereby conflicting with the objectives of sustainable development. Nevertheless, recent developments suggest that ammonia can now be produced via piezocatalytic nitrogen fixation,[178–180] which capitalises on clean mechanical energy, thus avoiding the drawbacks associated with the Haber-Bosch method.

Dai *et al.*,[181] enhanced the nitrogen reduction by pairing $KTa_{0.75}Nb_{0.25}O_3$ (KTN) with CuS as shown in **Figure 2.26(a)**[181] to serve as electron trappers, thereby increasing the electrons longevity. This composite achieved an ammonia formation rate that was 7.4 times higher than KTN alone. The introduction of simulated sunlight to the CuS/KTN further accelerated ammonia production, with a 5.86-fold increase, attaining a rate of 212.20 μmol L^{-1} g^{-1} h^{-1}. In another study by the same group, the adoption of composite materials and the coupling of photocatalysis techniques led to an even greater increase in ammonia production. They conducted experiments to see how well KTN ($KTa_{0.75}Nb_{0.25}O_3$), Bi_2S_3, and a blend of 0.25% Bi_2S_3/KTN could convert nitrogen (N_2) into ammonia when exposed to both simulated sunlight and ultrasonic vibrations[182]. They wanted to check whether the reactions driven by light (photocatalytic) and vibrations (piezocatalytic) could work effectively at the same time. The Bi_2S_3 sample produced around 99.6 μmol L^{-1} g^{-1} h^{-1} of ammonia, which was reasonably much the same rate as when it was just exposed to sunlight. This outcome suggests that vibrations alone didn't really help to make more ammonia. However, results were different with KTN and the 0.25% Bi_2S_3/KTN composite. Both of these materials made more ammonia when sunlight and vibrations were applied together, compared to stimulated sunlight alone. Specifically, the 0.25% Bi_2S_3/KTN sample reached a high ammonia production rate of 581.0 μmol L^{-1} g^{-1} h^{-1}. The results indicate that the Bi_2S_3/KTN material is capable of using energy from both light and vibrations to produce a higher amount of ammonia. They consider that if modifications of the structure of the

Bi_2S_3/KTN catalyst and the conditions of the reaction, they could potentially increase the rate of ammonia generation even further.

Moreover, piezocatalysis has recently been explored for converting CO_2 gas into valuable chemical fuels like CO and a range of hydrocarbons. The study conducted by Phuong *et al.*,[183] represents the first demonstration of piezocatalytic CO_2 reduction using lithium-doped potassium sodium niobate powders with composition $(K_{0.5}Na_{0.5})_{0.97}Li_{0.03}NbO_3$ (KNLN) (**Figure 2.26(b)**).[183]

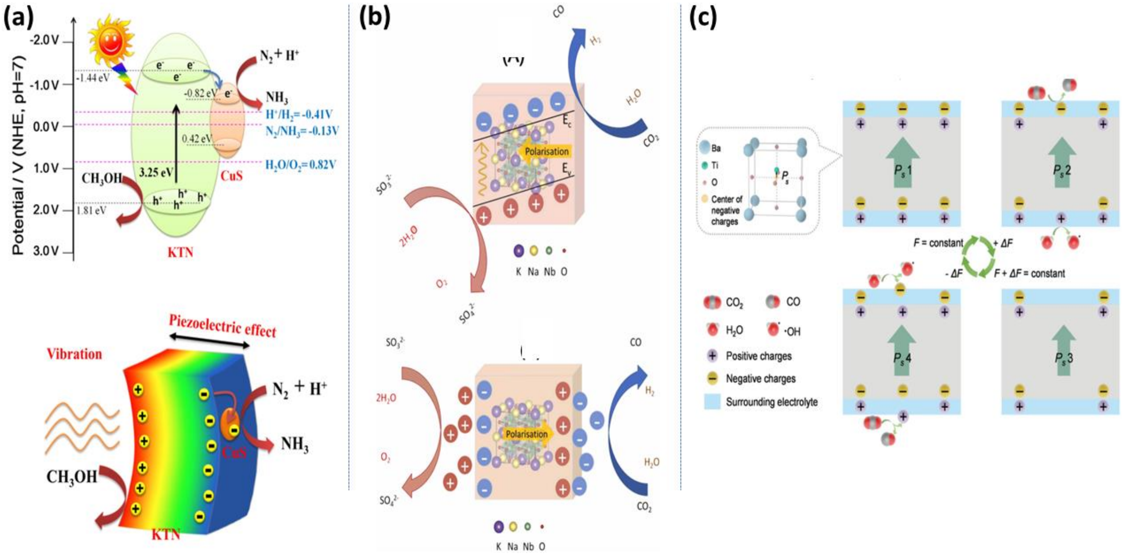

Figure 2.26 Integrated catalytic mechanisms for (a) N_2 Fixation by using CuS/KTN composite. Adapted from Ref[181] (b) Process for CO_2 reduction and H_2 production by using (KNLN). Adapted from Ref[183] (c) the Reduction of CO_2 by using $BaTiO_3$. Adapted from Ref[184]

A novel experimental setup was developed to prevent the agglomeration of ferroelectric particles at high concentrations during sonication, allowing for an in-depth examination of how CO_2 gas concentration, dissolved species, and catalyst loading influence piezocatalytic performance. In typical electrocatalytic, photocatalytic, or sonolytic reactions, CO_2 reduction and water splitting occur concurrently. Yet, in their study, hydrogen evolution is substantially suppressed when using the Li-doped potassium sodium niobate powders in an alkaline catalyst mixture under optimal CO_2 gas conditions. They achieved close selectivity for CO_2 reduction at a gas-phase CO_2 concentration of 1%. They also identified an optimal catalyst concentration of 100 mg L^{-1}, which yielded a maximum CO production rate of 438 µmol $h^{-1}g^{-1}$. Beyond this concentration, the piezocatalytic activity declined due to increased particle collisions and agglomeration, leading to reduced catalytic surfaces. The study also discovered that bicarbonate ions are the active dissolved CO_2 species in piezocatalysis, with their concentration peaking in neutral to weakly alkaline conditions. The addition of a hole scavenger such as Na_2SO_3 can improve catalytic performance, but excessive amounts reduce CO_2 reduction selectivity by reducing the availability of active bicarbonate ions in highly alkaline conditions. This research provides valuable insights into the effects of gas-phase composition, catalyst loading, and scavenger type on CO_2 reduction.

Ma *et al.*,[184] observed that upon activation by ultrasonic vibrations, $BaTiO_3$ nanofibers efficiently converting CO_2 into CO with nearly 100% selectivity, achieving a peak CO yield of 63.3 μmol g^{-1} without requiring any sacrificial agents (**Figure 2.26(c)**).[184] This robust capability for CO_2 reduction is attributable to $BaTiO_3$, which produces a sufficient piezoelectric induced potential to surpass the redox potential of CO_2, reducing the free energy barrier during vibrational stress. In a way to piezocatalysis for CO_2 reduction, this process has similarly been applied to the conversion of methane (CH_4).

Zhou *et al.*,[185] studied hydroxyapatite (HAp) ($Ca_{10}(PO_4)_6(OH)_2$), a material that exhibits a piezoelectric coefficient ranging from 1 to 16 pm V^{-1}. Its ferroelectric properties arise from the ordered orientation of hydroxide ions (OH^-) along the crystallographic directions. This intrinsic characteristic of HAp acts as a catalyst to facilitate the breakdown of methane into smaller molecular compounds. The piezoelectric nature of HAp is confirmed by the typical butterfly-shaped curve obtained by plotting the output amplitude against the applied voltage, indicative of its ability to generate electric charge in response to mechanical pressure (**Figure 2.27(a)**). This phenomenon was supported further by experiments that measured transient current responses, where substantial variation in the current was recorded with and without the application of ultrasonic stimulation (**Figure 2.27(b)**).

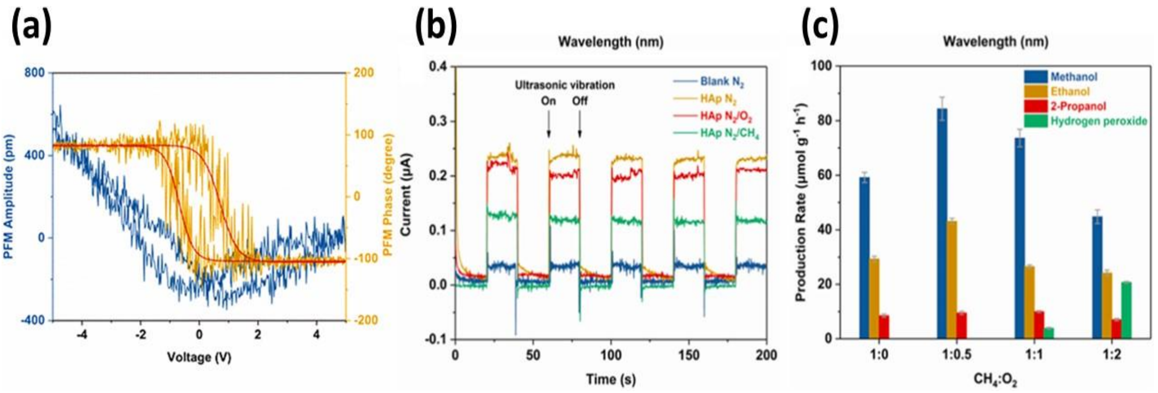

Figure 2.27 (a) The PFM reveals a butterfly-shaped amplitude and hysteresis loops of Hap (b) Transient current responses of HAp under variable atmospheric conditions (c) Liquid yields from HAp-mediated methane conversion at different methane-to-O_2 ratios. Adapted from Ref[185]

Notably, the current achieved its maximum in the presence of nitrogen atmosphere and demonstrated a decline upon the introduction of oxygen and methane, suggesting that both O_2 and CH_4 are activated using the HAp catalyst. Through this catalytic action, methane is transformed into various liquid products, specifically methanol, ethanol, and 2-propanol, with their highest observed production rates being 84.4, 43.2, and 9.6 μmol g^{-1} h^{-1} respectively, operating under a methane-to-oxygen ratio of 1:0.5 (**Figure 2.27(c)**).[185]

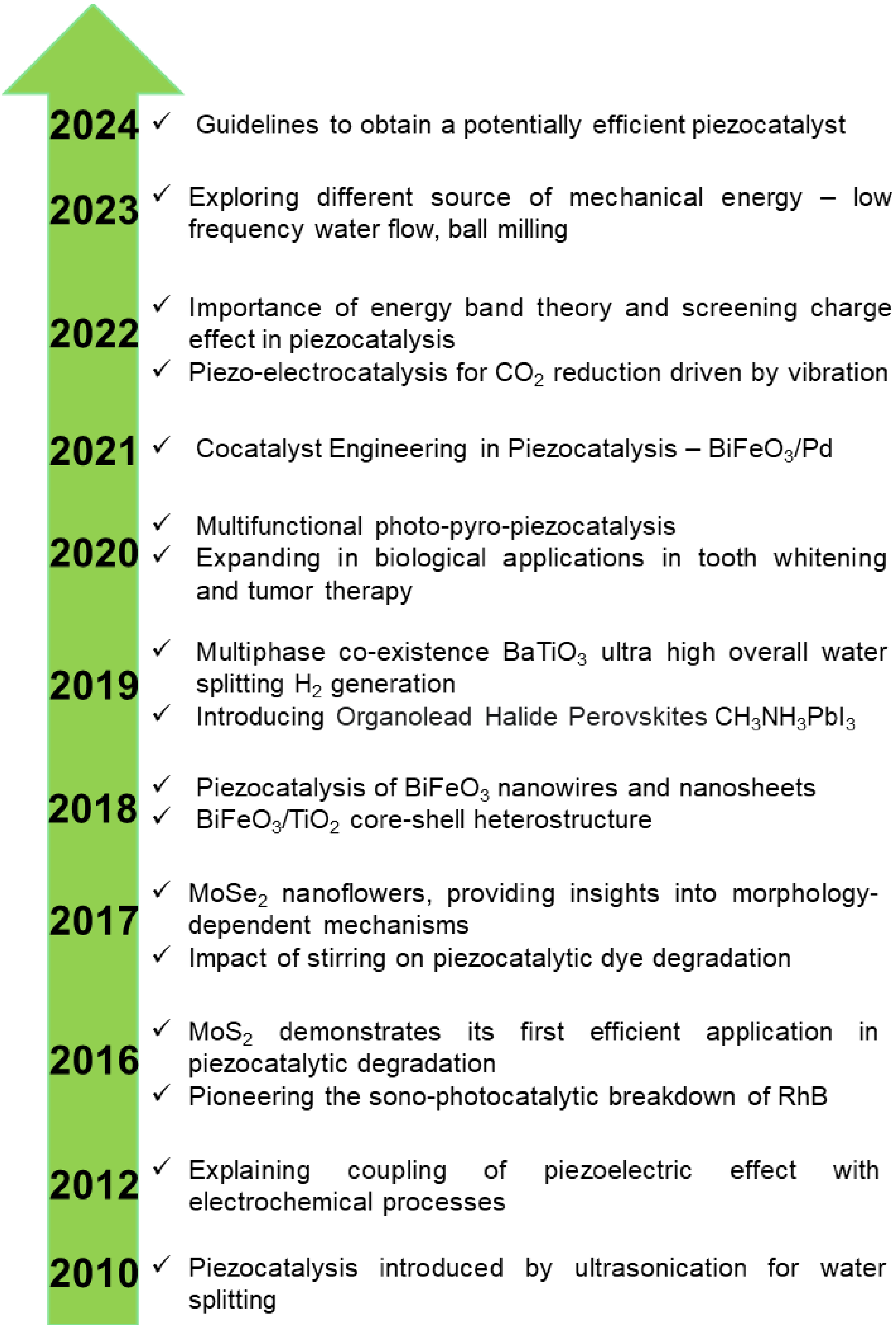

2024
- ✓ Guidelines to obtain a potentially efficient piezocatalyst

2023
- ✓ Exploring different source of mechanical energy – low frequency water flow, ball milling

2022
- ✓ Importance of energy band theory and screening charge effect in piezocatalysis
- ✓ Piezo-electrocatalysis for CO_2 reduction driven by vibration

2021
- ✓ Cocatalyst Engineering in Piezocatalysis – $BiFeO_3/Pd$

2020
- ✓ Multifunctional photo-pyro-piezocatalysis
- ✓ Expanding in biological applications in tooth whitening and tumor therapy

2019
- ✓ Multiphase co-existence $BaTiO_3$ ultra high overall water splitting H_2 generation
- ✓ Introducing Organolead Halide Perovskites $CH_3NH_3PbI_3$

2018
- ✓ Piezocatalysis of $BiFeO_3$ nanowires and nanosheets
- ✓ $BiFeO_3/TiO_2$ core-shell heterostructure

2017
- ✓ $MoSe_2$ nanoflowers, providing insights into morphology-dependent mechanisms
- ✓ Impact of stirring on piezocatalytic dye degradation

2016
- ✓ MoS_2 demonstrates its first efficient application in piezocatalytic degradation
- ✓ Pioneering the sono-photocatalytic breakdown of RhB

2012
- ✓ Explaining coupling of piezoelectric effect with electrochemical processes

2010
- ✓ Piezocatalysis introduced by ultrasonication for water splitting

Figure 2.28 Chronological timeline illustrating the evolution and key milestones in the field of piezocatalysis, highlighting the significant discoveries, developments, and advancements over time

In particular, hydroxyl radicals (·OH) formed from the redox reactions of oxygen and water are proposed to initiate the attack on C–H bonds in methane, leading to its conversion into lower alcohols. Remarkably, this transformation occurred without the production of undesired by-products such as CO_2 or CO. This research extends the potential pathways for methane conversion, incorporating C–C coupling and reducing over-oxidation of methanol, drawing upon the principles of piezocatalysis.

Overall, the comprehensive literature review has provided a solid foundation for understanding the theoretical principles, research progress, and challenges associated with piezocatalysis. While significant milestones have been achieved, as depicted in **Figure 2.28**, several knowledge gaps and unexplored avenues remain. The next chapter aims to delve deeper into these gaps, outlining the specific objectives and research questions that this study seeks to address. By building upon the existing body of knowledge and leveraging the insights gained from the literature, this research endeavours to contribute novel findings and insights to the field of piezocatalysis, potentially paving the way for future advancements and practical applications.

CHAPTER 3. EXPERIMENTAL METHODOLOGY

In this chapter, the materials, experimental procedures, and analytical techniques used to synthesise and characterise BTO, BTO-metal, and BTO-metal oxide piezocatalysts are discussed. Additionally, their performance for hydrogen generation and RhB organic dye degradation is evaluated. The piezocatalytic studies were conducted under both an ultrasonication bath and magnetic stirring.

All chemicals were analytical grade, obtained from commercial Sigma-Aldrich and Nanografi suppliers, and were used without further processing.

3.1 EXPERIMENTAL SYNTHESIS PROCEDURE FOR BTO, BTO-METAL, AND BTO-METAL OXIDES

3.1.1 SYNTHESIS OF BTO

The synthesis of barium titanate powders was achieved through a sequence of steps beginning with a traditional solid-state approach. Stoichiometric ratios of barium carbonate and titanium dioxide were utilised as the fundamental starting materials. These substances were then processed in a Retsch PM100 planetary ball mill, with zirconia media and ethanol, to form a homogeneous mixture. This milling was conducted over five hours at 200 rpm, with a 1:10 ratio of powder mass to zirconia balls. To prevent excessive heat, milling was paused every 20 minutes for 10 minutes. After this, a 250 µm sieve was used for particle size refinement. The BTO powders obtained from these processes were then treated in air at temperatures of 900°C, 1000°C, and 1200°C, for two hours each, yielding BTO samples referred to by their calcination temperatures as BTO-900°C, BTO-1000°C, and BTO-1200°C. The thermal treatment was paced at 5°C min^{-1}. For enhanced uniformity of as-synthesised calcined powders underwent a second round of ball milling, following the same procedure as initially employed.

3.1.2 SYNTHESIS OF BTO-METAL

BTO was synthesised by a simple solid-state technique as discussed earlier. The BTO prepared at 1200°C was quite hard to grind with mortar and pestle due to its coarse texture, making the combination with Pt very difficult. The BTO prepared at 1000°C was softer, allowing facile mixing with Pt. Since platinum is an expensive metal, it is important to use it efficiently. Therefore, catalysts with different loadings of Pt were synthesised. These materials are referred to as PtX, where X is the mass of Pt added to 1 g of BTO. For example, Pt100 was made by adding 1 g of BTO-1000°C powder and then combined with 100 mg platinum nanopowder (< 15 nm, Nanografi, 99.9%) using a mortar and pestle for approximately 1 hour. The mixed powder was then calcined at 1200°C for 2 hours. The heating and cooling rate for this procedure was maintained at 5°C per minute. Finally, the as-synthesised powders were thoroughly mixed using a mortar and pestle in preparation for further analysis.

3.1.3 SYNTHESIS OF BTO-METAL OXIDES

Following the procedure to synthesise BTO discussed earlier, to prepare BTO-Fe_2O_3, BTO-Co_3O_4, BTO-CuO, BTO-NiO, 3 g of BTO-1000°C powders were combined with 300 mg of metal oxide nanopowder. All metal oxides, commercially purchased from Sigma-Aldrich, have a uniform particle size of 50 nm. The mixture was ground with a mortar and pestle for approximately 1 hour. The combined powders were then sintered at 1200°C for a period of 2 hours, employing a heating and cooling rate of 5°C per minute. Following this, the resultant BTO-metal oxide powders were meticulously mixed using a mortar and pestle to ensure uniformity for subsequent analytical studies.

3.2 CHARACTERISATION TECHNIQUES

3.2.1 X-RAY DIFFRACTION (XRD)

X-ray diffraction is a technique employed to ascertain the crystallographic structure of a material. When a crystalline sample is irradiated with X-rays, it produces a diffraction pattern. By analysing this pattern and applying Bragg's law, detailed information about the material's structure, including interatomic distances and crystal lattice orientation, can be derived $(\mathbf{n\lambda = 2d * sin\theta})$. By measuring the diffraction angles $(\boldsymbol{\theta})$ and knowing the wavelength of the X-ray beam $(\boldsymbol{\lambda})$, the interplanar spacing $(\mathbf{d})$ can be calculated. As each material has a characteristic interplanar spacing, XRD allows the identification of crystalline phases present in the materials and the determination of unit cell dimensions. The instrument used for X-ray diffraction in this instance is a Bruker D8 Advance. To analysis the phase structure of the polycrystalline material, which utilises monochromatic Cu Kα radiation with a wavelength of 1.54 Å produced under an operational setting of 40 kV voltage and 40 mA filament current. For data acquisition, the diffractometer scans at 2θ angles ranging from 10° to 80°. The data are collected in increments of 0.01° (step size) with a scanning rate of 0.6° per minute.

3.2.2 SCANNING ELECTRON MICROSCOPY (SEM) AND ENERGY DISPERSIVE X-RAY SPECTROSCOPY (EDS)

Scanning Electron Microscopy, utilising a Zeiss Supra 55 VP instrument, was employed for investigating the surface morphology of the powders. The SEM is fitted with an Energy-Dispersive X-ray spectroscopy system, specifically the Oxford Instruments XMax detector, which enables the identification of the chemical composition within the sample. The EDS system works by detecting the characteristic X-rays that are emitted from the sample when it is bombarded with electrons; these X-rays are unique to each element, allowing for elemental analysis and mapping of the sample's surface composition.

3.2.3 BRUNAUER-EMMET-TELLER (BET) SURFACE AREA ANALYSIS

The specific surface area of the powders was ascertained using the Brunauer-Emmett-Teller method, which involves nitrogen adsorption isotherms. The measurements were performed on a Gemini VII 3.03 nitrogen adsorption apparatus by Micromeritics Instruments. Through the BET analysis, detailed information regarding the surface area and pore characteristics of the powders can be obtained, which are essential factors impacting their functionality in diverse applications.

3.2.4 RAMAN SPECTROSCOPY

Raman spectroscopy was utilised to evaluate the crystalline orientation of the ceramic powders. The XploRATM Plus system from Horiba, Japan, fitted with a 535 nm laser excitation, was employed for this analysis. This technique utilises the inelastic scattering of monochromatic light from the laser to provide information about the crystal structure and phase composition of the ceramic powders.

3.2.5 X-RAY PHOTOELECTRON SPECTROSCOPY (XPS)

The surface elemental composition was examined by X-ray photoelectron spectroscopy on a Thermo Scientific Kα photoelectron spectrometer. This instrument employed monochromatic Al Kα radiation to probe into the sample. Detailed scans were recorded focusing on the dominant peaks for elements, such as C (1s), O (1s), Ba (3d), Ti (3d), and Pt (4f), at a pass energy of 50 eV. The peaks were analysed using Casa XPS software, and for charge correction, the binding energy scale was calibrated to the adventitious carbon peak at 285.0 eV.

3.2.6 GAS CHROMATOGRAPHY (GC)

The composition of the outlet gas was analysed by inline gas chromatography (HP 5890 Series II, Agilent Technologies), which utilised a thermal conductivity detector (TCD) to determine the various gas components. For regulating the flow rate of argon, a mass flow controller (SEC-4400R) was employed, while the total flow rate for each experiment was verified using a soap-film bubble flowmeter.

3.2.7 UV-VIS SPECTROSCOPY

UV-vis spectroscopy is a powerful technique for estimating the optical energy band gap of powdered samples, particularly semiconductors. The diffuse reflectance UV-vis spectroscopy (DRS-UV) covers a wide wavelength range and often incorporates an integrating sphere for accurate measurement of the diffuse reflected light from powder samples. Barium sulfate is commonly used as a reflectance standard due to its high diffuse reflectance across the UV-vis spectrum. The Kubelka-Munk function is then applied to the reflectance data to analyse the absorption coefficient and estimate the bandgap energy. For quantitative analysis of solutions, such as the RhB dye concentration, UV spectrophotometry provides precise measurements based on absorbance at characteristic wavelengths. For RhB, the characteristic absorption peak is at 554 nm,(ChemSpider ID 6439) which can be measured using instruments such as the Shimadzu-2600i and HP 8453 UV-Vis spectrophotometers, ensuring an accurate determination of the dye concentration in the solution.

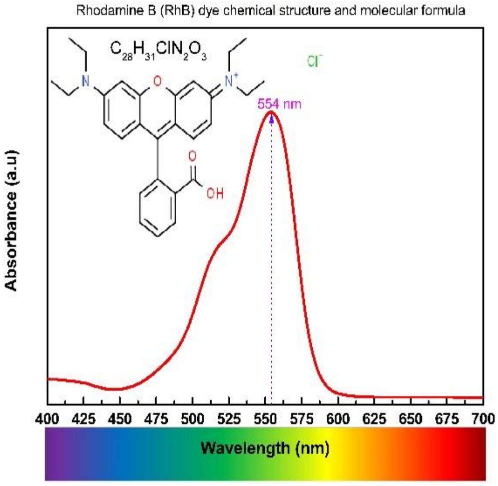

Figure 3.1 Rhodamine B dye characteristic absorption wavelength of 554 nm

3.3 PIEZOCATALYTIC DYE-DEGRADATION OF BTO AND BTO-METAL OXIDES

The piezocatalytic activity of the synthesised BTO at different temperatures, commercial BTO, and BTO-metal oxide (BTO-Fe_2O_3, BTO-Co_3O_4, BTO-CuO, and BTO-NiO) were evaluated by degrading Rhodamine B (RhB, Merck). In a standard experiment, a predetermined amount of BTO is introduced into a 100 ml Erlenmeyer flask sourced from Biohal which contains a Rhodamine B dye solution. This solution's concentration varies between 5 and 200 mg/L. A PTFE-coated magnetic stir bar from Isolab, 8 mm in diameter and 40 mm in length, is used to mechanically stir the solution. The stirring speed is ranging from 120 rpm to 620 rpm, increasing in 100 rpm increments, and the procedure is carried out in the absence of light at ambient temperature. Subsequent to a specified duration of reaction time, the BTO particles were separated from the mixture using centrifugal filtration. The concentration of RhB remaining in the solution was then quantified using an HP 8453 and Shimadzu-2600i UV-visible spectrophotometer. In the experiments with BTO-metal oxide variants, each composite (BTO-Fe_2O_3, BTO-Co_3O_4, BTO-CuO, and BTO-NiO) was used to treat a 50 mL RhB solution at a concentration of 5 ppm. A total of 100 mg of catalyst, equated to a loading of 2 g L^{-1}, was added to the dye solution for each trial, conducted at ambient temperature. The control experiments were conducted under the same conditions but without any catalyst; they consisted of alumina and pure BTO samples. Both the control sets and those containing the catalyst were stirred at a speed of 900 rpm. To begin with, a 1 ml aliquot of the dye solution was collected following a 30-minute period without stirring, which was used to determine the adsorption-desorption equilibrium, referred to as the C_0

reference. Following this, 2 ml aliquots of the RhB solution were taken at the 24-hour mark for analysis using UV-visible spectroscopy. Post-collection, these samples were subjected to centrifugation at 9000 rpm for a duration of 10 minutes to facilitate the separation of the catalyst particles. The remaining RhB concentration was quantified with a UV-2600i spectrophotometer. **Figure 3.1** illustrates the absorption of the dye at its characteristic wavelength of 554 nm.

3.4 PIEZOCATALYTIC HYDROGEN PRODUCTION OF BTO-METAL EXPERIMENT

Before starting each experiment, the ultrasonic cleaning bath (model 60W-TP01 from Taiwan Total Metre) was filled with 630 mL of water. For each trial, a 100 mL Erlenmeyer flask was placed in the centre of the ultrasonication bath, with a 10 mm distance from the bottom of the flask to the bottom of the ultrasonication bath. This centering of the flask was maintained for each experimental trial using a custom 3D printed holder (**Figure 5.6**), as discussed in **Section 5.2.1** . Initially, to start with a baseline for the sonication process, the piezocatalyst powder was added to a mixture containing 2% methanol by volume in distilled water and agitated with a magnetic stirrer as the preliminary parameter. Subsequently, this solution was saturated with argon gas, flowing at roughly 14 mL/min for a duration between 45 minutes and 1 hour, to achieve efficient particle dispersion and improve hydrogen production. The stirrer bar was then removed from the solution and held at the top of the sealed reactor using a magnet prior to further experiments (**Figure 5.6**). Argon was continuously bubbled through the flask to maintain the concentration of dissolved gases. The argon gas flow was governed by a mass flow controller, with a soap-film bubble flowmeter ensuring accuracy of the total flow rate during each experiment. To maintain the temperature of the ultrasonic bath at a consistent 35°C, a temperature control system paired with a thermocouple and enhanced by a peristaltic pump and an external Peltier cooler was employed. The experimental apparatus for investigating the piezocatalytic generation of hydrogen was photographically illustrated in **Figure 5.7**. The image depicts the configuration of the reaction vessel, piezocatalytic material, and associated instrumentation components. The gaseous products evolving from the piezocatalytic process were subjected to inline chromatographic analysis to determine their composition quantitatively, with a focus on monitoring the hydrogen yield.

3.5 PIEZOCATALYTIC HYDROGEN PEROXIDE PRODUCTION EXPERIMENT

The experimental parameters utilised for the hydrogen generation tests were replicated for the piezocatalytic production of hydrogen peroxide under similar conditions. To quantify the hydrogen peroxide concentrations, the iodometric technique was employed. In this method, the reaction between iodide ions and hydrogen peroxide forms triiodide ions (I^{3-}), the concentration of which can be determined by their absorbance at a specific wavelength indicative of the H_2O_2 present. These ions exhibit light absorption at a wavelength of 352 nm. To begin the analytical process, 2 ml samples were taken from the sonicated reactor contents and then transferred into a quartz cuvette. This cuvette already contained a series of reagents: a 10^{-4} M solution of ammonium molybdate, 0.75 ml of 0.10 M potassium biphthalate buffer, and 0.75 ml of a mixed solution comprised of 0.4 M potassium iodide and 0.06 M sodium hydroxide. These reagents facilitate the quantification of hydrogen peroxide through the iodometric method.

The cuvette with the reacting mixture was allowed to stand for a short interval before the solution was analysed using an HP 8453 UV-vis spectrophotometer. The analysis of the dye concentrations, both before and after the reaction, was conducted using UV-vis spectroscopy. This method allowed for the accurate quantification by assessing the specific absorption maxima, indicative of their respective concentrations. **Figure 3.2** presents a detailed schematic diagram of the experimental apparatus, outlining the key components and their configuration for piezocatalytic H_2 and H_2O_2 production. This visual comparison between the schematic and practical setup allows for a comprehensive understanding of the experimental design.

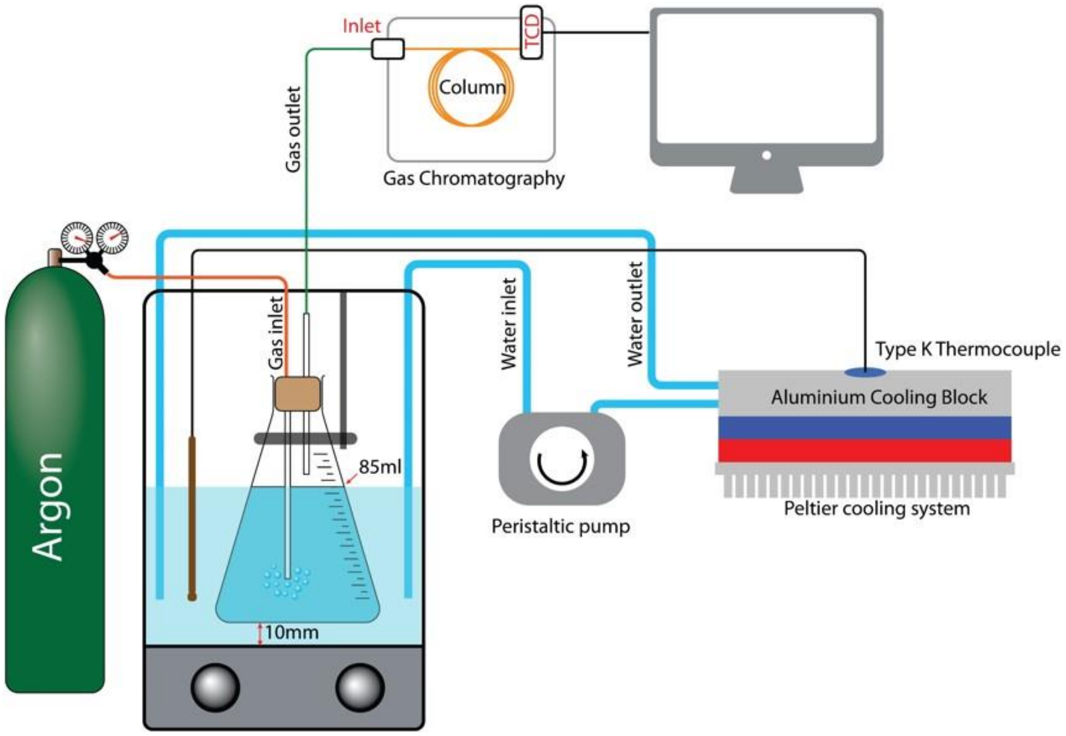

Figure 3.2 Illustrative representation of the experimental setup, detailing the major components and layout utilised in piezocatalytic hydrogen generation

CHAPTER 4. IMPACT OF PIEZOCATALYTIC DYE DEGRADATION USING BTO NANOPARTICLES

Declarations: The research work in this chapter has been published.

4.1 INTRODUCTION

This chapter offers a comprehensive study of the role that stirring plays in the process of piezocatalytic dye degradation. The investigation explores the utilisation of a piezoelectric material as an important point, examining how mechanical stress, induced by stirring, can increase the degradation of organic dye pollutants. The scope of the investigation includes a thorough evaluation of the structural analysis using different calcination temperature, stirring parameters, including the rate, volume of the vessel, catalyst loading, and atmospheric effect with their significant influence on the efficiency of dye degradation. The study carefully examines the mechanisms by which mechanical agitation potentially facilitates the piezocatalytic activity, thereby providing an understanding of the interaction between mechanical stirring and chemical processes. The following sections will describe the investigative procedure, from the systematic preparation of samples through to the measurements of their piezocatalytic activity.

4.2 RESULTS AND DISCUSSION

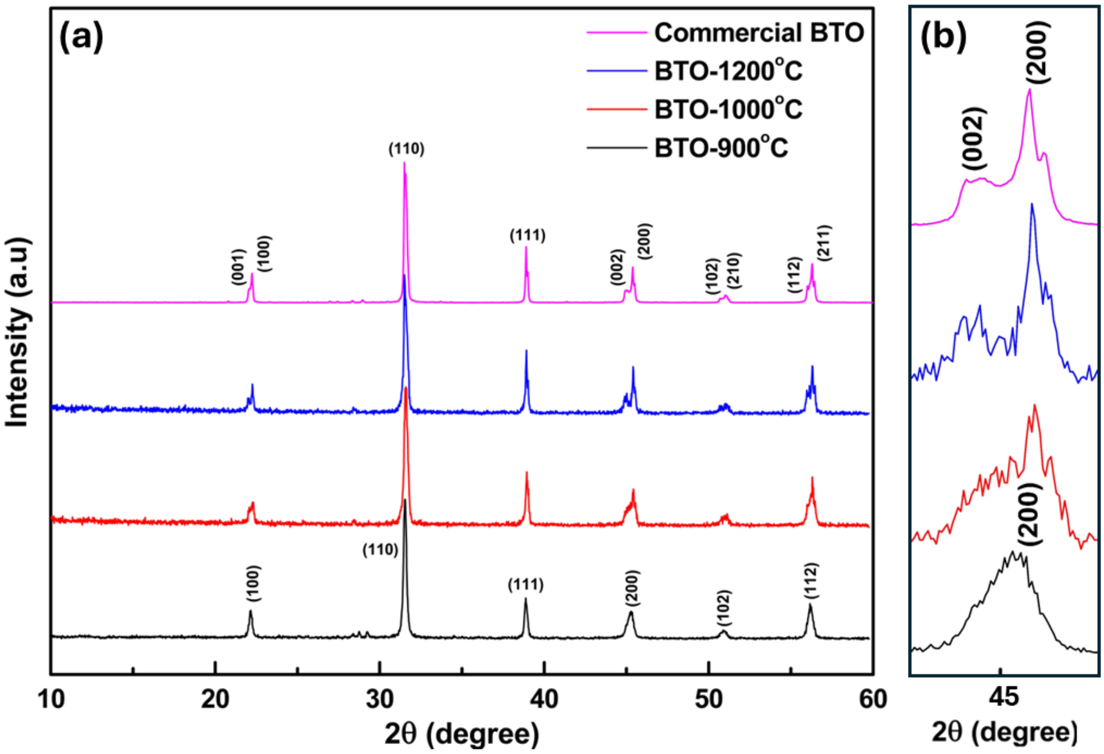

Figure 4.1 (a)The comparison of XRD diffractograms for BTO annealed at 900°C, 1000°C, 1200°C, and the diffractogram of commercial BTO (b) inset XRD data of tetragonal peak splitting at 2θ ~ 45°

XRD analysis reveals that the observed peaks can be attributed to the distinctive perovskite structure that characterises BTO, with a particular alignment to its tetragonal crystallographic phase. The correspondence of the observed diffraction pattern is confirmed through JCPDS file number 05-0626. The extent of tetragonal distortion appears to be greater in the synthesised BTO sample annealed at 1200°C with no detectable impurity phases compared to the commercially obtained BTO powder. The degree of this distortion plays a critical role in the ferroelectric and piezoelectric properties of the material because it is typically related to the c/a ratio in the tetragonal unit cell. The tetragonal distortion of the unit cell is evidenced by the peak splitting of (002) and (200) at 2θ ~ 45°. Similarly, the well-defined peaks in the XRD pattern for the synthesised BTO at different temperatures 900°C and 1000°C show an indication of high purity. The XRD data confirms the synthesis of phase-pure perovskite BTO at 1200°C, which exhibits a potentially greater degree of tetragonal distortion compared to both the other annealed BTO samples and the commercially acquired BTO, as depicted in the **Figure 4.1**.

The morphologies of the as-synthesised BTO samples that were used as piezocatalysts were analysed by SEM, as shown in **Figure 4.2**. The SEM micrographs show that the particle size gradually increases with increasing annealing temperature. The BTO-900°C shows some small particles combined with larger primary particles. The average primary particle size of BTO-900°C is smaller than 500 nm. Upon heating, the smaller particles agglomerate into the larger particle to produce a larger average size of the primary particle of around 700 nm for BTO-1000°C. There is evidence of necking and preliminary stages of sintering with particles growing to exceed 700 nm with some particles growing bigger than 1 µm for BTO-1200°C as shown in **Figure 4.2(c)**.

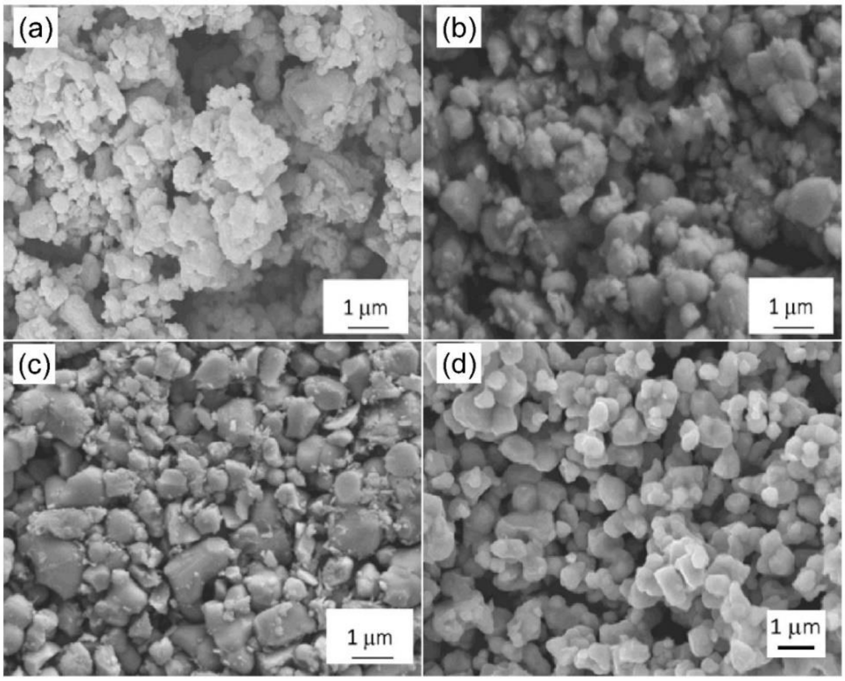

Figure 4.2 SEM images for (a) BTO-900°C (b) BTO-1000°C (c) BTO-1200°C (d) commercial BTO

SEM analysis of BTO particle sizes synthesised at varying temperatures: 480 nm (BTO-900°C), 690 nm (BTO-1000°C), 790 nm (BTO-1200°C), and 770 nm for the commercial BTO as revealed in **Figure 4.3**.The determination of the tetragonality of BTO using XRD spectra is complicated due to the overlapping characteristic peaks of the tetragonal and cubic phases.

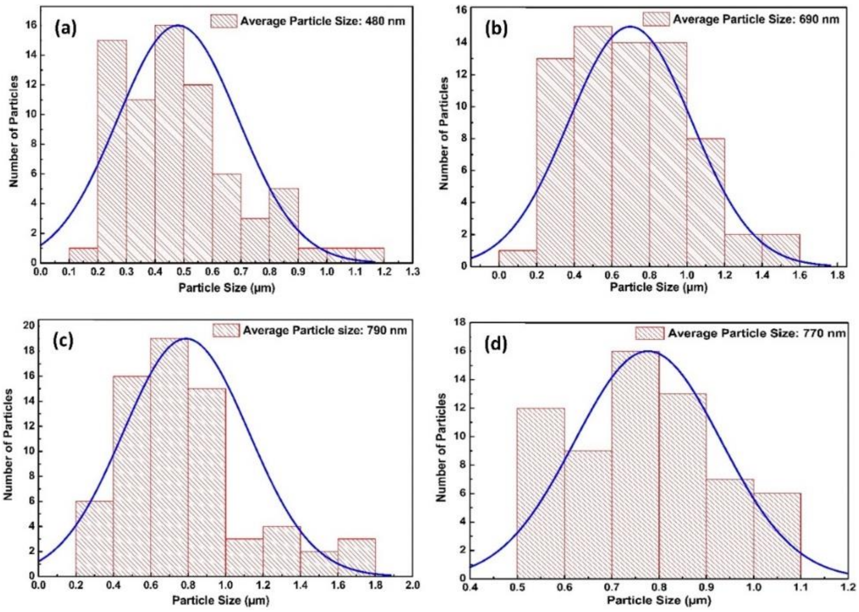

Figure 4.3 Particle size normal distribution of BTO samples synthesised at different temperatures, with (a) BTO-900°C, (b) BTO-1000°C, (c) BTO-1200°C, and (d) commercial BTO, as measured by SEM analysis

Raman spectroscopy has been widely used to study the tetragonal to cubic symmetry of BTO, as it can confirm the presence of the tetragonal phase even when XRD measurements only show the formation of the cubic phase. Specifically, the sharp peak at

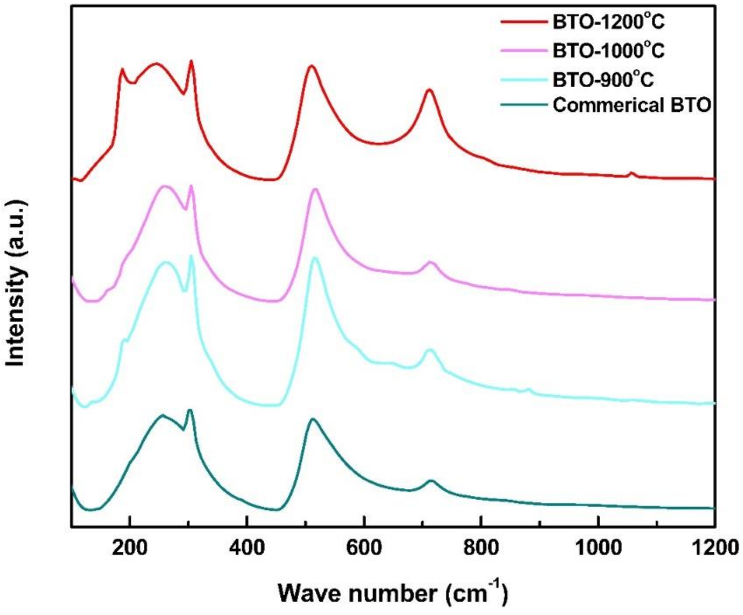

Figure 4.4 Raman spectra of the as-prepared and commercial BTO samples

305 cm^{-1} and a broader peak at 720 cm^{-1} in the Raman spectrum are indicative of the tetragonal phase.[186,187] The Raman spectra of the synthesised BTO samples, as depicted in **Figure 4.4**, consistently exhibited characteristic peaks confirming the presence of the tetragonal phase, irrespective of the synthesis conditions. However, variations in the scattering intensities of the characteristic peaks were observed in the as-prepared BTO samples at different calcination temperatures, indicating that the tetragonality of the synthesised BTO is influenced by the calcination temperature. Specifically, the BTO sample calcined at 1200°C displayed the highest amount of tetragonal phase, while there was no significant difference in the tetragonal-cubic symmetry of the BTO samples calcined at 900°C and 1000°C.

Furthermore, all synthesised samples exhibited higher tetragonality compared to commercial BTO The N_2 adsorption-desorption isotherm analysis revealed a single hysteresis loop between relative pressures of 0.05 and 0.25 for the BTO samples. The specific surface area of the BTO samples, measured at different calcination temperatures (BTO-900°C, BTO-1000°C, and BTO-1200°C), was determined to be 3.96 m^2g^{-1}, 2.52 m^2g^{-1}, and 1.61 m^2g^{-1}, respectively. In contrast, the specific surface area of commercial BTO was found to be only 1.4 m^2g^{-1}. Notably, the specific surface area of BTO decreased with an increase in the heat treatment, indicating a reduction in surface area attributed to sintering where particles agglomerate and coalesce, leading to a decrease in the overall surface area.

4.2.1 IMPACT OF BTO STRUCTURAL PROPERTIES ON PERFORMANCE

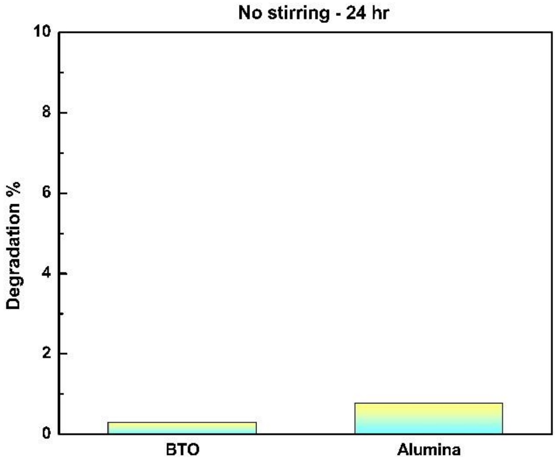

Figure 4.5 No stirring - 24 hours experiment

To eliminate the effects of low-grade mechanical energy on the degradation of RhB dye by piezoelectric catalyst, the adsorption experiments were conducted without magnetic stirring. A 100 mg sample of the BTO-1200°C catalyst was added to 50 ml of a RhB solution with a concentration of 5 mg/L. It was found that RhB adsorption on BTO particles was minimal. Notably, Al_2O_3, a non-ferroelectric material used as a reference catalyst, showed a marginally adsorption than BTO after 24 hours without any stirring (**Figure 4.5**).

Previously, [51,188,189] studies have established that only the tetragonal phase of BTO, due to its ferroelectric nature, contributes to the piezocatalytic activity, unlike the centrosymmetric and non-ferroelectric cubic phase; the cubic phase is centrosymmetric and is therefore not ferroelectric. Therefore, it was expected that BTO-1200°C, with its higher tetragonality achieved through higher calcination temperature, would exhibit piezocatalytic activity. To verify this role of tetragonality, the degradation of RhB dye was investigated using different BTO samples. Each experiment utilised 40 mg of BTO powder (as-synthesised and commercial) to treat 20 mL of 5 mg/L RhB solution under stirring at 520 rpm for varying durations. After centrifugation and analysis, the results confirmed the hypothesis. As shown in **Figure 4.6(a) and (b)**, BTO-1200°C achieved 93% RhB degradation within 240 minutes. Furthermore, the excellent fit of the data to a pseudo-first-order kinetic model (adjusted R-square > 0.99) across independent experiments (indicated by each data point in Figure 4.6**)** underscores the reproducibility and validity of the study. The rate of RhB degradation, denoted by 'K_{obs}', utilising BTO calcined at 1200°C is determined to be 0.011 min^{-1}. This rate is significantly higher, ~3.5 times greater compared to BTO samples calcined at reduced temperatures, and ~13 times greater in comparison to the commercially available BTO. It has been demonstrated that BTO-1200°C presents the greatest degree of tetragonal distortion, which is likely responsible for its piezocatalytic performance, despite having a smaller BET surface area and larger particle size.

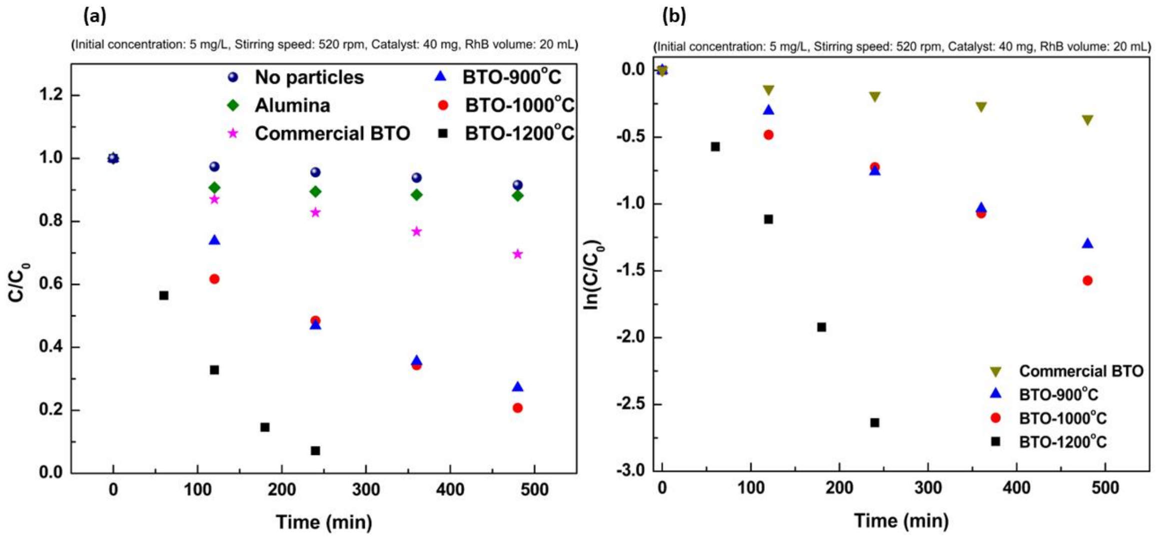

Figure 4.6 (a) Comparative analysis of RhB piezocatalytic degradation over time with various samples; (b) Kinetics of reaction rate fitting

Additionally, the relatively weakened piezocatalytic efficiency of the commercial BTO is likely due to both its lowest degree of tetragonal distortion and the smallest BET surface area. Control experiments utilising non-ferroelectric material and blank tests were conducted to verify the piezocatalytic function of the ferroelectric BTO. These tests included using commercial alumina and conducting trials without introducing any particles. **Figure 4.6(a)** reveals that simply agitating the RhB solution at high speeds without particles causes a minor reduction in RhB concentration, likely due to friction caused by the stirring mechanism. When non-ferroelectric alumina is added to the solution, there is a more pronounced decrease in RhB levels, which could reduce the additional friction provided by the solid particles. Nonetheless, the comparison between the ferroelectric BTO and non-ferroelectric alumina (Al_2O_3) exhibits a substantial distinction in performance, highlighting the critical role of dipoles in facilitating chemical transformation.

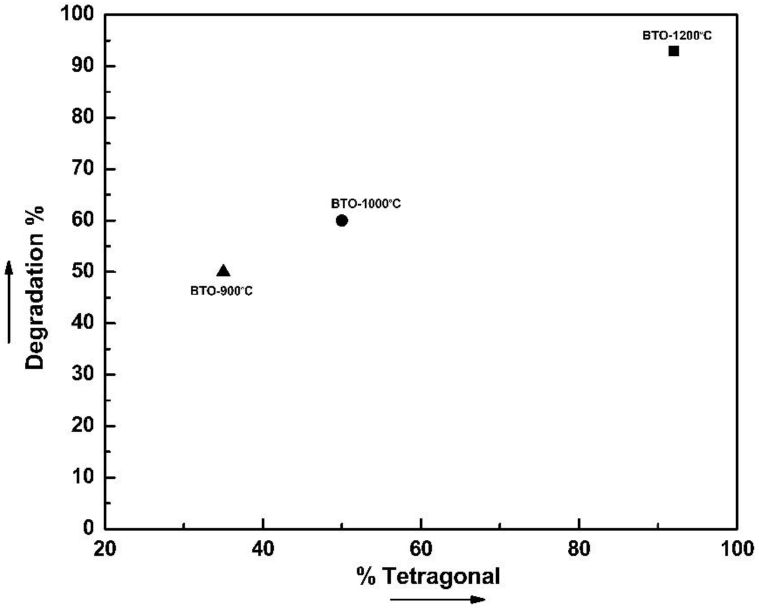

Figure 4.7 Degradation % of BTO as a function of tetragonality for different annealing temperatures (900°C, 1000°C, 1200°C)

Further the study investigates the relationship between the annealing temperature, crystal structure, and degradation efficiency of synthesised BTO as shown in **Figure 4.7** by using the Profex refinement software. By analysing samples annealed at various temperatures to understand how changes in tetragonality influence the material's performance in degradation applications. The findings suggest that higher annealing temperatures enhance the tetragonality of BTO, which in turn improves its degradation percentage. These insights could be crucial for optimising the processing conditions of BTO for various energy and environmental applications.

4.2.2 INFLUENCE OF CATALYTIC PROCESS PARAMETERS

In an investigatory analysis, the influence of variable catalyst mass was meticulously evaluated through the degradation kinetics of RhB dye. Aqueous dye solutions were prepared, each with a volume of 20 mL and a uniform RhB concentration of 5 mg/L. The solutions were subjected to continuous magnetic agitation at a rotational speed of 520 rpm over a duration of 120 minutes. This experiment was conducted in the context of varying quantities of barium titanate synthesised at a calcination temperature of 1200°C, which exhibits a highly tetragonal crystal structure conducive to piezocatalytic processes. **Figure 4.8(a)**, which catalogues the experimental outcomes, indicates that a negligible degradation rate, estimated at 2%, was observed when the catalytic material was absent, underscoring the necessity of the catalyst in the degradation mechanism of the RhB dye. Furthermore, the introduction of a minimal quantity of the piezocatalyst, specifically 1 mg of BTO-1200°C, was sufficient to considerably augment the piezocatalytic degradation efficiency of the RhB solution, improving it by up to 12%. The experimental evidence further revealed a direct correlation between the piezocatalyst loading and the degradation efficiency, with the latter increasing in response to increased BTO concentrations. Notably, an optimal BTO-1200°C loading level of 20 mg, corresponding to a catalyst concentration of 1 mg/mL, was identified as the most effective amount for achieving enhanced piezocatalytic degradation efficiency. Continuing the examination of BTO loading levels, it was observed that beyond the established optimal concentration, a higher loading of BTO surprisingly led to a reduction in the Rhodamine B degradation efficiency.

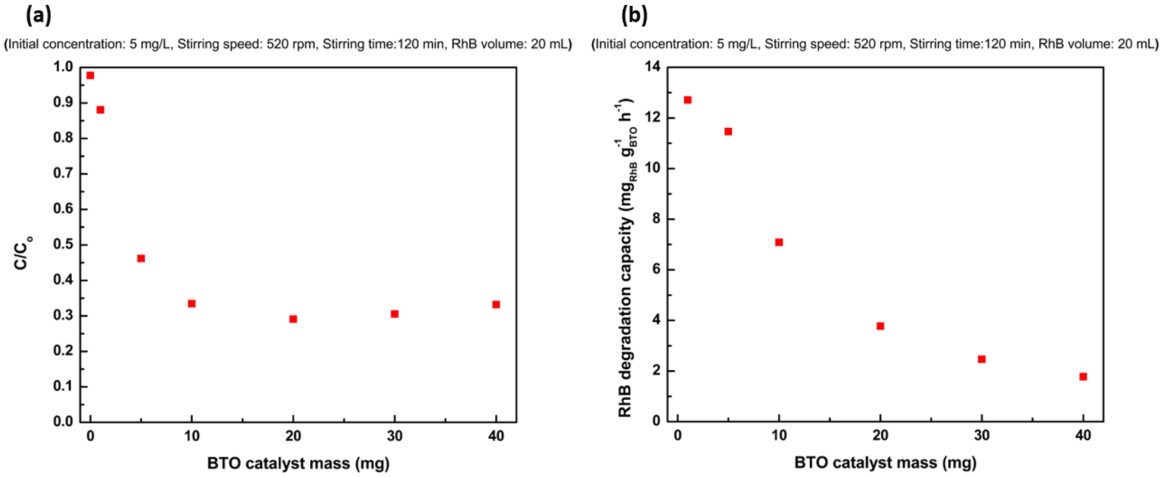

Figure 4.8 Effect of catalyst mass on piezocatalytic activity (a) Kinetics plot of RhB degradation; (b) Amount of RhB degraded by catalyst

This reduction is attributed to the increased probability of collisions among the piezocatalyst particles themselves.[95] These interparticle collisions can potentially disrupt the efficiency of the piezoelectric reactions, overlooking the expected increase in degradation performance and thereby establishing an upper limit on the advantageous concentration of the piezocatalyst. According to the findings of Zhu *et al.*,[145] an increase in the concentration of BZT-BCT fibers leads to mutual interference, which adversely affects the overall piezoelectric potential. Corroborating this, an analysis focused on the efficiency of BTO—specifically the ratio of RhB degraded to the catalyst amount presented in **Figure 4.8(b)**—indicates that the piezocatalytic performance of BTO declines as more catalyst is added. It becomes apparent that when magnetic stirring is employed, catalyst particles colliding is an inevitable consequence. However, this phenomenon can be substantially reduced, or even eliminated, when low doses of the catalyst are dispersed with the aid of ultrasound vibration.

In this investigation, the influence of mechanical agitation on the piezocatalytic degradation efficiency of organic contaminants, such as RhB, is critically examined. The change of stirring intensity and the variation in catalyst BTO loading are hypothesised to significantly influence the piezocatalytic activity. The application of a magnetic stirrer imparts rotational motion to the reaction mixture, thereby inducing mechanical stress on the surface of BTO particles, which activates their piezoelectric effect.[125,144] An increase in rotational speed not only intensifies this effect but also modifies fluid dynamics, potentially introducing vortices and impacting gas entrainment.[190,191]

The degradation efficiency of RhB by BTO catalysts is influenced by the mechanical forces applied through the stirring action of a magnetic stirrer, as well as hydrodynamic effects such as gas entrainment and vortex formation at the liquid surface. Recognising the possible differential influence of these factors at varying catalyst concentrations, a systematic assessment of the piezocatalytic degradation of RhB was undertaken. An aqueous solution with a RhB concentration of 5 mg/L was treated piezocatalytically in a 20 mL volume with BTO dosages of 5 mg and 20 mg, which had undergone calcination at 1200°C. The objective of this study was to elucidate the effects of BTO loading on RhB degradation kinetics within a range of hydrodynamic conditions created by different stirring speeds. The investigation confirmed that the increased rotational speeds facilitated by a magnetic stirrer correlated with enhanced piezocatalytic degradation of RhB. This trend persists across different catalyst loadings and is substantiated by the data in **Figure 4.9(a)**.

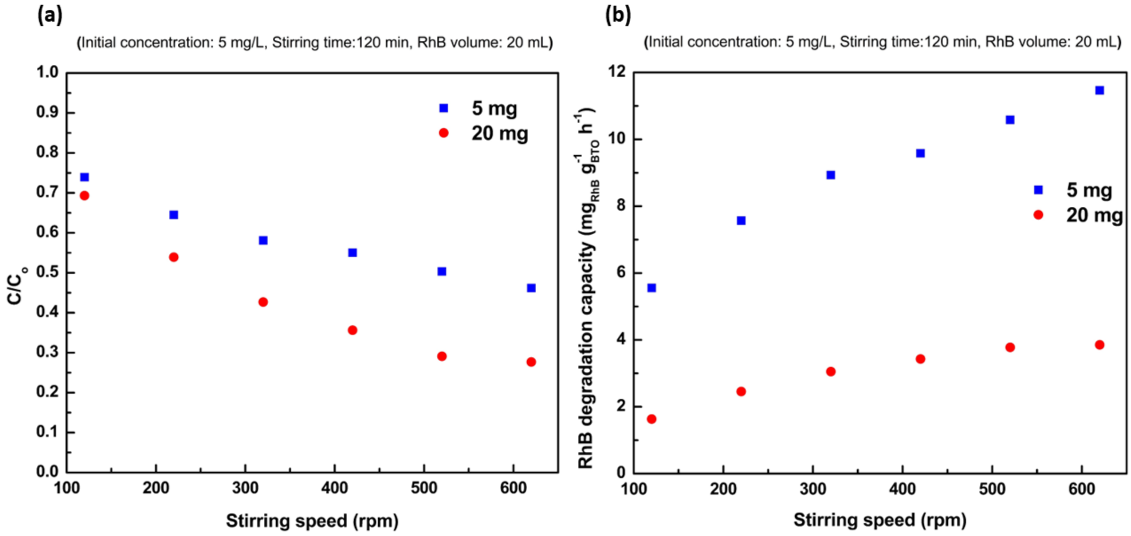

Figure 4.9 Variation in Degradation Efficiency with Stirring Speed (a) Kinetics plot of RhB degradation; (b) Amount of RhB degraded by catalyst

At a lower barium titanate concentration of 5 mg, a direct linear relationship was observed between the stirrer speed and the degradation efficiency of RhB. Conversely, at a higher BTO concentration (20 mg), the efficiency exhibited a nonlinear response, tending towards a plateau. This saturation behaviour suggests limited gains in catalytic activity at higher speeds, possibly due to the increased frequency of collisions among the more abundant catalytic particles (**Figure 4.9(b)**). Previous studies[190] have demonstrated that the volume of air entrained in a reactor is inversely proportional to the liquid column height due to the progressive increase of gravitational forces. To explore the influence of these conditions on the piezocatalytic degradation process, experiments were conducted with variable volumes (5 ml and 10 ml) of a RhB solution with a consistent concentration of 5 mg/L.

These tests varied both the catalyst loading and the solution volume to investigate the behaviour under different air entrainment conditions. To ascertain the reproducibility and accuracy of the observed reaction rates, each experimental condition was replicated across a minimum of four different time intervals. These repetitions allowed for the calculation of the observed rate constant ($\mathrm{K_{obs}}$). The dataset consistently conformed to a pseudo-first-order kinetic model with a high degree of fit, as evidenced by an adjusted R-square value exceeding >0.99. **Figure 4.10** illustrates that within a constant catalyst concentration, the reaction system containing a 5 ml volume exhibits the higher observed reaction rate constant ($\mathrm{K_{obs}}$). This phenomenon could potentially be explicated by two mechanisms: Firstly, the minimisation of liquid column height augments the incorporation of air, which can enhance the mass transport of reactants to the catalytic sites;[190] Secondly, the reduction in fluid depth is correlated with an increase in tangential flow velocity, which consequently exerts amplified stress upon the BTO particulates, possibly invigorating the piezocatalytic activity [192]. The efficiency of RhB degradation reached a steady state with increased catalyst concentrations when treating a 10 ml RhB solution.

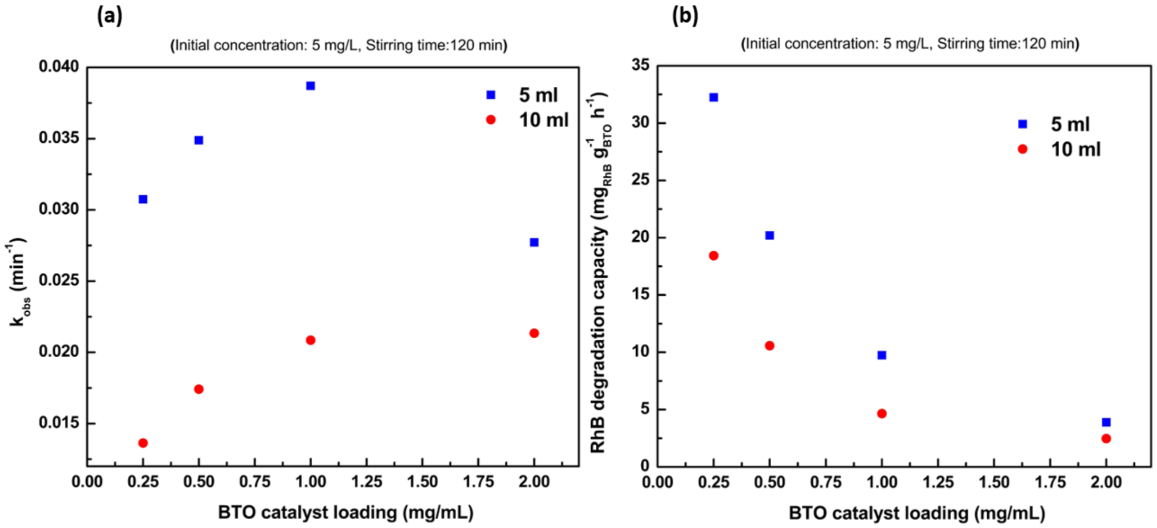

Figure 4.10 Influence of Catalyst Loading and Volume on Degradation Performance (a) Kinetics plot of RhB degradation (b) Amount of RhB degraded by catalyst

Furthermore, the rate constant of RhB degradation ($\mathrm{K_{obs}}$) exhibited an increase with the BTO concentration up to 1 mg/ml. Beyond this concentration, continuing to raise the

BTO levels to 2 mg/ml while treating 5 ml of RhB led to a significant decline in observed rates. This trend could be due to enhance turbulence at reduced liquid volumes, leading to more frequent collisions among BTO particles. Such interactions can diminish the total piezocatalytic effect, as piezoelectric potentials of opposing signs may neutralise one another. To enhance the degradation efficacy, a catalyst loading of 1 mg/ml was selected for subsequent investigation. Experiments were conducted to ascertain the Langmuir-Hinshelwood constants, maintaining a consistent BTO catalyst concentration of 1 mg/ml, and varying the liquid volume across different RhB solutions. Subsequent analysis utilised **Eq. 2.2** resulted in the data presented in **Figure 4.11**.

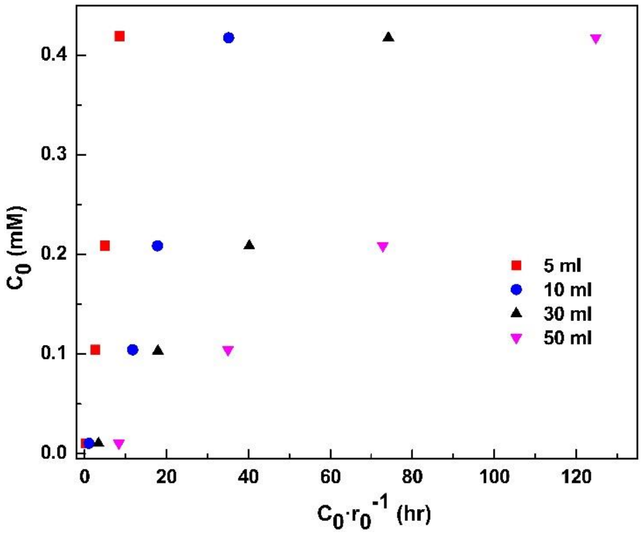

Figure 4.11 The correlation plots demonstrated linearity as evidenced by a high coefficient of determination ($R^2 > 0.99$)

Table 4.1 Effect of liquid volume on the kinetic rate constants of piezocatalytic degradation of RhB under mechanically agitated conditions

RhB solution volume	50 mL	30 mL	10 mL	5 mL
k, $mM.h^{-1}$	0.003	0.006	0.012	0.050

Table 4.1 outlines the rate constant ($'K_{obs}'$) values observed from the experiments. Observations from the **Table 4.1**, indicate a pronounced rise in the rate constant related to the reduction of liquid volume, which presents an atypical phenomenon given the constancy of other experimental parameters, including the agitation velocity and the quantity of catalyst employed. Subsequent experiments were methodically conducted to probe this anomaly by systematically varying the liquid volume, while maintaining a RhB concentration of 5 mg/L, in both air and argon conditions.

4.2.3 IMPACT OF AIR AND ARGON ATMOSPHERES ON PIEZOCATALYTIC EFFICIENCY OF BTO

A comprehensive analysis of RhB degradation kinetics revealed a decline in RhB concentration in relation to its initial value, mathematically described as the ratio C/C_0, over time (t). Through this temporal assessment, the observed rate constant, designated as k, was quantified. This rate constant is crucial as it quantifies the rate at which RhB degradation occurs, which in turn is a direct measure of the piezocatalytic activity inherent to ferroelectric barium titanate.

Furthermore, the capacity of BTO-1200°C to degrade RhB was evaluated, further supporting its efficacy as a piezoelectric catalyst. The results of these measurements have been systematically compiled and are visually presented in **Figure 4.12**. Comparative kinetics of RhB degradation under piezocatalysis with barium titanate synthesised at 1200°C. **Figure 4.12(a)** illustrates that the change in RhB liquid volume has a direct relation to the kinetics plot evidenced by the data, under the influence of the piezocatalytic activity of BTO in two distinct gaseous environments: air and an atmosphere of argon. The initial concentration of RhB was maintained at 5 mg/L, while the concentration of BTO catalyst was set to 1 mg/mL. The differential behaviour observed across the two environments highlights the atmospheric effect on the efficacy of BTO piezocatalytic activity.

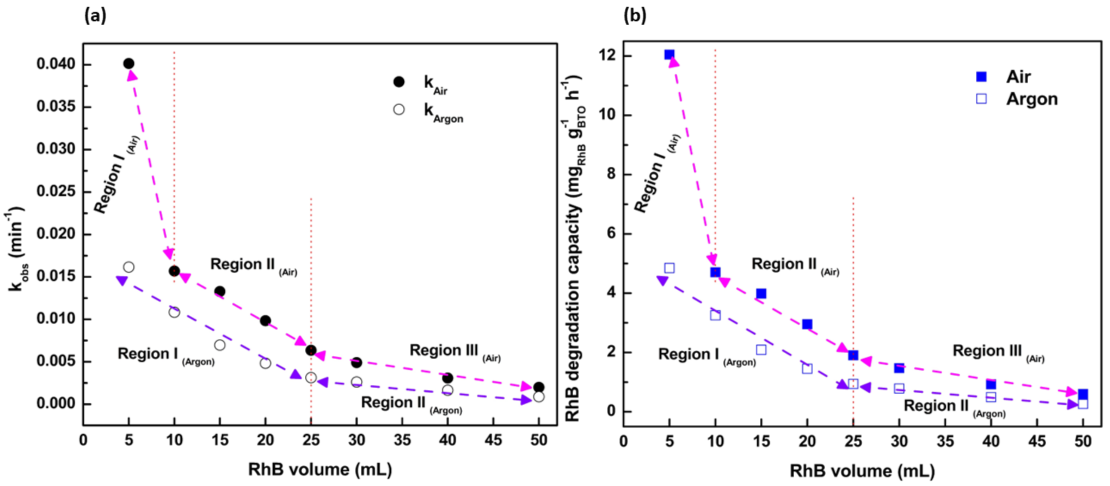

Figure 4.12 Comparative analysis of the (a) rate and (b) efficiency of piezocatalytic degradation of RhB using BTO-1200°C in both air and argon atmospheres (RhB concentration: 5 mg/L, BTO catalyst concentration: 1 mg/mL)

The experimental observations, particularly under aerated conditions, unveiled three distinct regimes based on the reaction volume of RhB. The first regime, termed Region I, corresponds to a low-volume setup where the RhB volume is less than 10 ml. The second, Region II, is defined for intermediate volumes, encompassing RhB volumes that range from 10 ml to 25 ml. Lastly, Region III pertains to high-volume conditions, designated for RhB reaction volumes greater than 25 ml. For each of these volumes in the different regimes, a contrast in the trends of the piezocatalytic activity of BTO was observed, suggesting the influence of RhB volume on BTO's degradation performance.

When these experiments were replicated in an inert argon atmosphere, effectively eliminating the presence of air and its constituent oxygen, the behaviour of the system modified significantly. In the absence of air environment, only two regimes were distinguished: a low-volume condition, corresponding to Region I (with RhB volume less than 25 ml), and a high-volume condition, corresponding to Region II (with RhB volumes greater than 25 ml). The omission of two distinct regions in argon atmosphere experiments compared to three regions under air implies that oxygen plays a pivotal role in modulating the piezocatalytic activity of BTO for RhB degradation. This study paves the way for a better understanding of the elements that influence the piezocatalytic degradation of RhB, and potentially, other organic contaminants. There are principally two pathways that facilitate the generation of reactive oxygen species (ROS), which are crucial in oxidative reactions and environmental remediation processes. The first method may result in the direct reduction of molecular oxygen (O_2) from either its gaseous state or when dissolved in solution. In this reaction, an electron (e^-) is added to an oxygen molecule, resulting in the formation of a superoxide anion radical ($^{\bullet}O_2^-$). This redox transformation occurs at a standard reduction potential of -0.33 V on the Normal Hydrogen Electrode (NHE), indicating that it's a thermodynamically favourable process under certain conditions **(Eq. 4.1)**.

$$O_2 + e^- \rightarrow {}^{\bullet}O_2^- \qquad -0.33\ \text{V (vs NHE)} \qquad \textbf{(Eq. 4.1)}$$

The second method derives from a water splitting mechanism. Here, a piezo-generated hole (h^+), which represents a positive charge carrier in stress-absorbing materials, interacts with a water molecule (H_2O). The hole positive charge effectively captures an electron from the water, leading to the simultaneous production of a hydroxyl radical ($HO^{\bullet}$) and a proton (H^+). This oxidative process occurs at a standard oxidation potential of +2.72 V with respect to the NHE, which reflects the energy required to drive this reaction in the forward direction. These reactions are fundamental to understanding the behaviour of ROS in various scientific disciplines, including the study of antioxidative defence mechanisms in biology, the degradation of pollutants in environmental chemistry, and the design of catalytic materials for energy conversion and storage. Both pathways reflect the intricacies of redox chemistry where electron transfer reactions are central to the dynamic formation of reactive intermediates that can further participate in a variety of chemical processes.

$$H_2O + h^+ \rightarrow HO^{\bullet} + H^+ \qquad +2.72\ \text{V (vs NHE)} \qquad \textbf{(Eq. 4.2)}$$

BTO is a material characterised by its inherent ferroelectric nature due to its ability to exhibit spontaneous electrical polarisation, which can be reversed by the application of an external electric field.

Intriguingly, BTO is also piezoelectric, meaning it can convert mechanical pressure into an electrical signal and vice versa. When a piezoelectric material like BTO is distorted mechanically, there is a displacement of charge within its structure, creating polarity and thus generating a charge on its surface. Electrons and holes, which are the fundamental charge carriers in semiconductors, migrate due to this generated surface charge. The mechanism behind this is inherently linked to BTO's substantial band gap energy, approximately 3.2 eV that separates the valence band and the conduction band within the material's electronic structure. This band gap is crucial, as it establishes an intrinsic electrochemical potential in the material. When mechanical energy is applied to BTO and surface charges are produced, this potential can catalyse electrochemical reactions if it exceeds certain energy thresholds required for specific redox processes.

In the context of water splitting, a reaction where water is dissociated into hydrogen and oxygen, the electrochemical potential from the piezoelectric effect can contribute to the generation of hydrogen gas. However, the potential must be higher than the reduction potential of hydrogen evolution to be effective, which is 0 V (vs, NHE) under standard conditions. For the formation of the superoxide anion radical ($^{\bullet}O_2^-$), the material's piezoelectrically generated potential must exceed the negative reduction potential of -0.33 V (vs NHE), which corresponds to the energy required to reduce molecular oxygen to its radical anion form. If the piezoelectric potential of BTO under mechanical stress remains below this reduction potential, the energy barrier for the production of superoxide radicals is not surmounted, and consequently, these ROS will not form. When considering the role of oxygen in the production of ROS crucial for degradation reactions, the absence of air significantly reduces the available dissolved oxygen in the solution. This reduction has a direct impact on the rate at which ROS are generated because these species often require oxygen as a reactant. Hence, in a controlled oxygen-depleted scenario, the reaction rate is typically lower.

In the specific case of RhB degradation, experiments demonstrate that the degradation rates under air-filled and argon-filled environments exhibit a similar pattern over time. However, when the experiment's liquid volume is limited to 5 mL, notable deviations occur in the RhB degradation behaviour. This suggests that under low-volume conditions, there may be a greater sensitivity to the availability of dissolved oxygen or possibly a shift in the piezocatalytic mechanisms in effect. In the observations of BTO-1200°C piezocatalytic activity, it is noted that there is a proportional increase in catalytic efficiency correlating with a decrease in RhB solution volume. This is likely due to the increase in the mechanical force applied during stirring, as seen in **Figure 4.12(b)** (Region III_{Air} and Region II_{Argon}). This trend remains consistent until the solution volume drops below 25 mL. At this juncture, the height of the dye solution falls beneath that of the magnetic stirring bar, which introduces an enhanced level of turbulence. Consequently, this change in the stirring dynamics leads to a noticeable alteration in the trend of catalytic activity, as depicted in Region II_{Air} – contrasting with what was observed in Region I_{Argon}. As the volume of the liquid phase containing RhB was reduced to 5 mL, a situation was created where a minimal depth of solution was present. Under such conditions, the catalytic efficiency of BTO might be influenced by the exposure to air due to the potentially lowered ionic strength at the BTO-solution interface. This reduction in ionic strength could minimise the formation of a Stern layer, which typically consists of specifically adsorbed ions on the catalyst surface. A less pronounced Stern layer may lead to enhanced piezoelectric activity, as there is less electrostatic screening by ions, hence facilitating greater availability of surface sites for ROS production. The generated ROS would rapidly interact with RhB due to the efficient agitation caused by the stirring action. As a result, the proximity and immediate interaction with gaseous oxygen, coupled with the efficient mixing provided by the stirring bar, likely contribute to the observed higher rates of RhB degradation, in contrast to an argon atmosphere. The emphasising mechanistic details of these observations are depicted in the graphical representation provided in **Figure 4.13**.

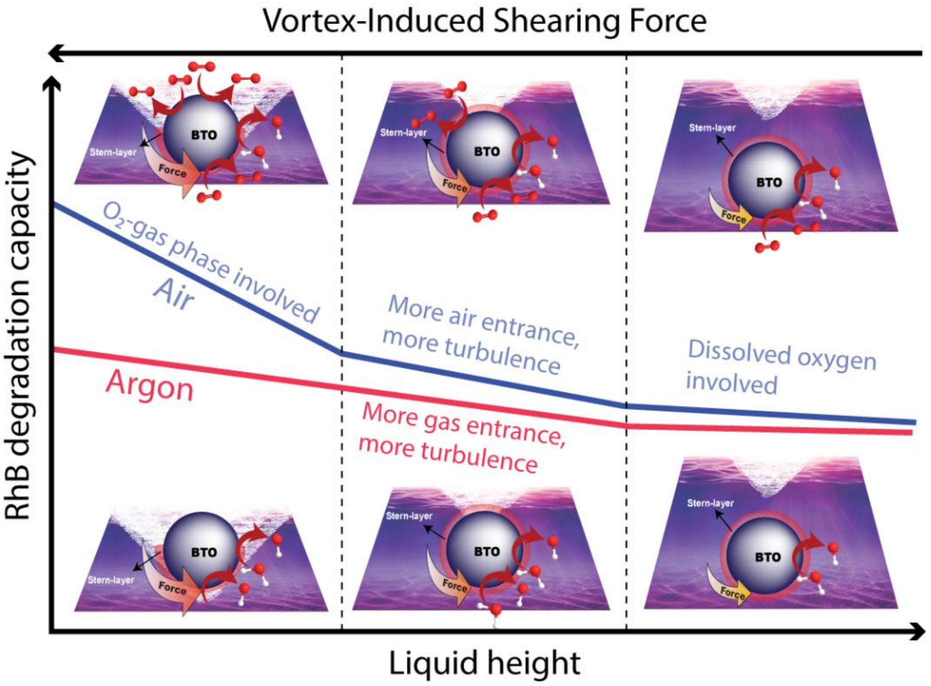

Figure 4.13 Effects of liquid volume and gas atmosphere on piezocatalytic activity: Linear growth in Region III, turbulence-boosted activity in Region II, and enhanced air-assisted degradation in Region I

The degradation efficacy for RhB observed in this study was determined to be 12.05 mg of dye per gram of catalyst material, achieved following a duration of 60 minutes under mechanical stirring conditions. This degradation rate is noteworthy as it stands on par with that achieved by other piezoelectric and photocatalytic materials, despite these being produced through more sophisticated and elaborate synthesis techniques. The relative performance metrics of these various catalytic materials, including the detailed experimental conditions and degradation capacities, are systematically compared, and compiled in **Table 4.2**.

Table 4.2 Comparative analysis of RhB degradation efficiency between various piezoelectric and photocatalytic materials

Method	Catalyst	RhB concentration (mg·L^{-1})	k_{obs} (min^{-1})	RhB degradation capacity (mg·g^{-1}·h^{-1})	Ref.
Piezocatalysis (driven by mechanical stirring)	BTO	5	0.040	12.05	**This work**
Piezocatalysis (driven by mechanical stirring)	$0.5Ba(Zr_{0.2}Ti_{0.8})O_3$-$0.5(Ba_{0.7}Ca_{0.3})TiO_3$ fibbers	2.5	0.340	12.8	145
Piezocatalysis (driven by ultrasound)	Self-modified black BTO_{-x} nanoparticles	10	0.009	5.4	193
Piezocatalysis (driven by ultrasound)	$BiFeO_3$ nanowires	5	0.045	10.8	150
Piezocatalysis (driven by ultrasound)	$NaNbO_3$ nanofibers	5	0.009	2.91	194
Piezocatalysis (driven by ultrasound)	$(Bi_{0.5}Na_{0.5})TiO_3$-based nanofibers	10	0.012	7.26	119
Piezocatalysis (driven by ultrasound)	$ZnSnO_3$ nanoparticles	2.25	0.045	12.15	128
Piezo-photocatalysis (driven by ultrasound)	$Bi_4Ti_3O_{12}$ nanosheets	5	0.214	64.2	104
Photocatalysis	Nanosized Ag_2S–ZnS loaded on cellulose	30	0.006	19.2	195

4.3 CONCLUSION

The results of this research emphasise the importance of the volume of the liquid as a key factor that affects the piezocatalytic efficiency of BTO in the breakdown of RhB in aqueous environments. The study suggests that the amount of water in the reaction system can influence the effective vibrations resulting from waste energy (such as mechanical agitation), which can be converted into piezoelectric charges on BTO particles. These charges then drive the environmental degradation process, transforming waste energy sources into valuable mechanisms to reduce pollutants in water, thereby contributing to sustainable and green chemical processes. This has implications for the design and optimisation of such systems to achieve maximum degradation efficiency by adjusting the liquid volume in which the catalyst is dispersed.

This work expands on the finding that the degree of tetragonality, which is a measure of the distortion of the crystal structure from a cubic to a more elongated tetragonal form, substantially influences the piezocatalytic ability of the ferroelectric BTO. The study has meticulously examined the influences of catalyst loading level, rotational speed, and liquid volume on the degradation efficiency of RhB. The key finding was that the degradation capacity tends to be greater in the presence of air than in an argon atmosphere. This suggests that molecular oxygen from air may potentially contribute to the piezocatalytic degradation process by reacting directly with RhB or by forming reactive oxygen species that facilitate the degradation.

Furthermore, the piezocatalytic activity exhibited by BTO shows a linear increase in both air and argon as the liquid volume decreases, which is referred to as Region III (air) and Region II (argon) (RhB volume > 25 ml). On the contrary, in Region II (RhB volume < 25 mL), the activity of BTO follows a different trend, possibly due to increased turbulence at lower volumes of liquid. The underlying mechanism for this increase in the degradation rate is attributed to a greater stirring or mixing force. This enhanced stirring force likely facilitates more collisions between the catalyst and dye molecules, thereby improving the degradation process. Additionally, the effectiveness of the BTO piezocatalyst was noted to improve in an air-containing environment. This is due to the increased turbulence at the boundary interface where liquid and air interact, which occurs when operating with low liquid volumes (~ 5 ml). The presence of greater surface turbulence improves the mass transfer and interaction between reactive species and the catalyst, which is conducive to the catalytic process. Moreover, the absence of a stern layer is likely due to the direct contact of BTO with the dye molecules without the interference of a diffuse ion layer.

The significance of these findings is that they reveal the crucial effects of liquid volume, induced turbulence, and mixing force on the piezocatalytic activity of BTO. Furthermore, these results demonstrate that catalytic degradation of dyes in water can be efficiently achieved at lower levels of mixing volume, which are substantially below those required for conventional ultrasonic degradation methods. Such insights could be highly beneficial for the design of more energy-efficient and cost-effective piezocatalytic systems for water purification or other relevant applications. The investigation presented in this chapter not only elucidates the vital factors influencing the piezocatalytic ability of BTO in dye degradation, but also sets the stage for probing into composite material systems. Specifically, the promising results obtained with BTO indicate further examination of combining it with metal oxides.

This chapter lays a substantial foundation for the following consideration of BTO-metal oxide composites, a topic that will be discussed in detail in Chapter 6. It serves as a continuation of this scientific investigation, detailing the methods, results, and implications of incorporating metal oxides into the BTO matrix, thus opening new avenues for piezocatalytic applications.

CHAPTER 5. ENHANCING PIEZOCATALYTIC HYDROGEN GENERATION BY BTO-METAL COMPOSITES

5.1 INTRODUCTION

The field of piezocatalysis is gaining attention as an innovative and eco-friendly area of study, focusing on using mechanical energy to initiate chemical reactions. With increasing research, piezocatalysts have been found capable of driving various complex chemical processes, including the conversion of organic compounds and the splitting of water. However, the effectiveness of piezocatalysis is often limited by the high relative permittivity characteristic of ferroelectric materials, which can hinder the movement of charge carriers necessary for chemical reactions, leading to slower reaction rates. This introduction sheds light on the advances made in addressing this limitation by adopting cocatalyst systems to improve carrier mobility and, consequently, increase reaction rates.

While progress has been made in improving piezocatalytic effectiveness, there are still gaps in understanding; Despite these advancements, finely detailed understandings of how piezocatalysis works behind piezocatalytic activity yet to be fully revealed. This work is dedicated to exploring the use of the piezoelectric effect for water splitting, aiming to produce valuable fuels like hydrogen. To build upon the research discussed previously, it's important to note that while there have been promising demonstrations of piezocatalytic hydrogen generation, the performance in terms of rates and efficiencies often falls short of practical expectations. A deeper understanding of the mechanisms at play is essential for refining the design of piezocatalysts, such as the barium titanate composites with metal nanoparticles. It is likely that the piezoelectric effect and the associated generation of electric charges are not solely responsible for the observed catalytic activity. Changes in the electronic band structure, induced by mechanical stress, may also play a contributory role, akin to that observed in photocatalysts. In this chapter, the results of integrating metals with barium titanate are examined.

Building upon the objective to enhance piezocatalytic activities for practical applications, metals with favourable characteristics such as Platinum, Rhodium, and Palladium, well-known for their inertness and high melting points, were identified. The research discussed herein aimed to incorporate these metals into the BTO matrix, to amplify the piezocatalytic efficacy of the resulting composites. This study provides evidence that ferroelectric substrates have positive effects on water splitting reactions, highlighting the need to differentiate between sonochemical and piezocatalytic effects in catalysis. Using a simple solid-state method to incorporate a platinum metal cocatalyst with barium titanate resulted in a four times increase in the hydrogen production rate compared to using pristine BTO or sonochemical processes without a catalyst. The BTO-Pt composite showed consistent piezocatalytic activity for up to 12 hours. Inconsistencies observed in water splitting rates were attributed to the mechanical detachment of platinum rather than changes in the catalyst's composition. This research confirms that combining materials in this manner can significantly improve piezocatalytic applications.

5.2 RESULTS AND DISCUSSION

As discussed in **Section 3.1**, the investigation process began with the synthesis of BTO mixed with commercially obtained Palladium (Pd), Rhodium (Rh), and Platinum (Pt) powders. The formation of oxides with Pd and Rh prompted the consideration of synthesising these materials under an inert atmosphere. However, such a method could complicate the synthesis process and deviate from the aim of developing a scalable and cost-effective approach. Therefore, the focus continues to be on optimising a straightforward solid-state synthesis method that offers a balance between the ease of preparation and the efficacy of the composites.

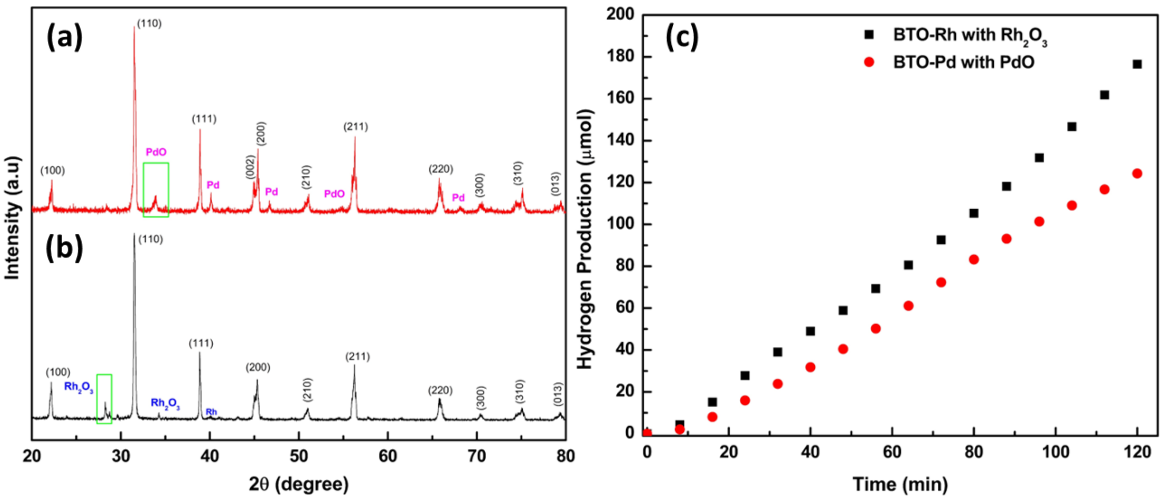

Figure 5.1 XRD of (a) BTO-Pd with PdO, (b) BTO-Rh with Rh_2O_3, and (c) Hydrogen production of BTO-Pd with PdO and BTO-Rh with Rh_2O_3

Although this approach embraces certain limitations, it aligns with the objective of a scalable synthesis technique. The experimental results demonstrated that synthesis challenges were indeed observed with the Pd and Rh compounds — notably oxide formation as confirmed by **Figure 5.1(a) and (b)**. Conversely, the BTO-Pt composite, which was sintered at 1200°C, did not present any oxide formation post-synthesis. This finding supports the decision to enhance the solid-state synthesis technique, highlighting its merit for further investigation into an effective and scalable approach to synthesise piezocatalytic materials. Additionally, the hydrogen production of BTO composites containing Pd and Rh, as well as their associated oxides, was evaluated as outlined in **Section 3.4**.

Contrary to the expectations, and despite thorough stirring, the particles did not remain evenly dispersed and quickly settled after the stop of stirring—a step that is critical for piezocatalytic evaluation before starting the experiment.[51] Moreover, the hydrogen production with these composites was considerably lower than that of the BTO-Pt composite. These results driven the investigation towards a more detailed exploration of the BTO-Pt composite, to better understand its piezocatalytic effectiveness and potential as a stable and efficient option for the study. The hydrogen production output also varied erratically, a phenomenon that was attributed to the agglomeration of particles caused by the sonication (**Figure 5.1(c)**).

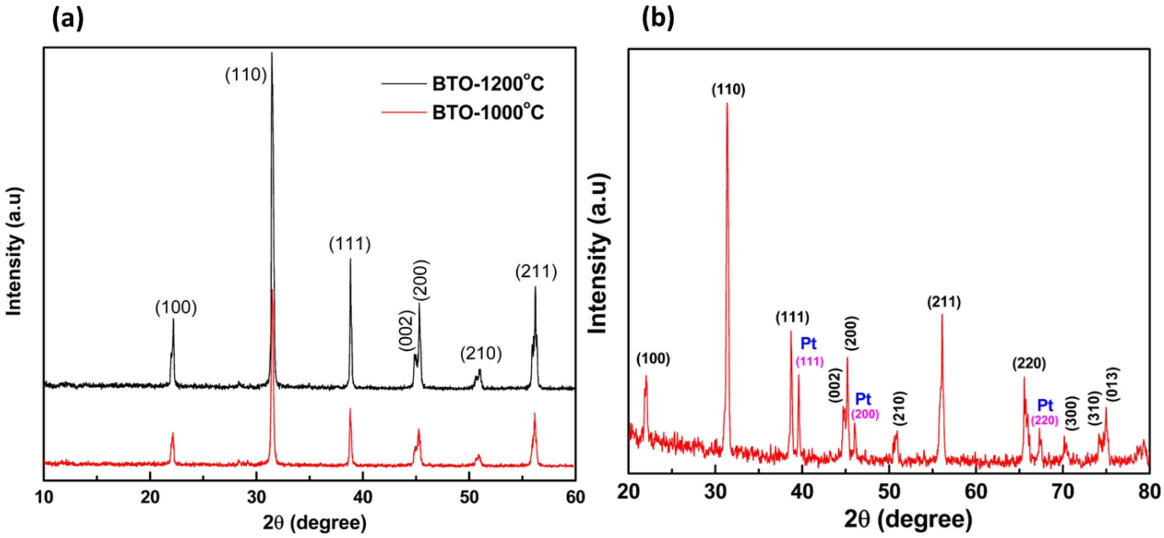

Figure 5.2 XRD of (a) comparison of BTO samples: increased tetragonality at 1200°C versus 1000°C (b) BTO/Pt

XRD analysis revealed that the BTO synthesised at 1200°C showed higher tetragonality than the sample prepared at 1000°C (BTO-1000°C), making the former the preferred reference material with a surface area of 2.2281 m^2 g^{-1} for subsequent piezocatalysis studies, as presented in **Figure 5.2(a)**. The BTO-1200°C possessed a gravel-like texture, posing a challenge for subsequent combination with Pt; in contrast, BTO-1000°C had a softer texture, facilitating an easier mixing with the Pt. After mixing, the powder was sintered at 1200°C for two hours, with the heating and cooling rates controlled at 5°C min^{-1}. The as-synthesised BTO/Pt powders were then finely ground in a mortar and pestle for further characterisation, as depicted in **Figure 5.2(b)**. XRD confirmed the tetragonality of BTO, indexed to JCPDS Card 05-0626, and showed peak splitting at 2θ ~ 45°, indicative of the (002) and (200) planes, which suggests a non-centrosymmetric structure and the presence of intrinsic polarisation. Additionally, the presence of metallic Pt was confirmed in BTO/Pt sample, indexed to JCPDS Card 04-0802, without any evidence of oxide formation. The BTO/Pt powder was dark grey, with a specific surface area of 1.0216 m^2 g^{-1}.

Particle size analysis via SEM (see **Figure 5.3(a)**) indicated that the BTO particles averaged 780 nm in diameter. Observation suggested sintering among the ceramic particles, resulting in a larger particle size compared to the pure BTO sample (**Figure 5.3(h)**). Furthermore, the large particle size when compared to the pure BTO sample can be accounted for by the difference between grinding by hand with a mortar and pestle rather than the use of a highly energetic ball mill.

The SEM analysis showed that high-temperature conditions led to the sintering of platinum with the barium titanate, causing platinum nanoparticles to bond to the ceramic surface. The platinum particles were distributed unevenly across the barium titanate, which was an anticipated outcome of the cocatalyst solid-state synthesis method. **Figure 5.3(b)** shows the presence of nanoparticles with an average diameter of 15 nm on the BTO particle surfaces. Elemental analysis via EDX, as indicated in **Figure 5.3(c-g)**, confirmed the presence of Pt in the sample; however, the distribution of Pt across the BTO particles was found to be non-uniform. The Pt-decorated samples exhibited a smaller specific surface area compared to undecorated BTO, an important consideration when examining reaction rates since, generally, a reduced surface area is associated with slower reaction kinetics.

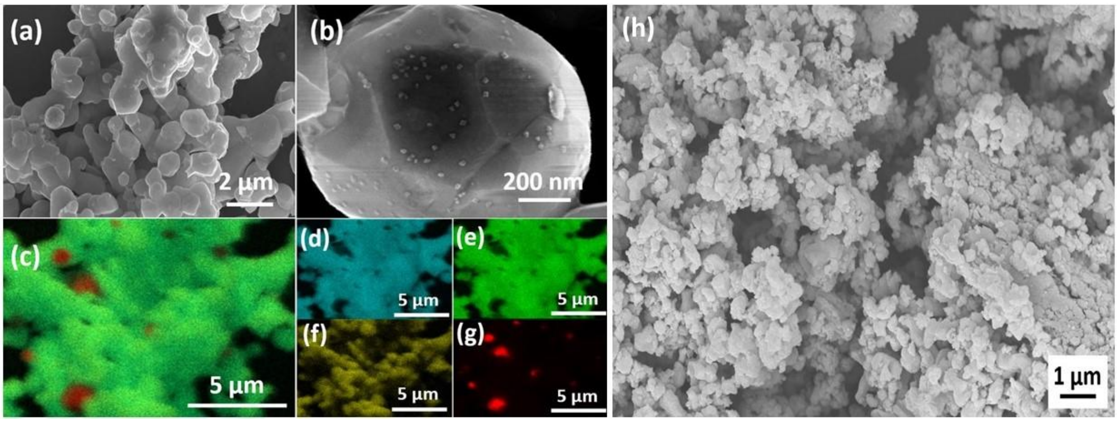

Figure 5.3 SEM of (a,b) BTO/Pt sample, (c) EDX analysis of the BTO/Pt catalyst, layered map of (d) barium (Ba), (e) titanium (Ti), (f) oxygen (O), (g) platinum (Pt), and (h) BTO-1200°C

Despite this, the findings reveal that the addition of Pt as a cocatalyst significantly increases the rate of product formation. In addition to the EDX findings, XPS analysis provided further insights into the surface composition and electronic states of the atoms. High-resolution XPS scans, detailed in **Figure 5.4(b)**, especially of the Pt 4f region, were consistently fitted with an asymmetric doublet. The Pt $4f_{5/2}$ peak, centered at 70.5 eV, confirmed that the nanoparticles exist in the metallic state, and no signs of oxidation to forms like PtO or PtO_2 were observed.[196]

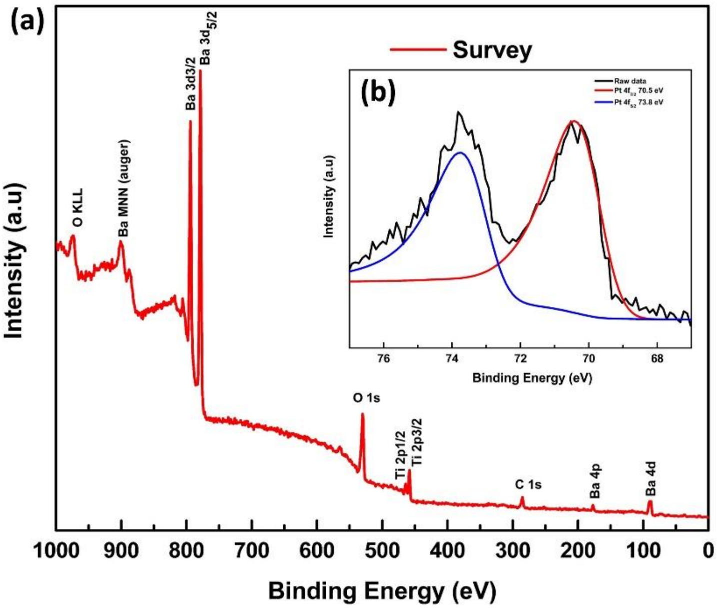

Figure 5.4 XPS of BTO/Pt calcined at 1200°C: (a) survey scan, (b) Pt4f scan (inset)

The Raman spectra indicates that both BTO and BTO/Pt exhibit similar spectral features consistent with tetragonal BTO, as evidenced by the characteristic peaks at 260 cm^{-1} (A_1(TO)), 305 cm^{-1} (B_1, E(TO+LO)), 515 cm^{-1} (A_1(TO), E(TO)), and 720 cm^{-1} (A_1(LO), E(LO)) (**Figure 5.5**) in the BTO/Pt spectrum [187]. The presence of the 305 cm^{-1} and 720 cm^{-1} bands provides evidence that a significant fraction of BTO crystallites retain tetragonal symmetry. The main characteristics that interested in BTO/Pt are effectively the same as those in the BTO spectrum. This suggests that the addition of Pt does not noticeably alter the basic symmetry of the BTO structure. By highlighting the Raman results primarily for the BTO/Pt composite, this analysis focuses on the material that is most relevant to the piezocatalysis studies.

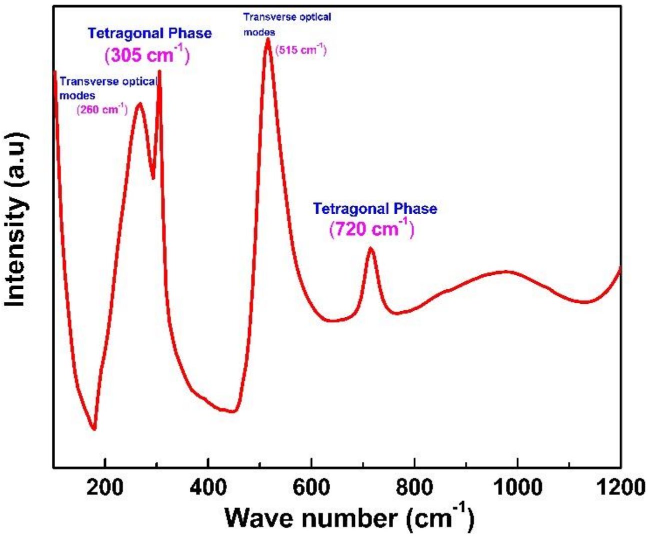

Figure 5.5 Raman spectrum of BTO/Pt at 1200°C

5.2.1 INVESTIGATION OF EXPERIMENTAL PARAMETERS

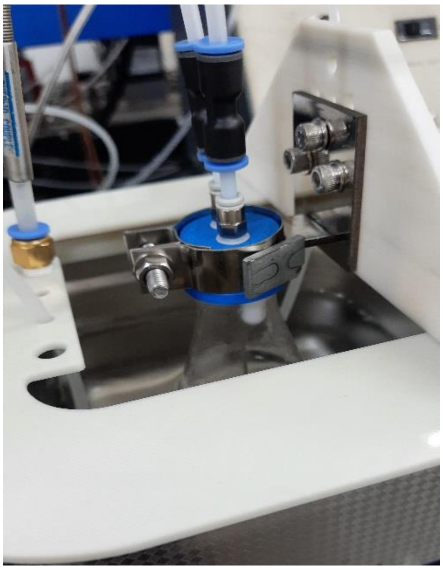

Figure 5.6 The custom-made 3D printed holder for reactor vessel

To minimise the number of influencing parameters in this work, the reactor position was fixed and the volume of water inside the sonication bath was the same for all experiments. Under the initial experimental conditions, a baseline was established with parameters set to a catalyst loading of 0.1 g L^{-1}, and a 2 vol% MeOH-DI mixture. The reactor vessel was placed 10 mm above the bottom of the ultrasonication bath. Reliable placement of the reactor was ensured using a custom-designed 3D-printed holder as shown in **Figure 5.6**. A photograph of the actual laboratory setup, which shows the arrangement of equipment and materials used in the piezocatalytic experiments for hydrogen generation, is presented in **Figure 5.7**.

Figure 5.7 Photograph of the actual laboratory setup

The same reactor vessel was consistently employed throughout all experiments. The study proceeded with investigations under varying conditions, including sonochemical, Pt-loaded BTO, catalyst concentration, and MeOH-DI solution concentrations to evaluate their impact on catalysis. This systematic approach served to optimise conditions and ensure comprehensive results. Moving forward with such a systematic methodology, the research delved into detailed assessment of varying catalyst parameters. In particular, the influence of different platinum loading levels on barium titanate substrates was a focal point for observing changes in catalytic efficacy.

As depicted in **Figure 5.8**, the Pt100 sample notably outperformed others in hydrogen production, indicating a potential optimal platinum loading range that warrants further in-depth investigation. As the study progressed, it became evident that increasing the platinum loading enhanced catalytic activity due to greater active site availability. However, there exists a critical threshold beyond which further platinum additions resulted in nanoparticle aggregation, counterproductively reducing effective surface area. For instance, loading 50 mg of platinum onto barium titanate may prevent excessive cluster size growth, enabling more homogeneous dispersion. However, such sparse loadings can also limit active site quantities. Furthermore, beyond nanoparticle distributions, their intrinsically catalytic activity as influenced by the underlying ferroelectric substrate also profoundly impacts performance. Therefore, this work sought to not only advance mechanistic comprehension of catalyst, but facilitate optimisation of platinum utilisation for more sustainable catalytic processes.

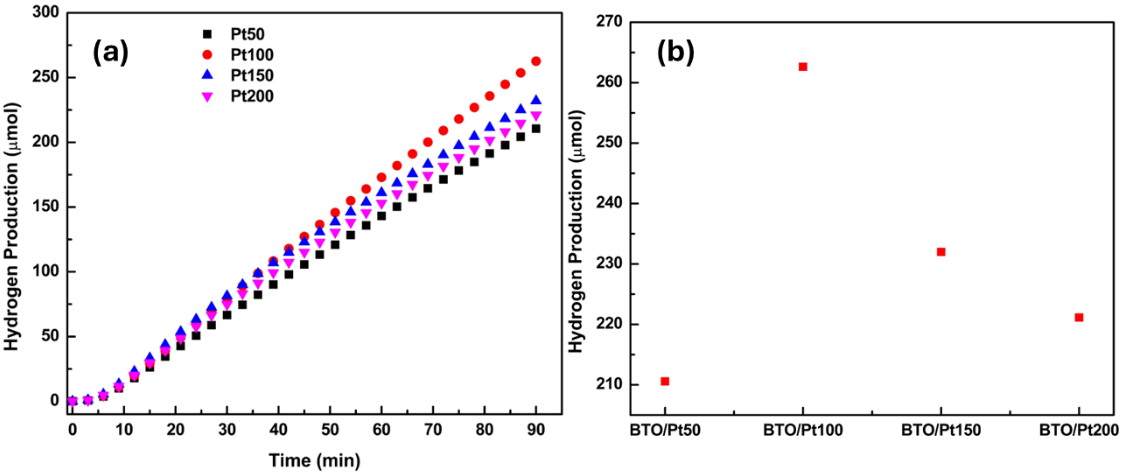

Figure 5.8 (a) Hydrogen production over time for various platinum loadings on barium titanate. (b) The Pt100 sample notably outperforms other samples (Pt50, Pt150, and Pt200), indicating a potential optimal platinum loading for maximising H_2 production.

In following experiments, a 100 mg platinum loading on BTO, referred to as BTO/Pt was utilised to investigate the impact of catalyst loading variation on piezocatalytic hydrogen production. An inverse correlation between catalyst loading and activity was observed, with higher loadings hindering hydrogen evolution rates as shown in **Figure 5.9(a) and (b)**. This confirms that catalyst loading is a significant factor in the catalytic performance, aligning with findings reported by Zhang *et al.*,[51] The importance of catalyst loading as a key factor of catalytic efficiency is thus highlighted. Based on the observed inverse correlation, an optimal catalyst loading level is proposed that would maximise the piezocatalytic output. Therefore, it is critical to carefully consider and optimise catalyst loading to achieve the highest activity from the ferroelectric material and to maximise the efficiency of hydrogen production. To investigate the impact of methanol (MeOH), the catalyst loading was kept constant at 0.1 g L^{-1}, while maintaining the solution amount at 85 g.

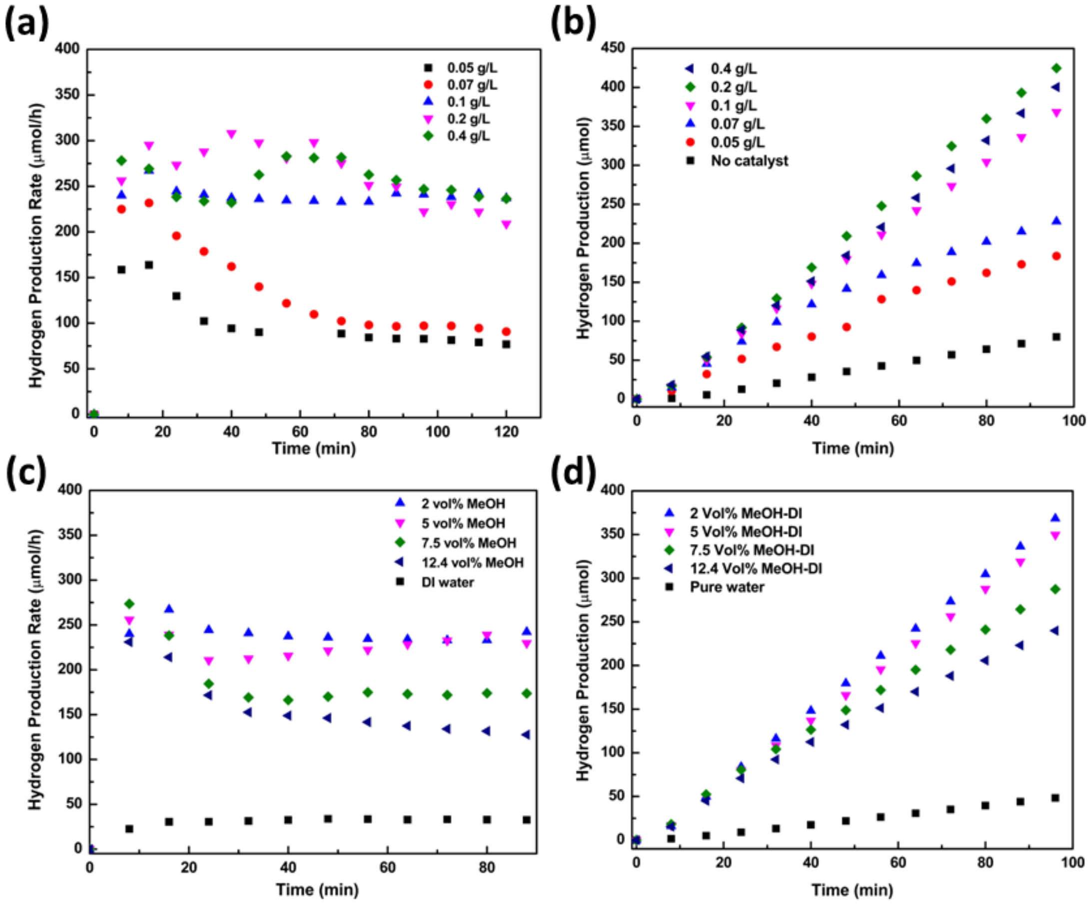

Figure 5.9 Comparative analysis of hydrogen production efficiency at various (a,b) catalyst loadings and (c,d) methanol concentrations

A methanol concentration of 2% in deionised water (2 vol% MeOH-DI) resulted in the maximum, most stable hydrogen production rate. Previous studies have established that varying the concentration of methanol can influence hydrogen production by changing the dynamics of radical concentrations and their reactivity.[197] At reduced methanol levels, the scavenging of hydroxyl radicals is effective, which facilitates increased hydrogen evolution. In contrast, higher amounts of methanol lead to reduced lower hydrogen generation rates. An investigation was conducted to explore methanol concentrations and identify the threshold that yields the highest efficiency in hydrogen production **(Figure**

5.9(c)). The results demonstrated that a 2 vol% MeOH resulted in the higher rate of hydrogen evolution, in line with the optimal methanol range suggested by earlier research. A decline in hydrogen production was observed when the concentrations were raised, confirming the principle that excessive methanol hampers the hydrogen generation process.

The optimal concentration for methanol determined in this study closely matches the previously reported ranges that optimise sonocatalytic hydrogen production,[197] confirming the existence of a methanol that maximises hydrogen production. At a methanol concentration of 2%, the scavenging of radicals enhances H_2 evolution, while concentrations above this level are counterproductive, reducing both radical yields and hydrogen production (**Figure 5.9(d)**).

When using a ferroelectric material (BTO), as demonstrated here, an immediate uptick in reaction rate is evident at the onset of the process. The development of a stable Stern layer is a typical behaviour for ferroelectric materials in solution due to their inherent polarisation. The introduction of external energy into this equilibrium state has a dramatic impact on the species bound to the surface, leading to a rapid increase in reaction products[57]. This activity necessitates diffusion to refurbish the ferroelectric surface with reactants. It is noted that for the first 20 to 30 minutes, there is an observable conditioning of the system, after which it transits to a steady state, as shown in **Figure 5.9(a) and (c)**.

5.2.2 THE ROLE OF METAL COCATALYST IN ENHANCING PIEZOCATALYTIC ACTIVITY

In this investigation, ultrasonication was utilised as the mechanical energy source, aligning with common methodologies in piezocatalytic systems research.[1,17,198] High-frequency acoustic waves transmitted through the material create alternating zones of high and low pressure, known as compression and rarefaction, respectively. Small bubbles can emerge during rarefaction, which then enlarge through subsequent cycles. Upon reaching a threshold size, these bubbles abruptly collapse—a phenomenon known as cavitation—thereby causing an environment considered by high intense energy with substantial pressure and temperature, as well as the generation of shock waves, intense shear forces, and turbulence. This cavitation event precipitates a sharp temperature rise, potentially surpassing 10^4 K for a brief time of 100 picoseconds within an area of 1 µm under ambient conditions.

Moreover, the vicinity of the imploding bubble might experience pressures approximately 60 kilobars. Besides these physical outcomes, the extreme conditions can catalyse energetic chemical processes, commonly referred to as sonochemistry or sonolysis.[199] Owing to the intricacies involved with ultrasonic bath, it is imperative that investigations account for both the sonochemical activities transpiring in the reaction vessel and the piezoelectric influences of the catalyst.[200] BTO without Pt nanoparticles was tested at a catalyst loading of 0.1 g L^{-1} with the amount of solution 85 g of 2 vol% MeOH-DI (**Figure 5.10(a)**).

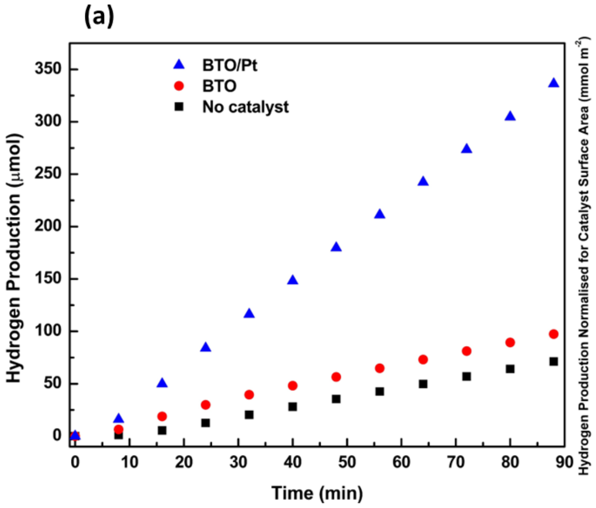

Figure 5.10 Comparative hydrogen production from sono-piezocatalysis with no catalyst, BTO, and BTO/Pt (85 g of 2% MeOH-DI, 0.1 g L^{-1} catalyst, 10 mm from ultrasonication bath base) and (b) Hydrogen generation per catalyst surface area

The BTO exhibited a slightly higher H_2 production rate than that observed in the absence of a catalyst, indicating the BTO was performing as a catalyst. It is important to note that the additional surface area provided by the BTO may have enabled further reactions to occur. This was investigated by introducing a non-ferroelectric material to the reaction vessel. Details of these findings will be discussed subsequently. In the case of BTO/Pt, the observed hydrogen generation rate was approximately four times greater than that of BTO alone.

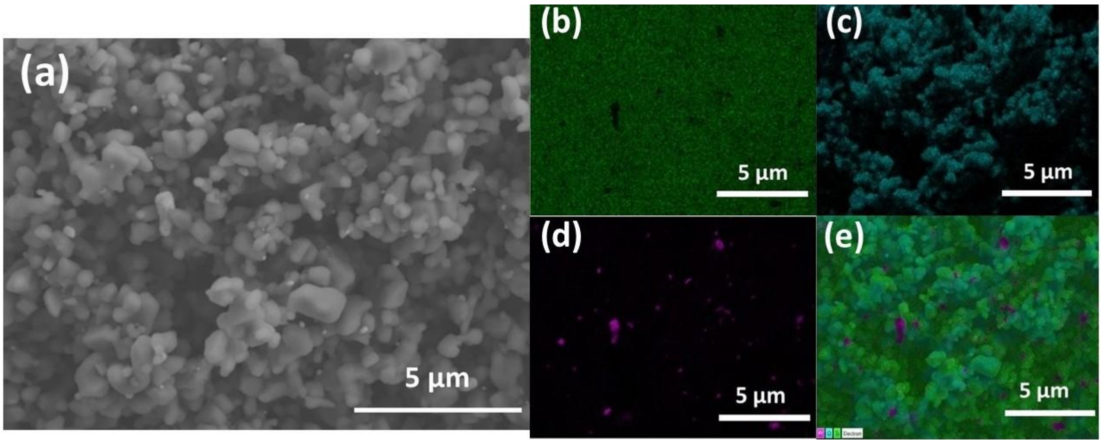

Figure 5.11 SEM of (a) TiO_2/Pt and EDS elemental analysis of (b) titanium (Ti), (c) oxygen (O), (d) platinum (Pt), and EDS layered map of (e) TiO_2/Pt

As mentioned previously, the cocatalyst surface area of a material is roughly half that of pure BTO. Consequently, when taking surface area into account, the increase in the normalised reaction rate for the BTO/Pt system becomes even more significant (**Figure 5.10(b)**). Choosing Pt as a metal cocatalyst is well-acknowledged for its efficacy in hydrogenation processes, attributed to its strong affinity for the adsorption of hydrogen. Hydrogen atoms easily adsorb onto the surface of Pt, but the bond is sufficiently weak to allow for the release of H_2 molecules from the catalyst's surface.

Furthermore, Pt is notable for its exceptional stability and long-term durability.[201] To verify that the observed increase in H_2 production was from the combined effect of Pt nanoparticles with the ferroelectric BTO support, control experiments were carried out with Pt nanoparticles alone and Pt with a non-ferroelectric support, specifically TiO_2. SEM/EDS analysis of the TiO_2/Pt is shown in **Figure 5.11**, which has a surface area of 2.4 m^2 g^{-1} for comparison with the BTO/Pt composite.

The H_2 production in these additional control experiments was found to be comparable to that observed in the absence of any catalyst, as illustrated in **Figure 5.12(a)**. This suggests that the ferroelectric nature of BTO is crucial for enhancing the catalytic reaction rate. The stability of a catalyst over time is a vital attribute for sustained chemical reactions. The BTO/Pt catalyst demonstrated consistent hydrogen production over a 24-hour period, with a stable rate observed for the initial 12 to 13 hours, as shown in **Figure 5.12(b)**.

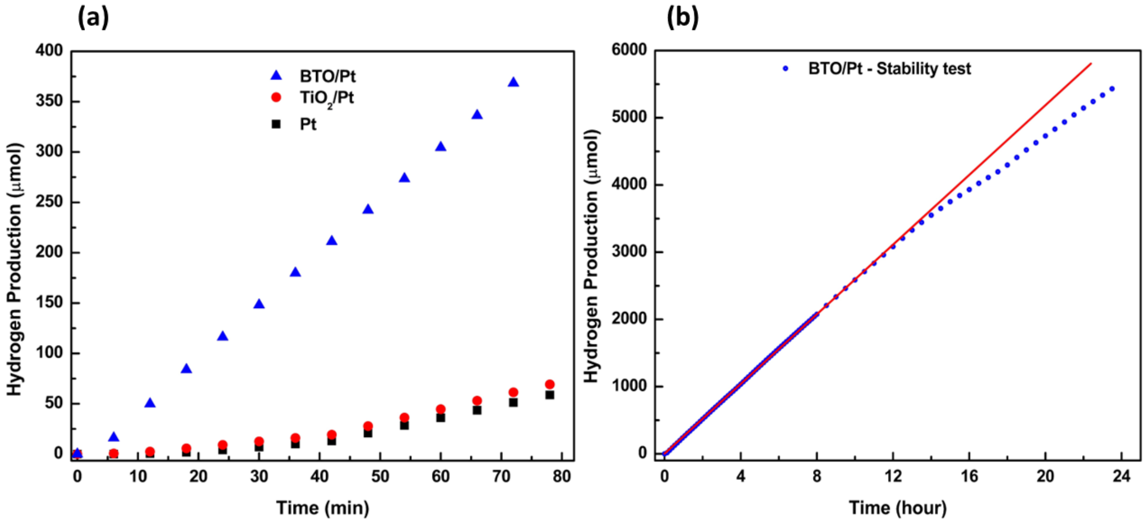

Figure 5.12 Control experiments for (a) H_2 production comparison using Pt, TiO_2-supported Pt, and BTO/Pt catalysts, and (b) stability test of H_2 evolution from BTO-Pt catalyst with trend analysis.

However, after approximately 12 to 13 hours, a deviation in the hydrogen production was observed. To further investigate potential morphological changes in the catalyst affecting piezocatalytic hydrogen generation, EDS analysis was conducted after the stability evaluation. The catalyst examined in the studies exhibits a reduction in the quantity of platinum nanoparticles on the BTO surface as compared with the catalyst that remained unused. The Ba/Pt ratio before the stability test was 17, while after the test it increased to 36. This change indicates a significant loss of platinum content, which is substantiated by the data presented in **Figure 5.13**.

Since platinum is the active component that facilitates the catalytic reaction (in this case, hydrogen generation), a reduction in platinum on the BTO surface could lead to decreased catalytic activity, which aligns with the reported reduction in hydrogen production. Previous studies have demonstrated that BTO remains highly stable under mechanical stimulation in aqueous environments. Therefore, it is hypothesised that the issue is associated with the process used to synthesis the cocatalyst system. To adequately address this concern, further investigation is required. Future research should concentrate on devising methods to enhance stability and exploring advanced techniques for the deposition of cocatalysts. It is important to note, however, that Pt detachment from the BTO surface has been observed in experiments. This phenomenon is attributed to mechanical abrasion rather than an inherent phase transition. To adequately address this concern, further investigation is required. Future research should concentrate on devising methods to enhance stability and exploring advanced techniques for the deposition of cocatalysts. It is important to note, however, that Pt detachment from the BTO surface has been observed in experiments. This phenomenon is attributed to mechanical abrasion rather than an inherent phase transition.

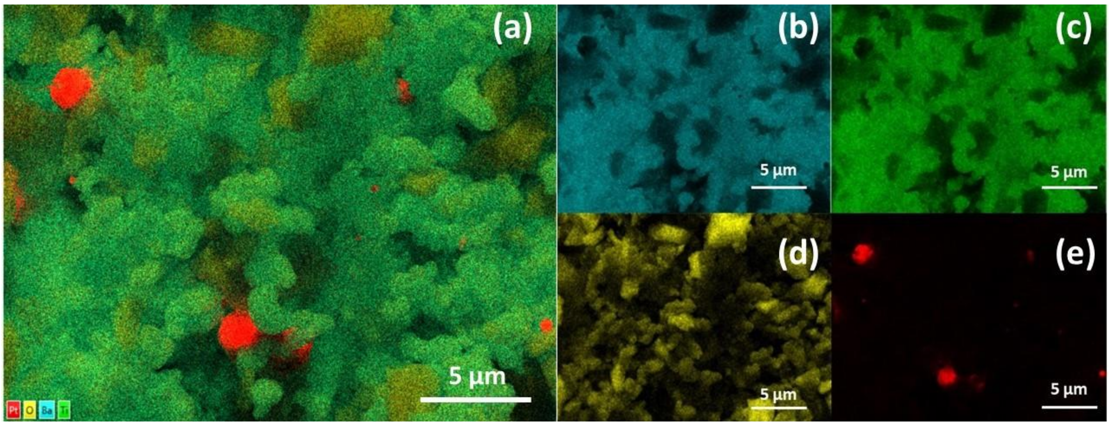

Figure 5.13 Post-stability test - EDS layered map of (a) BTO/Pt catalyst, and Elemental analysis of (b) barium (Ba), (c) titanium (Ti), (d) oxygen (O), and (e) platinum (Pt)

In evaluating the energy efficiency of the BTO/Pt catalyst during the extended hydrogen production experiment, the efficiency was determined to be 0.034%. This estimate accounted for the total volume of H_2 produced, the higher heating value of hydrogen at 286 kJ/mol, and the energy input from the ultrasonic bath, quantified as 116.732 kWh per gram of hydrogen. Such measures of energy efficiency are vital for assessing the practicality and sustainability of catalytic systems for industrial applications. It is important to acknowledge that piezoelectric materials have a theoretical limit to the efficiency of converting mechanical energy into electrical energy. The electromechanical coupling coefficient of barium titanate varies between 0.3 and 0.5,[14,35] indicating that the highest possible efficiency would be 50% under ideal conditions of energy harvesting.

Although this efficiency (0.034%) is relatively high when compared to efficiencies reported for similar experiments in existing literature, it's important to consider how different conditions impact these outcomes. For instance, the production of gases during certain chemical reactions can also be a measure of efficiency in energy conversion processes.

Additionally, experiments conducted in the absence of methanol allowed for the assessment of the BTO/Pt catalyst using pure water, which aimed to elucidate the underlying reaction mechanism responsible for the production of both hydrogen (**Figure 5.14(a)**) and hydrogen peroxide (**Figure 5.14(b)**). The splitting of pure water traditionally involves concurrent oxidation and reduction reactions. Consequently, the oxidative byproducts of pure water splitting were examined to discern their effects on the efficiency of energy conversion systems. The lack of observed O_2 suggests the potential formation of alternative byproducts, like H_2O_2 and $^{\cdot}OH$ radicals. Accurate measurement of H_2O_2 can be performed utilising iodometric titration, as noted by Wang *et al.*,[202] The results indicate yields that are stoichiometrically consistent, with approximately 25 μmol of H_2 and 24 μmol of H_2O_2 produced from the splitting of water. This suggests that the platinum catalyst not only promotes hydrogen production, but also facilitates the formation of hydrogen peroxide during the water splitting process. This multifunctionality of the BTO/Pt in promoting both H_2 and H_2O_2 plays a significant finding that has implications for selectivity of the catalyst.

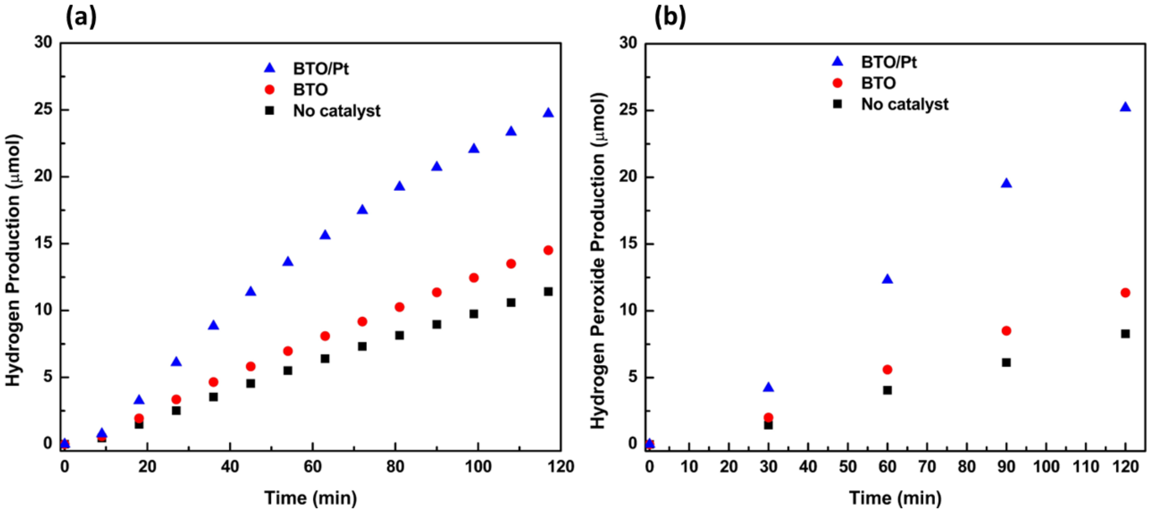

Figure 5.14 Comparison of BTO/Pt, BTO, and no catalyst systems for (a) hydrogen production and (b) hydrogen peroxide production

It is hypothesised that the production of hydrogen peroxide occurs via two separate mechanisms: initially, the water reduction reaction is driven by electrons generated from piezoelectric effect.

$$^{\cdot}O_2^- + e^- + 2H^+ \rightarrow H_2O_2 \quad (E^0 = +1.44\text{ V vs NHE}) \quad \textbf{(Eq. 5.1)}$$

Secondly, the oxidation of water molecules is driven by the piezoelectrically generated holes.

$$2H_2O + 2h^+ \rightarrow H_2O_2 + 2H^+ \; (E^0 = +1.76\text{ V vs NHE}) \quad \textbf{(Eq. 5.2)}$$

Therefore, the study successfully presents a catalytic system designed to transform mechanical energy into chemical energy via water splitting.[203] The reported efficiencies for the evolution of H_2 and H_2O_2 were 0.0012% and 0.0014%, respectively.

Comprehensive calculations are provided to explain the reported efficiency values. It’s important to note that while these processes can lead to the production of hydrogen peroxide and hydrogen gas, the efficiency and yield of the reactions are highly dependent on the specific properties and defects of the piezoelectric material used, as well as the ambient conditions such as presence of other ions or molecules, and the intensity of the mechanical force applied. The efficiency of the experiments can be attributed to multiple factors. A primary consideration is the relative volume of the sonication bath to that of the reaction vessel. With the bath being substantially larger, only a fraction of the total energy generated by the sonication process is effectively transferred to the reactive species within the vessel.

Consequently, this leads to a lower overall energy transfer efficiency, impacting the experiment's results. It is crucial to optimise the energy transfer process to maximise efficiency, which may involve adjusting the sonication parameters or redesigning the experimental setup to ensure more targeted energy application to the reactants. The efficiency of energy transfer to piezocatalysts in sonication experiments is influenced by various factors aside from bath volume. These include ultrasonic amplitude, sonication duration, and acoustic intensity. Optimising these parameters is key to enhancing the energy transfer and improving experimental outcomes. The selection of the reaction vessel is crucial, as factors like wall thickness, material composition, and shape significantly affect how ultrasonic waves propagate, directly impacting the efficiency of energy transfer to the piezocatalysts. Of course, the available power and frequencies of the ultrasonic bath are expected to play a role in the piezocatalytic processes.[139]

Furthermore, the BTO particles employed in this study were not specifically optimised for maximum energy efficiency. Using particles with a morphology that allows for more deformation, like nanorods,[204] could potentially offer a stronger piezoelectric response and enhance energy harvesting efficiency. Altering the experimental parameters has the potential to increase the H_2 evolution rate beyond what was observed in this study. Nonetheless, the primary aim here was not to optimise H_2 production but to maintain consistency. Such consistency allowed for clear differentiation between H_2 production from sonochemical and piezocatalytic reactions. Understanding this balance provided essential insights into piezocatalyst performance. Comparing results in the field of piezocatalysis can be challenging, given variations in the input power source, frequency, position, reactor volume, specific piezoelectric material used, and selection of cocatalysts. Although absolute efficiency is preferred, a relative performance indicator compared to other experimental data can also be useful.

Notably, the International Organisation for Standardisation (ISO) repository contains standard test protocols for evaluating catalyst performance. For instance, ISO 10678:2010 specifies the global standard for photocatalytic activity of fine ceramics for UV radiation-induced methylene blue degradation. However, there is currently no standardised protocol for assessing piezocatalytic activity. Thus, it is essential to provide a general estimate of the overall catalytic process efficiency.

A comparative analysis with appropriate literature values has been conducted to attain a preliminary understanding of efficiency in experimental systems. Data from previous studies were utilised for comparison between the current work on piezocatalysts and those documented in literature. As indicated in **Table 5.1**, the methodology utilising BTO/Pt shows promise and currently stands at the forefront of the sono-piezocatalytic field. The importance of considering the contributions from both sonochemistry and piezochemistry is underscored by control experiments. These findings collectively highlight the intricacies associated with using ultrasonication baths for precise chemical analyses.

Table 5.1 Piezocatalytic hydrogen production using ultrasound as an energy source

Piezocatalyst	Reagents/ Solution	Energy Source	H_2 evolution rate (µmol h^{-1})	H_2 evolution rate per gram (mmol h^{-1} g^{-1})	Experimental Catalyst Performance (µmol h^{-1} g^{-1} Wh^{-1})	Experimental Energy Efficiency (%)	Ref.
BTO@Pt	20% MeOH-DI	1 MHz, 2 W	1.53*	0.03*	15*	0.0060*	169
$BiFeO_3$	10 ml Na_2SO_3 (0.05 M)	45 kHz, 100 W	124.1	0.12*	1.2*	0.0098*	113
CdS	0.35 mol/l Na_2S 0.25 mol/l Na_2SO_3	40 kHz, 150 W	7.85*	0.16*	1.06*	0.0004*	205
MoS_2/Fe/ Peroxy-monosulfate	20 mg/l Pollutants	40 kHz, 300 W	27.03*	0.9*	3*	0.0007*	206
$BiFeO_3$/Pd	0.05M Na_2SO_3	24/40/80 kHz, 100 W	11.4	1.14*	11.4*	0.0009*	167
MoS_2 using Glutathione	Fe^{2+}	35/53 kHz, 280 W	62.5*	1.25*	4.46*	0.0018*	85
Bulk g-C_3N_4	0.1 M Glucose	40 kHz, 240 W	5.38*	2.69	11.2*	0.0002*	147
Ultrathin g-C_3N_4	0.1 M Glucose	40 kHz, 240 W	16.7*	8.35	34.8*	0.0005*	147

$Bi_2Fe_4O_9$	10% MeOH-DI	40 kHz, 200 W	11.4*	5.7*	28.5*	0.0004*	207
$Bi_4Ti_3O_{12}$	50% MeOH-DI	40 kHz, 300 W	13.5*	1.35*	4.5*	0.00036*	208
Au-$Bi_4Ti_3O_{12}$	DI	40 kHz, 100 W	4*	0.2*	1.95*	0.00032*	105
$(Bi_{0.5}Na_{0.5})TiO_3$	10% MeOH-DI	40 kHz, 100 W	11.4*	0.38	3.8*	0.00091*	168
BTO powder	10% MeOH-DI	40 kHz 180 W	26.97*	0.9	5*	0.0012*	209
$SrTiO_3$/Pt	20% MeOH-DI	45 kHz, 60 W	~63*	~0.63*	~10.5*	0.0083*	210
BTO - nanosheets	15% Triethanolamine	40 kHz, 100 W	0.92*	0.09*	0.92*	0.00007*	211
$KNbO_3/MoS_2$/Pt	15% Triethanolamine	40 kHz, 110 W	1.92*	0.1*	0.87*	0.00014*	212
$Sr_{0.5}Ba_{0.5}Nb_2O_6$/ $Sr_2Nb_2O_7$	15% Triethanolamine	40 kHz, 110 W	1.1*	0.11*	1*	0.00005*	155
Bi_2WO_6	20% Triethanolamine	40 kHz, -n/a-	3.83*	0.2*	-n/a-	0.0003*	136
BTO nanosheets {001} facets	10% MeOH-DI	35 kHz, 180 W	15.25*	0.31*	1.72*	0.0007*	213
Ultrathin ZnS nanosheets	DI	27 kHz 100 W	5.4*	1.08	10.8*	0.00043*	149
0.7$BiFeO_3$–0.3BTO	50 ml H_2O/MeOH	40 kHz, 100 W	39.66*	1.32	13.22*	0.0032*	214
$PbTiO_3$/CdS	0.1 M Na_2S and 0.1 M Na_2SO_3.	40 kHz, 100 W	4.01*	0.40*	4.01*	0.00032*	215
$LiNbO_3$-type $ZnSnO_3$ nanowires (NWs)	50% EtOH-DI	40 kHz, 250 W	34.53*	3.45*	13.81*	0.001*	148
Nanofluid BTO	10% MeOH-DI	40 kHz, 60 W	132	13.2*	2200*	0.0174*	51
BTO/Pt	2% MeOH-DI	40 kHz, 60 W	255.02	30	500	0.034	This Work
BTO/Pt	DI	40 kHz, 60 W	9	1.06	17.65	0.0012	This Work

*Units were converted, or calculations made based on data provided in the reference.

In this study, energy efficiency calculations were conducted separately for two systems: the MeOH-DI mixture and the pure water system. The experimental energy efficiencies of the ultrasonication experiments can be approximated by comparing the calorific value of the hydrogen gas generated during the tests against the electrical energy consumed by the ultrasonication bath. Over the 13-hour duration of the experiment, the BTO/Pt catalyst sustained an average hydrogen production rate of 255.02 µmol h^{-1}. Given that hydrogen has a molar mass of 2.016 g mol^{-1}, this equates to a production of 0.514 mg(H_2) every hour. With the ultrasonic bath operating at a power of 60 watts, it consumes 0.06 kWh of energy over the period of one hour. The energy consumption per gram of H_2 can then be estimated as follows:

$$\frac{0.06\ kWh}{0.000514\ g(H_2)} = 116.732\ kWh\ g^{-1}(H_2) \quad \textbf{(Eq. 5.3)}$$

The energy content of the H_2 produced is calculated by multiplying the higher heating value of H_2 by the moles of H_2 produced. This yields

$$286\ kJ\ mol^{-1} * 0.00025502\ mol = 0.0729\ kJ \ \textbf{(Eq. 5.4)}$$

In this study, the energy consumption of the ultrasonic bath, which is noted in kWh, is considered. For the purpose of precise scientific analysis and to facilitate the comparison with other energy measurements, it is often necessary to convert this value into kJ. The conversion factor is given as $1\ kWh\ equals\ 3.6\ MJ$.

To demonstrate this conversion, let us consider an experimental session where the ultrasonic bath consumes 0.06 kWh. The energy consumption in MJ can be calculated as follows:

$$0.06\ kW\ h * 3.6\ MJ\ kW\ h^{-1} = 0.216\ MJ \ \textbf{(Eq. 5.5)}$$

Since 1 MJ is equivalent to 1000 kJ, further conversion yields the energy consumption in kilojoules: Therefore, the energy used by the ultrasonic bath for the specified experimental conditions is 216 kJ.

To calculate the energy conversion efficiency for the production of hydrogen (H_2) as part of a long-duration experiment, the following relationship can be used:

$$Efficiency\ (\eta) = \frac{Energy\ Output}{Energy\ Input} * 100\% \ \textbf{(Eq. 5.6)}$$

Here, energy output refers to the energy content of the produced hydrogen, and energy input is the energy used to produce the hydrogen. Given that the energy content of the hydrogen produced is 0.0729 kJ and the energy input is 216 kJ,

$$\eta = \frac{0.0729\ kJ}{216\ kJ} = 0.03375\% \ \textbf{(Eq. 5.7)}$$

Therefore, the calculated energy conversion efficiency for the hydrogen production in this experimental setup is approximately 0.034%.

Given an electromechanical coupling coefficient of BTO at 0.49,[35] and a theoretical yield of hydrogen at maximum efficiency of 49%, the relative efficiency of the experiment based on its actual efficiency, which is 0.034%, can be determined using this formula:

$$Relative\ Efficiency = \frac{Experimental\ Efficiency}{Theoretical\ Maximum\ Efficiency} * 100\% \ \textbf{(Eq. 5.8)}$$

$$Relative\ Efficiency = \frac{0.0344\%}{49\%} * 100\% \ \cong \ 0.1\ \% \ \textbf{(Eq. 5.9)}$$

Based on the prior calculations performed for the MeOH-DI system, the energy output from hydrogen generated via pure water can be similarly considered, which is calculated as follows:

$$286\ kJ\ mol^{-1}\ *\ 0.000009\ mol\ =\ 0.002574\ kJ\ \textbf{(Eq. 5.10)}$$

Given that the ultrasonic bath uses 216 kJ of energy per hour, the overall energy conversion efficiency for the pure DI water experiment can be calculated:

$$\frac{0.002574\ kJ}{216\ kJ} * 100\% \cong 0.0012\% \ \textbf{(Eq. 5.11)}$$

When assessing the efficiency of the system studied, it is important to consider not just the energy content of the produced hydrogen, but also the presence of byproducts like hydrogen peroxide (H_2O_2). The formation of H_2O_2 indicates that additional redox reactions are occurring beyond just hydrogen generation. These extra reactions can impact the calculated efficiency. Furthermore, the energy required to drive these electrochemical reactions leading to H_2O_2 production needs to be factored into the efficiency calculation. As reported by Liu *et al.*,[216] an electrochemical potential of 1.76 eV is thermodynamically necessary to enable the chemical reactions that form H_2O_2. Therefore, to evaluate the overall energy efficiency of this system, the value of the hydrogen may be considered together with the energy demands associated with facilitating the additional redox reactions that produce H_2O_2 as a byproduct.

$$E_{chemical}\ =\ 2n_{H_2}E_tN_Ae\ \textbf{(Eq. 5.12)}$$

$$\Rightarrow 2\ *\ 0.000009\ mol\ H_2 *\ 1.76 *\ 6.023 *\ 10^{23} * 1.602\ *\ 10^{-19}\ \textbf{(Eq. 5.13)}$$

$$\Rightarrow 3.05675\ J\ \approx 3.05675 * 10^{-6}\ MJ\ \textbf{(Eq. 5.14)}$$

Dividing Eq. 5.14 by $\frac{3.6\ MJ}{1\ kWh}$ gives:

$$E_{chemical} = \frac{3.05675 * 10^{-6}\ MJ}{\frac{3.6\ MJ}{1\ kWh}} \cong 0.85 *\ 10^{-6}\ kWh\ \textbf{(Eq. 5. 15)}$$

The energy conversion efficiency is then:

$$\frac{0.85 * 10^{-6}\ kWh}{0.06\ kWh} * 100\ \% \approx 0.0014\% \ \textbf{(Eq. 5.16)}$$

5.2.3 EXPLAINING THE MECHANISM OF PIEZOCATALYSIS

The mechanisms governing piezocatalysis, specifically those driving hydrogen production via sonochemical reactions, are not fully understood and continue to be a topic of active research. Two primary theories—energy band theory and the screening charge effect—are often considered to explain piezocatalytic activity. However, this alone doesn't fully account for the catalytic activity. Energy band theory suggests that mechanical stress modifies the electronic structure of the catalyst, resulting in band tilting. This alteration brings the conduction band closer to the reduction potential of hydrogen, facilitating electron transfer to hydrogen ions and thus promoting hydrogen generation.

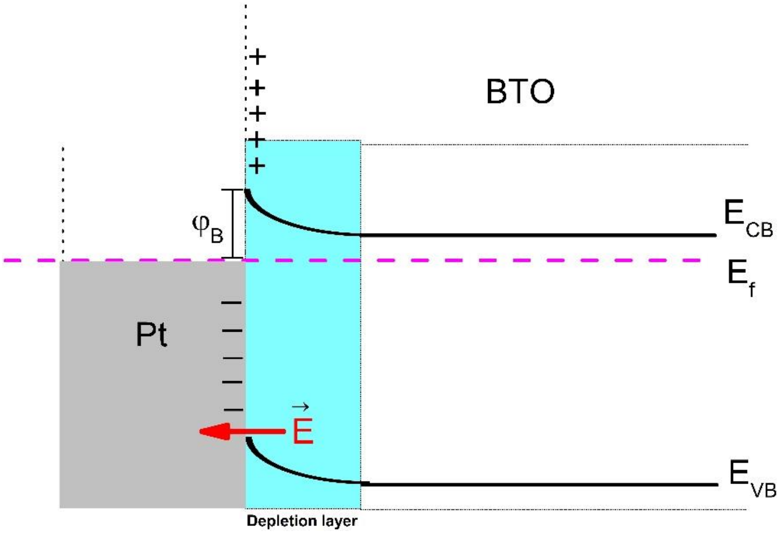

Figure 5.15 Illustration of a Schottky barrier formation where a ferroelectric material contacts Pt

The important observation is that a ferroelectric comes into contact with Pt, a Schottky barrier forms at their interface. This barrier arises from the difference in work functions between the two materials as depicted in **Figure 5.15**. For instance, the piezoelectric effect has the capability to modulate the barrier height at heterojunction interfaces and regulate the kinetics of reactions. It is noteworthy that the ferroelectric characteristics of BTO result in band bending at the juncture between the ferroelectric material and the metal (**Figure 5.16(a)**). This phenomenon is becoming more comprehensively understood in ferroelectric systems and relates to the intrinsic depolarisation field present within such materials. Upon the application of mechanical stress, the intrinsic depolarisation field within piezoelectric materials is modified, an occurrence associated to the direct piezoelectric effect. As a result, mobile charge carriers within the material are displaced and migrate in response to the changes in the depolarisation field.

At the same time, spatial charge separation serves to reduce the likelihood of electron-hole recombination. Lower recombination leads to higher carrier densities available for redox reactions that are central to the catalytic process. Prior research[217] have shown that acoustic excitation in piezoelectric materials can influence the recombination of charge carriers through band tilting effects.

A similar mechanism is proposed for piezocatalysis, wherein the coupled mechanical energy assists in band tilting, which facilitates charge separation, as shown in **Figure 5.16(b)**. This is further illustrated by the graphical representation of the piezocatalysis process mechanism (**Figure 5.17**). When ultrasound is applied, it causes the band structure to oscillate, which promotes the movement of electrons over the barrier between BTO and Pt. This action leads to a spatial separation of mobile charge carriers and forms a diode-like barrier that prevents the reverse flow of electrons. Pt acts as an electron sink through this interaction, which postpones the recombination of charge carriers while promoting the rapid reduction of protons on the surface of the Pt cocatalyst. Advancing the understanding of semiconductor-metal interfacial interactions, the piezoelectric effect presents a method to adjust the interfacial barrier height. This introduces a novel approach to modulate the band structure at the interface without physical modification or rearrangement of its chemical composition.[37]

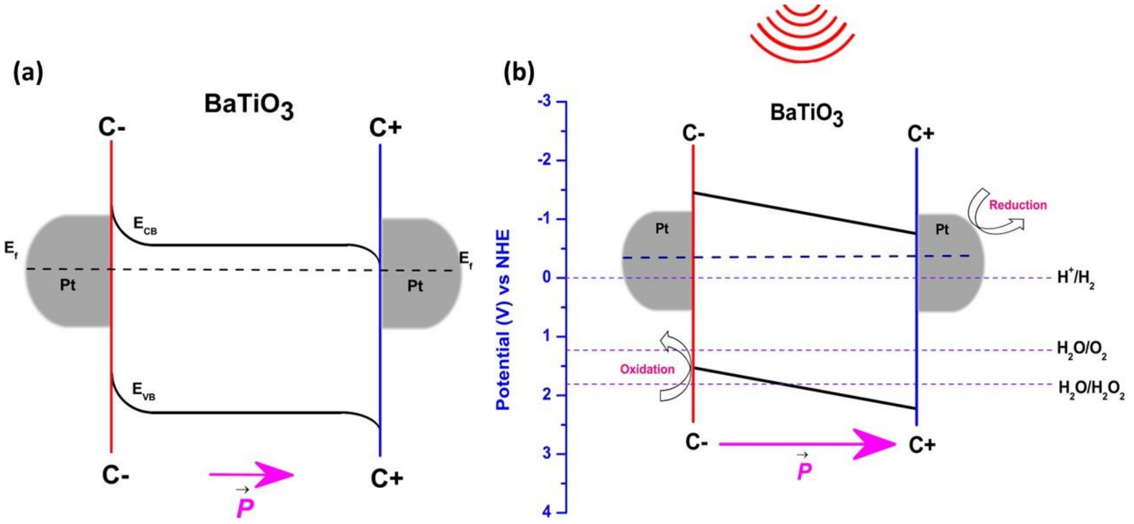

Figure 5.16 Schematic representation of the mechanism of piezocatalysis

(a) After contact, Pt metal and BTO exhibit band bending due to intrinsic polarisation

(b) Band tilting occurs as a result of exerted mechanical input energy, i.e., during ultrasonication

While the exact processes governing piezocatalysis remain under debate, it is suggested that the piezoelectric effect and alterations in the electronic band structure of the catalyst play roles in enhancing catalytic performance. The present study emphasises piezoelectric effects and the integration of a cocatalyst with ferroelectric material, reporting an increase fourfold of hydrogen production rates compared to pristine BTO. The influence of sonochemical effects due to acoustic cavitation is also acknowledged. The current aim is to enhance and demonstrate increased activity, with future research planned to deepen the understanding of the underlying operational processes, as the mechanisms of piezocatalysis remain an open field for investigation.

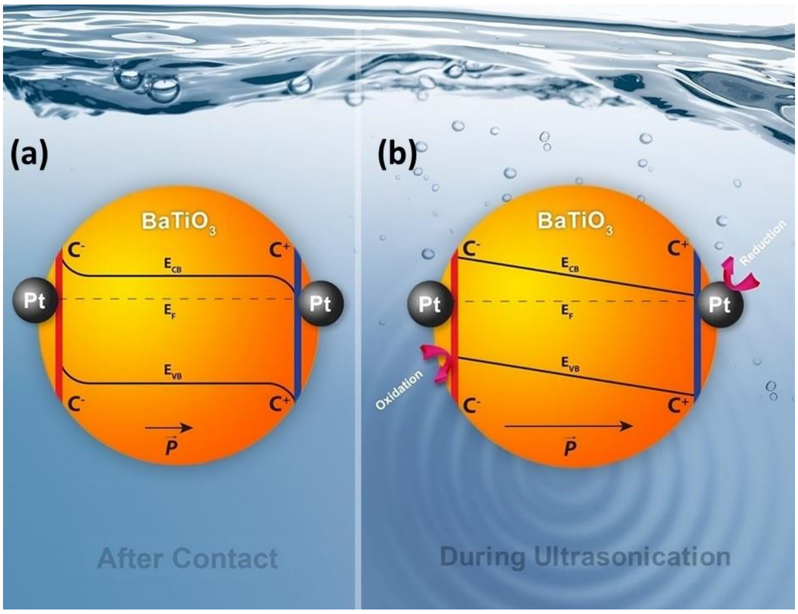

Figure 5.17 Graphical representation of the mechanism of piezocatalysis

5.3 CONCLUSION

This study has successfully demonstrated the generation of hydrogen and hydrogen peroxide from water splitting using a BTO/Pt piezocatalyst, synthesised via a simple and scalable solid-state mixing method. The significant enhancements in reaction rates and proven efficiency underline the potential of piezocatalysis as a renewable source for valuable H_2 and H_2O_2. The primary objectives were to develop and evaluate a BTO/Pt cocatalyst for hydrogen production from water splitting. The key results have validated BTO/Pt as an effective catalyst for this application. The BTO/Pt cocatalyst was synthesised using a simple solid-state mixing technique, offering advantages over traditional wet chemical processes, particularity in the ease of scaling up and the independence from chemical solvents. This approach presents a practical option for industrial applications, with BTO's inherent ferroelectric properties making it an exceptional substrate for piezocatalysis.

Conversely, materials such as TiO_2 that lack such ferroelectric characteristics show much less efficacy. The addition of Pt nanoparticles as a cocatalyst, serving as catalytic hotspots for hydrogen evolution and facilitating electron transfer. The combined effect of ferroelectric BTO with Pt nanoparticles significantly enhances hydrogen generation compared to using the materials independently. Although the current results may not be fully optimised for H_2 generation, they are significant, demonstrating a fourfold increase in production and an efficiency of 0.034%.

These findings highlight the conversion of mechanical energy from ultrasonic vibrations into chemical energy. With continued fine-tuning of the cocatalyst and experimental conditions, further improvement in these efficiencies is achievable. Advancing the fundamental understanding of how piezocatalysis operates can lead to enhanced performance in activity, reaction specificity, and overall stability. Effective control and distribution of nanoparticles could enhance the performance of the piezocatalyst. In this study, the synthesis method, which is both simple and high-performing, demonstrates great promise for commercial hydrogen production.

Beyond hydrogen generation, piezocatalysis could hold promise for a range of renewable energy processes. The potential of hybrid systems that combine piezocatalysis with photocatalysis for water splitting, harnessing mechanical vibrations and solar power, is remarkable. This study significantly expands the application scope of piezocatalysis and paves the way for complex chemical transformations to be driven by mechanical forces.

CHAPTER 6. ENHANCING PIEZOCATALYTIC DYE DEGRADATION WITH BTO-METAL OXIDE HETEROSTRUCTURES

6.1 INTRODUCTION

Building on the advances explored in Chapter 4, this chapter delves into the scope of piezocatalytic dye degradation using BTO-metal oxides (CuO, Fe_2O_3, Co_3O_4, and NiO) as a pivotal component in wastewater treatment. The piezocatalytic properties of barium titanate enable it to convert vibrational energy, such as that from stirring, which can then drive the chemistry of organic dye pollutants. This process presents a novel and ecofriendly avenue to address the challenges of dyes in industrial waste. A critical aspect of this investigation involves dissecting the process parameters, such as the agitation speed and catalyst loading, which collectively can drastically influence the degradation efficiency. Equally significant is the search for the optimisation of these parameters to enhance the degradation process while maintaining economic feasibility and scalability for industrial applications. This chapter aims to reveal the subtle intricacies of the piezocatalytic mechanism and to refine the operational conditions to achieve maximal efficacy. To verify the theoretical factors of piezocatalysis with empirical evidence, this research incorporates a variety of analytical techniques. Such scrutiny aids in isolating the active species involved and in explaining the degradation pathways, thus providing an understanding of the underlying mechanisms. The findings suggested in this chapter seek to fortify the foundation laid in previous sections and to propel piezocatalysis from a promising prospect to a practical solution for dye pollution. In the pursuit of environmental sustainability, the work presented here synthesises the collective efforts, aiming to enrich the environmental remediation.

6.2 RESULTS AND DISCUSSION

XRD patterns of BTO-metal oxide composites showing diffraction peaks indicative of the crystalline structure of barium titanate and loaded metal oxides (CuO, NiO, Fe_2O_3, and Co_3O_4) as shown in **Figure 6.1(a)**. As found that there exist diffraction peaks with 2θ values was confirmed to tetragonal BTO phase, according to the JCPDS card no. 05-0626. Among them, the peak at 45° was split into two small peaks at 2θ = 44.8° for (002) and 45.4° for (200). The splitting was a typical feature of tetragonal BTO. Each metal oxide has a unique crystalline configuration, which is reflected in its XRD profile, thus allowing the identification of the structural differences between metal oxides based on their diffraction patterns.

Two diffraction peaks 31.3° (104) and 34.3° (110) corresponds to Fe_2O_3 (JCPDS card no. 33-0664). The diffraction peak of 35.6° (002) assigned to CuO (JCPDS card no.

05-661) and the diffraction peaks of 37.3° (111), 43.3° (200), and 62.9° (220) indexed to the characteristics of NiO (JCPDS card no. 47-1049). The diffraction peak at 36.9° (311) attributed to Co_3O_4 phase (JCPDS card no. 65-3103).

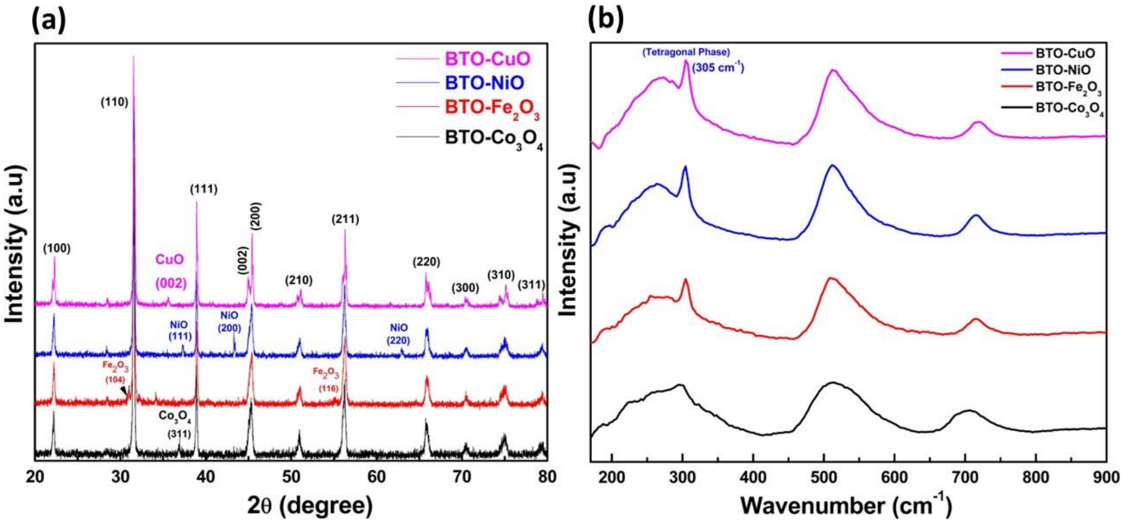

Figure 6.1 (a) XRD patterns of BTO-metal oxides and (b) Raman spectra of BTO-metal oxides

The peak of all metal oxides characteristics peak was observed in low intensity due to the low cocatalyst loading as discussed in **Section 3.1.3**. BTO-CuO exhibits a characteristic XRD pattern that hints at a tetragonal crystal structure, as evidenced by the peak splitting observed at 2θ = 45°. This peak splitting is a signature feature in the diffraction pattern, indicative of the tetragonal nature of the crystal lattice in BTO-CuO. In contrast, XRD patterns of other metal oxides may not display this specific peak splitting, suggesting that they might not have the tetragonal crystal structure characteristic of BTO.

To further confirm the tetragonal phase within each BTO-metal oxide composite, Raman spectroscopy was utilised in this study. The Raman spectra illustrate the characteristic vibrational modes of the tetragonal BTO phase and reveal the effects of metal oxide loading on lattice dynamics, focusing on the identification of distinct vibrational modes associated with ferroelectric order and tetragonal symmetry.

As shown in **Figure 6.1(b)**, Raman spectrum of tetragonal BTO-metal oxides (CuO, NiO, and Fe_2O_3) exhibits three prominent peaks at around 305 cm^{-1}, 515 cm^{-1}, and 717 cm^{-1} which corresponds to perovskite phase of barium titanate in the tetragonal phase. The presence of characteristic modes associated with ferroelectric order around 305 cm^{-1} and tetragonal symmetry at around 717 cm^{-1}. However, the peak at 305 cm^{-1} for the BTO-Co_3O_4 composite is not pronounced. In conjunction with the XRD results, this suggests that the BTO-Co_3O_4 composite does not exhibit a tetragonal structure. For other BTO-metal oxide composites, aside from BTO-CuO, the peak at 305 cm^{-1} is less intense, indicating the possibility of a mixed presence of cubic and tetragonal phases. To gain a deeper understanding of the synthesis and crystal structure of BTO-metal oxides, Rietveld refinement analysis is necessary.

Importantly, this comprehensive analysis could elucidate the relationship between structural phases and catalytic behaviours particularly how surface modifications due to metal oxide interactions could impact piezocatalytic activity. This study is presently centered on the ferroelectric nature of BTO-metal oxide composites and the way in which metal oxide support may enhance piezocatalytic activity. The adsorptive properties of nanoparticles are vital to their role in degrading pollutants, as they directly affect the efficiency of catalysis by influencing surface interactions.

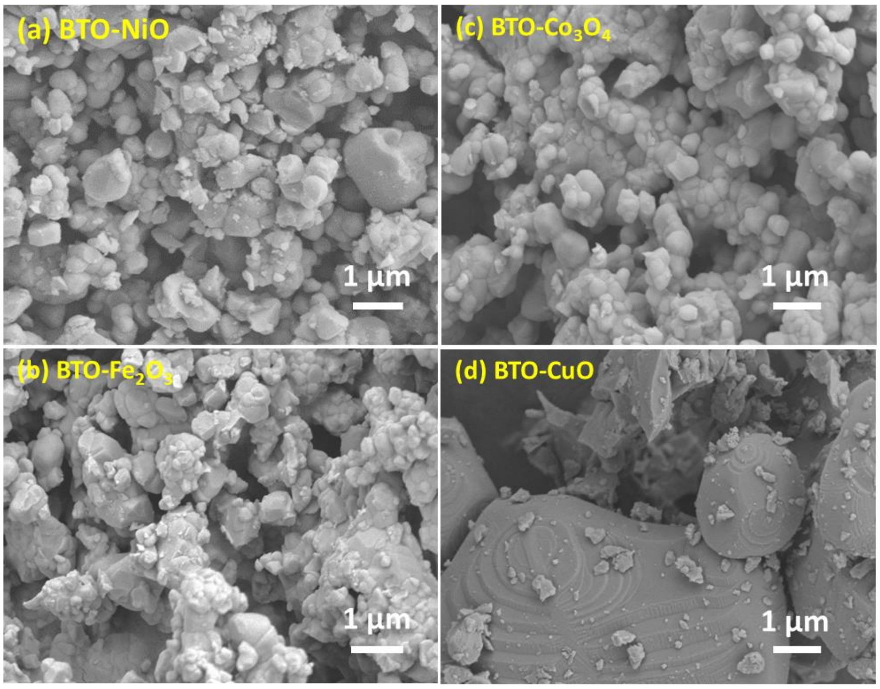

Figure 6.2 SEM of BTO-metal oxides (a) BTO-NiO, (b) BTO-Fe_2O_3, (c) BTO-Co_3O_4, and (d) BTO-CuO

To assess adsorption's impact on the degradation efficiency of BTO-metal oxide composites, nitrogen (N_2) adsorption-desorption isotherm analyses were conducted. These tests are critical for understanding the surface area and porosity of nanoparticles, which in turn affect their catalytic properties. It was observed that each nanoparticle sample displayed a distinguished and narrowly defined hysteresis loop, particularly within the relative pressure range of 0.05 to 0.25, indicating specific pore distribution and surface characteristics that may correlate with piezocatalytic performance. This finding is indicative of the complex interplay between material morphology and their related functional properties in environmental applications.

Correlating these isotherm results with the degradation performance suggests that the adsorption of dye molecules onto the nanoparticle surface is not the dominant mechanism responsible for the degradation. This conclusion is supported by the specific surface area values of the nanoparticles, which are relatively low and suggest a limited capacity for adsorption. The measured surface areas are as follows: BTO-Fe_2O_3 – 2.0196 m^2 g^{-1}, BTO-NiO – 1.2403 m^2 g^{-1}, BTO-Co_3O_4 – 1.0152 m^2 g^{-1} , and BTO-CuO – 0.5676 m^2 g^{-1}. Given the relatively low specific surface area values, there is an indicated limited adsorption capacity for these materials.

Figure 6.2 depicts the SEM micrographs of the BTO-metal oxides synthesised at 1200°C. During this thermal treatment, the non-ferroelectric copper oxide nanoparticles, each with a diameter of approximately 50 nm, fused onto the surface of BTO particles. At the sintering temperature of 1200°C, copper oxide was in a liquid phase, which facilitated its coating on the surface of the BTO particulates. This liquid sintering mechanism promoted increased crystallinity and peak splitting in the XRD pattern of BTO and enhance the piezoelectric properties,[218] as evidenced by the data in **Figure 6.2(d)**.

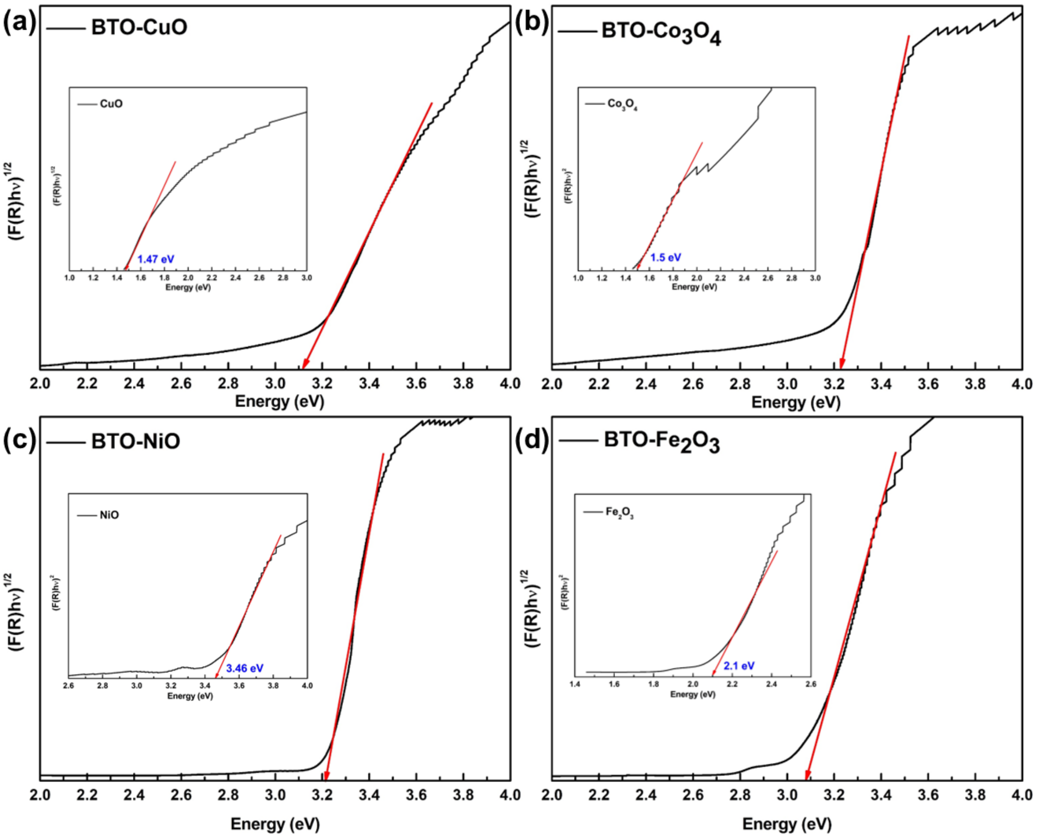

Figure 6.3 DRS-UV Band gap measurements for BTO-Metal oxide interfaces and pure metal oxides: Main **Figure**s show band gaps for (a) BTO-CuO, (b) BTO-Co_3O_4, (c) BTO-NiO, and (d) BTO-Fe_2O_3 composites, with insets highlighting the band gaps of the respective pure metal oxides

The improved crystalline quality of the BTO component resulting from the synthesis can be attributed to the liquid phase enhancing atomic diffusion and mass transport during particle consolidation at elevated temperature. The melting point of nanoparticles is influenced by various factors, including the specific composition, properties, and particle size. Generally, nanoparticles exhibit lower melting points than bulk materials because of their high surface area-to-volume ratio.[219] For example, copper oxide nanoparticles typically melt between 1200°C and 1300°C, the exact temperature depending on the size of the particles. In this study using commercial copper oxide powder with a particle size of approximately 50 nm in diameter, the synthesis of the BTO-CuO catalyst involved liquid sintering between powder particles, resulting in the formation of larger particles with sizes exceeding 2 to 3 µm. Subsequently, the synthesised material was grinded with a mortar and pestle for further analysis.

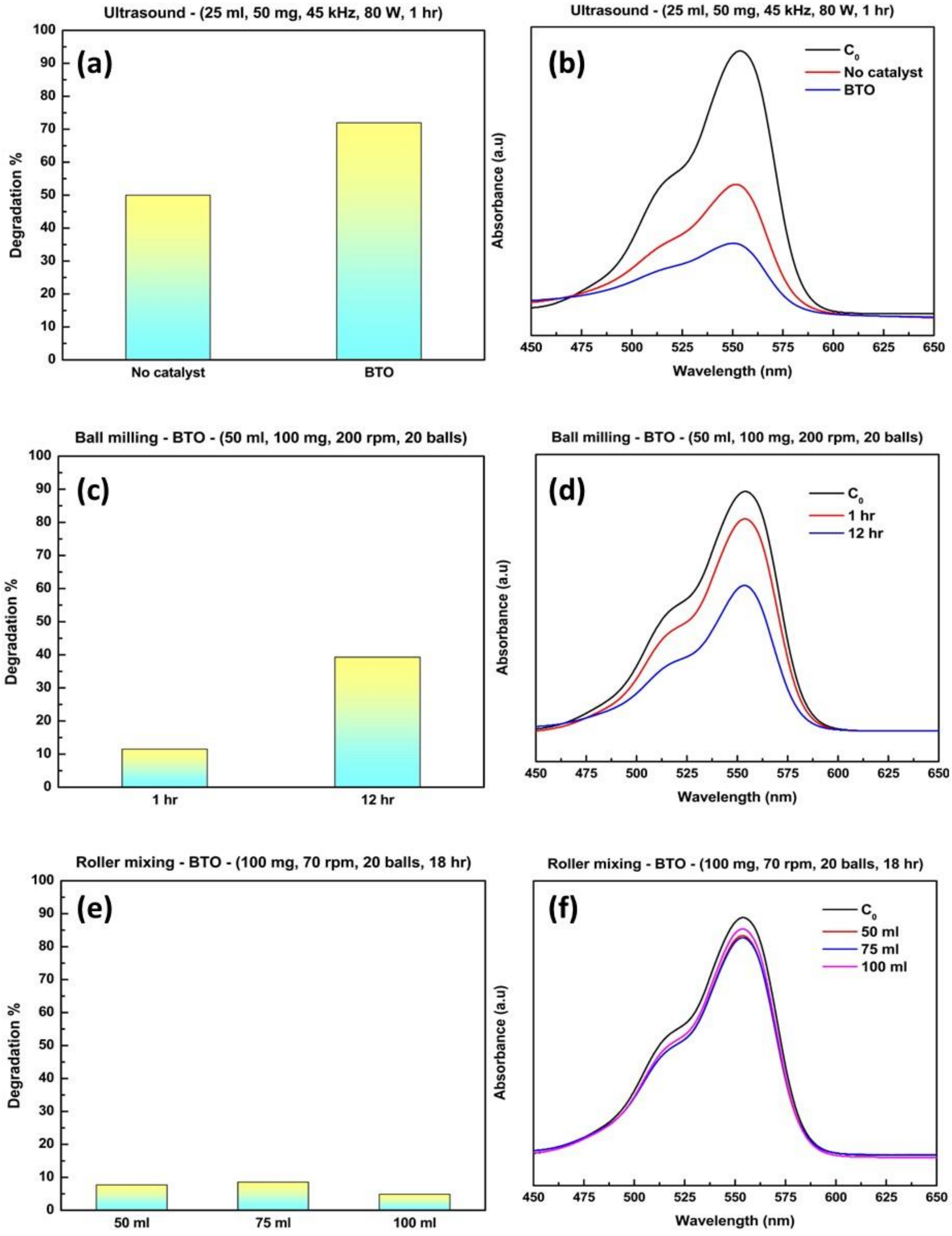

Figure 6.4 Degradation % and UV-Vis spectrum of BTO by using different input energy source for piezocatalytic studies (a,d) Ultrasound (b,e) Ball-milling (c,f) Roller-mixing

Furthermore, SEM observations revealed the random distribution of particles smaller than 1 µm in size in the larger powder particles. Overall, the presence of liquid phase copper oxide during sintering beneficially modified the microstructure and crystallinity of BTO in the piezocatalyst material. Furthermore, the effectiveness of ferroelectric piezocatalysts can be better understood by examining the band structures when different materials are combined, and the estimated band gap values were analysed through DRS-UV technique as shown in **Figure 6.3**.

To further investigate this potential, this study investigates various input energy sources for driving the piezocatalytic degradation process, including ultrasound, ball milling, and roller mixing (**Figure 6.4**). The efficacy of each method requires evaluation based on the optimisation of operational parameters, which followed standard laboratory-scale procedures. The results indicate that the ultrasound technique produces greater mechanical stress, leading to enhanced degradation percentages in comparison to other mechanical energy inputs. Clearly, piezocatalytic activity is influenced by both the input mechanical energy and the specific experimental conditions used. The primary aim of this research is to assess the effectiveness of piezocatalytic processes under conditions that utilise low-energy stirring as a mechanical input. This research provides valuable insights into ferroelectric catalytic systems, enhancing scientific understanding and informing the future development of highly efficient piezocatalysts, particularly through the investigation of RhB dye degradation. The degradation percentage of RhB, designated as ‘D’, is determined by measuring the absorbance initially and at time ‘t’, which is represented by **Eq.6.1**,

$$D = \frac{C_o - C_t}{C_o} * 100\% \quad \textbf{(Eq.6.1)}$$

‘$\mathrm{C_o}$’ represents the initial peak absorbance of the solution, indicating the concentration of RhB prior to degradation, while ‘$\mathrm{C_t}$’ denotes the peak absorbance recorded at a specific time during the process, reflecting the concentration post-degradation.

6.2.1 INFLUENCES ON PIEZOCATALYTIC EFFICIENCY: FROM STIRRING DYNAMICS TO ENVIRONMENTAL FACTORS

In the context of piezocatalysis, controlling the reaction volume is in fact an important factor as it influences the concentration of reactants and the distribution of stress in piezoelectric materials, which can affect the rate of catalytic reactions, as discussed in Chapter 4. However, for this particular set of experiments, the volume was kept constant (50 ml) to meticulously evaluate the effects of catalyst loading and stirring speed on dye degradation. This approach was taken to deliberately limit the number of variables and ensure that the observed results were attributed solely to the changes in catalyst concentration and mechanical agitation.

In future studies, investigating the influence of reaction volume on piezocatalytic efficiency could indeed offer valuable insights, but for the current experimental scope, maintaining a constant volume was necessary to yield clear, interpretable results regarding the relationship between stirring speed and catalyst loading. This controlled approach has yielded significant findings. The efficiency of piezocatalytic dye degradation is greatly influenced by the interaction of the stirring speed and catalyst loading. Initial observations at lower stirring speeds of 300 rpm and 500 rpm revealed an unexpected trend. With a catalyst loading of 1 mg per ml, dye degradation was relatively low, at 12% and 10%, respectively. Doubling the catalyst to 2 mg per ml at these speeds did not enhance the degradation efficiency as expected; degradation decreased to 5% at 300 rpm and even further to 4% at 500 rpm. It is hypothesised that at these lower agitation speeds, the higher catalyst concentration could lead to particle agglomeration, resulting in a reduced number of active sites for catalysis because of the decreased effective surface area.

A contrasting pattern emerged when the stirring speeds were increased to 700 rpm and 900 rpm. At 700 rpm with 1 mg per ml of catalyst, degradation saw an uplift to 18%, which is indicative of improved dye and catalyst interactions due to increased mixing. The system efficiency peaked at this stirring speed with a catalyst loading of 2 mg per ml, achieving a degradation of 36%, suggesting optimal dispersion and utilisation of the catalyst. At the highest stirring speed of 900 rpm, the degradation rates for loadings of 1 mg per ml and 2 mg per ml were 17% and 40%, respectively (**Figure 6.5**).

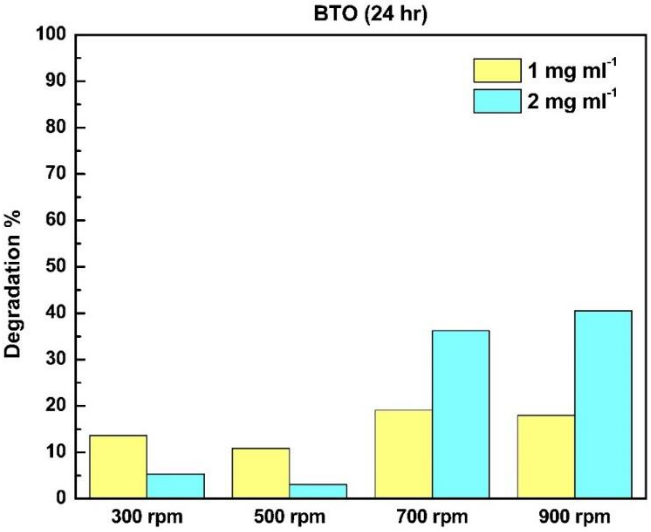

Figure 6.5 Impact of catalyst amount and agitation speed on reaction efficacy

At this speed, the kinetic energy of the system likely maximises reactant mixing and accessibility to catalytic sites, demonstrating that intensified agitation facilitates the breakdown of dye molecules more effectively. Collectively, these results emphasise the balance required for efficient piezocatalytic operations. Although mechanical agitation is crucial for ensuring reactants are well-dispersed and in close contact with catalyst particles, there is a clear threshold beyond which increased catalyst concentration can lead to aggregation, negatively impacting the degradation process.

On the contrary, at higher stirring rates, increased catalyst loading significantly amplifies efficiency, pointing toward the importance of optimising both the stirring speed and the catalyst concentration. This synergy between agitation and catalyst concentration has substantial implications for the scale-up of piezocatalytic processes, suggesting that careful optimisation can lead to more effective and sustainable wastewater treatment.

Building on the previous observations concerning the efficiency of piezocatalytic dye degradation and its dependency on stirring speed and catalyst loading, to evaluate the related energy consumption of the piezocatalytic process, a lab-scale energy monitor plug was used to monitor continuous magnetic stirring over a 24-hour period. The energy usage was found to be minimal for both high and low stirring speeds, recorded at 0.063 kWh for 900 rpm and 0.052 kWh for 300 rpm, respectively. This implies that the mechanical agitation contributed only slightly to overall energy consumption, where the slight increase at higher speeds could be due to the generation of frictional heat rather than an elevated demand on the stirring motor. These findings highlight the efficiency of the piezocatalytic process not only in terms of dye degradation but also in its low energy requirement, suggesting its suitability for sustainable and cost-effective scale-up applications.

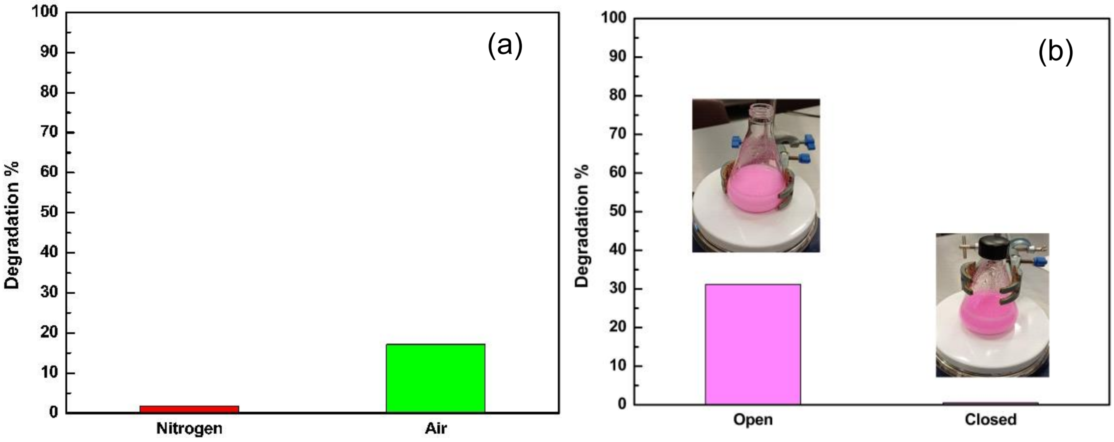

Figure 6.6 Variation in Piezocatalytic Performance under (a) N_2 and Air Conditions and (b) Open and Closed Erlenmeyer flasks

In assessing the influence of N_2 and air atmosphere on piezocatalytic activity, the experiments conducted show that the presence of atmospheric air and nitrogen significantly influences the degradation process of organic dyes when using BTO. The piezoelectric properties of BTO were utilised to induce charge separation under mechanical stress, which led to the generation of reactive oxygen species that notably increased the efficiency of dye degradation. The piezoelectric properties of BTO were leveraged to induce charge separation under mechanical stress, leading to the production of reactive oxygen species that significantly increased dye degradation efficiency. Initial results indicated that degradation rates were markedly higher in an air atmosphere, reaching 17%, as opposed to just 1.8% in a nitrogen atmosphere. The presence of atmospheric oxygen was found to be critical, driving redox reactions and enhancing the generation of ROS, which are vital for the effective catalytic breakdown of dye molecules.

Optimisation of experimental parameters uncovered that the use of 50 ml reaction volume with 100 mg of BTO catalyst over a period of 24 hours resulted in the most effective degradation under different atmospheric conditions. This was achieved through careful elimination of air in nitrogen-controlled experiments to highlight the comparison, employing a freeze-pump-thaw method and Schlenk-line techniques, ensuring precise control over the reaction's environmental exposure (**Figure 6.6(a)**). Furthermore, to investigate the impact of reactor configuration and oxygen interaction on the degradation capabilities of BTO, comparative experiments were conducted using both sealed and unsealed Erlenmeyer flasks. The results revealed that degradation rates were markedly greater in the unsealed flask than in the sealed one. These outcomes underscore the critical function of atmospheric oxygen in facilitating the degradation reaction. The open entry of air and the resultant turbulent mixing within the unsealed flask serve to enhance the reaction effectively, leading to a substantial uptick in the rate of degradation, as depicted in **Figure 6.6(b)**. These experiments collectively highlight the necessity of oxygen in the surrounding atmosphere for the efficient piezocatalytic degradation of organic dyes. Such results serve not only to expand the understanding of the BTO reaction dynamics but also underscore the importance of reactor design and environmental control in optimising catalytic processes for practical wastewater treatment.

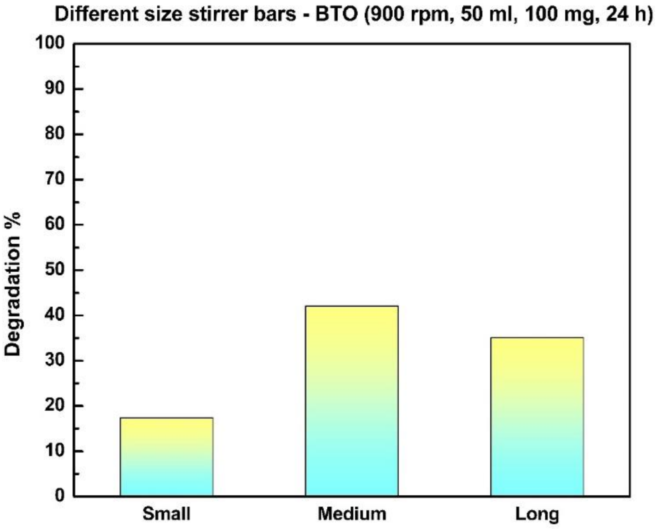

Figure 6.7 Variations in piezocatalytic performance with different stirrer bar sizes: An observational study

Furthermore, the data presented in **Figure 6.7** reveal that the size of the stir bar has a considerable impact on the piezocatalytic degradation efficiency of RhB with a BTO catalyst. Stir bars of medium and long lengths show substantially higher RhB degradation percentages, approximately 35-42%, in comparison to those observed with the small stir bar, which is around 17%. This suggests the importance of shear stress and turbulence in enhancing reactant mass transfer during the piezocatalytic process. While medium and long bars create more shear stress, leading to increased air integration, the negligible differences in degradation rates between them indicate the presence of an optimal flow regime for the piezocatalytic reaction.

Table 6.1 Physical specifications of varying ISOLAB stirrer bars and a VWR stirrer bar

ISOLAB stirrer bar	**Length (mm)**	**Thickness (mm)**	**Width (mm)**	**Mass (grams)**
Small	30.35	6.07	2.28	2.95
Medium	39.34	7.43	2.79	6.37
Long	50.86	8.12	2.85	10.22
VWR stirrer bar	**Length (mm)**	**Thickness (mm)**	**Width (mm)**	**Mass (grams)**
Long	50.4	7.2 mm	2.82	7.3

Table 6.2 Observed experimental phenomena at different stirring rates and catalyst loadings

Stirring Rate (rpm)	0 mg ml^{-1} (blank)			1 mg ml^{-1}			2 mg ml^{-1}		
	Dew	Splashes	Catalyst on side wall	Dew	Splashes	Catalyst on side wall	Dew	Splashes	Catalyst on side wall
300	X		-	X			X		
500	X		-	X			X		
700	X	X	-	X	X	X	X	X	X
900	X	X	-	X	X	X	X	X	X

There is a hypothesis that localised mixing around the medium bar promotes higher catalyst-dye interactions, as supported by **Table 6.1**, which indicates the dimensions of stirrer bars play a significant role in catalytic activity. The observed irregular wobbling of the magnetic bar with the medium and long stirrer bars may contribute to stress-induced catalyst activation. Further work is needed to fully elucidate the specific effects of stir bars on piezocatalytic performance. The degradation exhibited a slight difference when comparing the VWR stirrer bar with ISOLAB stirrer bars, indicating that the dimensions of the stirrer bar significantly influence the degradation of organic pollutants. **Table 6.2** presents the outcomes of piezocatalytic experiments performed at different stirring speeds (300, 500, 700, 900 rpm) and catalyst concentrations (0, 1, 2 mg/ml). The experiments noted three key observations: condensation forming on the underside of the watch glass above the beaker, liquid splashing, and the scattering of the catalyst along the inner walls of the reaction vessel. These phenomena help to understand the interactions between the mechanical stirring action and the piezocatalytic reaction as reported by Wu *et al.*,[220].

This research enhances the understanding of radical generation in the piezocatalytic processes of BTO, providing insights that are also applicable in the field of photocatalysis. Free radicals, being highly reactive species with unpaired electrons, play an indispensable role in catalytic reactions, including piezocatalysis. Although scavenging experiments are commonly conducted to trace radical formation, the Schneider *et al.*,[221] investigation suggests that the utility of scavengers, such as methanol (h^+) and p-benzoquinone ($^{\bullet}O_2^-$), may be limited due to their low specificity. These substances have been observed to produce various secondary radical species, which may interfere with the primary degradation pathway. Significantly, this study's findings caution against an overlook on scavengers for deducing systematic insights, as such an approach could unclear the true degradation mechanisms. The interact with other species presents in the system further complicates the degradation process.

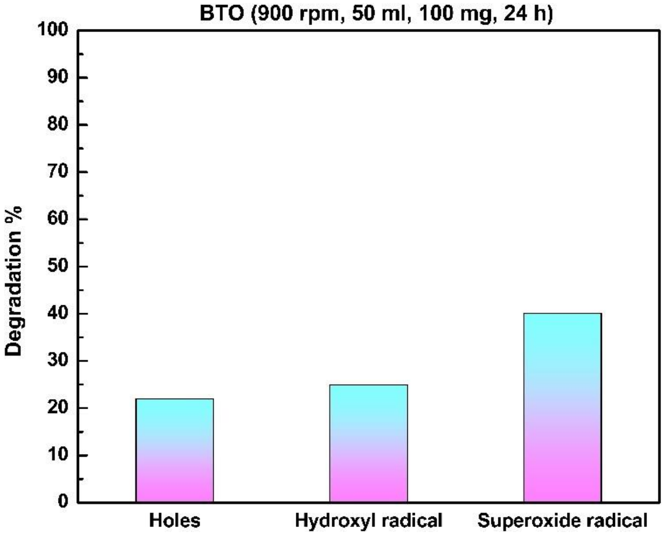

Figure 6.8 Impact of scavengers on the piezocatalytic degradation of dye using BTO, highlighting the role of various reactive species in the process

Therefore, a meticulous evaluation of scavenger species is imperative to enable a precise interpretation of the piezocatalytic degradation processes. **Figure 6.8** results suggest that the $^{\cdot}OH$ and h^+ radicals are generated and act as the primary reactive species in the piezocatalytic process. To delve into the intricacies of radical involvement in piezocatalytic processes, further investigation is paramount. A further approach to confirm the generation of radicals is the application of Electron Spin Resonance (ESR) techniques. This sophisticated method allows for the detection and identification of transient free radicals, providing direct evidence of their existence and behaviour during the piezocatalytic reaction. The data collected from ESR studies could not only validate the initial findings from the scavenger studies but also contribute a more comprehensive understanding of the mechanistic pathways involved in the reaction. Implementing this technique will enable a more precise characterisation of the radical species generated, thereby enhancing the overall insight into the piezocatalytic degradation process.

6.2.2 IMPROVING PIEZOCATALYTIC EFFICIENCY THROUGH THE USE OF METAL OXIDE COCATALYSTS

The experiment starts with control tests using no catalyst and alumina, a non-ferroelectric material, to establish a baseline for comparison with the ferroelectric barium titanate (BTO), as shown in **Figure 6.9(a)**.

Upon applying mechanical stirring as an external force, the degradation efficiencies observed were 8% for no catalyst, 6% for alumina, and 20% for BTO. Subsequently, adding metal oxides like Co_3O_4, Fe_2O_3, CuO, and NiO to BTO led to enhanced degradation percentages in all these metal oxide-loaded BTO experiments. However, BTO-Co_3O_4 and BTO-Fe_2O_3 exhibited lower degradation efficiencies compared to BTO-CuO and BTO-NiO, as evident from **Figure 6.9(b)**.

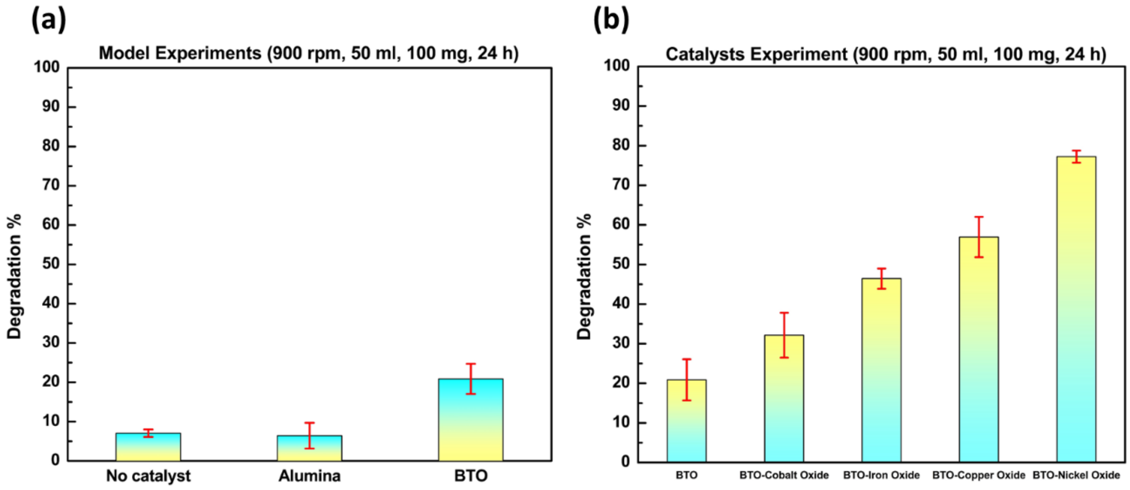

Figure 6.9 Investigating piezocatalytic reactions of (a) BTO-Metal oxides and (b) model experiments in the dark conditions

Structural analysis revealed that BTO-Co_3O_4 lacked tetragonal peak splitting at 2θ=45° in XRD analysis (**Figure 6.1(a)**) and the tetragonal phase peak at 305 cm^{-1} in Raman spectra (**Figure 6.1(b)**), indicating an absence of ferroelectric properties, which could contribute to its decreased degradation performance. In contrast, BTO-Fe_2O_3 displayed less intense tetragonal phase peaks, suggesting mixed phases that could interfere with polarisation. BTO-CuO exhibited peak splitting and a sharp tetragonal phase peak, while BTO-NiO showed a slight shoulder peak in XRD analysis and the sharp tetragonal phase peak in Raman Spectra.

The initial research examined the ferroelectric properties of piezoelectric mixed with metal oxides. This has been done without fully optimising the processes of material synthesis and catalyst application. The goal was to synthesise materials suitable for piezocatalysis studies with low-energy mechanical inputs. Attempts to explain the resulting data used the theory of energy band to understand the basic principles of heterostructure systems.

In piezocatalysis it is recognised that heterostructures that contain powdered nanostructured compounds show a greater catalytic efficiency compared to individual nanomaterials.[156,175,222,223] Effectiveness is influenced by the complexity of the heterostructure boundary, where interfacial charge and polarisation impacts are critical. The absence of these interfacial qualities can have a significant impact on piezocatalytic effectiveness. At these boundaries, the ferroelectric properties of the materials can lead to the production of surface charges that can be negative or positive as a result of ferroelectric polarization.

Although these charges can be generated by the piezoelectric effect, they may also reflect local chemical differences at the boundary. In general, the charges produced by ferroelectric polarisation tend to be larger than those caused by local chemical variations. For example, variations in electron affinity between materials can cause potential changes at the interface. This can lead to the bending of energy bands—the bending upwards with negative polarization or the bending downwards with positive polarisation.[224]

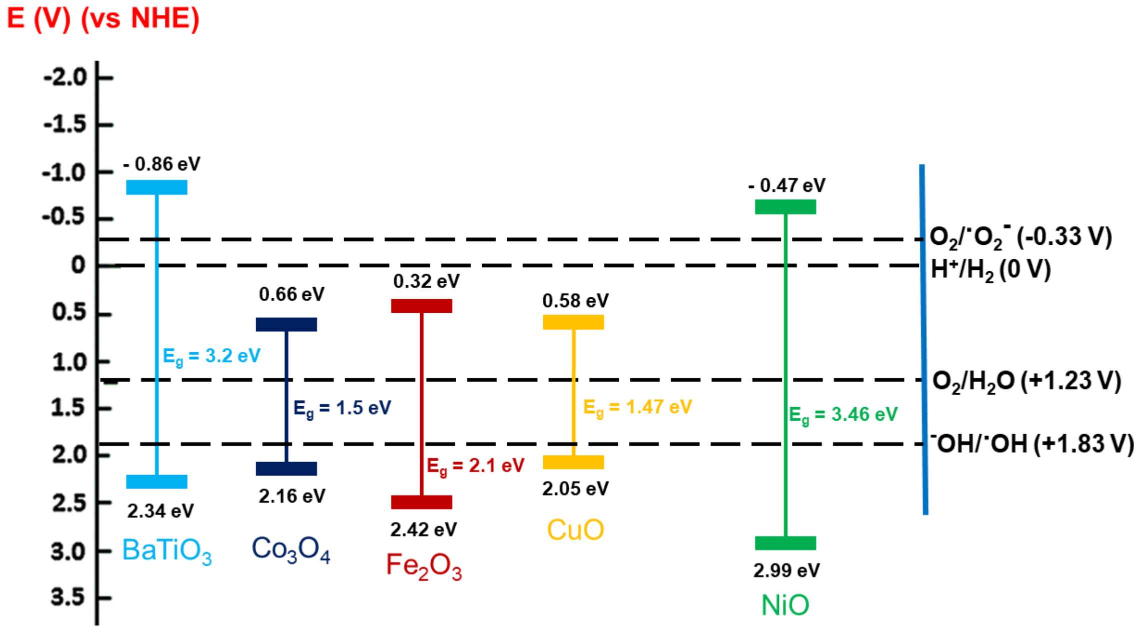

Figure 6.10 The band edge positions of oxidation and red studied semiconductor metal oxides are depicted in coloured bars.

To understand the mechanisms by which heterostructures of BTO-Metal oxides facilitate the catalytic reaction and the subsequent degradation of contaminants by the piezoelectric effect, a theoretical framework for charge transfer processes is proposed. The relative position of the band edges for BTO and metal oxides is determined by empirical equations, enabling basic charge dynamics responsible for the observed catalytic activity. The energies of the conduction and valence band positions can be calculated using,

Table 6.3 Calculated electronegativity, bandgap energies, and conduction and valence band edge potentials of various semiconductors

Metal oxide compounds	Absolute electronegativity (χ) (eV)	Estimated energy band-gap E_g (eV)	Calculated conduction band edge potential (eV)	Calculated valence band edge potential (eV)
$BaTiO_3$	5.24	3.2	-0.86	2.34
NiO	5.76	3.46	-0.47	2.99
CuO	5.81	1.47	0.58	2.05
Fe_2O_3	5.87	2.1	0.32	2.42
Co_3O_4	5.91	1.5	0.66	2.16

$$E_{CB} = \chi - E_e - (0.5 * E_g)$$ **(Eq. 6.2)**

$$E_{VB} = \chi - E_e + (0.5 * E_g)$$ **(Eq. 6.3)**

Where 'X' is the absolute electronegativity, E_g is the energy bandgap; E_{CB} and E_{VB} are the conduction band and valence band potentials, respectively. This formula considers the material's electronegativity, the energy level of free electrons on the hydrogen scale (E_e), and the material's own band gap energy. Based on formula, the conduction and valence band positions were calculated as depicted in **Table 6.3**. For n-type $BaTiO_3$, the Fermi level, which indicates the energy level at which electrical conduction occurs, is reportedly 0.1 eV below its conduction band edge.[189]

In a P-N type heterojunction, a combination of a p-type semiconductor, which predominantly carries positive charge carriers, and an n-type semiconductor, which predominantly carries negative charge carriers. The potentials at the bands are crucial as they determine the material's capability for engaging in redox reactions—specifically, the generation of reactive oxygen species such as hydroxyl radicals ($^{\cdot}OH$) and superoxide radicals ($^{\cdot}O_2^-$). These radicals act as effective oxidising agents and are important to the piezocatalytic breakdown of contaminants. Theoretical analysis suggests that in order to produce $^{\cdot}OH$ radicals, a semiconductor must have a positive valence band potential, one that is higher than the standard redox potential of the $^-OH/^{\cdot}OH$, which is +1.83 V vs NHE. In contrast, the formation of superoxide anion radicals ($^{\cdot}O_2^-$), necessitates that a semiconductor's conduction band potential be more negative than the standard redox potential of $O_2/^{\cdot}O_2^-$, which is -0.33 V vs NHE,[225] as depicted in **Figure 6.10**.

A possible piezocatalytic mechanism of BTO-CuO heterostructures is proposed as follows: the combination of the n-type semiconductor barium titanate (BTO) with the p-type semiconductor copper oxide (CuO) results in a composite material with good compatibility, largely due to the small difference in their lattice structures. Notably, when the nanocomposite is in contact with oxygen molecules, they are chemisorbed onto the surface. This adsorption creates a region on the surface where there are fewer electrons. Such a change lowers the concentration of adsorbed oxygen and increases the number of acceptor sites in the CuO part of the matrix. This alteration affects the electrical conductivity of the layer that interacts with surrounding species. Consequently, it increases the nanocomposite's resistance, and simultaneously, the energy barrier that forms at the junction between CuO and BTO becomes smaller.[222]

The research conducted by Joshi *et al.*,[226] provides significant advances in understanding the energetic dynamics at the nanointerface of CuO/BTO heterojunctions. Utilising DRS-UV, the investigation substantiates the formation of these type I heterostructures, characterised by an interfacial built-in potential and energy band bending. Energy band alignment analyses validate the classification of the heterostructure's band as type I (straddled band gap), depicting CuO's energy bands as intercalated within the energy bands of the tetragonal-structured BTO as depicted in **Figure 6.10**. Detailed investigations employing XPS are necessary to elucidate the fine particulars of this energetic configuration.[227] Moreover, the observed enhancement in photocatalytic efficiency with this straddled band gap arrangement, as reported by Joshi *et al.*,[226] should be considered.

Similarly, Naseri *et al.*,[228] studied type I heterostructures made of CuO and ZnO nanofibers. They proposed that when electrons from the conduction band of ZnO transfer to the CuO interface, it initiates a series of reactions governed by an interface charge transfer model.[229] A similar mechanism can be applied to the BTO-CuO heterostructure discussed here. It is assumed that holes from the valence band of BTO transfer to the valence band of CuO nanoparticles across the interface between the two materials. This transfer of holes helps collect them and reduces the recombination rate of electron-hole pairs generated by the piezoelectric effect in BTO.[230]

When mechanical stress is applied, the intrinsic piezoelectric properties of BTO cause positive and negative charges to accumulate on opposite sides of the material. This enhances the separation and transport of charge carriers (electrons and holes). If BTO has been electrically poled to increase its piezoelectric behaviour, this effect is expected to be even stronger, leading to improved piezocatalytic performance. Essentially, the piezoelectric effect in BTO aids in separating and transporting charges, while the BTO-CuO heterostructure facilitates charge transfer and collection, reducing recombination. This synergistic effect significantly enhances the catalytic function of the BTO-CuO heterostructures for applications like piezocatalysis. The unique properties of the BTO-CuO heterojunction facilitate efficient dynamics of charge carriers (electrons and holes), which is essential for advancing piezocatalytic applications, especially in degrading organic contaminants. However, in this study, the polarisation orientation of the ferroelectric BTO powder was not systematically controlled.

It has been suggested that the geometry and size of transition metal and metal oxide nanoparticles on ferroelectric substrates can significantly impact polarisation effects, either enhancing or reducing them. When metal oxide layers are too thick, their influence on polarisation declines, making them behave like non-polar systems. Cui *et al.*,[231] observed no impact on polarisation with nanoparticles smaller than 15 nm. In contrast, the 50 nm metal oxide nanoparticles used in this study may hinder polarisation effects. Therefore, the random orientation of polarisation in the BTO powder could explain the observed results. Considering the heterojunction formed between BTO and CuO, charge carriers migrate according to the alignment of their respective conduction and valence bands. While the BTO-CuO heterojunction facilitates efficient charge carrier dynamics for piezocatalysis, the lack of controlled polarisation orientation in the BTO powder and the relatively large size of CuO nanoparticles may have hindered the full potential of polarisation effects in this study.

From the XRD analysis, the BTO-NiO system may exhibit a mixed structure of cubic and tetragonal phases. However, Raman spectroscopy shows a prominent peak corresponding to the tetragonal phase. Considering the ferroelectric properties of BTO, it has a valence band potential of +2.34 eV. This potential is high enough to generate hydroxyl radicals ($^{\cdot}OH$) by oxidising OH^- ions in water. Conversely, NiO has a valence band potential of +2.99 eV, which also facilitates the generation of $^{\cdot}OH$ radicals. Additionally, NiO has a conduction band potential of -0.47 eV. This negative potential is sufficient to promote the reduction of oxygen (O_2) to superoxide radicals ($^{\bullet}O_2^-$), as it is more negative than the standard redox potential of $O_2/^{\bullet}O_2^-$. The valence band potentials of both BTO and NiO are favourable to generating hydroxyl radicals for oxidation reactions. Furthermore, the conduction band potential of NiO can facilitate the reduction of oxygen to superoxide radicals, which are highly reactive species beneficial for catalytic processes.

When NiO and BTO form a heterojunction, their energy bands align in a way that promotes charge separation and reduction of electron-hole recombination. Under mechanical stress (piezocatalysis), BTO generates electron-hole pairs. Due to the band alignment at the heterojunction interface, electrons tend to transfer from the conduction band (CB) of BTO to the CB of NiO, while holes move from the valence band (VB) of NiO to the VB of BTO. This charge transfer separates the electron-hole pairs, reducing their recombination rate. The built-in electric field at the interface, caused by band bending, further assists in separating the charges. The accumulated electrons in the NiO CB can then participate in reduction reactions, such as converting O_2 to superoxide radicals ($^{\bullet}O_2^-$). Simultaneously, the holes in the BTO VB can oxidise OH^- to form hydroxyl radicals ($^{\cdot}OH$).

This efficient separation and directed movement of charge carriers at the BTO-NiO heterojunction led to enhanced catalytic activity and improved piezocatalytic performance.

However, it's important to note that NiO itself, despite not being a strong piezoelectric material, can facilitate mechano-catalytic overall water splitting, as discussed by Ikeda *et al.*,[31,34], Domen *et al.*,[32], Hara *et al.*,[33,232]. These studies suggest that NiO can facilitate mechano-catalytic overall water splitting, although NiO is not regarded as a material with outstanding piezoelectric properties.[175]

Additionally, while the piezoelectric catalytic activity of the BTO-NiO heterostructure may improve with varying NiO concentrations, excessive NiO loading can cause agglomeration, reducing heterojunction structures and obstructing active sites on the BTO surface, thereby hindering piezocatalytic reactions. Several reports have highlighted the complexities involved in achieving optimal catalytic performance in piezocatalytic systems like BTO-metal oxide heterostructures. To enhance the efficiency of piezocatalytic activity, identifying the optimal concentration of the metal oxide during synthesis is crucial. In this study, prototyping was conducted using a BTO to metal oxide ratio of 1:10. However, future studies are needed to explore the impact of altering metal oxide loading concentrations as a key factor in improving the piezocatalytic performance.

A possible pathway of degradation process,

$$\text{BTO-metal oxide} \rightarrow h^+ + e^- \quad \textbf{(Eq. 6.4)}$$

$$h^+ + OH^- \rightarrow {}^{\cdot}OH \quad \textbf{(Eq. 6.5)}$$

$$e^- + O_2 \rightarrow {}^{\cdot}O_2^- \quad \textbf{(Eq. 6.6)}$$

$$\text{RhB} + {}^{\cdot}OH\ (h^+ \text{ or } {}^{\cdot}O_2^-) \rightarrow CO_2 + H_2O \quad \textbf{(Eq. 6.7)}$$

While the BTO-metal oxide heterostructures like BTO-NiO and BTO-CuO show synergistic effects in enhancing dye degradation rates under piezocatalysis, the exact mechanisms behind the performance enhancement by NiO particles under magnetic stirring are not entirely clear.

A crucial question that remains unanswered is how the composition of coating materials at the bottom of the reaction vessels can profoundly influence the catalytic activity of these metal oxide particles. The varying degrees of effectiveness among different metal oxide catalysts, as highlighted by Hara *et al.*,[33] pioneering work in 2000, continue to pose a significant challenge. Uncovering this could lead to a deeper understanding of piezocatalytic processes and advancements in the degradation of organic pollutants. This influence extends not only to the extent of dye breakdown but also to the specific pathways through which the degradation occurs. Recent findings by Cui *et al.*,[233], have confirmed NiO's exceptional capability among different metal oxides in producing hydrogen and oxygen from water through magnetic stirring. Complementary studies by Lei *et al.*,[234] have demonstrated the intricate tribo-catalytic effects of NiO particles that aid in converting water and carbon dioxide within reactors featuring various types of coated bases.

However, what remains unclear is why the two catalysts, BTO-NiO and BTO-CuO, despite their synergistic effects on dye degradation rates, exhibit differing efficiencies when it comes to the mechanisms and pathways of dye decomposition. These complex dynamics between their interactions with the reactor environment raise intriguing questions about the mechanistic pathways of dye degradation in piezocatalytic processes.

Further research is needed to examine these interactions and find the fundamental reasons behind these catalytic behaviours, which could unlock new avenues for the development of more effective methods for treating contaminated water. Insights can be gained by studying the interface behaviours between ferroelectrics and metal oxides, which are significantly influenced by the inherent properties of the metal oxides, such as their electronic structure and work function. These properties can alter the alignment of energy bands, modify energy barrier heights, and affect the band bending at the contact point with ferroelectrics. The behaviour of electrons at this interface, and thus the overall band alignment, can be influenced by the specific metal oxide chosen.

According to Rietwyk *et al.*,[235] the work functions of metal oxides such as CuO, NiO, Co_3O_4, and Fe_2O_3 can vary due to factors like crystal structure and synthesis methods. Detailed investigations, combining experimental and theoretical work, are crucial for understanding these effects. Techniques like Ultraviolet Photoelectron Spectroscopy (UPS) are critical in precisely characterising the work functions and Fermi levels in such materials, especially powders. Contemporary research is focusing on combining ferroelectric materials with metal oxides to unlock their potential for catalysing reactions via mechanical pressure in piezocatalysis while unveiling the complex underlying chemical mechanisms.

At this stage, a plausible explanation for the mechanism behind the differences in degradation rates in piezocatalytic activity resulting from mechanical stirring is yet to be established, as debates persist regarding the role of stirring—whether it induces tribocatalytic or piezocatalytic effects. From studies thus far, it is understood that the crystal structure of the synthesised heterostructure and its band diagram can provide a reasonable explanation for the mechanism. This domain presents a substantial opportunity for future research, anticipated to enhance the comprehensive understanding of the underlying processes.

In this study, reusability of the catalyst considered as a vital for environmental remediation methods, as it significantly influences the economic and environmental viability of the process. Recycling experiments were conducted wherein the piezocatalyst, after usage, was subjected to centrifuge-assisted separation, followed by washing procedures intended for its subsequent reuse. Unfortunately, the washing process led to a substantial loss of the piezocatalyst, indicating a need for strategies to mitigate this loss to ensure the process's viability on a larger scale as shown in **Figure 6.11**. The reduction in catalyst quantity between cycles implies that fresh catalyst must be added to maintain the degradation efficiency for each cycle of RhB treatment. Consequently, it became an operational requirement to replenish the RhB dye concentration to avoid the catalyst loss after every recycling attempt, ensuring consistency in experimental conditions and the reliability of the data obtained.

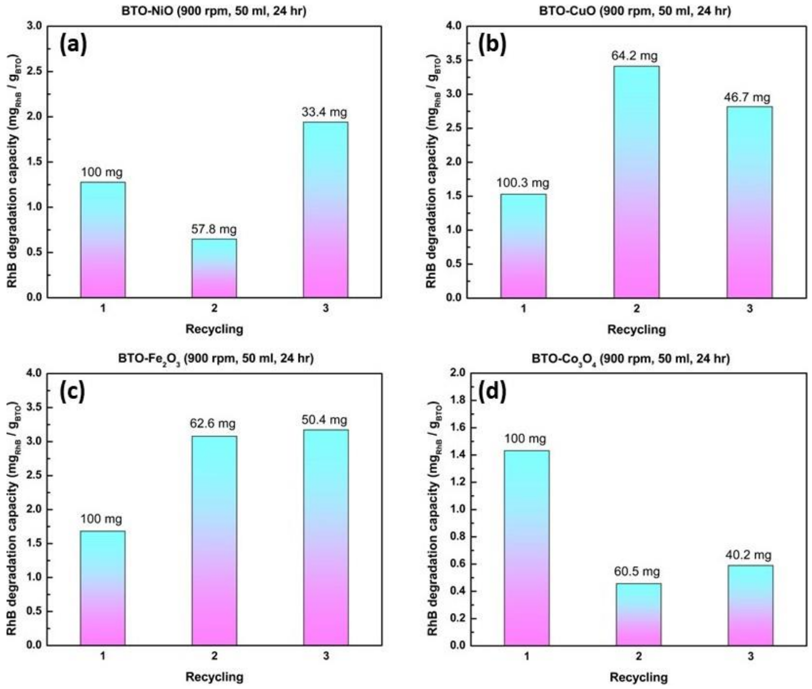

Figure 6.11 Cyclic performance of BTO-metal oxide composites in the piezocatalytic degradation of RhB over multiple recycling trials

Furthermore, the recycling efficiency of catalysts is a crucial factor in their practical application and economic feasibility. Typically, catalysts exhibit an initial period of stability where their activity remains stable, demonstrating high degradation efficiency. However, this is followed by a gradual decline in efficiency as the number of cycles increases. The rate and extent of this degradation can vary significantly depending on the catalyst's composition, reaction conditions, and recycle methods employed. Important factors contributing to catalyst degradation may include structural changes, surface fouling, chemical transformations, and physical degradation due to handling or reaction conditions. Understanding these degradation mechanisms is essential for developing strategies to extend catalyst lifespan, such as optimising reaction parameters and designing more robust catalysts. The shape of the degradation curve can provide insights into the degradation mechanisms and guide research efforts towards improving catalyst stability and recyclability as shown in **Figure 6.12**.

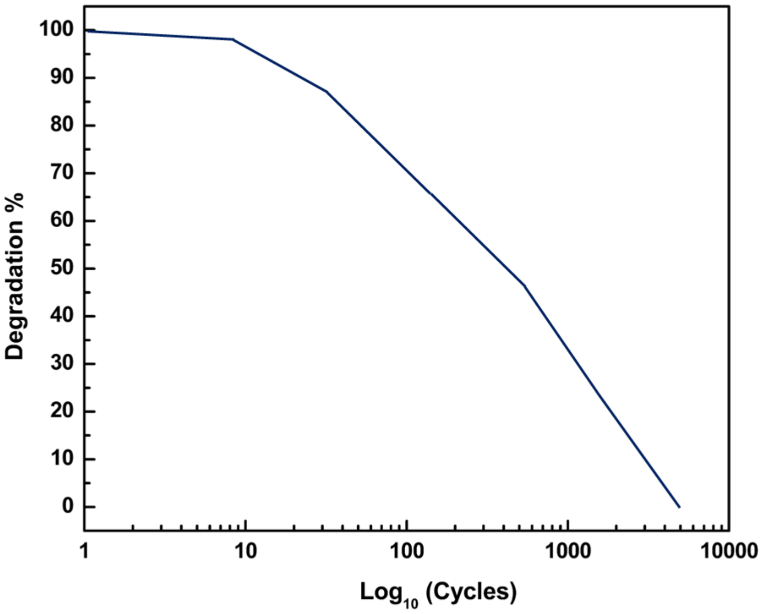

Figure 6.12 Illustrates a general trend observed in the degradation of catalyst performance over number of cycles

6.3 CONCLUSION

The piezocatalytic study investigated the degradation of RhB using BTO as the ferroelectric piezocatalyst material, combined with various metal oxides (Co_3O_4, Fe_2O_3, CuO, and NiO). The control experiments without a catalyst and with non-ferroelectric alumina established baseline degradation efficiencies. BTO exhibited a higher degradation efficiency than the controls, attributed to its ferroelectric properties. Structural analysis indicated that the absence of ferroelectric properties in BTO-Co_3O_4 contributed to decreased RhB degradation, while BTO-Fe_2O_3 exhibited mixed-phase structures potentially interfering with polarisation. BTO-CuO and BTO-NiO showed peak splitting and tetragonal phase peaks, aligning with favourable catalytic performance.

The study proposed a theoretical background based on energy band theory to understand the charge transfer processes in BTO-metal oxide heterostructures. The relative positions of the conduction and valence band edges were calculated, indicating the potential for generating reactive oxygen species (ROS) like hydroxyl and superoxide radicals, which play a crucial role in piezocatalytic degradation. The formation of BTO-CuO and BTO-NiO heterojunctions facilitated efficient charge separation and transport, thereby enhancing catalytic activity. The proposed mechanisms involve the migration of electrons and holes between the respective conduction and valence bands of BTO and the metal oxides, driven by the band alignment at the heterojunction interface. The study acknowledged the contribution of the mechano-catalytic effect, particularly for NiO, despite its non-piezoelectric properties. However, the influence of magnetic stirring on enhancing the catalytic activity of these particles remains unclear, warranting further investigation. The reusability of the piezocatalyst was addressed, revealing a substantial loss of catalyst during the washing process for recycling. This issue highlighted the need for strategies to mitigate catalyst loss and ensure the economic and environmental viability of the process on a larger scale.

Overall, the study provided insights into the piezocatalytic degradation of organic pollutants using BTO-metal oxide heterostructures, proposing theoretical mechanisms based on energy band theory and charge transfer processes. However, further research is necessary to optimise the synthesis procedures, catalyst loading, and catalyst recovery, as well as to elucidate the complex interactions between the catalysts and the reactor environment, which could lead to the development of more effective piezocatalytic systems for water treatment applications.

CHAPTER 7. CONCLUSION AND FUTURE WORK

In conclusion, this thesis successfully explored the potential of utilising the intrinsic polarisation field of ferroelectrics to enhance the efficiency of piezocatalytic processes such as hydrogen generation and dye degradation. By integrating a cocatalyst and leveraging both low- and high-energy inputs for mechanical stirring and ultrasound, the study sheds light on the innovative ways to catalyse these environmentally crucial reactions. The utilisation of a prototypical ferroelectric material $BaTiO_3$, chosen for its accessible ferroelectric phases, along with a facile synthesis approach, highlights a scalable and cost-effective pathway for synthesis of piezocatalysts. The investigative comparison of barium titanate across different temperatures has underscored the importance of structural analysis in optimising piezocatalytic activity.

This comprehensive approach not only demonstrates the promise of ferroelectric materials in catalysis but also sets the foundation for future research to refine such technologies for energy applications. With these insights, advancements in sustainable energy and environmental remediation can be anticipated, moving toward a cleaner and greener future. Building upon the foundational work of exploiting ferroelectric materials in piezocatalysis, the thesis delved into the synergistic effects that metal and metal oxide cocatalysts have on the overall mechanism within the composites. This exploration is pivotal because it opens avenues for further understanding the intricate relationship between ferroelectric materials and their cocatalysts, which is crucial for advancing the field of catalysis.

There is currently uncertainty regarding which mechanism—energy band theory or screening charge effect—applies to specific piezocatalytic reactions or materials. This ambiguity inhibits the application of only one theory to a given reaction system. It is critical to investigate and identify forms that could clearly indicate which mechanism is more suited for particular reactions, and also to define the conditions under which each theory operates effectively. Manipulating the conductivity of piezocatalysts may offer insights into distinguishing the actual mechanism for specific reactions. The energy band theory requires a precise understanding of the effect of piezoelectricity on semiconductor properties. A quantitative analysis is needed to elucidate the relationship between piezoelectric induced potential and its impact on band configuration, electronic energy levels, redox capacities, and charge migration kinetics. Experimental and theoretical approaches should be combined to bring further clarity to this aspect.

Investigating the screening charge effect demands in situ analysis of real-time piezocatalytic reactions to observe changes in surface potential, adsorption and movement of screening charges, and their eventual depletion. Advanced scanning probe microscopy techniques, like scanning surface potential microscopy and piezoresponse force microscopy, should be employed for this purpose. Since screening charges in piezocatalysis can derive from different sources, such as electrons, ions, holes, cationic vacancies, and polar molecules, it is necessary to examine how these varied charge carriers with distinct energy states influence the reactions. This research could yield new insights into the diverse effects of charge carriers on piezocatalytic processes. Sonochemical effects of ultrasound, which are often not accounted for, should not be neglected in piezocatalysis research. Control experiments must be conducted to isolate the influence of sonocatalysis from piezocatalysis, especially in applications like piezocatalytic water treatment, hydrogen peroxide synthesis, and reactive oxygen species generation. This will ensure that the observed piezocatalytic effects are not prevented by other unrelated chemical or physical processes. It is essential to implement appropriate control experiments to distinguish between the catalytic activities directly attributable to the piezoelectric effect and those that may result from ultrasound-induced acoustic cavitation or other source of mechanical input energy phenomena. This distinction is key in validating the effectiveness and understanding the unique properties of piezocatalysts.

Overall, the complexity of piezocatalytic systems calls for a comprehensive analysis that includes rigorous experimental controls, theoretical modelling, and in situ characterisation techniques. By doing so, researchers can provide a more complete picture of the piezocatalytic processes and their potential applications, while also setting a clear course for future innovation and optimisation in the field of piezocatalysis. Conducting control experiments to differentiate between sonocatalysis and piezocatalysis is crucial, as both processes can be involved in systems utilised for water treatment and generation of reactive oxygen species.

A clear distinction between these effects will allow for a more accurate understanding of piezocatalysis. By addressing these issues and considering these directives, it will be possible to better understand the fundamentals of piezocatalytic processes and to refine the design of efficient piezocatalytic systems for targeted applications. A multidisciplinary approach drawing from materials science, chemistry, physics, and engineering is recommended to tackle these complex issues and to advance the application of piezocatalysis as a sustainable technology. Further progress in this field will hinge on unravelling these complexities and leveraging the unique capabilities of piezocatalysts for environmental and energy-related applications. The research has established that the chemistry driving piezocatalytic processes is complex and continues to be the subject of ongoing investigations. This constant evolution of understanding reflects the promising yet rapidly developing nature of this area of study, indicating that there is still much to be understood about the underlying mechanisms.

Looking ahead, future research is focused on the profound effects that the composition, morphology, surface chemistry, and crystal structure of piezoelectric particles have on their catalytic behaviour. These factors are anticipated to be critical in fine-tuning the piezocatalytic properties and in maximising their efficiency. Hence, the work presented in this thesis not only contributes to the existing body of knowledge but also lays the groundwork for future advances that could enhance catalytic processes within the domains of sustainable energy and environmental remediation efforts.

REFERENCES

1 N. Meng, W. Liu, R. Jiang, Y. Zhang, S. Dunn, J. Wu and H. Yan, *Prog. Mater. Sci.*, 2023, **138**, 101161.

2 J. L. Giocondi and G. S. Rohrer, *J. Phys. Chem. B*, 2001, **105**, 8275–8277.

3 J. L. Giocondi and G. S. Rohrer, *Chem. Mater.*, 2001, **13**, 241–242.

4 Z. Zhang, P. Sharma, C. N. Borca, P. A. Dowben and A. Gruverman, *Appl. Phys. Lett.*, 2010, **97**, 243702.

5 T. L. Wan, L. Ge, Y. Pan, Q. Yuan, L. Liu, S. Sarina and L. Kou, *Nanoscale*, 2021, **13**, 7096–7107.

6 J. Garra, J. M. Vohs and D. A. Bonnell, *Surf. Sci.*, 2009, **603**, 1106–1114.

7 S. Shiva Kumar and V. Himabindu, *Mater. Sci. Energy Technol.*, 2019, **2**, 442–454.

8 G. Centi and J. Čejka, *ChemSusChem*, 2019, **12**, 621–632.

9 R. Al-Tohamy, S. S. Ali, F. Li, K. M. Okasha, Y. A.-G. Mahmoud, T. Elsamahy, H. Jiao, Y. Fu and J. Sun, *Ecotoxicol. Environ. Saf.*, 2022, **231**, 113160.

10 Z. Mamiyev and N. O. Balayeva, *Catalysts*, 2022, **12**, 1316.

11 M. D. Nothling, J. E. Daniels, Y. Vo, I. Johan and M. H. Stenzel, *Angew. Chem. Int. Ed.*, 2023, **62**, e202218955.

12 J. Zhu, L. Hu, P. Zhao, L. Y. S. Lee and K.-Y. Wong, *Chem. Rev.*, 2020, **120**, 851–918.

13 C. Wang, N. Tian, T. Ma, Y. Zhang and H. Huang, *Nano Energy*, 2020, **78**, 105371.

14 C. R. Bowen, H. A. Kim, P. M. Weaver and S. Dunn, *Energy Env. Sci*, 2014, **7**, 25–44.

15 J. Park, D.-G. Lee, S. Hur, J. M. Baik, H. S. Kim and H.-C. Song, *Actuators*, 2023, **12**, 177.

16 S. Li, Z. Zhao, J. Zhao, Z. Zhang, X. Li and J. Zhang, *ACS Appl. Nano Mater.*, 2020, **3**, 1063–1079.

17 H. Sudrajat, I. Rossetti and J. C. Colmenares, *J. Mater. Chem. A*, 2023, **11**, 24566–24590.

18 R. Djellabi, M. F. Ordonez, F. Conte, E. Falletta, C. L. Bianchi and I. Rossetti, *J. Hazard. Mater.*, 2022, **421**, 126792.

19 G.-J. Lee, E.-K. Park, S.-A. Yang, J.-J. Park, S.-D. Bu and M.-K. Lee, *Sci. Rep.*, 2017, **7**, 46241.

20 S. Shao, J. Zhang, Z. Zhang, P. Zheng, M. Zhao, J. Li and C. Wang, *J. Phys. Appl. Phys.*, 2008, **41**, 125408.

21 X.-L. Shi, H. Wu, Q. Liu, W. Zhou, S. Lu, Z. Shao, M. Dargusch and Z.-G. Chen, *Nano Energy*, 2020, **78**, 105195.

22 J. Valasek, *Phys. Rev.*, 1921, **17**, 475–481.

23 C. H. Ahn, K. M. Rabe and J.-M. Triscone, *Science*, 2004, **303**, 488–491.

24 K.-C. Kao, *Dielectric phenomena in solids: with emphasis on physical concepts of electronic processes*, Academic Press, Amsterdam ; Boston, 2004.

25 E. A. Neppiras, *J. Sound Vib.*, 1972, **20**, 562–563.

26 T. Hoshina, *J. Ceram. Soc. Jpn.*, 2013, **121**, 156–161.

27 S. Wada, H. Yasuno, T. Hoshina, S.-M. Nam, H. Kakemoto and T. Tsurumi, *Jpn. J. Appl. Phys.*, 2003, **42**, 6188–6195.

28 E. Kim, A. Steinbrück, M. T. Buscaglia, V. Buscaglia, T. Pertsch and R. Grange, *ACS Nano*, 2013, **7**, 5343–5349.

29 R. Asiaie, W. Zhu, S. A. Akbar and P. K. Dutta, *Chem. Mater.*, 1996, **8**, 226–234.

30 I. C. Amaechi, R. Katoch, G. Kolhatkar, S. Sun and A. Ruediger, *Catal. Sci. Technol.*, 2020, **10**, 6274–6284.

31 S. Ikeda, T. Takata, T. Kondo, G. Hitoki, M. Hara, J. N. Kondo, K. Domen, H. Hosono, H. Kawazoe and A. Tanaka, *Chem. Commun.*, 1998, 2185–2186.

32 K. Domen, S. Ikeda, T. Takata, A. Tanaka, M. Hara and J. N. Kondo, *Appl. Energy*, 2000, **67**, 159–179.

33 M. Hara, M. Komoda, H. Hasei, M. Yashima, S. Ikeda, T. Takata, J. N. Kondo and K. Domen, *J. Phys. Chem. B*, 2000, **104**, 780–785.

34 S. Ikeda, T. Takata, M. Komoda, M. Hara, J. N. Kondo, K. Domen, A. Tanaka, H. Hosono and H. Kawazoe, *Phys. Chem. Chem. Phys.*, 1999, **1**, 4485–4491.

35 K.-S. Hong, H. Xu, H. Konishi and X. Li, *J. Phys. Chem. Lett.*, 2010, **1**, 997–1002.

36 M. B. Starr, J. Shi and X. Wang, *Angew. Chem. Int. Ed.*, 2012, **51**, 5962–5966.

37 J. Shi and M. B. Starr, *Adv. Mater.*, 2012, **24**, 4683–4691.

38 Z. Zhang and J. T. Yates, *Chem. Rev.*, 2012, **112**, 5520–5551.

39 M. B. Starr and X. Wang, *Nano Energy*, 2015, **14**, 296–311.

40 M. B. Starr and X. Wang, *Sci. Rep.*, 2013, **3**, 2160.

41 K. Wang, C. Han, J. Li, J. Qiu, J. Sunarso and S. Liu, *Angew. Chem. Int. Ed.*, 2022, **61**, e202110429.

42 S. Chen, P. Zhu, L. Mao, W. Wu, H. Lin, D. Xu, X. Lu and J. Shi, *Adv. Mater.*, 2023, **35**, 2208256.

43 Y. Wang, X. Wen, Y. Jia, M. Huang, F. Wang, X. Zhang, Y. Bai, G. Yuan and Y. Wang, *Nat. Commun.*, 2020, **11**, 1328.

44 K. Kubota, Y. Pang, A. Miura and H. Ito, *Science*, 2019, **366**, 1500–1504.

45 M. Kumar, I. Kebaili, R. Vaish, J. El Ghoul and M. U. Khandaker, *Mater. Today Commun.*, 2023, **37**, 107306.

46 S. Dubey, A. Gaur, N. Alfryyan, Z. A. Alrowaili, M. S. Al-Buriahi and R. Vaish, *Int. J. Appl. Ceram. Technol.*, 2023, **20**, 3725–3734.

47 X. Liao, H. Xie, B. Liao, S. Hou, Y. Yu and X. Fan, *Nano Energy*, 2022, **94**, 106890.

48 C. Porwal, A. Gaur, V. S. Chauhan and R. Vaish, *Surf. Interfaces*, 2023, **42**, 103391.

49 L. Song, T. Zhang, S. Zhang, J. Wei and E. Chen, *ACS Sustain. Chem. Eng.*, 2022, **10**, 5129–5137.

50 M. Chai, W. Tong, Z. Wang, Z. Chen, Y. An and Y. Zhang, *J. Hazard. Mater.*, 2022, **430**, 128446.

51 Y. Zhang, H. Khanbareh, S. Dunn, C. R. Bowen, H. Gong, N. P. H. Duy and P. T. T. Phuong, *Adv. Sci.*, 2022, **9**, 2105248.

52 C. Xu, P. Ravi Anusuyadevi, C. Aymonier, R. Luque and S. Marre, *Chem. Soc. Rev.*, 2019, **48**, 3868–3902.

53 L. Liu and A. Corma, *Nat. Rev. Chem.*, 2021, **5**, 256–276.

54 L. Chen, J. Ren and Z. Yuan, *Adv. Energy Mater.*, 2023, **13**, 2203720.

55 Z. Jiang, X. Tan, J. Xu and Y. Huang, *ACS Appl. Nano Mater.*, 2022, **5**, 7588–7597.

56 J. Li, Z. Liu, J. Zhou and Z. Guo, *New J. Chem.*, 2022, **46**, 20844–20854.

57 M. R. Morris, S. R. Pendlebury, J. Hong, S. Dunn and J. R. Durrant, *Adv. Mater.*, 2016, **28**, 7123–7128.

58 G. Shu, Y. Lin, R. Zhong, X. Su, S. Guo, C. Wang, C. Zhou, L. Song, L. Xie, K. Ma and H. Yue, *Chem. Eng. J.*, 2023, **463**, 142310.

59 H. Wang, H. Zhang, Z. Long and H. Shi, *Catal. Sci. Technol.*, 2023, **13**, 2239–2246.

60 D. You, L. Liu, Z. Yang, X. Xing, K. Li, W. Mai, T. Guo, G. Xiao and C. Xu, *Nano Energy*, 2022, **93**, 106852.

61 I. C. Amaechi, A. Hadj Youssef, A. Dörfler, Y. González, R. Katoch and A. Ruediger, *Angew. Chem. Int. Ed.*, 2022, **61**, e202207975.

62 D. L. Chapman, *Lond. Edinb. Dublin Philos. Mag. J. Sci.*, 1913, **25**, 475–481.

63 M. Gouy, *J. Phys. Théorique Appliquée*, 1910, **9**, 457–468.

64 O. Stern, *Z. Für Elektrochem. Angew. Phys. Chem.*, 1924, **30**, 508–516.

65 Z. L. Wang and W. Wu, *Natl. Sci. Rev.*, 2014, **1**, 62–90.

66 G. Prasanna, H.-D. P. Nguyen, S. Dunn, A. Karunakaran, F. Marken, C. R. Bowen, B.-N. T. Le, H.-D. Nguyen and T.-P. T. Pham, *Nano Energy*, 2023, **116**, 108794.

67 Q. I. Rahman, A. Ali, N. Ahmad, M. B. Lohani, S. K. Mehta and M. Muddassir, *J. Nanosci. Nanotechnol.*, 2020, **20**, 7716–7723.

68 S. Asgari, G. Mohammadi Ziarani, A. Badiei and S. Iravani, *Mater. Adv.*, 2023, **4**, 6092–6117.

69 R. Francke and R. D. Little, *ChemElectroChem*, 2019, **6**, 4373–4382.

70 Y. Jiao and J. F. Stoddart, *Tetrahedron*, 2022, **126**, 133065.

71 X. Wang, J. Song, J. Liu and Z. L. Wang, *Science*, 2007, **316**, 102–105.

72 C. Pan, J. Zhai and Z. L. Wang, *Chem. Rev.*, 2019, **119**, 9303–9359.

73 X. Xu, Y. Jia, L. Xiao and Z. Wu, *Chemosphere*, 2018, **193**, 1143–1148.

74 Y.-M. You, W.-Q. Liao, D. Zhao, H.-Y. Ye, Y. Zhang, Q. Zhou, X. Niu, J. Wang, P.-F. Li, D.-W. Fu, Z. Wang, S. Gao, K. Yang, J.-M. Liu, J. Li, Y. Yan and R.-G. Xiong, *Science*, 2017, **357**, 306–309.

75 A. M. A. Leguy, J. M. Frost, A. P. McMahon, V. G. Sakai, W. Kockelmann, C. Law, X. Li, F. Foglia, A. Walsh, B. C. O'Regan, J. Nelson, J. T. Cabral and P. R. F. Barnes, *Nat. Commun.*, 2015, **6**, 7124.

76 W.-Q. Liao, D. Zhao, Y.-Y. Tang, Y. Zhang, P.-F. Li, P.-P. Shi, X.-G. Chen, Y.-M. You and R.-G. Xiong, *Science*, 2019, **363**, 1206–1210.

77 K.-S. Hong, H. Xu, H. Konishi and X. Li, *J. Phys. Chem. C*, 2012, **116**, 13045–13051.

78 B. Yuan, J. Wu, N. Qin, E. Lin and D. Bao, *ACS Appl. Nano Mater.*, 2018, **1**, 5119–5127.

79 D. Liu, C. Jin, F. Shan, J. He and F. Wang, *ACS Appl. Mater. Interfaces*, 2020, **12**, 17443–17451.

80 H. Lin, Z. Wu, Y. Jia, W. Li, R.-K. Zheng and H. Luo, *Appl. Phys. Lett.*, 2014, **104**, 162907.

81 M. Wang, Y. Zuo, J. Wang, Y. Wang, X. Shen, B. Qiu, L. Cai, F. Zhou, S. P. Lau and Y. Chai, *Adv. Energy Mater.*, 2019, **9**, 1901801.

82 Dan Tan, M. Willatzen and Z. L. Wang, *Nano Energy*, 2019, **56**, 512–515.

83 K. H. Michel and B. Verberck, *Phys. Rev. B*, 2011, **83**, 115328.

84 K.-A. N. Duerloo, M. T. Ong and E. J. Reed, *J. Phys. Chem. Lett.*, 2012, **3**, 2871–2876.

85 Y. Su, L. Zhang, W. Wang, X. Li, Y. Zhang and D. Shao, *J. Mater. Chem. A*, 2018, **6**, 11909–11915.

86 K. Wang, D. Shao, L. Zhang, Y. Zhou, H. Wang and W. Wang, *J. Mater. Chem. A*, 2019, **7**, 20383–20389.

87 H. Wang, X. Zhang and Y. Xie, *ACS Nano*, 2018, **12**, 9648–9653.

88 L. B. Drissi, S. Sadki and K. Sadki, *J. Phys. Chem. Solids*, 2018, **112**, 137–142.

89 J. M. Wu, W. E. Chang, Y. T. Chang and C. Chang, *Adv. Mater.*, 2016, **28**, 3718–3725.

90 J.-H. Lin, Y.-H. Tsao, M.-H. Wu, T.-M. Chou, Z.-H. Lin and J. M. Wu, *Nano Energy*, 2017, **31**, 575–581.

91 M.-H. Wu, J.-T. Lee, Y. J. Chung, M. Srinivaas and J.-M. Wu, *Nano Energy*, 2017, **40**, 369–375.

92 J. M. Wu, Y.-G. Sun, W.-E. Chang and J.-T. Lee, *Nano Energy*, 2018, **46**, 372–382.

93 M. Xu, M. Lu, G. Qin, X. Wu, T. Yu, L. Zhang, K. Li, X. Cheng and Y. Lan, *Angew. Chem. Int. Ed.*, 2022, **61**, e202210700.

94 H.-Y. Lin, K. T. Le, P.-H. Chen and J. M. Wu, *Appl. Catal. B Environ.*, 2022, **317**, 121717.

95 P. T. Thuy Phuong, Y. Zhang, N. Gathercole, H. Khanbareh, N. P. Hoang Duy, X. Zhou, D. Zhang, K. Zhou, S. Dunn and C. Bowen, *iScience*, 2020, **23**, 101095.

96 G. Singh, M. Sharma and R. Vaish, *Commun. Mater.*, 2020, **1**, 100.

97 Y. Wang, Y. Xu, S. Dong, P. Wang, W. Chen, Z. Lu, D. Ye, B. Pan, D. Wu, C. D. Vecitis and G. Gao, *Nat. Commun.*, 2021, **12**, 3508.

98 H. Hu, W. Feng, X. Qian, L. Yu, Y. Chen and Y. Li, *Adv. Mater.*, 2021, **33**, 2005062.

99 X. Wang, X. Dai and Y. Chen, *Small*, 2023, **19**, 2301693.

100 S. Xu, W. Zhang, C. Wang, W. Peng, G. Shi, Z. Cui, P. Fu, M. Liu, Y. He, X. Qiao and X. Pang, *Polymer*, 2022, **252**, 124949.

101 S. Li, Z. Zhao, D. Yu, J.-Z. Zhao, Y. Su, Y. Liu, Y. Lin, W. Liu, H. Xu and Z. Zhang, *Nano Energy*, 2019, **66**, 104083.

102 H. Yu, J. Li, Y. Zhang, S. Yang, K. Han, F. Dong, T. Ma and H. Huang, *Angew. Chem. Int. Ed.*, 2019, **58**, 3880–3884.

103 H. Huang, S. Tu, C. Zeng, T. Zhang, A. H. Reshak and Y. Zhang, *Angew. Chem. Int. Ed.*, 2017, **56**, 11860–11864.

104 Q. Tang, J. Wu, X.-Z. Chen, R. Sanchis-Gual, A. Veciana, C. Franco, D. Kim, I. Surin, J. Pérez-Ramírez, M. Mattera, A. Terzopoulou, N. Qin, M. Vukomanovic, B. J. Nelson, J. Puigmartí-Luis and S. Pané, *Nano Energy*, 2023, **108**, 108202.

105 R. Lei, X. Fu, N. Chen, Y. Chen, W. Feng and P. Liu, *Catal. Sci. Technol.*, 2022, **12**, 7361–7368.

106 S. Tu, H. Huang, T. Zhang and Y. Zhang, *Appl. Catal. B Environ.*, 2017, **219**, 550–562.

107 Z. Kang, N. Qin, E. Lin, J. Wu, B. Yuan and D. Bao, *J. Clean. Prod.*, 2020, **261**, 121125.

108 X. Deng, P. Chen, R. Cui, W. Huang, Y. Wu, X. Wang and C. Deng, *Appl. Catal. B Environ.*, 2023, **339**, 123148.

109 A. Hao, X. Ning, Y. Cao, J. Xie and D. Jia, *Mater. Chem. Front.*, 2020, **4**, 2096–2102.

110 M. Kumar, R. Vaish and S. ben Ahmed, *J. Am. Ceram. Soc.*, 2022, **105**, 2309–2322.

111 F. Wang, J. Zhang, C.-C. Jin, X. Ke, F. Wang and D. Liu, *Nano Energy*, 2022, **101**, 107573.

112 R. Zhao, H. Zhu, L. Feng, Y. Zhu, B. Liu, C. Yu, S. Gai and P. Yang, *Small*, 2023, **19**, 2301349.

113 H. You, Z. Wu, L. Zhang, Y. Ying, Y. Liu, L. Fei, X. Chen, Y. Jia, Y. Wang, F. Wang, S. Ju, J. Qiao, C. Lam and H. Huang, *Angew. Chem. Int. Ed.*, 2019, **58**, 11779–11784.

114 W. Amdouni, M. Fricaudet, M. Otoničar, V. Garcia, S. Fusil, J. Kreisel, H. Maghraoui-Meherzi and B. Dkhil, *Adv. Mater.*, 2023, **35**, 2301841.

115 J. Long, Y. Qian, W. Tian, N. Li, D. Chen, Q. Xu, H. Li and J. Lu, *Chem. Eng. Sci.*, 2023, **278**, 118936.

116 D. Shao, L. Zhang, S. Sun and W. Wang, *ChemSusChem*, 2018, **11**, 527–531.

117 M. Ismail, Z. Wu, L. Zhang, J. Ma, Y. Jia, Y. Hu and Y. Wang, *Chemosphere*, 2019, **228**, 212–218.

118 M. Wu, J. Yong, H. Zhang, Z. Wang, Z. P. Xu and R. Zhang, *Adv. Healthc. Mater.*, 2023, **12**, 2301497.

119 D. Liu, Y. Song, Z. Xin, G. Liu, C. Jin and F. Shan, *Nano Energy*, 2019, **65**, 104024.

120 A. Ranjan, K.-Y. Hsiao, C.-Y. Lin, Y.-H. Tseng and M.-Y. Lu, *ACS Appl. Mater. Interfaces*, 2022, **14**, 35635–35644.

121 D.-M. Liu, J.-T. Zhang, C.-C. Jin, B.-B. Chen, J. Hu, R. Zhu and F. Wang, *Nano Energy*, 2022, **95**, 106975.

122 J. Jang, K. Kim, J. Yoon and C. B. Park, *Biomaterials*, 2020, **255**, 120165.

123 S. Masimukku, Y.-C. Hu, Z.-H. Lin, S.-W. Chan, T.-M. Chou and J. M. Wu, *Nano Energy*, 2018, **46**, 338–346.

124 Y. Zhang, X. Huang and J. Yeom, *Nano-Micro Lett.*, 2019, **11**, 11.

125 Y. Feng, L. Ling, Y. Wang, Z. Xu, F. Cao, H. Li and Z. Bian, *Nano Energy*, 2017, **40**, 481–486.

126 W. Tong, Y. Zhang, H. Huang, K. Xiao, S. Yu, Y. Zhou, L. Liu, H. Li, L. Liu, T. Huang, M. Li, Q. Zhang, R. Du and Q. An, *Nano Energy*, 2018, **53**, 513–523.

127 Y. Bai, J. Zhao, Z. Lv and K. Lu, *Ceram. Int.*, 2019, **45**, 15065–15072.

128 A. Biswas, S. Saha and N. R. Jana, *ACS Appl. Nano Mater.*, 2019, **2**, 1120–1128.

129 J. Dolai, A. Biswas and N. R. Jana, *ACS Appl. Nano Mater.*, 2022, **5**, 14038–14050.

130 F. Meng, Z. Wang, B. Huo, J. Wang, D. Li, W. Hao, W. Ma, J. Qi, P. Cui, Z. Zhu and Y. Wang, *Appl. Surf. Sci.*, 2023, **619**, 156782.

131 P. Li, C. Tang, X. Xiao, Y. Jia and W. Chen, *Friction*, 2022, **10**, 1127–1133.

132 Z. Ren, J. Xie, X. Li, L. Guo, Q. Zhang, J. Wu, Y. Li, W. Liu, P. Li, Y. Fu, K. Zhao and J. Ma, *J. Colloid Interface Sci.*, 2023, **632**, 271–284.

133 Y. Qin, M. Zhu, Y. Tang, X. Chen, F. Wang and X. Fan, *Chem. Eng. J.*, 2023, **469**, 143911.

134 J. Ayarza, Z. Wang, J. Wang, C.-W. Huang and A. P. Esser-Kahn, *ACS Macro Lett.*, 2020, **9**, 1237–1248.

135 R. Su, H. A. Hsain, M. Wu, D. Zhang, X. Hu, Z. Wang, X. Wang, F. Li, X. Chen, L. Zhu, Y. Yang, Y. Yang, X. Lou and S. J. Pennycook, *Angew. Chem. Int. Ed.*, 2019, **58**, 15076–15081.

136 X. Xu, L. Xiao, Z. Wu, Y. Jia, X. Ye, F. Wang, B. Yuan, Y. Yu, H. Huang and G. Zou, *Nano Energy*, 2020, **78**, 105351.

137 C. Wang, C. Hu, F. Chen, T. Ma, Y. Zhang and H. Huang, *Nano Energy*, 2023, **107**, 108093.

138 R. Chauhan, G. K. Dinesh, B. Alawa and S. Chakma, *Chemosphere*, 2021, **277**, 130324.

139 S. S. Rashwan, I. Dincer, A. Mohany and B. G. Pollet, *Int. J. Hydrog. Energy*, 2019, **44**, 14500–14526.

140 B. S. Massey and A. J. Ward-Smith, *Mechanics of fluids*, Taylor & Francis, London ; New York, 8th ed., 2006.

141 X. Chen, L. Liu, Y. Feng, L. Wang, Z. Bian, H. Li and Z. L. Wang, *Mater. Today*, 2017, **20**, 501–506.

142 J. Shi, S. Yang, Z. Zheng, J. Li, L. Wang, W. Zeng, L. Yang, Y. Xiong, Z. Jin and X. Tao, *J. Mater. Chem. A*, 2023, **11**, 7596–7604.

143 S. Lan, B. Jing, C. Yu, D. Yan, Z. Li, Z. Ao and M. Zhu, *Small*, 2022, **18**, 2105279.

144 Y. Feng, H. Li, L. Ling, S. Yan, D. Pan, H. Ge, H. Li and Z. Bian, *Environ. Sci. Technol.*, 2018, **52**, 7842–7848.

145 R. Zhu, Y. Xu, Q. Bai, Z. Wang, X. Guo and H. Kimura, *Chem. Phys. Lett.*, 2018, **702**, 26–31.

146 S. Zhou, J. Hao, M. Zhou, X. Qiao and X. Pang, *Appl. Catal. Gen.*, 2022, **629**, 118406.

147 C. Hu, F. Chen, Y. Wang, N. Tian, T. Ma, Y. Zhang and H. Huang, *Adv. Mater.*, 2021, **33**, 2101751.

148 Y. Wang and J. M. Wu, *Adv. Funct. Mater.*, 2020, **30**, 1907619.

149 W. Feng, J. Yuan, L. Zhang, W. Hu, Z. Wu, X. Wang, X. Huang, P. Liu and S. Zhang, *Appl. Catal. B Environ.*, 2020, **277**, 119250.

150 F. Mushtaq, X. Chen, M. Hoop, H. Torlakcik, E. Pellicer, J. Sort, C. Gattinoni, B. J. Nelson and S. Pané, *iScience*, 2018, **4**, 236–246.

151 M. Banoo, R. S. Roy, M. Bhakar, J. Kaur, A. Jaiswal, G. Sheet and U. K. Gautam, *Nano Lett.*, 2022, **22**, 8867–8874.

152 Y. Lin, S. Lai and J. M. Wu, *Adv. Mater.*, 2020, **32**, 2002875.

153 X. Zhou, B. Shen, A. Lyubartsev, J. Zhai and N. Hedin, *Nano Energy*, 2022, **96**, 107141.

154 Y. Cheng, J. Chen, P. Wang, W. Liu, H. Che, X. Gao, B. Liu and Y. Ao, *Appl. Catal. B Environ.*, 2022, **317**, 121793.

155 J. Dai, N. Shao, S. Zhang, Z. Zhao, Y. Long, S. Zhao, S. Li, C. Zhao, Z. Zhang and W. Liu, *ACS Appl. Mater. Interfaces*, 2021, **13**, 7259–7267.

156 X. Zhou, S. Wu, C. Li, F. Yan, H. Bai, B. Shen, H. Zeng and J. Zhai, *Nano Energy*, 2019, **66**, 104127.

157 S. Jia, Y. Su, B. Zhang, Z. Zhao, S. Li, Y. Zhang, P. Li, M. Xu and R. Ren, *Nanoscale*, 2019, **11**, 7690–7700.

158 L. Shi, C. Lu, L. Chen, Q. Zhang, Y. Li, T. Zhang and X. Hao, *J. Alloys Compd.*, 2022, **895**, 162591.

159 C. Yu, M. Tan, Y. Li, C. Liu, R. Yin, H. Meng, Y. Su, L. Qiao and Y. Bai, *J. Colloid Interface Sci.*, 2021, **596**, 288–296.

160 T. Cheng, W. Gao, H. Gao, S. Wang, Z. Yi, X. Wang and H. Yang, *Mater. Res. Bull.*, 2021, **141**, 111350.

161 E. Lin, J. Wu, N. Qin, B. Yuan and D. Bao, *Catal. Sci. Technol.*, 2018, **8**, 4788–4796.

162 J. Dolai, A. Biswas, R. Ray and N. R. Jana, *ACS Appl. Mater. Interfaces*, 2022, **14**, 26443–26454.

163 Y. Wei, Y. Zhang, W. Geng, H. Su and M. Long, *Appl. Catal. B Environ.*, 2019, **259**, 118084.

164 R. Lei, X. Fu, N. Chen, Y. Chen, W. Feng and P. Liu, *Catal. Sci. Technol.*, 2022, **12**, 7361–7368.

165 X. Zhou, F. Yan, B. Shen, J. Zhai and N. Hedin, *ACS Appl. Mater. Interfaces*, 2021, **13**, 29691–29707.

166 J. Feng, J. Sun, X. Liu, J. Zhu, Y. Xiong and S. Tian, *Environ. Sci. Nano*, 2019, **6**, 2241–2252.

167 G. Yang, Q. Chen, W. Wang, S. Wu, B. Gao, Y. Xu, Z. Chen, S. Zhong, J. Chen and S. Bai, *ACS Appl. Mater. Interfaces*, 2021, **13**, 15305–15314.

168 D. Liu, X. Sun, L. Tan, J. Zhang, C.-C. Jin and F. Wang, *Ceram. Int.*, 2023, **49**, 20343–20350.

169 W. Xu, K. Li, L. Shen, X. Liu, Y. Chen, J. Feng, W. Zhao, L. Zhao, W. Zhou, W. Wang and J. Li, *ChemCatChem*, 2022, **14**, e202200312.

170 E. Lin, Z. Kang, J. Wu, R. Huang, N. Qin and D. Bao, *Appl. Catal. B Environ.*, 2021, **285**, 119823.

171 X. Liu, L. Shen, W. Xu, W. Kang, D. Yang, J. Li, S. Ge and H. Liu, *Nano Energy*, 2021, **88**, 106290.

172 L. Wang, J. Wang, C. Ye, K. Wang, C. Zhao, Y. Wu and Y. He, *Ultrason. Sonochem.*, 2021, **80**, 105813.

173 K. Wang, Z. Guan, X. Liang, S. Song, P. Lu, C. Zhao, L. Yue, Z. Zeng, Y. Wu and Y. He, *Ultrason. Sonochem.*, 2023, **100**, 106616.

174 C. Yu, M. Tan, C. Tao, Y. Hou, C. Liu, H. Meng, Y. Su, L. Qiao and Y. Bai, *J. Adv. Ceram.*, 2022, **11**, 414–426.

175 K. Wang, B. Li, C. Zhao, S. Yuan, C. Zhang, X. Liang, J. Wang, Y. Wu and Y. He, *Ultrason. Sonochem.*, 2023, **92**, 106285.

176 D. Masekela, N. C. Hintsho-Mbita, S. Sam, T. L. Yusuf and N. Mabuba, *Arab. J. Chem.*, 2023, **16**, 104473.

177 L. Chen, W. Zhang, J. Wang, X. Li, Y. Li, X. Hu, L. Zhao, Y. Wu and Y. He, *Green Energy Environ.*, 2023, **8**, 283–295.

178 M. Frank, Y. Bulut, L. Czympiel, R. Weißing, V. Nahrstedt, M. Wilhelm, M. Grosch, A. Raauf, A. Verma, T. Fischer and S. Mathur, *Nanotechnology*, 2021, **32**, 465601.

179 F. Peng, J. Lin, H. Li, Z. Liu, Q. Su, Z. Wu, Y. Xiao, H. Yu, M. Zhang, C. Wu, W. Wang and C. Lu, *Nano Energy*, 2022, **95**, 107020.

180 S. Zhang, D. Chen, Y. Guo, R. Zhang, Y. Zhao, Z. Huang, J. Fan, J. C. Ho and C. Zhi, *Mater. Today*, 2023, **66**, 17–25.

181 X. Dai, L. Chen, Z. Li, X. Li, J. Wang, X. Hu, L. Zhao, Y. Jia, S.-X. Sun, Y. Wu and Y. He, *J. Colloid Interface Sci.*, 2021, **603**, 220–232.

182 L. Chen, X. Dai, X. Li, J. Wang, H. Chen, X. Hu, H. Lin, Y. He, Y. Wu and M. Fan, *J. Mater. Chem. A*, 2021, **9**, 13344–13354.

183 P. T. T. Phuong, D.-V. N. Vo, N. P. H. Duy, H. Pearce, Z. M. Tsikriteas, E. Roake, C. Bowen and H. Khanbareh, *Nano Energy*, 2022, **95**, 107032.

184 J. Ma, S. Jing, Y. Wang, X. Liu, L. Gan, C. Wang, J. Dai, X. Han and X. Zhou, *Adv. Energy Mater.*, 2022, **12**, 2200253.

185 Y. Zhou, H. Wang, X. Liu, S. Qiao, D. Shao, J. Zhou, L. Zhang and W. Wang, *Nano Energy*, 2021, **79**, 105449.

186 B. D. Begg, K. S. Finnie and E. R. Vance, *J. Am. Ceram. Soc.*, 2005, **79**, 2666–2672.

187 H. Hayashi, T. Nakamura and T. Ebina, *J. Phys. Chem. Solids*, 2013, **74**, 957–962.

188 Y. Cui, J. Briscoe and S. Dunn, *Chem. Mater.*, 2013, **25**, 4215–4223.

189 Y. Cui, J. Briscoe, Y. Wang, N. V. Tarakina and S. Dunn, *ACS Appl. Mater. Interfaces*, 2017, **9**, 24518–24526.

190 P. Kumar, M. Prajapati, A. K. Das and S. K. Mitra, *Ind. Eng. Chem. Res.*, 2018, **57**, 6538–6552.

191 T. Mahmud, J. N. Haque, K. J. Roberts, D. Rhodes and D. Wilkinson, *Chem. Eng. Sci.*, 2009, **64**, 4197–4209.

192 D. Kim and D. Kim, *Chem. Eng. Sci.*, 2021, **243**, 116787.

193 M. Ji, J. H. Kim, C.-H. Ryu and Y.-I. Lee, *Nano Energy*, 2022, **95**, 106993.

194 H. You, X. Ma, Z. Wu, L. Fei, X. Chen, J. Yang, Y. Liu, Y. Jia, H. Li, F. Wang and H. Huang, *Nano Energy*, 2018, **52**, 351–359.

195 T. K. M. P. Kumar and S. K. A. Kumar, *Photochem. Photobiol. Sci.*, 2019, **18**, 148–154.

196 A. S. Aricò, A. K. Shukla, H. Kim, S. Park, M. Min and V. Antonucci, *Appl. Surf. Sci.*, 2001, **172**, 33–40.

197 Y. Wang, D. Zhao, H. Ji, G. Liu, C. Chen, W. Ma, H. Zhu and J. Zhao, *J. Phys. Chem. C*, 2010, **114**, 17728–17733.

198 S. Tu, Y. Guo, Y. Zhang, C. Hu, T. Zhang, T. Ma and H. Huang, *Adv. Funct. Mater.*, 2020, **30**, 2005158.

199 H. Kalhori, I. C. Amaechi, A. H. Youssef, A. Ruediger and A. Pignolet, *ACS Appl. Nano Mater.*, 2023, **6**, 1686–1695.

200 F. Bößl and I. Tudela, *Curr. Opin. Green Sustain. Chem.*, 2021, **32**, 100537.

201 I. E. L. Stephens, A. S. Bondarenko, U. Grønbjerg, J. Rossmeisl and I. Chorkendorff, *Energy Environ. Sci.*, 2012, **5**, 6744.

202 C. Wang, C. Hu, F. Chen, H. Li, Y. Zhang, T. Ma and H. Huang, *Adv. Funct. Mater.*, 2023, **33**, 2301144.

203 Y. Cui, F. Wang, P. Yuan, W. Liu, B. Fang, Z. Wang and Y. Pu, *ACS Sustain. Chem. Eng.*, 2024, **12**, 3595–3607.

204 A. Sharma, U. Bhardwaj, D. Jain and H. S. Kushwaha, *ACS Omega*, 2022, **7**, 7595–7605.

205 J. Wang, C. Hu, Y. Zhang and H. Huang, *Chin. J. Catal.*, 2022, **43**, 1277–1285.

206 W. Liu, P. Fu, Y. Zhang, H. Xu, H. Wang and M. Xing, *Proc. Natl. Acad. Sci.*, 2023, **120**, e2218813120.

207 Y. Du, T. Lu, X. Li, Y. Liu, W. Sun, S. Zhang and Z. Cheng, *Nano Energy*, 2022, **104**, 107919.

208 S. C. Chang, P.-H. Chen, Y.-C. Chen and J. M. Wu, *Int. J. Hydrog. Energy*, 2024, **50**, 15–25.

209 J. Ai, C. Jin, D. Liu, J. Zhang and L. Zhang, *ChemCatChem*, 2023, **15**, e202201316.

210 Y. Jiang, M. Li, Y. Mi, L. Guo, W. Fang, X. Zeng, T. Zhou and Y. Liu, *Nano Energy*, 2021, **85**, 105949.

211 C. Yu, M. Tan, Y. Li, C. Liu, R. Yin, H. Meng, Y. Su, L. Qiao and Y. Bai, *J. Colloid Interface Sci.*, 2021, **596**, 288–296.

212 S. Jia, Y. Su, B. Zhang, Z. Zhao, S. Li, Y. Zhang, P. Li, M. Xu and R. Ren, *Nanoscale*, 2019, **11**, 7690–7700.

213 Q. Tang, J. Wu, D. Kim, C. Franco, A. Terzopoulou, A. Veciana, J. Puigmartí-Luis, X. Chen, B. J. Nelson and S. Pané, *Adv. Funct. Mater.*, 2022, **32**, 2202180.

214 Y. Sun, X. Li, A. Vijayakumar, H. Liu, C. Wang, S. Zhang, Z. Fu, Y. Lu and Z. Cheng, *ACS Appl. Mater. Interfaces*, 2021, **13**, 11050–11057.

215 X. Huang, R. Lei, J. Yuan, F. Gao, C. Jiang, W. Feng, J. Zhuang and P. Liu, *Appl. Catal. B Environ.*, 2021, **282**, 119586.

216 J. Liu, Y. Zou, B. Jin, K. Zhang and J. H. Park, *ACS Energy Lett.*, 2019, **4**, 3018–3027.

217 S. Shoaee, J. Briscoe, J. R. Durrant and S. Dunn, *Adv. Mater.*, 2014, **26**, 263–268.

218 H. J. Lee, H. Ryu, M. Bae, Y. K. Cho and S. Nahm, *J. Am. Ceram. Soc.*, 2006, **89**, 3529–3532.

219 O. A. Yeshchenko, I. M. Dmitruk, A. A. Alexeenko and A. M. Dmytruk, *Phys. Rev. B*, 2007, **75**, 085434.

220 M. Wu, H. Lei, J. Chen and X. Dong, *J. Colloid Interface Sci.*, 2021, **587**, 883–890.

221 J. T. Schneider, D. S. Firak, R. R. Ribeiro and P. Peralta-Zamora, *Phys. Chem. Chem. Phys.*, 2020, **22**, 15723–15733.

222 S. Joshi, S. J. Ippolito, S. Periasamy, Y. M. Sabri and M. V. Sunkara, *ACS Appl. Mater. Interfaces*, 2017, **9**, 27014–27026.

223 A. Adiba, Waris, S. Munjal, M. Z. Khan and T. Ahmad, *Eur. Phys. J. Plus*, 2023, **138**, 408.

224 Y. Diamant, S. Chappel, S. G. Chen, O. Melamed and A. Zaban, *Coord. Chem. Rev.*, 2004, **248**, 1271–1276.

225 Y. Wen, M. Feng, P. Zhang, H.-C. Zhou, V. K. Sharma and X. Ma, *ACS EST Eng.*, 2021, **1**, 804–826.

226 S. Joshi, R. K. Canjeevaram Balasubramanyam, S. J. Ippolito, Y. M. Sabri, A. E. Kandjani, S. K. Bhargava and M. V. Sunkara, *ACS Appl. Nano Mater.*, 2018, **1**, 3375–3388.

227 M. T. Qamar, M. Aslam, I. M. I. Ismail, N. Salah and A. Hameed, *ACS Appl. Mater. Interfaces*, 2015, **7**, 8757–8769.

228 A. Naseri, M. Samadi, N. M. Mahmoodi, A. Pourjavadi, H. Mehdipour and A. Z. Moshfegh, *J. Phys. Chem. C*, 2017, **121**, 3327–3338.

229 S. J. A. Moniz and J. Tang, *ChemCatChem*, 2015, **7**, 1659–1667.

230 R. Marschall, *Adv. Funct. Mater.*, 2014, **24**, 2421–2440.

231 Y. Cui, S. M. Goldup and S. Dunn, *RSC Adv.*, 2015, **5**, 30372–30379.

232 M. Hara and K. Domen, *J. Phys. Chem. B*, 2004, **108**, 19078–19078.

233 X. Cui, H. Wang, H. Lei, X. Jia, Y. Jiang, L. Fei, Y. Jia and W. Chen, *ChemistrySelect*, 2023, **8**, e202204146.

234 H. Lei, X. Jia, H. Wang, X. Cui, Y. Jia, L. Fei and W. Chen, *Coatings*, 2023, **13**, 396.

235 K. J. Rietwyk, D. A. Keller, A. Ginsburg, H. Barad, M. Priel, K. Majhi, Z. Yan, S. Tirosh, A. Y. Anderson, L. Ley and A. Zaban, *Adv. Mater. Interfaces*, 2019, **6**, 1802058.

APPENDICES

APPENDIX A – PUBLICATIONS

(1) Prasanna *et al*., *Impact of stirring regime on piezocatalytic dye degradation using BaTiO$_3$ nanoparticles***.** Nano Energy, ISSN: 2211-2855, Vol: 116, Page: 108794.

APPENDIX B – INTERNATIONAL CONFERENCE AND RESEARCH EXCHANGE

1. Royal Society International Travel grant for Research Exchange

   Institute of Chemical Technology, Ho Chi Minh City, Vietnam – 25th February 2023 to 27th March 2023.

2. Presentation talk - BaTiO$_3$/Pt Hybrid Material for Enhanced Piezocatalytic H$_2$ Production

   12th Joint International Conference – Piezo2023 with Ferroelectrics: Electroceramics for End Users XII edition celebrated from 6th November 2023 to 8th November 2023 in Scotland.

APPENDIX C – LONDON SOUTH BANK UNIVERSITY SUMMER SCHOOL CONFERENCE

1. Poster Presentation

   1st Year LSBU Summer School 2020/2021.

2. Presentation talk – “The effects of sonochemical and piezo-sonochemical on the rate of hydrogen production”

   3rd Year LSBU Summer School 2022/2023.